2003

Electron collision studies of cesium using a magneto-optical trap.

John Alexander. MacAskill
University of Windsor

ELECTRON COLLISION STUDIES OF CESIUM USING A MAGNETO-OPTICAL TRAP

by
John Alexander MacAskill

A Dissertation
Submitted to the Faculty of Graduate Studies and Research
through the Department of Physics
in Partial Fulfilment of the Requirements for
the Degree of Doctor of Philosophy at the
University of Windsor

Windsor, Ontario, Canada

2003

ABSTRACT

Experiments involving a magneto-optical trap (*MOT*) as the target in electron impact cross section studies were carried out. The use of a MOT allows the kinematic properties of the target atoms, and their electronic states, to be controlled via operating parameters of the MOT's lasers. A MOT is capable of saturating the excited state of a gaseous target of atoms and provides a unique opportunity to measure exotic collision processes. Measurements use a trap-loss technique to relate the loss rate of atoms from the trap due to electron interactions to a collision cross section. Total scattering cross section measurements are given for the $6^2S_{1/2}$ ground state and the $6^2P_{3/2}$ excited state of cesium. The excited state measurement is the first measurement of its kind. Total ionization cross sections are also presented for the both the $6^2S_{1/2}$ ground state and $6^2P_{3/2}$ excited state. The ionization cross sections are measured by adjusting the radiation force of the MOT lasers to damp the elastic scattering component of the total cross section. The ionization cross section for the excited state is the first experimental determination of its kind. Full details of the experimental apparatus and the analysis procedure are presented. The results of this experiment are combined with other experimental data and compared to the most recent calculations.

To the memory of
Donald Morrison and Margaret MacAskill

and

To my

grandmother
Muriel Morrison

parents
John and Donelda,

and brothers
Kenzie and Kirk

Thank You

-'s sibhse mo ràmh air a' chuan stoirmeil

ACKNOWLEDGEMENTS

I wish to thank my supervisor Bill McConkey for giving me the opportunity to work on this experiment. My time spent at the University of Windsor has been very rewarding. I consider myself quite fortunate to have been able to work with such an experienced, patient and considerate supervisor, and friend. I have also benefited greatly from the guidance and assistance of Wladek Kedzierski, particularly in the development of the experimental system.

I wish to thank Jolanta Domyslawska for her help with the development and operation of the first MOT constructed at the University of Windsor. I am also grateful to Cormac McGrath for his help with the construction and operation of the second MOT system. I am grateful to William van Wijngaarden for the use of one of his lasers, and for providing the cesium vapour cells used in this experiment.

The efforts of the Physics Department's support staff are also deserving of recognition. Erik Clausen, Louis Beaudry, and Sinisa Jezdic have contributed greatly to the development of the experimental apparatus. They have consistently offered expertise, insight and materials whenever necessary, many times with little or no notice.

I owe thanks to Walter Kauppila and Talbert Stein of Wayne State for allowing us to use their unpublished data. In addition, I wish to thank Igor Bray, Klaus Bartschat, Kurt Becker, Philip Bartlett, and Andris Stelbovics for performing their cross section calculations and offering valuable theoretical input. I also wish to thank Bill Baylis and Uwe Thumm for insightful discussions.

I am grateful to the Natural Sciences and Engineering Research Council of Canada (*NSERC*), the Canadian Institute for Photonics Innovation (*CIPI*), and the Canadian Foundation for Innovation (*CFI*) for the financial support of this research. I am also grateful for the scholarship awards of NSERC and the University of Windsor.

I owe a special thanks to Cormac McGrath, Charles Malone, Mat Halls, and Dominic Seccombe for their friendship and distracting me from the research when I needed it the most.

TABLE OF CONTENTS

LIST OF FIGURES

CHAPTER 1. INTRODUCTION

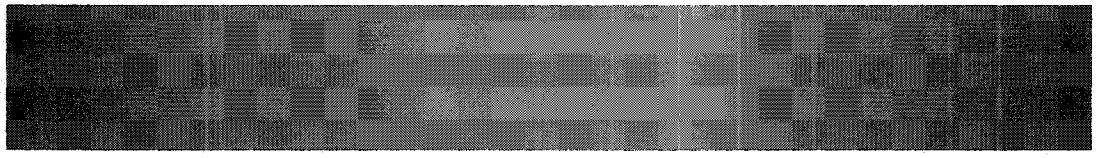

Simulated flame emission spectrum for cesium taken from webmineral.com* made using spectroscopic data from NIST

* (http://webmineral.com/chem/Chem-Cs.shtml)

1.1 Motivation

The research presented in this dissertation is an application of laser cooling and trapping to perform precise measurements of absolute electron-collision cross sections in cesium. There are two primary goals of this research. The first goal is to assist in establishing the technique of measuring cross sections with targets of magneto-optically trapped atoms, first demonstrated by Schappe [SCHAP 95]. The second goal is to extend the existing cross section database in the literature for cesium.

Dr. C. Lin's group at the University of Wisconsin-Madison published the results of the first application of magneto-optically trapped atoms for measuring absolute electron collision cross sections for Rubidium in 1995 [SCHAP 95]. The ability to make such cross section measurements with a magneto-optical trap (*MOT*) has three appealing features. Absolute cross sections can be measured without making any absolute determination of the target density which provides a major simplification to the data analysis over more traditional experimental techniques. In addition, the thermal velocities of atoms in a MOT are orders of magnitude less than those in an atomic beam, which means any momentum changes are more pronounced. Finally, a MOT works on an optical pumping scheme that saturates the population of atoms in the excited state. Consequently, one can make cross section measurements for atoms in the excited state almost as easily as for the ground state. Cross sections involving excited states are vital to the understanding of all branches of plasma physics, from astrophysics to plasma displays.

There are many reasons for measuring data involving cesium. Cesium has a wide range of applications within both pure and applied fields. Perhaps the greatest known application of cesium is its use in atomic clocks. The second is defined using a Ramsey microwave transition of the cesium ground electronic state.

Cesium also has applications to medical imaging and cancer treatment using various radioisotopes. It is also used in a variety of detectors, primarily for IR photodetection and for increasing the efficiency of channel electron multipliers in the vacuum ultraviolet. It is also used for producing ion sources, e.g. cesium sputter ion sources, and for spin-polarized electron sources, e.g. CsO coated GaAs photocathodes [ALLEY 95], [OMORI 91]. Within

the vacuum industry, cesium is used extensively as a getter. There are also a few applications of cesium within the chemical industry for hydrogenation of some organic compounds. Cesium studies are important for the understanding and development of the production, handling and disposal of low-energy plasmas. These plasmas are used in a variety of applications ranging from lighting sources, television and computer displays, and microcircuit lithography using plasma etching [BECKE 00].

Cesium is also used for the study of high temperature plasmas with particular emphasis on fusion. Cesium is of great interest to members of the theoretical community since it is a hydrogenic atom that displays larger relativistic effects than its lighter counterparts. Cesium can be used as a diagnostic for categorizing stars [CAITL 00]. Cesium is also used as an ion propulsion system for deep space probes and satellites [SOVEY 99].

Cesium MOT's were in abundance when this project began, but had never been used for the purposes of electron scattering. As such, the technology for building a cesium MOT was well established and the construction process could progress with relative ease. A further motivation for choosing cesium as the target was that discrepancies were present in the published cesium cross sections at that time. One of the most quoted sources for the cesium total cross section was R. Brode [BRODE 29], which dated back to 1929, and his experimental technique had several deficiencies which made the results questionable. Thus no reliable total cross section measurements were available at energies greater than 20 eV. Significant advances were also being made on the theoretical side, and we were fortunate to team up with the world leaders within this area, Dr. I. Bray and Dr. A. Stelbovics from Australia and Dr. K. Bartschat from the USA. Our experiment provided the motivation for their calculations and the result was very beneficial for all parties involved.

This research began in 1999 with the construction of a cesium MOT in Prof. Bill McConkey's Electronic and Photonic Collisions Laboratory at the University of Windsor. The construction of the MOT took approximately a year to complete. An additional half year was spent aligning and testing until finally in December of 2000, the MOT was successfully operated for the first time. The electron system incorporated with the MOT was then tested for beam quality and stability for a variety of operating conditions for approximately six

months following the first successful operation of the trap. The first reliable electron scattering signals were observed in September of 2001 and the first cross section using the cesium MOT target was measured in December 2001 [MACAS 02].

A list of design improvements was made during the first year of operation of the incorporated electron-MOT system. Following the completion of the first cross section measurement, the original electron-MOT system was replaced with an entirely new, second generation electron-MOT system in June of 2002. This new system was designed with the list of improvements in mind. There were a variety of reasons for implementing this second system, namely, to allow more accurate measurements over an extended energy range, to allow additional detectors to be installed in vacuum, and finally to make servicing the internal components speedier and more convenient.

1.2 Cesium Physical Properties

Cesium was discovered in 1860, by Robert Wilhelm Bunsen and Gustav Robert Kirchhoff of Germany. They were performing spectroscopy on mineral water samples from Durkheim which produced two bright blue spectral lines. The name cesium is actually derived from the Latin word "caesius" meaning "heavenly blue" attributed to the brightness of these spectral lines.

Cesium is a silvery, gold coloured metal that is quite soft and ductile. It is the most massive of the naturally occurring alkali metals (Francium only exists as short-lived isotopes). Cesium is the most electropositive element and also has the lowest ionization potential on the periodic table. Cesium metal is the least abundant of the naturally occurring alkali metals. The terrestrial abundance is roughly 3 ppm. The solar system abundance is given a value of 80, in comparison with atomic hydrogen which is given an abundance factor of 10^{12}. Cesium metal is derived mainly from the mineral *pollucite*, $(Cs,Na)_2Al_2Si_4O_{12}\cdot(H_2O)$, which has the largest percentage content of cesium at 27.98%. Other minerals with high yields of cesium include *nanpingite*, $Cs(Al,Mg,Fe^{++},Li)_2(Si_3Al)O_{10}(OH,F)_2$, with a 24.51% cesium content, and *avogadrite*, $(K,Cs)BF_4$, with a 22.25% cesium content.

The vapour pressure of cesium is given by the following empirical relations [NESME 63]

$$\log_{10} P_v = -219.482\,00 + \frac{1088.676}{T} - 0.083\,361\,85\,T + 94.887\,52 \log_{10} T \quad (\textit{solid phase}) \qquad 1.1a$$

$$\log_{10} P_v = 8.221\,27 - \frac{4006.048}{T} - 0.000\,601\,94\,T - 0.196\,23 \log_{10} T \quad (\textit{liquid phase}) \qquad 1.1b$$

The vapour pressure curve defined by these relations is given in Figure 1.1.

For this experiment, we are dealing with a cesium target in the gas phase. Using the empirical relations of Eq. 1.1, we find that the vapour pressure of cesium at room temperature, 298 K, is approximately 1.26×10^{-6} Torr. We now wish to find the speed distribution associated with a cesium gas at this temperature. Using the familiar Maxwell-Boltzmann speed function for a three-dimensional gas

$$f(v) = \sqrt{\frac{2}{\pi}} \frac{v^2}{\left[k_B T/M\right]^{3/2}} \exp\left(-\frac{Mv^2}{2k_B T}\right) \qquad 1.2$$

for cesium with mass M, at temperature, T, in Kelvin, and where k_B is the Boltzmann

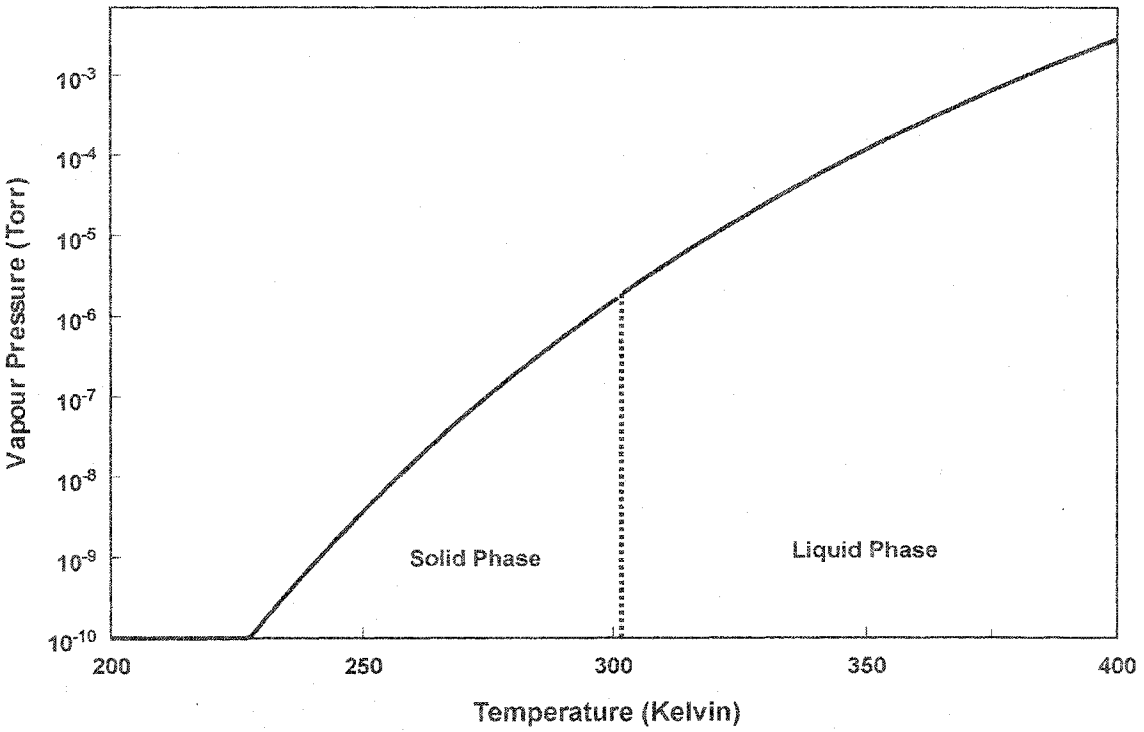

Figure 1.1: Vapour pressure curve for cesium including both solid and gas phases. The melting point, shown by the dashed line, is at 301.59K.

constant. It is sometimes more convenient to work with a compact form of Eq. 1.2, where a mean speed defined by

$$\tilde{v} = \sqrt{k_B T/M} \qquad 1.3$$

is used, in which case the Maxwell-Boltzmann speed function reduces to

$$f(v) = \sqrt{\frac{2}{\pi}} \frac{v^2}{\tilde{v}^3} \exp\left(-\frac{v^2}{2\tilde{v}^2}\right) \qquad 1.4$$

Three velocities that are typically derived from Eq. 1.4 to characterize the speed distribution are the most probable speed, v_{mp}, the average speed, v_{ave}, and the root-mean-square speed,

v_{rms}. These quantities can be expressed in terms of the mean speed given in Eq. 1.3, and for a three-dimensional gas, are

$$v_{mp} = \sqrt{2}\tilde{v} \qquad v_{rms} = \sqrt{3}\tilde{v} \qquad v_{ave} = \sqrt{\frac{8}{\pi}}\tilde{v} \tag{1.5}$$

Using a temperature of 298 K, we find that for cesium, these characteristic velocities are

$$v_{mp} = 193.1\ ms^{-1} \qquad v_{rms} = 236.5\ ms^{-1} \qquad v_{ave} = 217.9\ ms^{-1}$$

A plot of the Maxwell-Boltzmann speed function is given in Fig. 1.2 . The thermodynamics

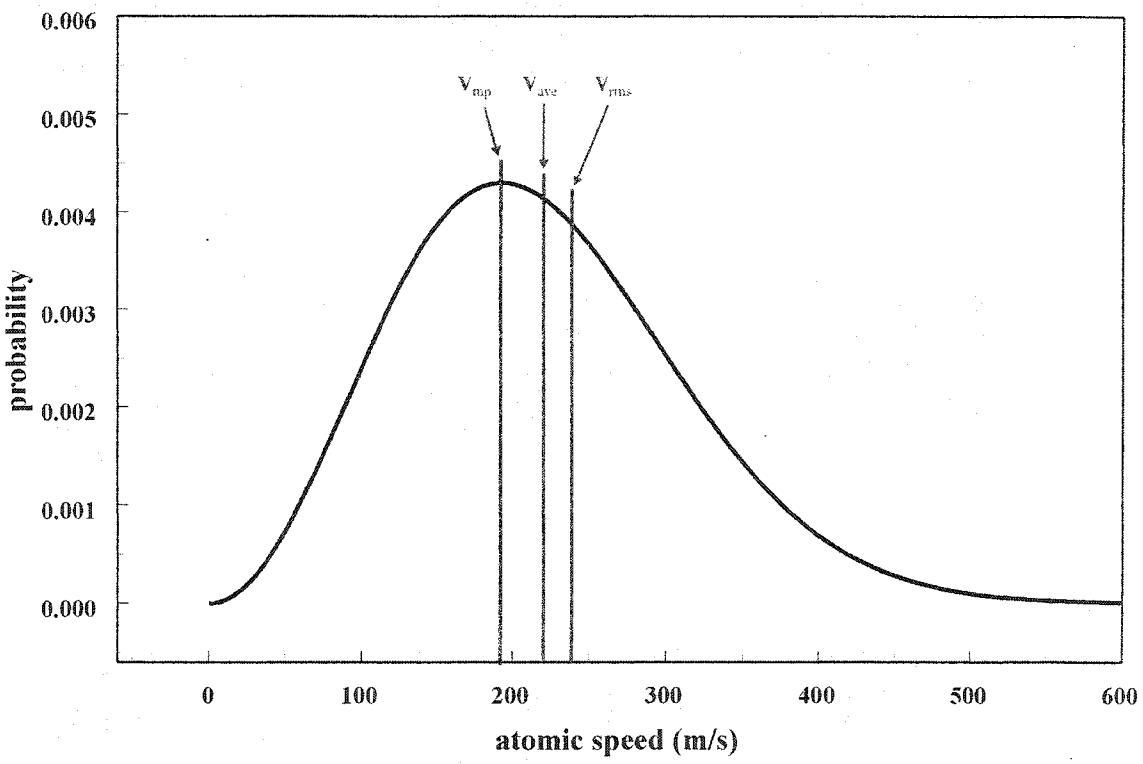

Figure 1.2: Maxwell-Boltzmann speed function for a cesium vapour at 298 K. Indicated on the graph are the locations of the three characteristic speeds v_{mp}=193.1 m s^{-1}, v_{ave} = 217.9 m s^{-1}, and v_{rms} = 236.5 m s^{-1}.

will be considered in greater detail later, for considerations of atomic collisions and the development of the trap-loss technique used to perform electron collision cross section measurements with a MOT. The characteristic speeds given here will also be useful in defining certain parameters for describing the MOT's performance, such as average stopping distance, and capture velocity.

Finally, as a lead-in to the following section, we need to know the electronic properties of cesium. Cesium contains 55 electrons, only one of these electrons is contained in the valence shell, making it one of the hydrogenic atoms. The electronic configuration of cesium is given by $1s^2 2s^2 2p^6 3s^2 3p^6 4s^2 3d^{10} 4p^6 5s^2 4d^{10} 5p^6 6s^1$, or more compactly by [Xe] $6s^1$. The most abundant, and only, stable isotope of cesium is ^{133}Cs. There are a large number of radioisotopes of cesium. These isotopes range from ^{113}Cs to ^{148}Cs, and have lifetimes that vary from 33μs for ^{113}Cs to 2.3×10^6 years for ^{135}Cs. The most common radioisotopes in use are ^{134}Cs and ^{137}Cs.

1.3 Cesium Atomic Structure

Cesium has a rich atomic structure that arises from fine and hyperfine structure interactions, which will be discussed in detail in the following sections. The fine structure interaction is responsible for splitting the 6P level of cesium into two separate levels. Transitions from these two levels to the ground state are usually referred to as the D lines, just as the case with the yellow D lines of sodium. The transitions from the cesium ground state to the first two P states of cesium are denoted as the D_1 line ($6P_{1/2}$) and D_2 line ($6P_{3/2}$). In the case of cesium, the wavelength separation of the D lines is approximately 42 nm. Comparing this separation with the 0.6 nm wavelength separation of the D lines in sodium, gives some idea of the relative strength of these fine structure interactions as one progresses to the heavier alkali metals. The hyperfine structure interactions split all levels, not just the

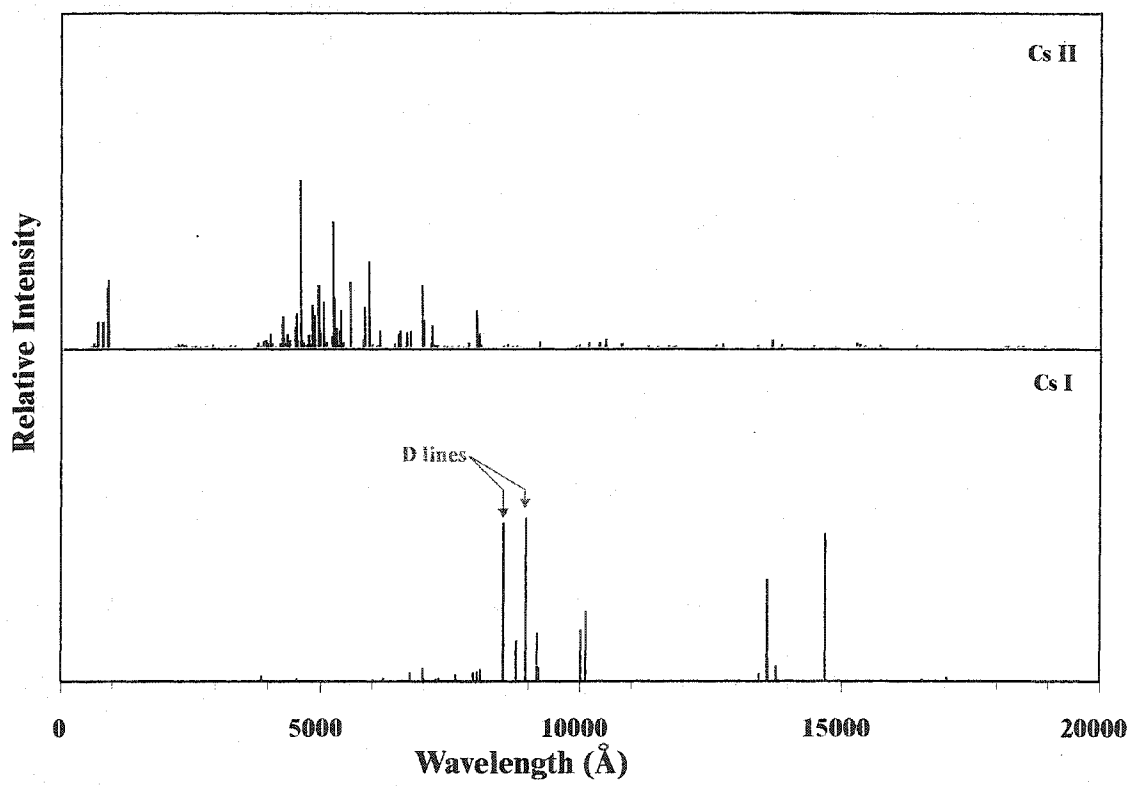

Figure 1.3: Spectral lines for neutral (Cs I), and for singly ionized (Cs II) cesium using spectroscopic data from the NIST database. Both spectra are for all possible sources, including flame and arc emission. Shown are the two D lines at 852 nm and 894 nm.

P levels. The sizes of these hyperfine splittings are typically much smaller than those resulting from the fine structure interactions.

The magneto-optical trap used in this research works on transitions from the ground

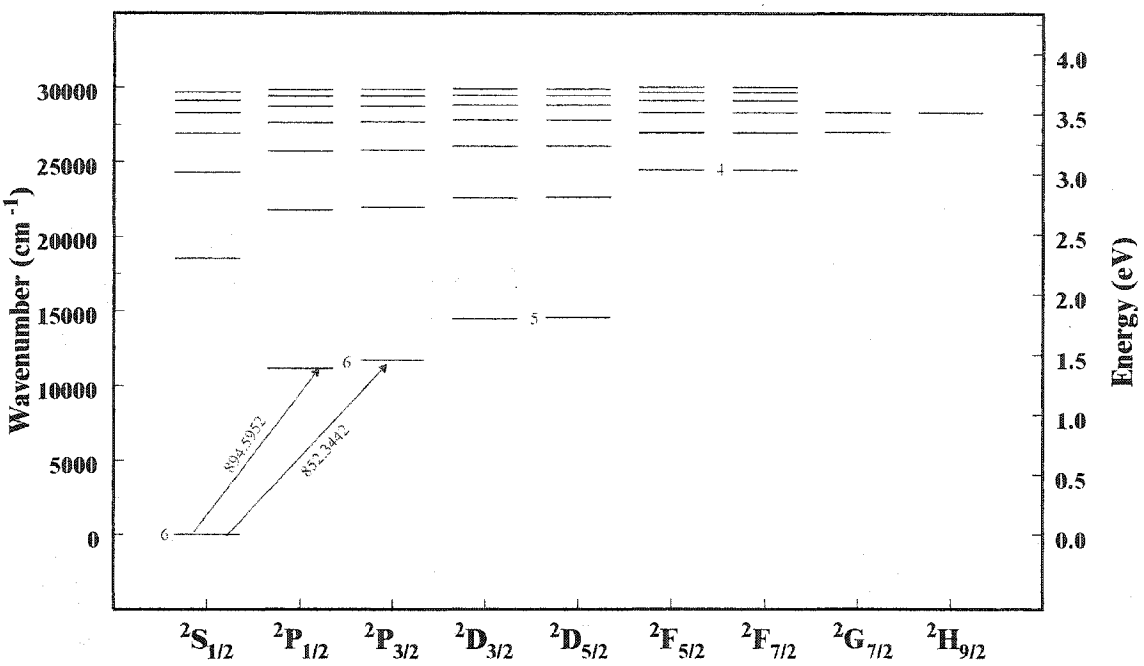

Figure 1.4: Grotrian level diagram for neutral cesium compiled using data from Charlotte Moore tables [MOORE 58], Weber and Sansonetti [WEBER 87], and the NIST spectroscopic database. The D lines are drawn in with the wavelengths displayed in nm. Not shown is the level of the first ionization potential at 3.89 eV.

state to the 6 $P_{3/2}$ excited state, the D_2 line. As such, this particular transition will be the main focus of our discussions.

To effectively perform any optical studies of the MOT, it is necessary to determine if there are any nearby transitions that could interfere or contaminate an observation at this wavelength. To assess the likelihood of such interference, it is necessary to examine the spectrum for cesium. Data from NIST, shown in Fig. 1.3, show the main spectral emissions for Cs and Cs^+. The Cs^+ emissions are included since any interaction with the electron beam will produce a substantial ion yield, whose emissions could also contaminate any optical observations. In addition to a cesium spectrum, a Grotrian diagram, shown in Fig 1.4, and transition table given in Table 1.1, are used to ascertain the nature of the transitions

Vacuum Wavelength(Å)	*Atomic Transition*	*Relative Intensity*	*Vacuum Wavelength*(Å)	*Atomic Transition*	*Relative Intensity*
3204.380			6588.319	$6^2P_{3/2} - 9^2S_{1/2}$	490
3206.180			6630.480	$5^2D_{5/2} - 8^2F_{5/2,7/2}$	97
3208.381			6725.126		3300
3210.882			6826.524	$5^2D_{3/2} - 7^2F_{5/2}$	200
3213.682			6872.337	$5^2D_{5/2} - 7^2F_{5/2,7/2}$	300
3217.083			6975.215	$6^2P_{3/2} - 7^2D_{5/2}$	4800
3220.984			6985.408	$6^2P_{3/2} - 7^2D_{3/2}$	980
3225.686			7230.515	$5^2D_{3/2} - 6^2F_{5/2}$	790
3225.886			7281.899	$5^2D_{5/2} - 7^2F_{5/2}$	130
3231.387			7281.959	$5^2D_{5/2} - 7^2F_{7/2}$	1100
3231.587			7610.989	$6^2P_{1/2} - 8^2S_{1/2}$	2600
3238.289			7946.061	$6^2P_{3/2} - 8^2S_{1/2}$	3300
3238.489			8017.931	$5^2D_{3/2} - 5^2F_{5/2}$	3500
3246.791			8081.159	$5^2D_{5/2} - 5^2F_{5/2}$	510
3247.091			8081.259	$5^2D_{5/2} - 5^2F_{7/2}$	4500
3257.594			8523.470	$6^2S_{1/2} - 6^2P_{3/2}$	59000
3257.994			8763.816	$6^2P_{1/2} - 6^2D_{3/2}$	15000
3271.398			8945.926	$6^2S_{1/2} - 6^2P_{1/2}$	61000
3271.898			9174.839	$6^2P_{3/2} - 6^2D_{5/2}$	18000
3289.503			9211.059	$6^2P_{3/2} - 6^2D_{3/2}$	5200
3290.203			10029.857	$5^2D_{3/2} - 4^2F_{5/2}$	19000
3314.010			10128.963	$5^2D_{5/2} - 4^2F_{5/2}$	4800
3314.910			10129.158	$5^2D_{5/2} - 4^2F_{7/2}$	26000
3348.419	$6^2S_{1/2} - 12^2P_{3/2}$		13431.661	$5^2D_{3/2} - 7^2P_{3/2}$	2900
3349.720	$6^2S_{1/2} - 12^2P_{1/2}$		13595.731	$6^2P_{1/2} - 7^2S_{1/2}$	38000
3398.833	$6^2S_{1/2} - 11^2P_{3/2}$		13610.012	$5^2D_{5/2} - 7^2P_{3/2}$	8400
3400.934	$6^2S_{1/2} - 11^2P_{1/2}$		13766.358	$5^2D_{3/2} - 7^2P_{1/2}$	5700
3477.755	$6^2S_{1/2} - 10^2P_{3/2}$		14702.958	$6^2P_{3/2} - 7^2S_{1/2}$	55000
3480.956	$6^2S_{1/2} - 10^2P_{1/2}$		16544.677	$7^2P_{1/2} - 8^2D_{3/2}$	820
3612.392	$6^2S_{1/2} - 9^2P_{3/2}$		17021.634	$7^2P_{3/2} - 8^2D_{5/2}$	1500
3618.293	$6^2S_{1/2} - 9^2P_{1/2}$		20148.531	$7^2P_{3/2} - 9^2S_{1/2}$	760
3877.214	$6^2S_{1/2} - 8^2P_{3/2}$	2100	22824.266		880
3889.678	$6^2S_{1/2} - 8^2P_{1/2}$	600	23050.330		1100
4556.531	$6^2S_{1/2} - 7^2P_{3/2}$	1000	23356.414	$7^2P_{1/2} - 7^2D_{3/2}$	3900
4594.431	$6^2S_{1/2} - 7^2P_{1/2}$	460	24263.663	$7^2P_{3/2} - 7^2D_{5/2}$	4400
5467.441	$6^2P_{1/2} - 10^2D_{3/2}$	60	24387.698	$7^2P_{3/2} - 7^2D_{3/2}$	850
5504.391		37	25777.078		890
5636.757	$6^2P_{3/2} - 10^2D_{5/2}$	100	25778.074		500
5665.575	$6^2P_{1/2} - 9^2D_{3/2}$	210	29326.050	$7^2S_{1/2} - 7^2P_{3/2}$	680
5747.298	$6^2P_{3/2} - 11^2S_{1/2}$	27	30119.273	$6^2P_{1/2} - 5^2D_{3/2}$	2800
5840.433	$6^2P_{1/2} - 10^2S_{1/2}$	59	30969.501	$7^2S_{1/2} - 7^2P_{1/2}$	610
5846.745	$6^2P_{3/2} - 9^2D_{5/2}$	300	34918.584	$6^2P_{3/2} - 5^2D_{5/2}$	1100
6012.141	$6^2P_{1/2} - 8^2D_{3/2}$	640	36149.926	$6^2P_{3/2} - 5^2D_{3/2}$	190
6035.747	$6^2P_{3/2} - 10^2S_{1/2}$	86	39197.756	$7^2P_{1/2} - 8^2S_{1/2}$	2
6214.806	$6^2P_{3/2} - 8^2D_{5/2}$	1000	39442.834		2
6219.307	$6^2P_{3/2} - 8^2D_{3/2}$	170	39444.825		1
6356.295	$6^2P_{1/2} - 9^2S_{1/2}$	320			

Table 1.1: Spectral lines of neutral cesium in the range 300 - 4000 nm

neighbouring the D_2 line.

The NIST database includes spectral lines for all sources, including arc discharge sources, and so the spectra in Fig 1.3 contains an abundance of lines that will not be present in this experiment. The list of transitions in Table1.1 allows us to clean up the spectra to isolate those transitions that could be problematic. On first inspection of Table 1.1, there are no optical emission processes for neutral cesium in the spectral region neighbouring the 852 nm D_2 line. The closest line is the 876 nm line, but this wavelength can be easily removed with a standard, narrow-band, interference filter. Furthermore, this transition originates from an excited state so the overall contribution will be minimal. Examining the spectra of singly-charged cesium shows that the strongest lines are bunched together around the "blue" region of the visible spectrum. Thus, we assume that any emissions from the continuum will be sufficiently far from the cesium D_2 line.

1.4 Hyperfine Structure

We will now proceed into a non-relativistic treatment of the interactions arising from the nuclear angular momentum. An in-depth review of hyperfine structure in the alkali atoms can be found in Arimondo *et al.* [ARIMO 77]. The following discussion will briefly mention the key points with particular emphasis on cesium. We begin with the hyperfine structure Hamiltonian used to describe the interaction of the angular momentum of the nucleus with that of the atomic electrons

$$\mathcal{H}_{\text{hfs}} = \sum_{k} \mathbf{T}^{(k)} \cdot \mathbf{M}^{(k)} \tag{1.6}$$

where $\mathbf{T}^{(k)}$ is a spherical tensor operator of rank k, describing the electronic portion of the interaction, while $\mathbf{M}^{(k)}$ is another spherical tensor operator of rank k, describing the nuclear component of the interaction. If the tensor rank is even the components **T** and **M** describe electric interactions, and if the tensor rank is odd, then the components describe magnetic interactions.

The $k = 0$ term gives the electric interaction of the electron with the spherical charge distribution of the nucleus. The $k = 1$ term gives the magnetic dipole coupling of the nuclear magnetic moment with the magnetic field created by the electron at the nucleus position.

$$\mathbf{M}^{(1)} = \mu_{\text{I}} = -g_{\text{I}}\mu_{\text{B}}\mathbf{I} \tag{1.7}$$

with μ_{B} the Bohr magneton, and **I** is the nuclear angular momentum. The convention used here is that the sign of the g-factor is taken opposite the associated magnetic moment. The first order electronic interaction is

$$\mathbf{T}^{(1)} = 2\frac{\mu_0}{4\pi}\mu_{\text{B}}\left\{\frac{\mathbf{L}}{r^3} - \frac{1}{r^3}\left[\mathbf{S} - 3\frac{\mathbf{S}\cdot\mathbf{r}}{r^2}\mathbf{r}\right] + \frac{2}{3}\frac{\delta(r)}{r^2}\mathbf{S}\right\} \tag{1.8}$$

with **L** the orbital angular momentum, **S** the spin angular momentum, and **r** the position vector of the electron. The first term of $\mathbf{T}^{(1)}$ describes the portion of the dipolar magnetic field at the nucleus resulting from the orbital motion of the electron. The second term is the field

attributed to the intrinsic angular momentum of the electron. The third and final term is referred to as a *contact interaction* that results from the field created by the electronic magnetization at the nuclear position. We note that through the dependence of the Dirac delta function $\delta(r)$, that this contact interaction is non-zero for only *s* electrons.

The next term in the hyperfine Hamiltonian is the electric quadrupole interaction where the electric portion is given by

$$\mathbf{T}^{(2)} = -\frac{e}{4\pi\varepsilon_0}\frac{1}{r^3}\mathbf{C}^{(2)} \qquad 1.9$$

Here, we have introduced the quantity $\mathbf{C}^{(k)}$ which is another tensor operator of rank *k*. This tensor operator is introduced to relate the various multipole contributions to normalized spherical harmonics, $Y_q^{(k)}$ in a compact form. The q^{th} component of $\mathbf{C}^{(k)}$ is given by

$$\mathbf{C}_q^{(k)} = \sqrt{\frac{4\pi}{2k+1}}\mathbf{Y}_q^{(k)} \qquad 1.10$$

The nuclear part of the interaction is

$$\mathbf{M}^{(2)} = -\frac{e}{2}\frac{\sqrt{6}Q}{I(2I-1)}(\mathbf{I}\cdot\mathbf{I})^{(2)} \qquad 1.11$$

where Q is a scalar quantity representing the nuclear quadrupole moment. There have been some studies of the higher order, magnetic octupole and electric hexadecapole interactions, but not in the alkali atoms.

To describe an atomic state while considering hyperfine structure the set of quantum numbers $\{J, I, F, m_F\}$ is used, where the quantum number *F* refers to the total angular momentum.

$$\mathbf{F} = \mathbf{I} + \mathbf{J} \qquad 1.12$$

with values of *F* given by

$$|I - J| \leq F \leq I + J \qquad 1.13$$

We note that throughout this dissertation, the term total angular momentum will be used in reference to the operator **F**. It is quite common to see total angular momentum being used in reference to the operator **J**. Strictly speaking, this is not correct as **J** refers to the total angular momentum of the electronic system without taking into account the nuclear angular momentum. The angular momentum of the electronic system, **J**, is defined as

$$\mathbf{J} = \mathbf{L} + \mathbf{S} \tag{1.14}$$

where values of J are given by the relation

$$|L - S| \leq J \leq L + S \tag{1.15}$$

We must now classify the conditions for good and bad quantum numbers. First, the quantum number, I, will always be classified as a good quantum number. The reason for this is that we will only be considering energies that are much less than those required for nuclear transitions. In cases where J is a good quantum number, that is when matrix elements of $\mathcal{H}_{\text{hfs}}$ with different J can be neglected, the hyperfine energy E_F is given by

$$E_F = \frac{1}{2}hAK + hB\frac{\frac{3}{2}K(K+1) - 2I(I+1)J(J+1)}{2I(2I-1)2J(2J-1)} \tag{1.16}$$

where the factor K has been introduced for brevity

$$K = F(F+1) - I(I+1) - J(J+1) \tag{1.17}$$

The constant A in the hyperfine splitting relation Eq. 1.16 is typically referred to as the hyperfine A constant or the magnetic dipole hyperfine constant. The constant B is referred to as the hyperfine B constant or the electric quadrupole hyperfine constant. It is important to note that the term with the electric quadrupole hyperfine constant is omitted for

Magnetic Dipole Constant	A ($6\,^2S_{1/2}$)	2.298 157 942 5 (exact)	GHz	[ARIMO 77]
	A ($6\,^2P_{3/2}$)	50.275 (3)	MHz	[TANNE 88]
Electric Quadrupole Constant	B ($6\,^2P_{3/2}$)	-0.53 (2)	MHz	[TANNE 88]

Table 1.2: Magnetic dipole and electric quadrupole constants for the hyperfine splittings in cesium of the D_2 transition. The values are listed along with their associated standard uncertainties and references.

calculations of splittings for states with $J = 1/2$.

The magnetic dipole and electric quadrupole values for the $6^2S_{1/2}$ and $6^2P_{3/2}$ states are given in Table 1.2. These values can be inserted into Eq. 1.16 to find the hyperfine energy splittings for both states. The results of these calculations are shown in the hyperfine manifold in Fig. 1.5.

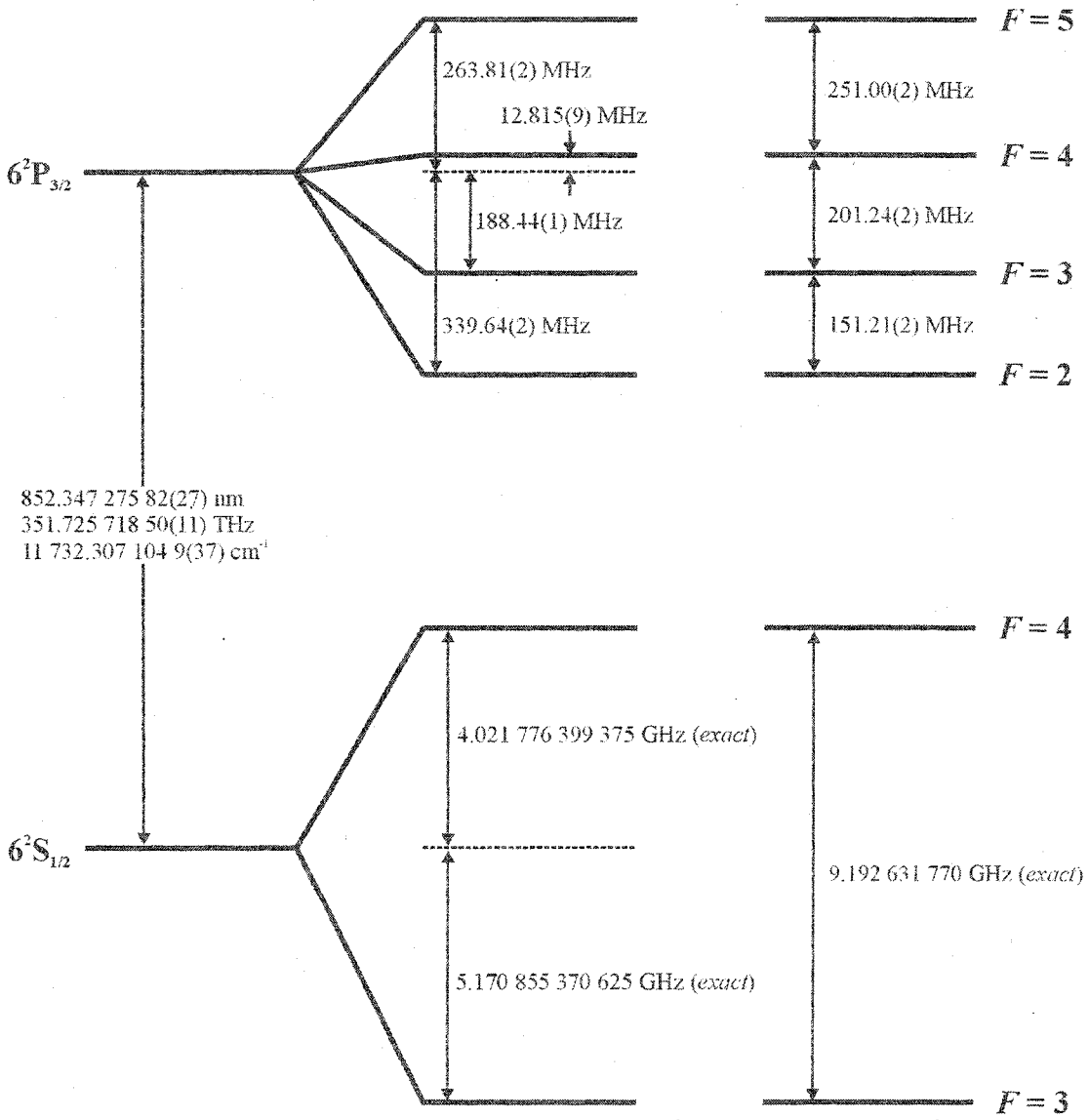

Figure 1.5: Manifold for the hyperfine levels of the $6^2S_{1/2}$ ground state and $6^2P_{3/2}$. The frequency separation of the hyperfine levels are shown along with their associated uncertainties were calculated using Eq. 1.16. Note that the ground state separations are exact and correspond to the Cs clocking transition for the definition of the second.

As we are ultimately interested in building a MOT, it is useful to look at how the hyperfine levels change in the presence of a magnetic field. The Hamiltonian for the interaction of an atom with a magnetic field is

$$\mathcal{H}_B = \frac{\mu_B}{\hbar}\left(g_S S_z + g_L L_z + g_I I_z\right)B_z \tag{1.18}$$

for a magnetic field taken along the z-axis. μ_B is the Bohr magneton, and the g_S, g_L, and g_I represent the electron spin, electron orbital, and nuclear g-factors. If the field splitting is small with respect to the fine-structure splitting, but large with respect to the hyperfine splitting, then L and S are coupled to J, and as before the quantum number I is always a good quantum number. So Eq. 1.18 is modified to give

$$\mathcal{H}_B = \frac{\mu_B}{\hbar}\left(g_J J_z + g_I I_z\right)B_z \tag{1.19}$$

with g_J the Landé g-factor that is given by

$$g_J = g_L \frac{J(J+1) - S(S+1) + L(L+1)}{2J(J+1)} + g_S \frac{J(J+1) + S(S+1) - L(L+1)}{2J(J+1)} \tag{1.20}$$

The magnetic field is strong enough in this case to completely decouple the interaction between I and J, so that F is no longer a good quantum number. In this case, the system is in a *Paschen-Back* regime for hyperfine structure.

However, if the Zeeman splittings are small in comparison with the hyperfine splittings, then F is a good quantum number and the system is in the regime of the *anomalous Zeeman effect* for hyperfine structure. In this case the interaction Hamiltonian is given by

$$\mathcal{H}_B = \mu_B g_F F_z B_z \tag{1.21}$$

with g_F the hyperfine Landé g-factor that is given by

$$g_F = g_J \frac{J(J+1) - I(I+1) + F(F+1)}{2F(F+1)} + g_I \frac{J(J+1) + I(I+1) - F(F+1)}{2F(F+1)} \tag{1.22}$$

The energy shifts of the hyperfine levels is then given by

$$\Delta E = \mu_B g_F m_F B_z \qquad 1.23$$

The splittings for the anomalous Zeeman effect were calculated using Eq's 1.22 and 1.23, for the $6^2S_{1/2}$ ground state and the $6^2P_{3/2}$ excited state. The results are shown in Figures 1.6 and 1.7.

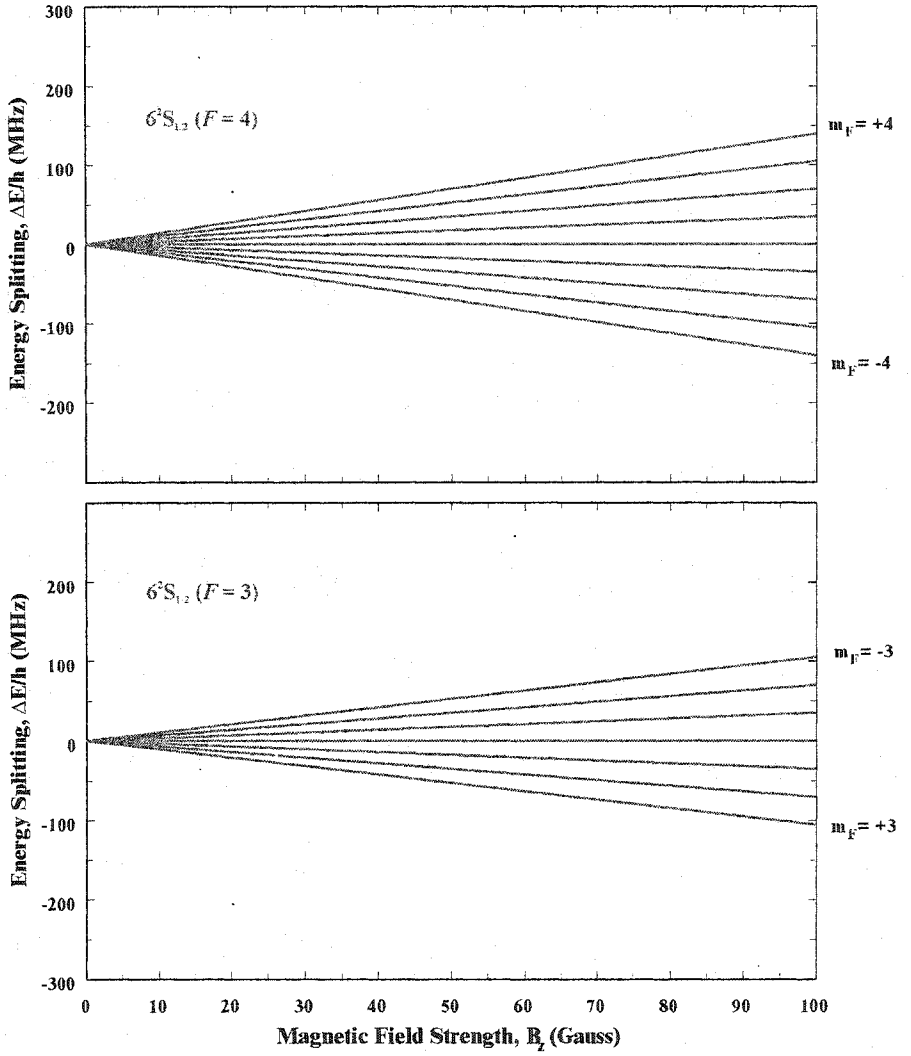

Figure 1.6: Energy splittings of the cesium ground state for the anomalous Zeeman effect. Note that the direction of increasing m_F for the two ground states are opposite.

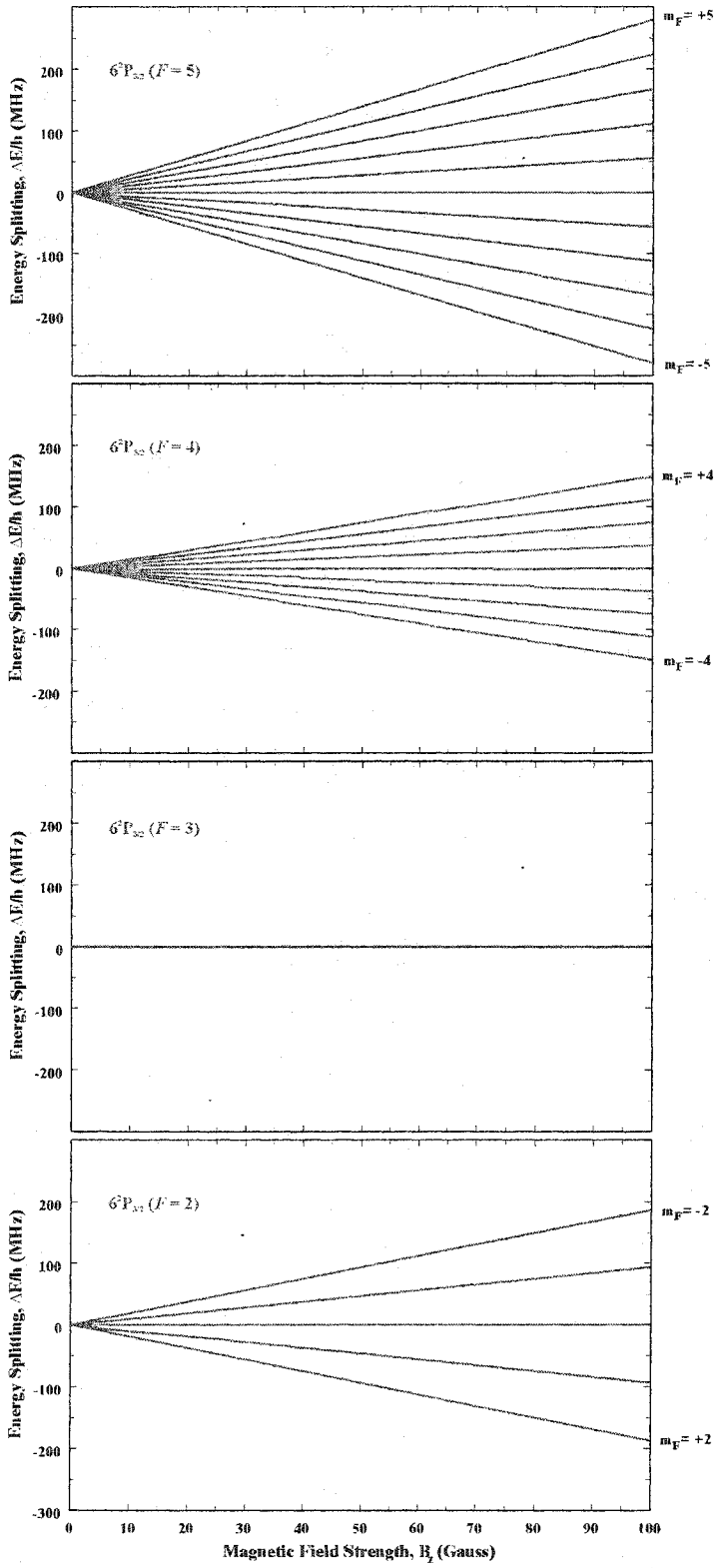

Figure 1.7: Splittings of the hyperfine levels of the $6^2P_{3/2}$ excited state for the anomalous Zeeman effect. There is virtually no splitting of the $F = 3$ hyperfine level. The fields used in the calculations are on the threshold of the transition to the Paschen-Back regime as the Zeeman splittings are comparable to the hyperfine splittings.

1.5 D_2 Transition Optical Properties

The MOT operated on the 852 nm resonance transition so it is beneficial, at this point, to discuss the properties of this resonance transition. Also, there are several hyperfine transitions embedded within the resonance transition, so some analysis is necessary to justify the choice of one particular hyperfine transition for trapping.

Table 1.3 lists the properties of the $6^2S_{1/2} \rightarrow 6^2P_{3/2}$ transition. It is worthwhile mentioning that the lifetime given in Table 1.3 will be the lifetime used for each of the

Frequency	ω_0	$2\pi \cdot 351.725\ 718\ 50(11)$ THz
Wavelength	λ	
Air		852.118 73 nm
Vacuum		852.347 275 82(27) nm
Wavenumber	k	11 732.207 104 9(37) cm^{-1}
Lifetime	τ	30.517(57) nsec
Natural Linewidth	Γ	32.768(62) MHz
Recoil Velocity	v_r	3.522 mm sec^{-1}
Doppler Shift (for $v = v_r$)	$\Delta\omega_D$	$2\pi \cdot 4.1327$ kHz

Table 1.3: Optical properties of the D_2 line

hyperfine levels contained within the $6^2P_{3/2}$ manifold. To make the assignment of the trapping laser transition to a hyperfine transition, it is necessary to evaluate the relative transition strengths of each hyperfine transition. To do so, use is made of the electric dipole matrix elements given in Appendix 4.

The coupling between two hyperfine levels in a resonant laser field is given by the electric dipole matrix element [STECK 01]

$$\langle F\, m_F \,|er|\, F'\, m_{F'} \rangle \qquad 1.24$$

For the purposes of calculating transition strengths, the matrix elements denoted by Eq. 1.24 can be expressed in terms of a reduced dipole operator and 6-*j* symbols

$$\langle F\|er\|F'\rangle = \langle J\|er\|J'\rangle(-1)^{F'+J+I+1}\sqrt{(2F'+1)(2J+1)}\begin{Bmatrix} J & J' & 1 \\ F' & F & I \end{Bmatrix} \qquad 1.25$$

Symmetry arguments can be invoked to simplify the matrix elements further to

$$S_{FF'} = (2F'+1)(2J+1)\begin{Bmatrix} J & J' & 1 \\ F' & F & I \end{Bmatrix}^2 \qquad 1.26$$

where $S_{FF'}$ is the relative transition strength for a transition from F to F'. Using the dipole elements in Appendix 4 with Eq. 1.26. gives the results listed in Table 1.4.

S_{45}	11/18	S_{34}	15/56
S_{44}	7/24	S_{33}	3/8
S_{43}	7/72	S_{32}	5/14

Table 1.4: Relative transition strengths for the $6^2S_{1/2} \rightarrow 6^2P_{3/2}$ transition.

These results are given relative to the D_2 transition matrix element

$$\langle J = 1/2 \| er \| J' = 3/2 \rangle \qquad 1.27$$

which has a numerical value of 4.4754 ea_0 [STECK 01]. From Table 1.4, we see that the strongest hyperfine transitions for the D_2 line are $F = 4$ to $F' = 5$, $F = 3$ to $F' = 3$ and $F = 3$ to $F' = 4$. The transitions used for the trapping and repumping laser frequencies are $F = 4$ to $F' = 5$ and $F = 3$ to $F' = 4$, respectively, as shown in Fig. 1.8. The $F = 3$ to $F' = 3$ transition cannot be used as the frequency of this transition coincides with that of a *crossover*, i.e. an experimental artifact of the technique used to obtain hyperfine absorption spectra (see Fig. 5.17).

Finally, we must consider the saturation intensities for the D_2 line. The saturation intensity is strongly dependent on the polarization of the coupling field. The values listed here were calculated by Steck [STECK 01]. The first case is for an isotropic light field driving the $F = 4$ to $F' = 5$. In this situation the saturation intensity has the value of 2.7020 mW cm^{-2}. The second case is for a far-detuned, π-polarized field. For this case, the saturation intensity is 1.6512 mW cm^{-2}. The last case is for a $\sigma^{\pm}$ polarized field driving the $|F = 4, m_F = \pm 4\rangle \rightarrow |F' = 5, m_{F'} = \pm 5\rangle$ transition, for which the saturation intensity is 1.1008 mW cm^{-2}.

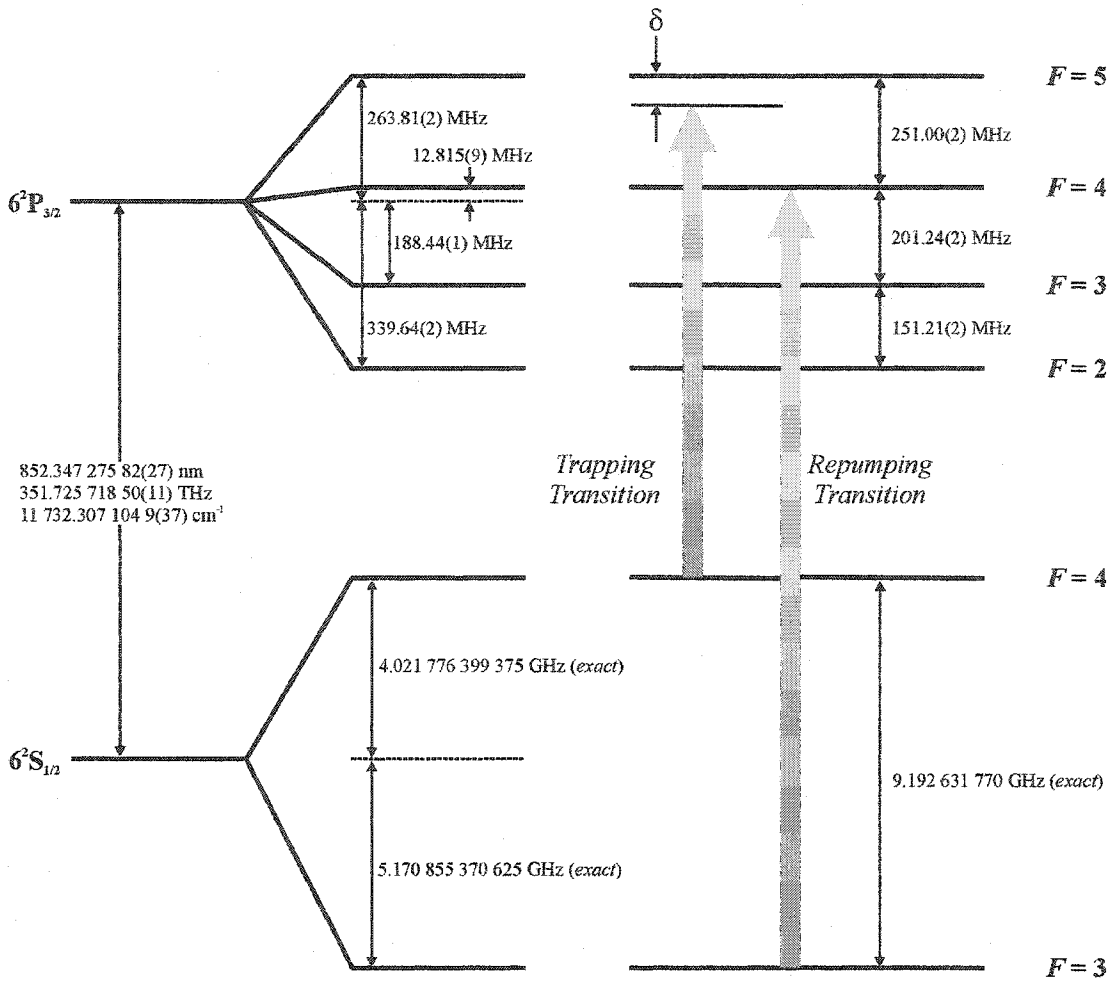

Figure 1.8: Hyperfine diagram from Fig. 1.5 modified to include the assignment of the MOT lasers to specific hyperfine transitions. Also shown is the detuning, δ, of the trapping laser, which is not to scale.

CHAPTER 2. LASER COOLING AND TRAPPING

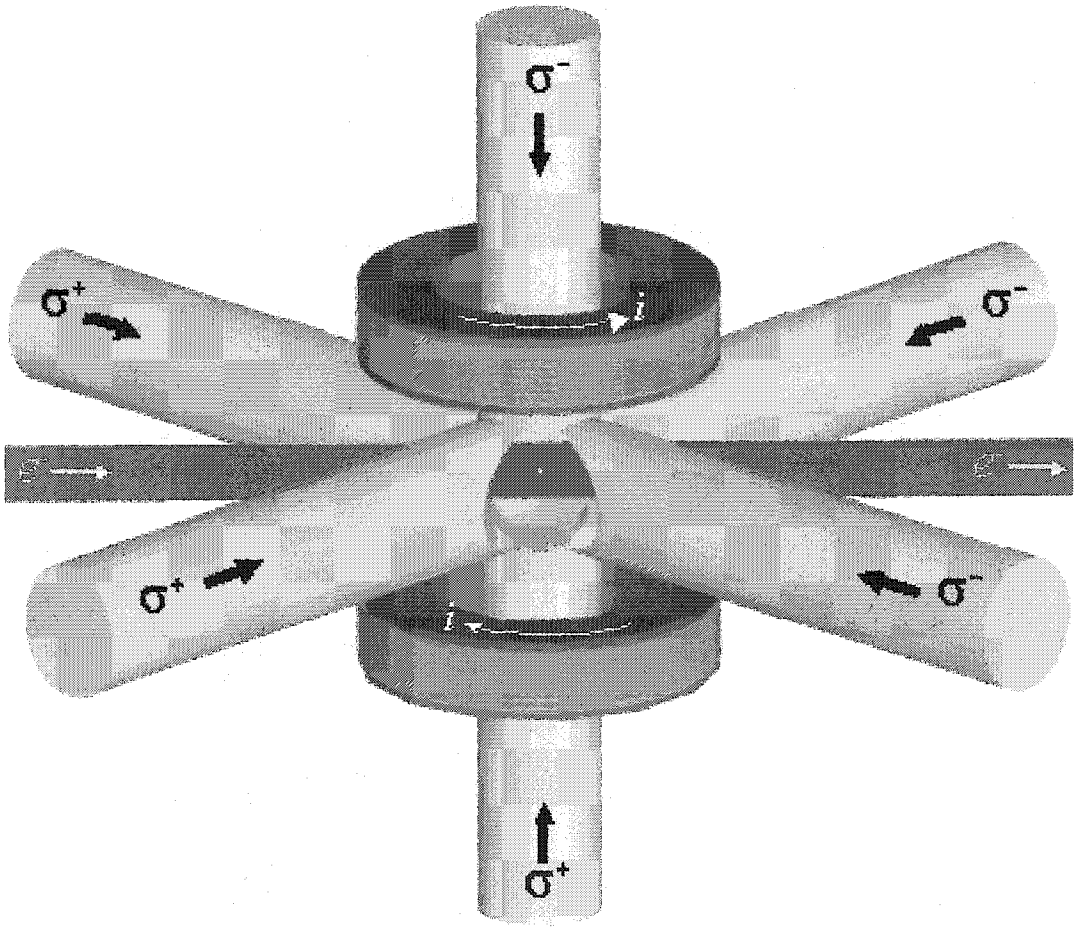

Arrangement of laser beams, magnetic coils, and electron beam used for the electron collision studies with a cesium MOT target.

2.1 Atom Photon Interactions

There are a variety of methods that are used for cooling and trapping atoms. A MOT is just one example of using light fields to control the motion or speed of atoms. The idea has been around for quite some time. The first ion trap dates back to 1975 [WINEL 75], while neutral atom traps were proposed the same year [HANSC 75]. The field progressed with the demonstration of the first neutral atom traps in 1986 [CHU 86], [MIGDA 85], [PRITC 86]. Since then the field has been steadily advancing with a growing number of applications that include Bose-Einstein condensation, atom optics and atom lasers, and slowing light with electromagnetically induced transparency to name a few.

Radiation fields can be used to either cool or trap a sample of atoms, depending on the properties of the field. If the field is dissipative, and used for cooling, then an additional mechanism must be used to trap the atoms, such as a magnetic confinement field. There have been considerable studies of the use of magnetic fields [BERGE 87] for the purpose of trapping atoms.

To begin, we start with the interactions of an atom with a light field. Then we will discuss how a light field can be used to apply a force on an atom. This gives us the tools necessary to discuss Doppler and sub-Doppler cooling mechanisms upon which a MOT operates. This will provide a full explanation of the optical component of a MOT, which will then lead us to a discussion of magnetostatic trapping fields. Finally, we will discuss the use of saturated absorption spectroscopy, a simple, effective means of referencing a laser frequency to an atomic transition, that provides for continuous operation of a MOT.

Sections 2.1and 2.2 will briefly discuss the basic working theory for describing the interaction of atoms with an incident laser field. The theory can be found, in much more detail, in sources such as Cohen-Tannoudji [COHEN 98], Metcalfe [METCA 99], and Meystre [MEYST 01].

2.1.1 Time-Dependent Perturbation Theory

The beginning point of our discussion of atom-photon interactions is to consider time

dependent perturbation theory for an atomic system in an electromagnetic field. The time-dependent Scrödinger equation is

$$\mathcal{H}\Psi(\mathbf{r},t) = i\hbar\frac{\partial}{\partial t}\Psi(\mathbf{r},t) \qquad 2.1$$

where $\mathcal{H}$ corresponds to the to the total Hamiltonian for an atom in a radiation field, and $\mathbf{r}$ is the coordinate of the electron. We can treat the electromagnetic interaction as a perturbation, such that

$$\mathcal{H}(t) = \mathcal{H}_0 + \mathcal{H}'(t) \qquad 2.2$$

with $\mathcal{H}_0$ is the field-free, time independent atomic Hamiltonian that satisfies

$$\mathcal{H}_0\varphi_n(\mathbf{r}) = E_n\varphi_n(\mathbf{r}) \qquad 2.3$$

where the eigenvalues, E_n, are given by

$$E_n = \hbar\omega_n \quad . \qquad 2.4$$

The eigenfunction $\Psi(\mathbf{r},t)$ can be expanded in terms of the field-free atomic eigenfunctions where the time-dependence is shifted from the atomic states to the coefficients $c_k(t)$.

$$\Psi(\mathbf{r},t) = \sum_k c_k(t)\varphi_k(\mathbf{r})\mathrm{e}^{-i\omega_k t} \quad . \qquad 2.5$$

Substituting the expanded Hamiltonian from Eq. 2.2, and the expanded wavefunction from Eq. 2.5 into Eq. 2.1 gives

$$\left[\mathcal{H}_0 + \mathcal{H}'(t)\right]\Psi(\mathbf{r},t) = i\hbar\frac{\partial\Psi(\mathbf{r},t)}{\partial t} = i\hbar\frac{\partial}{\partial t}\sum_k c_k(t)\varphi_k(\mathbf{r})\mathrm{e}^{-i\omega_k t} \quad . \qquad 2.6$$

Eq. 2.6 can be simplified by premultiplying by $\langle c_j(t)|$ and integrating over all position space

to get

$$i\hbar\frac{\partial c_j(t)}{\partial t} = \sum_k c_k(t)\langle\varphi_j|\mathcal{H}'(t)|\varphi_k\rangle e^{i(\omega_j-\omega_k)t} \qquad 2.7$$

which cannot be solved except to use perturbation theory and to make certain simplifying assumptions about the initial state of the system.

So far the treatment has used a classical radiation field, which does not create a problem. Such an assumption is quite valid for purposes of discussing laser cooling. One difficulty with Eq. 2.7 is the use of a large number of states. Another difficulty is the use of a perturbation theory where the fractional populations of the higher lying states must be small in order to treat with perturbation theory. One way of bypassing this is to restrict the number of states to a ground state and a single excited state. This is the Rabi two-level problem.

2.1.2 Rabi Two-Level Problem

We begin the Rabi two-level problem by considering only the ground and excited states, denoted φ_g and φ_e, respectively. Because our discussion will be restricted to considerations of lasers, this is an adequate treatment to pursue. The monochromatic radiation field of a laser will be used to couple two states, effectively reducing the atomic system to a two-level system. After reducing the number of states, we can write Eq. 2.7 for both states to get

$$i\hbar\frac{\partial c_g(t)}{\partial t} = c_e(t)\langle\varphi_g|\mathcal{H}'(t)|\varphi_e\rangle e^{-i(\omega_g-\omega_e)t} \qquad 2.8a$$

$$i\hbar\frac{\partial c_e(t)}{\partial t} = c_g(t)\langle\varphi_e|\mathcal{H}'(t)|\varphi_g\rangle e^{i(\omega_e-\omega_g)t} \qquad 2.8b$$

where the matrix elements describe the coupling between the ground and excited state brought on by the radiation field. The Hamiltonian in Eq. 2.8 can be expressed in terms of the electric dipole operator

$$\mathcal{H}'(t) = -e\mathcal{E}(\mathbf{r},t)\cdot\mathbf{r} \qquad 2.9$$

where $\mathcal{E}$ is the electric field operator. Eq. 2.9 is then inserted into Eq. 2.8 to solve for the time evolution of the atomic system. However, to solve the equations requires the use of two approximations [METCA 99]. The first is the electric dipole approximation (*EDA*) which states that the spatial variation of the amplitude of the electric field can be neglected over the atomic dimension. This is quite a reasonable assumption, as the wavelength of light used for most cooling and trapping applications is in the visible to near-infrared region of the spectrum, while an atomic dimension is of the order of a nanometer. The second approximation is the so-called rotating wave approximation (*RWA*) which states that terms of the order of ω_l^{-1} can be neglected in comparison with those of the order of $(\omega_l - \omega_a)^{-1}$.

To proceed, we consider the electric field of a plane wave travelling along the z direction

$$\mathcal{E} = \mathrm{E}_0 \hat{\varepsilon} \cos\left(kz - \omega_l t\right) \tag{2.10}$$

with $\hat{\varepsilon}$ the unit polarization vector, and E_0 the amplitude of the field. At this point it is convenient to introduce the quantity, Ω, the Rabi frequency, which is defined as

$$\Omega = -\frac{e\mathrm{E}_0}{\hbar}\langle e|r|g\rangle \tag{2.11}$$

The Rabi frequency can be used to simplify the matrix elements of Eq. 2.8 by using the result

$$\left\langle \varphi_e \left| \mathcal{H}'(t) \right| \varphi_g \right\rangle = \hbar\Omega \cos\left(kz - \omega_l t\right) \tag{2.12}$$

The differential equations of Eq. 2.8 are decoupled, and then simplified using the result of Eq. 2.12 to get

$$\frac{\mathrm{d}^2 c_g(t)}{\mathrm{d}t^2} - \mathrm{i}\delta\frac{\mathrm{d}c_g(t)}{\mathrm{d}t} + \frac{\Omega^2}{4}c_g(t) = 0 \tag{2.13a}$$

$$\frac{\mathrm{d}^2 c_e(t)}{\mathrm{d}t^2} + \mathrm{i}\delta\frac{\mathrm{d}c_e(t)}{\mathrm{d}t} + \frac{\Omega^2}{4}c_e(t) = 0 \tag{2.13b}$$

The analysis discussed here for the Rabi two-level problem requires that the interaction Hamiltonian, $\mathcal{H}'(t)$, be of a form where the diagonal matrix elements can be absorbed into the field-free, atomic Hamiltonian, $\mathcal{H}_0$. This leaves only one, off-diagonal element to be solved for in Eq. 2.7. The treatment so far provides an adequate description of stimulated processes induced by the driving force of the field on the atom. However, there is no convenient means of taking into account spontaneous emission. Spontaneous emission is the key component to cooling atoms with a radiation field as it is the only irreversible process. The theoretical treatment we need to fully describe laser cooling must be able to account for spontaneous emission. The easiest way to incorporate spontaneous emission is to use the density matrix, from which we can obtain the optical Bloch equations to give a full description of emission and absorption processes.

2.1.3 Optical Bloch Equations

As mentioned above, the starting point is the density matrix. Recall that the definition of the density matrix is

$$\rho = |\psi\rangle\langle\psi| \quad . \tag{2.14}$$

If we expand the wavefunction ψ in terms of the basis set $\{\varphi_n\}$ such that

$$\psi = \sum_{i=1}^{n} c_i \varphi_i \quad . \tag{2.15}$$

The matrix elements are then given by

$$\rho_{ij} = \langle\varphi_i|\psi\rangle\langle\psi|\varphi_j\rangle = c_i c_j^* \quad . \tag{2.16}$$

$$\langle A\rangle = \mathrm{Tr}(\rho A) \quad . \tag{2.17}$$

We can define the expectation value of an operator, A to be

To describe a mixed state, the density matrix takes the form

$$\rho = \sum_i p_i \left|\psi_i\right\rangle\left\langle\psi_i\right| \qquad 2.18$$

where p_i is the probability of finding the system in state i.

To treat spontaneous emission, we consider a two-level atom in the excited state at time $t = 0$. As times progresses, the atom has a chance of remaining in the excited state, or making a transition to the ground state. The wavefunction for the system can be written as

$$\left|\Psi\right\rangle = \alpha(t)\left|e, 0\right\rangle + \sum_S \beta_S(t)\left|g, 1_S\right\rangle \quad . \qquad 2.19$$

Rewriting Eq. 2.19 in a manner similar to that of Eq. 2.5 gives

$$\left|\Psi\right\rangle = c_{e,0}\mathrm{e}^{-i\omega_e t}\left|e, 0\right\rangle + \sum_S c_{g,1_S}\mathrm{e}^{-i(\omega_g+\omega)t}\left|g, 1_S\right\rangle \qquad 2.20$$

where the first value in the kets represents the atomic state and the second value represents the population of photons in the vacuum field. The summation index, S, is the mode of spontaneous emission given by wavevector and polarization ($\mathbf{k}$,ε). The atomic system is initially in a pure state that evolves into a mixed state. Using Eq. 2.20 with the time-dependent Schrödinger equation to form a set of differential equations analogous to Eq. 2.8.

$$i\frac{\mathrm{d}c_{e,0}(t)}{\mathrm{d}t} = \sum_S c_{g,1_S}(t)\Omega_S\mathrm{e}^{-i(\omega-\omega_a)t} \qquad 2.21a$$

$$i\frac{\mathrm{d}c_{g,1_S}(t)}{\mathrm{d}t} = c_{e,0}(t)\Omega_S^*\mathrm{e}^{i(\omega-\omega_a)t} \qquad 2.21b$$

where Ω_S is the vacuum Rabi frequency which is given in terms of the electric dipole moment, μ, and the electric field per photon $\mathbf{E}_p$.

$$\hbar\Omega_S = -\mu\cdot\mathbf{E}_p \quad . \qquad 2.22$$

The dipole moment is given by

$$\mu = e\langle e|\mathbf{r}|g\rangle \tag{2.23}$$

and the electric field per photon, or energy density is

$$\mathbf{E}_p = \sqrt{\frac{\hbar\omega}{2\epsilon_0 \mathrm{V}}}\,\boldsymbol{\varepsilon} \tag{2.24}$$

where V represents an arbitrary volume, that eventually is dropped from the calculation. To solve Eq. 2.21, the equations must first be decoupled and then some statistical mechanics has to be used to count the photon modes, which requires integrating with respect to all spatial coordinates and then with time. The result of this treatment is

$$\frac{\mathrm{d}c_{e,0}(t)}{\mathrm{d}t} = -\frac{\gamma}{2}c_{e,0}(t) \tag{2.25}$$

where we have defined γ to be

$$\gamma = \frac{\omega^3\mu^2}{3\pi\epsilon_0\hbar\mathrm{c}^3} \tag{2.26}$$

and allows one to define the lifetime, τ, of the excited state

$$\tau = \frac{1}{\gamma} \tag{2.27}$$

Now that we have a means of describing the effect of spontaneous emission on the atomic system, we can begin the derivation of the optical Bloch equations. The time dependent Schrödinger equation, using the density matrix formalism, is given by

$$i\hbar\frac{\mathrm{d}\rho}{\mathrm{d}t} = \left[\mathcal{H},\rho\right] \tag{2.28}$$

which, for a two-level atomic system, gives

$$\rho = \begin{pmatrix} \rho_{ee} & \rho_{eg} \\ \rho_{ge} & \rho_{gg} \end{pmatrix} = \begin{pmatrix} c_e c_e^* & c_e c_g^* \\ c_g c_e^* & c_g c_g^* \end{pmatrix} \quad . \tag{2.29}$$

The optical Bloch equations are obtained from combining Eq. 2.28 and 2.29 together, and decoupling the system of equations as in Eq. 2.13. As an example, considering the element, ρ_{gg}, we have

$$\frac{\mathrm{d}\rho_{gg}}{\mathrm{d}t} = \frac{\mathrm{d}c_g}{\mathrm{d}t} c_g^* + c_g \frac{\mathrm{d}c_g^*}{\mathrm{d}t} \tag{2.30}$$

to which we can insert the results of Eq. 2.8 to get

$$\frac{\mathrm{d}\rho_{gg}}{\mathrm{d}t} = \left[\frac{c_e \mathcal{H}'_{ge} e^{-i\omega_a t}}{i\hbar} \right] c_g^* - c_g \left[\frac{c_e^* \mathcal{H}'_{eg} e^{+i\omega_a t}}{i\hbar} \right] \tag{2.31}$$

where we have used a compact form of denoting the matrix elements, $\langle e|\mathcal{H}'|g\rangle = \mathcal{H}'_{eg}$. Eq. 2.31 can be simplified using Eq. 2.12. with the cosine portion rewritten in terms of complex exponentials. Then the RWA and EDA can be applied to drop all exponential terms except those with exponents containing $\delta = \omega_l - \omega_a$. Doing this, allows one to rewrite Eq. 2.31 in terms of the Rabi frequency

$$\frac{\mathrm{d}\rho_{gg}}{\mathrm{d}t} = \frac{i}{2}\left(\Omega^* \rho_{eg} \mathrm{e}^{-i\delta t} - \Omega \rho_{ge} \mathrm{e}^{i\delta t} \right) \quad . \tag{2.32}$$

At this point, we can build in the effects of spontaneous emission, using Eq. 2.25. After performing some simplifications, we obtain the optical Bloch equations in their final form

$$
\begin{aligned}
\frac{d\rho_{gg}}{dt} &= \gamma\rho_{ee} + \frac{i}{2}\left(\Omega^{*}\tilde{\rho}_{eg} - \Omega\tilde{\rho}_{ge}\right) \\
\frac{d\rho_{ee}}{dt} &= -\gamma\rho_{ee} + \frac{i}{2}\left(\Omega\tilde{\rho}_{ge} - \Omega^{*}\tilde{\rho}_{eg}\right) \\
\frac{d\tilde{\rho}_{ge}}{dt} &= -\left(\frac{\gamma}{2} + i\delta\right)\tilde{\rho}_{ge} + \frac{i}{2}\Omega^{*}\left(\rho_{ee} - \rho_{gg}\right) \\
\frac{d\tilde{\rho}_{eg}}{dt} &= -\left(\frac{\gamma}{2} - i\delta\right)\tilde{\rho}_{eg} + \frac{i}{2}\Omega\left(\rho_{gg} - \rho_{ee}\right)
\end{aligned}
\qquad 2.33
$$

There are several concepts, such as optical pumping, that are relevant to the operation of a MOT and are built upon these equations. However, we will end our analysis at this point. The reader is redirected to other sources such as Cohen-Tannoudji[COHEN 98] for a full discussion of optical pumping and other phenomena.

Now that we have the optical Bloch equations we can use the results to determine the steady state, fractional populations of the atomic states coupled by the laser field, which will become important in future discussions of our electron collision cross sections, or they can be used to derive an expression for the radiation force on an atom.

2.2 Radiation Force

The necessary criteria for cooling and trapping atoms is to make the absorption process for the atoms sensitive to both position (trapping) and velocity (cooling). We will consider now the radiation force on an atom, at rest and in motion, to see how it depends on the atomic motion.

The radiation force on an atom can be thought of simply as the product of the photon scattering rate and the photon momentum. Hence we see the relevance of the development of the optical Bloch equations from the previous section. To begin, we use the Ehrenfest Theorem to form a quantum mechanical force operator , $\mathcal{F}$, defined as

$$\mathrm{F} \rightarrow \langle \mathcal{F} \rangle = \frac{\mathrm{d}}{\mathrm{d}t}\langle p \rangle \tag{2.34}$$

using the definition of the time evolution operator of the

$$\frac{\mathrm{d}}{\mathrm{d}t}\langle p \rangle = \frac{i}{\hbar}\langle [\mathcal{H}, p] \rangle \tag{2.35}$$

allows one to restate Eq. 2.34 as

$$\langle \mathcal{F} \rangle = -\left\langle \frac{\partial \mathcal{H}}{\partial z} \right\rangle \tag{2.36}$$

The Hamiltonian used here is the same as in Eq. 2.9, as it is the force from the radiation field that we are interested in.

$$\langle \mathcal{F} \rangle = e\left\langle \frac{\partial}{\partial z}(\mathcal{E} \cdot \mathbf{r}) \right\rangle \tag{2.37}$$

If we again invoke the EDA, the derivative can be moved out of the expectation value

$$\mathrm{F} = e\frac{\partial}{\partial z}\langle \mathcal{E} \cdot \mathbf{r} \rangle \tag{2.38}$$

Using Eq. 2.17 to relate the force to the density matrix gives

$$\mathrm{F} = \hbar\left(\frac{\partial\Omega}{\partial z}\rho_{eg}^{*} + \frac{\partial\Omega^{*}}{\partial z}\rho_{eg}\right) \quad . \tag{2.39}$$

Before inserting the density matrix element ρ_{eg} into the above equation, it is useful to apply some complex analysis to Eq. 2.39 so that we may examine the real and imaginary components of the force equation. Using a logarithmic derivative [BROWN 96] of the form

$$\frac{\mathrm{d}}{\mathrm{d}z}\Omega = \left(q_r + iq_i\right)\Omega \tag{2.40}$$

we can express Eq. 2.39 as

$$\mathrm{F} = \hbar q_r\left(\Omega\rho_{eg}^{*} + \Omega^{*}\rho_{eg}\right) + i\hbar q_i\left(\Omega\rho_{eg}^{*} - \Omega^{*}\rho_{eg}\right) \tag{2.41}$$

This is the generalized force equation that can be used for a wide variety of applications. We will concentrate on two specific cases, relevant to laser cooling and trapping. The first case is for a standing wave from a laser, and the second is a travelling wave.

2.2.1 Stationary Atom

For a travelling wave such as that in Eq. 2.10, the electric field is

$$E(z) = E_0\cos\left(kz - \omega_l t\right) = \frac{E_0}{2}\left(\mathrm{e}^{+i\left(kz-\omega_l t\right)} + \mathrm{e}^{-i\left(kz-\omega_l t\right)}\right) \quad . \tag{2.42}$$

Using this to define a Rabi frequency for the general force equation in Eq. 2.41, it is found from Eq. 2.40 that the term $q_r = 0$ and $q_i = k$. Since only q_i is non-zero, we have the case of a field that varies in phase, but has a constant amplitude.

For a standing wave of the form

$$E(z) = E_0\cos(kz)\left(\mathrm{e}^{-i\omega_l t} + \mathrm{e}^{+i\omega_l t}\right) \tag{2.43}$$

we perform a similar analysis to that for the travelling wave to find that $q_r = -k \tan(kz)$ and $q_i = 0$. The situation is opposite to that of the travelling wave, as we now have a spatial variation in the amplitude, but a fixed phase. To proceed in solving for the general force equation in Eq. 2.41, we need to have an expression for the density matrix element, ρ_{eg}, which requires solving the optical Bloch equation in Eq. 2.33. To do so, we make a variable transformation, $w = \rho_{gg} - \rho_{ee}$

$$\frac{dw}{dt} = \frac{d\rho_{gg}}{dt} - \frac{d\rho_{ee}}{dt} = \gamma(1 - w) - i\left(\Omega\rho_{eg}^{*} - \Omega^{*}\rho_{eg}\right) \tag{2.44}$$

$$\frac{d\rho_{eg}}{dt} = -\left(\frac{\gamma}{2} - i\delta\right)\rho_{eg} + iw\frac{\Omega}{2} \tag{2.45}$$

and consider the steady state solution, where the time derivatives go to zero, to find

$$w = \frac{1}{1 + 2\dfrac{|\Omega|^2}{\gamma^2 + 4\delta^2}} = \frac{1}{1 + \dfrac{s_0}{1 + 4\delta^2/\gamma^2}} \tag{2.46}$$

$$\rho_{eg} = \frac{i\Omega}{2\left(\gamma/2 - i\delta\right)\left(1 + \dfrac{s_0}{1 + 4\delta^2/\gamma^2}\right)} \tag{2.47}$$

where we have introduced the on-resonance saturation parameter, s_0, defined as

$$s_0 = \frac{2|\Omega|^2}{\gamma^2} = \frac{I}{I_s} \tag{2.48}$$

with I_s the saturation intensity. The saturation intensity is a parameter that is specific to a transition and defined by

$$I_s = \frac{\pi hc}{3\lambda^3\tau} \tag{2.49}$$

After solving for w and ρ_{eg} in Eq's. 2.46 and 2.47, we can solve for the excited state fraction,

ρ_{ee}, by combining the definition of w and using the fact that Tr(ρ) =1 to get

$$\rho_{ee} = \frac{1}{2}\frac{s_0}{1+ s_0 + 4\delta^2/\gamma^2} \qquad 2.50$$

We now have expression for the elements of the density matrix, obtained from solving the steady state, optical Bloch equations given in Eq. 2.33. Using the result in Eq. 2.47 allows us to solve for the general radiation force in Eq. 2.41.

$$\mathrm{F} = \frac{\hbar s}{1+ s}\left(-\delta q_r + \frac{1}{2}\gamma q_i\right) \quad . \qquad 2.51$$

The force is defined using the saturation parameter, s, that is related to the *on-resonance saturation parameter*, s_0 by

$$s = \frac{s_0}{1+ 4\delta^2/\gamma^2} \quad . \qquad 2.52$$

For zero detuning ($\delta = 0$), we have $s = s_0$ and the force in Eq. 2.51 reduces to

$$\mathrm{F} = \hbar k \frac{\gamma}{2}\frac{s_0}{s_0 + 1} \qquad 2.53$$

which is just the photon momentum multiplied by the photon scattering rate.

The radiation force takes on different forms depending on the type of radiation field applied to the atomic system. Considering the two special cases of travelling and standing waves discussed earlier in Eq's. 2.42 and 2.43 shows how a radiation field can be used to either cool a sample of atoms or to trap them. For the case of a travelling wave, such as that in Eq. 2.42, we have $q_r = 0$ and $q_i = k$. Substituting these values into Eq. 2.51 gives
This is a force that corresponds to absorption followed by spontaneous emission, which gives rise to the name *spontaneous* light force. Since spontaneous emission is an irreversible process, this force is also referred to as a *dissipative* force. It is this dissipation that gives rise to the cooling effect of a near-resonant radiation field. Consequently, it is a spontaneous light

force that is used for the MOT. This force cannot be increased without limit since the rate of spontaneous emission is limited by the excited state fraction which has a high-intensity limit of 1/2. Eventually, as the intensity of the laser field increases, stimulated emission processes begin to dominate, since there is no corresponding limiting factor for stimulated emission processes.

We now examine another force that arises from a radiation field comprised of a standing wave, such as that in Eq. 2.43. We discussed that this type of light field has $q_r = -k$ tan(kz) and $q_i = 0$. Proceeding as before with the travelling wave, we find that

$$F_{dip} = \frac{2\hbar k\delta s_0 \sin 2kz}{1 + 4s_0 \cos^2 kz + 4(\delta/\gamma)^2} \quad . \qquad 2.55$$

This force is a *dipole* force due to the resemblance with the force of a classical electric dipole. It is also referred to as a *reactive* force. This force is proportional to the gradient of the electric field. The dependence of the force on the laser detuning, δ, has the interesting feature of putting the atoms in a high or low field seeking state, depending on the sign of the detuning. For $\delta < 0$, the force drives the atoms to regions with an intensity maxima. Conversely, for $\delta > 0$, the force will drive atoms to regions with an intensity minima. The dipole force is also a conservative force, which means that it cannot be used to cool a sample of atoms, but can be used to trap atoms.

So far we have only considered the radiation forces for stationary atoms. Our goal is to use radiation forces to slow atoms to rest from some thermal velocity. Which brings us to the next section where we consider the influence of radiation forces on a atoms in motion.

2.2.2 Atoms in Motion

To study the interaction of a laser field with a moving atom, we must treat the velocity of the atom as a perturbation, as the optical Bloch equations with a built-in velocity dependence are difficult, if not impossible, to solve analytically. A common approach to incorporating velocity dependence begins with modifying the Rabi frequency so that it satisfies

$$\frac{d\Omega}{dt} = \frac{\partial\Omega}{\partial t} + v\frac{\partial\Omega}{\partial z} = \frac{\partial\Omega}{\partial t} + v(q_r + iq_i)\Omega \qquad 2.56$$

where we have used the logarithmic derivative as in Eq. 2.40. Modifying the derivatives in Eq's. 2.44 and 2.45 similarly, we have

$$\frac{dw}{dt} = \frac{\partial w}{\partial t} + v\frac{\partial w}{\partial z} = \frac{\partial w}{\partial t} - \frac{2vq_r s}{(1+s)^2} \qquad 2.57$$

$$\frac{d\rho_{eg}}{dt} = \frac{\partial\rho_{eg}}{\partial t} + v\frac{\partial\rho_{eg}}{\partial z} = \frac{\partial\rho_{eg}}{\partial t} - \frac{iv\Omega}{2(\gamma/2 - i\delta)(1+s)}\left[q_r\left(\frac{1-s}{1+s}\right) + iq_i\right] \qquad 2.58$$

We can now proceed in a similar fashion as in the previous section for stationary atoms. For a travelling wave, we have $q_r = 0$. The end result of the analysis for the force for the travelling wave is

$$F = \hbar q_i \frac{s\gamma/2}{1+s}\left(1 + v\frac{2\delta q_i}{(1+s)(\delta^2 + \gamma^2/4)}\right) \quad . \qquad 2.59$$

This force can be separated into two parts. The first part is independent of velocity and corresponds to the force for an atom at rest, while the second is a velocity-dependent force, damping the motion. We simplify Eq. 2.59 to

$$F = F_0 - \beta v \qquad 2.60$$

with

$$\beta = -\hbar k^2 \frac{4s_0(\delta/\gamma)}{\left(1 + s_0 + (\delta/\gamma)^2\right)^2} \qquad 2.61$$

We note that the force in Eq. 2.60 is never zero, even for stationary atoms so that the field is always exerting a force on the atom.

Proceeding to the case of the standing wave, where we have $q_r = -k \tan(kz)$ and $q_i = 0$, we find

$$F = \hbar k \frac{s_0 \delta \gamma^2}{2\left(\delta^2 + \gamma^2/4\right)} \left(\sin 2kz + kv \frac{\gamma(1 - \cos 2kz)}{\left(\delta^2 + \gamma^2/4\right)} \right) \quad . \tag{2.62}$$

We can separate Eq. 2.62 into a simplified form as was done with in Eq. 2.60 for the force of a travelling wave. However since we are now dealing with a standing wave, and the associated force is comprised of oscillatory terms, we will consider the spatial average of the force. The first term, corresponding to $\sin(2kz)$, is zero after averaging. Using the same argument with $\cos(2kz)$, the averaged force is

$$F = -\beta v \tag{2.63}$$

where the damping coefficient β, is

$$\beta = -\hbar k^2 \frac{8 s_0 \left(\delta/\gamma\right)}{\left(1 + \left(2\delta/\gamma\right)^2\right)^2} \quad . \tag{2.64}$$

In contrast to the force from the travelling wave, the force for the standing wave can be zero.

We have shown how a laser field can be used to supply a force to an atom, and how that force can be dependent on the atomic velocity. The next step is to show how this force is implemented and leads to Doppler cooling and optical molasses.

2.3 Doppler Cooling

To perform Doppler cooling, it is necessary to configure the laser field to provide a dissipative force, as shown in Eq. 2.54. This field will provide effective cooling for atoms travelling anti-parallel to the propagation vector of the field, but will not cool for atoms travelling parallel. To account for this a second field is added to the first, but travelling in the opposite direction. This gives two counter-propagating, travelling waves, whose amplitudes simply add together. (These two counter-propagating beams should not be confused with the standing wave of the previous section). This method of laser cooling without a trapping mechanism creates an optical molasses (*OM*).

The total force of the field, denoted $\mathbf{F}_{OM}$, is

$$\mathbf{F}_{OM} = \mathbf{F}_{+} + \mathbf{F}_{-} \tag{2.65}$$

where we have used $\mathbf{F}_{+}$ and $\mathbf{F}_{-}$ to refer to each of the fields (incident and returning, right and left, etc.). The component fields are given by

$$\mathbf{F}_{\pm} = \pm\hbar\boldsymbol{k}\frac{\gamma}{2}\frac{s_0}{1+s_0+\left[2\left(\delta\mp\left|\omega_D\right|\right)/\gamma\right]^2} \tag{2.66}$$

where we have introduced the quantity ω_D, the Doppler shift

$$\omega_D = -\boldsymbol{k}\cdot\mathbf{v} \quad . \tag{2.67}$$

This allows us to write the total force as

$$\mathbf{F}_{OM} \cong \frac{8\hbar k^2\delta s_0}{\gamma\left(1+s_0+\left(2\delta/\gamma\right)^2\right)^2}\mathbf{v} \quad . \tag{2.68}$$

What we have so far is a pair of counter-propagating laser fields for one direction, giving us an optical molasses, or cold sample of atoms, in one dimension only. We are dealing with a three-dimensional gas, which requires three pairs of counter-propagating laser fields to lower the total energy of the atoms.

We now consider the effects of these radiation forces on the atomic system to demonstrate Doppler cooling and the formation of an optical molasses. In Fig. 2.1 we have an atom moving to the right, with a velocity, **v**, along a pair of counter-propagating laser beams. The laser beams are of a frequency ω_l, and have wavevectors, $+\boldsymbol{k}$ and $-\boldsymbol{k}$. The laser frequency is slightly below the atomic transition frequency, $\omega_a = E_{eg} / \hbar$. Using Eq. 2.67, we see that the Doppler shift is positive for the beam travelling opposite the atomic motion, while the Doppler shift is negative for the beam travelling parallel to the atomic motion. Since the laser frequency is below the atomic transition (red-shifted), then the atom will absorb from the $-\boldsymbol{k}$ beam. In other words, while the lasers share the same frequency in the lab frame, in the atomic frame the beam travelling towards the atom is Doppler shifted closer to resonance with the atomic transition. The other beam appears Doppler shifted further from resonance. Thus the absorption is more likely to occur from the beam travelling opposite the atomic motion.

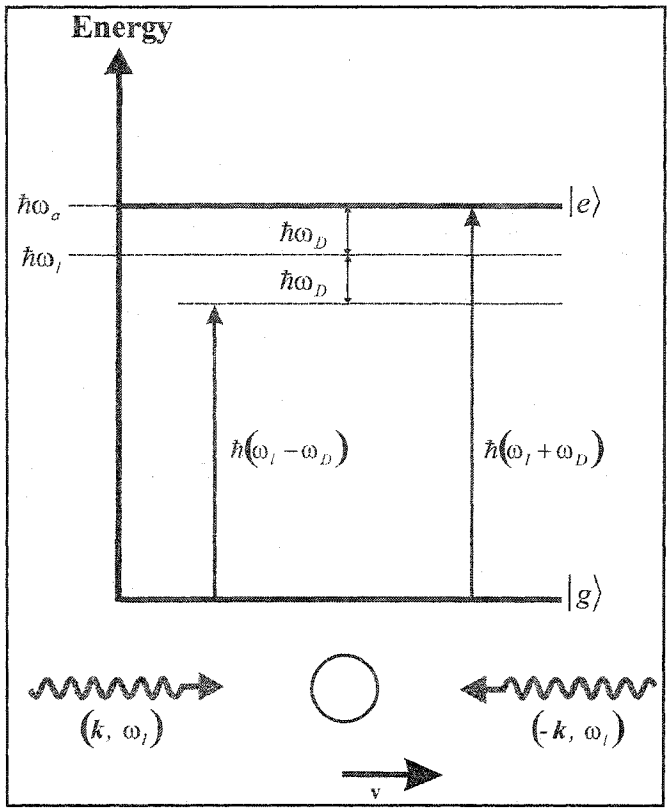

Figure 2.1: Diagram illustrating velocity dependent absorption for a moving atom.

Since the absorption is always from the same beam, for a given atomic velocity, and the decay is predominantly spontaneous emission which occurs over all directions, the net effect is transfer of momentum from the radiation field to the atom. Many such absorption-emission events, effectively slow the atom to near-zero speeds. Of course this cooling mechanism cannot be used to reach a zero speed of the atom since the minimum atomic momentum corresponds to a photon recoil.

We now have counter-propagating laser beams along three mutually orthogonal directions. The laser frequency is adjusted to be red-shifted from the atomic transition frequency. The magnitude of the red-shifted detuning (for cooling with a spontaneous light force) is typically one half of the natural linewidth of the transition. This geometry of detuned laser fields is sufficient for producing an optical molasses. A cloud of cold atoms is produced from this configuration of laser beams with the average atomic velocity at or near the Doppler velocity (see Eq. 2.72). However, the atoms are not localized to any region of space. To do so requires an additional field, a magnetostatic field for the MOT, to provide a restoring force to the atoms about some central trapping region. For magnetostatic trapping, the laser configuration discussed here must be altered to include circularly polarized laser fields. We will discuss this later in Section 2.5. The implementation of circularly polarized laser fields also has the effect of producing a polarization gradient that gives rise to sub-Doppler cooling mechanisms which we will discuss in the next section.

Before proceeding to sub-Doppler cooling, we will discuss some common terms and concepts used to describe the performance of laser cooling for a particular experiment. The performance of a laser cooling experiment is often characterized in terms of limiting velocities and their corresponding temperatures. Although temperature is often used in discussions of laser cooling, strictly speaking such a quantity has no physical meaning, at least in the thermodynamics sense, when used with samples of cold atoms. It is impossible to establish a thermal equilibrium for the laser cooled atoms with their surroundings, and so the thermodynamics definition of temperature cannot be applied. To achieve laser cooling it is necessary to isolate the atoms from the surroundings in order for the laser cooling to be effective. Despite this, temperature is commonly used within the laser cooling community to provide a convenient means of quantifying the kinetic energy of the cooled sample.

First, we consider the *capture velocity* and the *capture temperature*. The capture velocity refers to the maximum velocity for an atom, that will allow absorption of the near-resonant laser field. The capture velocity is defined in terms of the cooling transition properties and the laser field,

$$v_c = \frac{\gamma}{k} \quad . \tag{2.69}$$

For the cesium D_2 line, this gives a capture velocity of 4.45 m sec^{-1}. From this we can define a capture temperature ($1/2\ Mv_c^2 = 1/2\ k_B T_c$)

$$k_B T_c = M\frac{\gamma^2}{k^2} \tag{2.70}$$

which for cesium is 0.316 K. These values classify the fastest moving atoms that can be contained in the MOT. An optical molasses is formed from the atoms with initial velocities, defined by the Maxwell Boltzmann distribution in Eq. 1.4, less than the capture velocity.

The next set of values commonly used are the *Doppler temperature* and *Doppler velocity*. The Doppler temperature is found by relating the thermal energy to the energy associated with the natural linewidth of the cooling transition

$$k_B T_D = \frac{\hbar\gamma}{2} \tag{2.71}$$

which gives a Doppler temperature for cesium of 125 μK. From Eq. 2.71, we can convert to a Doppler velocity by relating the thermal and kinetic energies to give

$$v_D = \sqrt{\frac{k_B T_D}{M}} \tag{2.72}$$

which for cesium is 88.5 mm sec^{-1}.The Doppler temperature and velocity correspond to the lower limits produced by Doppler cooling. Consequently, they are sometimes referred to as the Doppler limit.

The last set of values are the *recoil velocity* and the *recoil temperature* that are found by relating to the momentum of a single photon. The recoil velocity is found by equating the photon momentum with the atomic momentum to give

$$v_r = \frac{\hbar k}{M} \quad . \tag{2.73}$$

This gives a recoil velocity for cesium of 3.52 mm sec^{-1}. The recoil temperature is then found from the recoil velocity

$$k_B T_r = \frac{\hbar^2 k^2}{M} \tag{2.74}$$

which for cesium results in a recoil temperature of 198 nK. These recoil values give the ultimate limit for cooling with optical processes due to the quantization of the radiation field.

From these temperatures and velocities, a variety of useful quantities can be defined. We can use the average thermal velocity for the background from Eq. 1.5 with the velocities discussed here to approximate the number of photon absorptions required to cool the atom to the Doppler or recoil temperature. For instance,

$$N_r = \frac{v_{mp}}{v_r} \tag{2.75}$$

which gives ~55 000 absorptions to reach the recoil temperature. Knowing the number of absorptions required to cool the atoms can give an estimate of the stopping (slowing) distance

$$\lambda_r = 2 v_{mp} N_r \tau \tag{2.76}$$

where the factor of 2 assumes that the slowing rate is half the maximum deceleration. A rough estimate for the stopping distance using Eq. 2.76 is 60 cm.

2.4 Sub-Doppler Cooling

We proceed now with a brief discussion of sub-Doppler cooling mechanisms. This research involves the use of a MOT. A MOT is constructed by placing the optical molasses formed from the three pairs of counter-propagating laser beams discussed in the previous section, in a static magnetic field so that we have a geometry as illustrated on the first page of this chapter. The laser beams are altered to provide a polarization gradient along each beam pair. The combination of magnetic fields and polarized light gives rise to optical pumping that allows the cooled atoms to be trapped. The optical pumping of the MOT has the consequence of providing colder average temperatures than those in an optical molasses.

In an attempt to provide an explanation of observed temperatures in a MOT that are below the Doppler limit, several theories have been put forward. The first theory is for a damping force that is dependent on the polarization gradient of the light field formed by two counter-propagating beams that are each linearly polarized but in orthogonal directions. For brevity, we will refer to this polarization scheme as the lin-perp-lin scheme [DALIB 89a]. The second theory is for counter-propagating laser beams where the first beam has a circular polarization opposite to the second beam, or the σ^+-σ^- scheme [DALIB 89a].

There are other theories for cooling atoms below the Doppler limit, such as magnetically induced laser cooling [DALIB 89], but we will restrict our discussion to the lin-perp-lin and σ^+-σ^- polarization theories as they are most relevant for the sub-Doppler cooling processes in a MOT.

For the lin-perp-lin polarization scheme, the combination of laser fields produces a polarization that has a very strong spatial dependence. The polarization, starting from linear changes to circular to linear orthogonal to circular orthogonal and back to its original polarization over half a wavelength, as shown in Fig. 2.2. The simplest case to consider is that of an atom with a $j = 1/2$ ground state. If we now consider a region where the light field has a pure σ+ polarization, due to optical pumping, an atom at this location will undergo absorption from the $m_j = 1/2$ sublevel to the $\Delta m_j = +1$ state. Following this with decay through spontaneous emission, we have $\Delta m_j = \pm 1, 0$, and the atom has a non-zero probability

of ending up in the $m_j = -1/2$ ground state sublevel. In so doing, it has undergone a net loss of energy, as illustrated in Fig. 2.3. So this configuration of the polarization causes a periodic variation of the energy of the ground state sublevels, giving rise to a series of hills and valleys, where absorption is most likely to occur near the top of a hill. Combining this with the effects of spontaneous emission, can ensure that an atom will, on average, decay to a valley and will continually have to climb a hill. This interpretation is the reason that the lin-perp-lin polarization gradient cooling is commonly referred to as Sysiphus cooling, after a character from Greek mythology who was condemned for eternity to push a boulder up a hill.

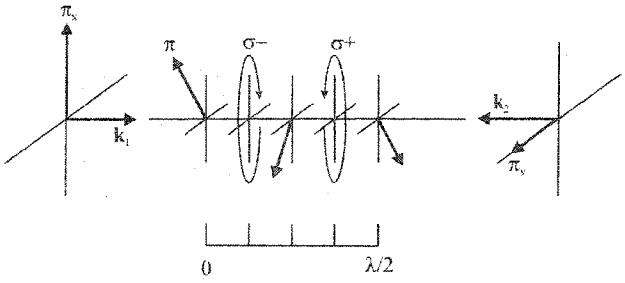

Figure. 2.2: Lin-perp-lin polarization scheme

The σ^+-σ^- polarization scheme also gives rise to a polarization gradient cooling mechanism, but in a different fashion. The sub-Doppler cooling mechanism with circularly polarized light is not quite as simple as for the previous case, due to the fact that there is no spatial variation of the ground state sublevel alignment. Hence, there is no Sysiphus effect. The spatial dependence of the polarization is shown in Fig. 2.4. This polarization gradient cooling mechanism works on the difference in scattering rate for moving atoms in a particular ground state sublevel, while illuminated with circularly polarized light. To briefly summarize, atoms moving towards the σ^+ beam will have a higher probability of being in a $m = +1$ state, and atoms moving towards the σ^- beam will have a higher probability of being in a $m = -1$ state. While in the $m = +1$ state, the atoms are much more efficient at

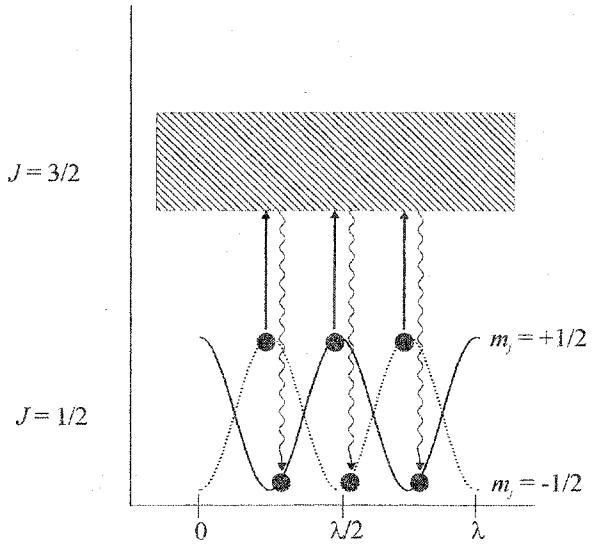

Figure 2.3: Diagram of the "Sysiphus effect"arising from the polarization gradient of a lin-perp-lin scheme with a $J = 1/2$ ground state atom.

scattering σ^+ light. If the sublevel populations are equal there is no polarization gradient cooling. However, if there is any imbalance in the sublevel population distribution, a large cooling effect can be produced.

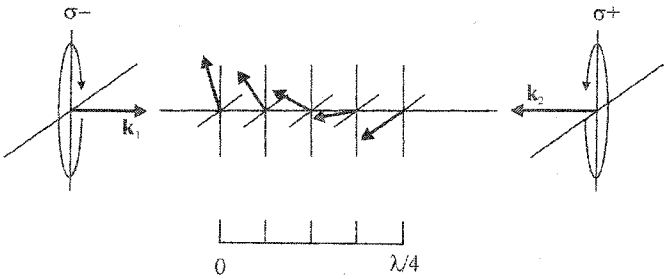

Figure 2.4: $\sigma^+ \sigma^-$ polarization scheme

Perhaps the simplest way to visualize the polarization gradient cooling for circularly polarized light is to think of it as essentially the same as Doppler cooling. However, instead of depending on velocity, the cooling is dependent on the difference in ground state sublevel populations that results from optical pumping.

2.5 Magnetostatic Traps for Neutral Atoms

One of the essential components of a magneto-optical trap is a static magnetic field that exhibits a B field minimum. The presence of such a field serves to lift the degeneracy of the atom's magnetic sublevels through the Zeeman shift. The goal of using such a magnetic field is to provide a restoring force to any atoms that are displaced from the field minimum. To achieve this, the magnetic field is constructed such that the field minimum coincides with the intersection of the three orthogonal, cooling laser beams. In doing so, the magnitude of the Zeeman shift varies with displacement from the trap center, and so the absorption rate and radiation force on the atom varies with displacement from the trap center.

There are a variety of magnetic trapping configurations in use. One can choose between permanent magnets, or electromagnetic coils. The field can be quadrupole, octupole, or higher order. There are elaborate coil geometries like the clover-leaf design, or the Ioffe coil where the coil runs like the seam on a baseball. The simplest field that can be used is a spherical quadrupole field produced from an anti-Helmholtz coil pair.

The expression for the magnetic field resulting from an anti-Helmholtz pair can be founding by taking the curl of the vector potential of a circular current loop. We begin with the basic definition for the magnetic field strength **B** which is the curl of the vector potential **A**.

$$\mathbf{B} = \nabla \times \mathbf{A} \tag{2.77}$$

the vector potential by definition is given by

$$\mathbf{A} = \frac{\mu I}{4\pi} \int_C \frac{\mathbf{dl}'}{r} \quad . \tag{2.78}$$

We consider first a single current loop of radius R, shown in Figure 2.5, situated with its center at $\rho = 0$, and z = A. Due to the geometry of the current loop, we choose a cylindrical polar coordinate system. We are free to choose our cylindrical coordinate system in such a way that the field point, $P(\rho, \phi, z)$, is oriented in the zx - plane, giving $\phi = 0$, since ϕ is

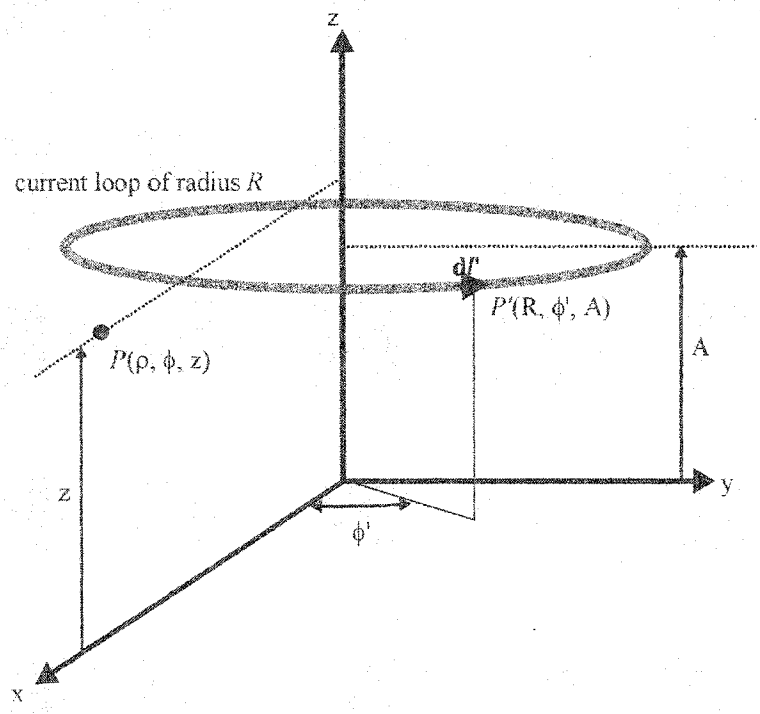

Figure 2.5: Circular current loop

cylindrically invariant under rotation. For such a configuration the circuit element $\mathbf{dl}'$ is situated at the source point P' (R, ϕ', A), and is given by

$$\mathbf{dl}' = \mathrm{R}\cos(\phi')\mathrm{d}\phi'\hat{\phi}' \qquad 2.79$$

The vector **r** is defined as the vector from the field point to the source point. In this case it is given by

$$\mathbf{r} = \left(\rho\hat{\rho} - \mathrm{R}\hat{\rho}'\right) + (\mathrm{z} - \mathrm{A})\hat{\mathrm{z}} \qquad 2.80$$

while the magnitude of **r** is

$$\mathrm{r} = |\mathbf{r}| = \sqrt{\mathrm{R}^2 + \rho^2 + (\mathrm{z} - \mathrm{A})^2 - 2\mathrm{R}\rho\cos(\phi')} \quad . \qquad 2.81$$

The vector potential **A**, has the following integral form for our circular coil

$$\mathbf{A} = \frac{\mu_0 \mathrm{I}}{4\pi}\int_0^{2\pi} \frac{\mathrm{R}\cos(\phi')\mathrm{d}\phi'}{\sqrt{\mathrm{R}^2 + \rho^2 + (\mathrm{z} - \mathrm{A})^2 - 2\mathrm{R}\rho\cos(\phi')}}\hat{\phi}' \quad . \qquad 2.82$$

The solution to this integral can be evaluated with the aid of Maple V6 numerical analysis software

$$\mathbf{A} = \frac{\mu_0 I}{2\pi\rho}\frac{1}{\sqrt{(R+\rho)^2+(z-A)^2}}\left[\left(1-\frac{1}{2}k^2\right)K(k)+\left(\frac{4R\rho}{k^2}\right)E(k)\right]\hat{\phi}' \quad . \qquad 2.83$$

The solution for the vector potential is given in terms of the complete elliptic integrals of the first and second kind, K(k) and E(k) respectively. The arguments to the elliptic integrals have the form

$$k = \sqrt{\frac{4R\rho}{(R+\rho)^2+(z-A)^2}} \quad . \qquad 2.84$$

Using the definition of the curl in cylindrical polar coordinates, and considering that the vector potential contains only a ϕ-component, the expression for the magnetic field becomes

$$\mathbf{B} = \frac{1}{\rho}\left[\left(-\frac{\partial}{\partial z}\rho A_\phi\right)\hat{\rho}+\left(\frac{\partial}{\partial \rho}\rho A_\phi\right)\hat{z}\right] \quad . \qquad 2.85$$

Using these properties of the derivatives for the elliptic integrals, we find that the magnetic field produced by our coil has the following components

$$B_z = \frac{\mu_0 I}{2\pi}\frac{1}{\sqrt{(R+\rho)^2+(z-A)^2}}\left[K(k)+\frac{R^2-\rho^2-(z-A)^2}{(R-\rho)^2+(z-A)^2}E(k)\right] \qquad 2.86$$

and

$$B_\rho = \frac{\mu_0 I}{2\pi\rho}\frac{(z-A)}{\sqrt{(R+\rho)^2+(z-A)^2}}\left[-K(k)+\frac{R^2+\rho^2+(z-A)^2}{(R-\rho)^2+(z-A)^2}E(k)\right] \qquad 2.87$$

where k has the same definition as given in Eq. 2.84.

The magnetic field produced from an Anti-Helmholtz pair of coils is determined by applying Eq's. 2.86 and 2.87 to each coil. The coils carry equal but opposite currents, and the coil centres are situated symmetrically about the origin at $\rho = 0$ and $z = \pm A$. The ρ- and

z- components of each coil add together to give the total radial and axial components of the field. The field produced by such a coil configuration has some interesting properties. First among these is that the magnetic field has a $|\mathbf{B}| = 0$ minimum at the origin. Over small distances, the field increases linearly with position in all directions. The field gradients are constant along any line through the origin, but vary in magnitude with polar direction. This results in a field that is not central. The magnetic fields for two sets of anti-Helmholtz coils used in this research are shown later in Fig. 5.22 and Fig. 6.9.

For an atom with magnetic moment μ, the force exerted by the magnetic field on the atom is given by

$$\mathbf{F} = \nabla(\mu \cdot \mathbf{B}) \quad . \tag{2.88}$$

From this, we clearly see that the magneto-static trapping force is conservative.

Modifying Eq. 2.66 now to include the Zeeman energy shift gives

$$\mathbf{F}_{\pm} = \pm \hbar \boldsymbol{k} \frac{\gamma}{2} \frac{s_0}{1 + s_0 + \left(2\delta_{\pm}/\gamma\right)^2} \tag{2.89}$$

where the detuning is now a function of both velocity, through the Doppler shift, and position, with the Zeeman splitting.

$$\delta_{\pm} = \delta \mp \boldsymbol{k} \cdot \mathbf{v} \pm \frac{\mu' \mathrm{B}}{\hbar} \tag{2.90}$$

with μ' given by

$$\mu' = \left(g_e m_e - g_g m_g\right)\mu_B \quad . \tag{2.91}$$

The radiation force can now be rewritten, as with Eq. 2.63, to take the form of a harmonic oscillator.

$$\mathbf{F} = -\beta \mathbf{v} - \kappa \mathbf{r} \tag{2.92}$$

where we have used a MOT spring constant, κ, defined as

$$\kappa = \frac{\mu'}{\hbar k}\beta A \qquad 2.93$$

where A is the magnetic field gradient.

To illustrate the magnetic trapping of neutral atoms in a MOT, a theoretical two level atom is shown in Fig. 2.6. The laser frequency is detuned by Δ in the lab frame. The σ^+ beam will couple to transitions with $\Delta m = +1$, while the σ^- beams couples to transitions with $\Delta m = -1$. With the geometry given in Fig. 2.6, the energetically favoured transition corresponds to the one with the lowest energy, which in this case is for a $\Delta m = -1$ transition, and requires absorption from the σ^- beam. Since this beam is travelling opposite the atomic motion, the laser field exerts a radiation force opposite the atomic motion. Since the m states are interchanged for negative positions, the opposite case holds if the atom were at $-z'$. In this way, the radiation force in a magnetic fields acts as a linear restoring force.

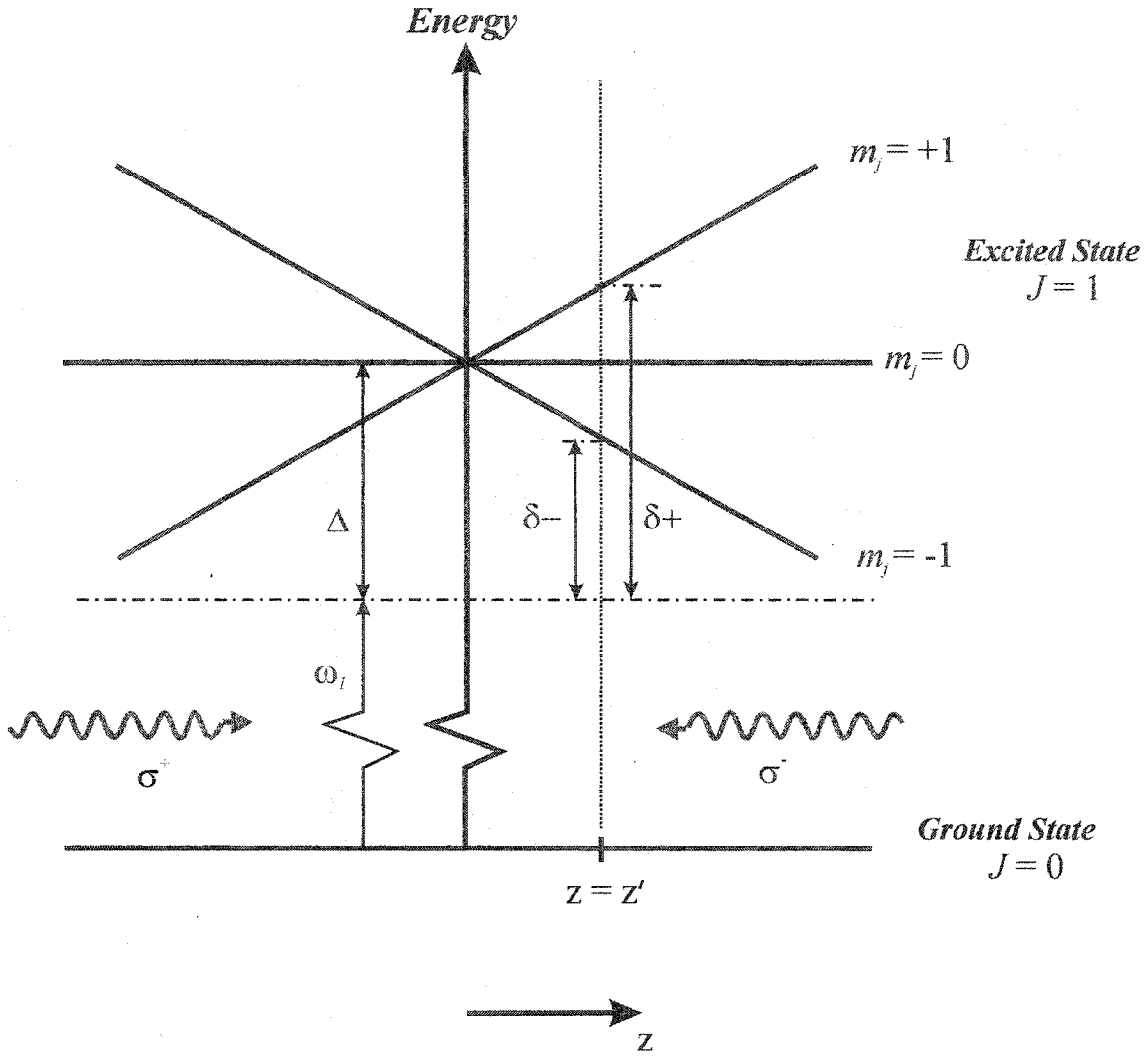

Figure 2.7: A theoretical two-level atom in a magnetic field, illuminated with two counter-propagating, frequency-detuned laser beams with opposite circular polarizations. The atom is at position z′ and travelling in the positive z direction.

CHAPTER 3. COLD ATOM COLLISIONS

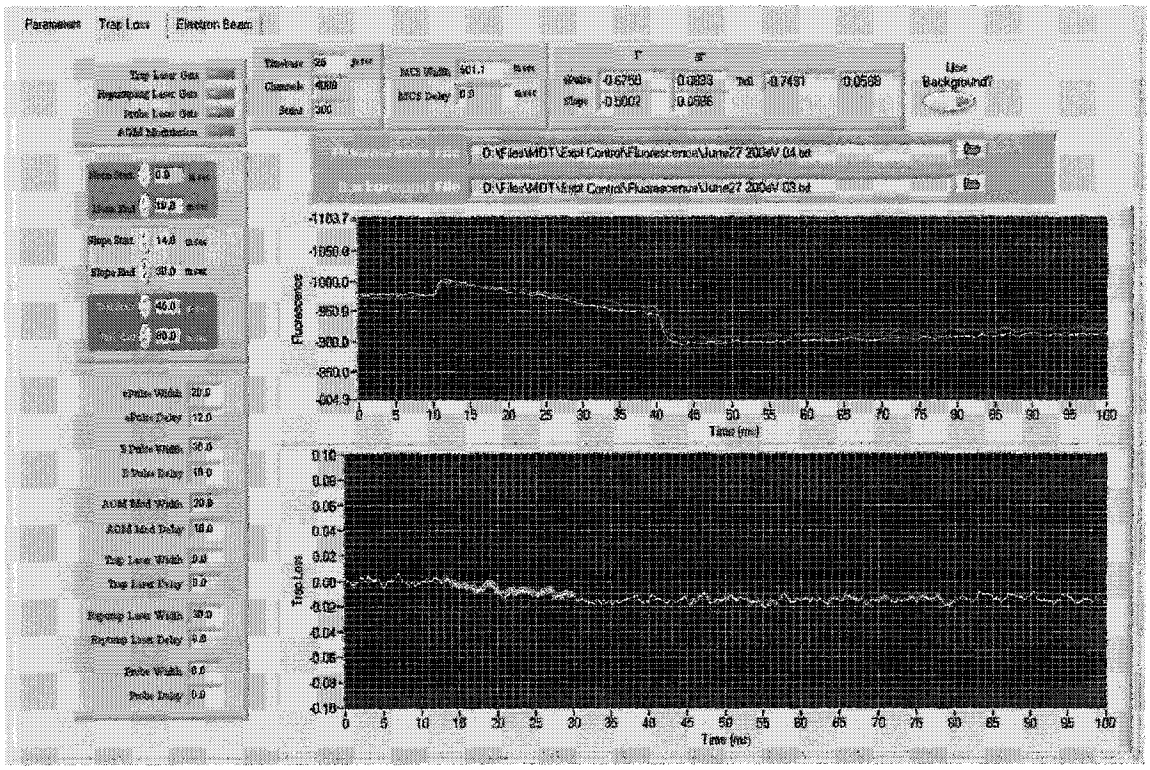

Labview analysis software used for analysing the fluorescent decays of the trap to determine the trap-loss rate due to electron collisions. The top curve shows fluorescence decays that result from cold atom and electron collisions. The bottom curve shows the isolated trap-loss for electron collisions

3.1 Thermal Atomic Collisions

We are ultimately interested in quantifying the loss rate of atoms from a MOT in order to determine collision cross sections for electron impact. To do so, we need to have some understanding of the atomic processes in a gas. The kinetic theory of gases is well understood and suitable for describing a gas of atoms in the classical regime. From it, we can perform some rudimentary studies of a cesium vapour.

As an example, we can calculate the mean free path for a cesium vapour in the MOT. Assuming a pressure, $P = 10^{-8}$ Torr = 133 x 10^{-6} Pa we can find the number density of atoms in the vapour from the ideal gas law

$$n = \frac{N}{V} = \frac{k_B T}{P} \quad . \tag{3.1}$$

We find the number density is $n = 3.22 \times 10^{14}$ m^{-3} . The mean free path is defined as

$$\lambda_{mfp} = \frac{1}{n\pi d^2} \quad . \tag{3.2}$$

The effective interaction distance, d, according to Estermann *et al.* [ESTER 47] for binary Cs collisions in a vapour is $d = 27.3 \times 10^{-8}$ cm. Substituting this into Eq. 3.2 gives a mean free path of

$$\lambda_{mfp} = 133 \text{ m} \quad .$$

This is somewhat useful for an estimate of how far, on average, an atom in the experimental chamber can travel before coming into contact with another constituent, but it is more convenient for the purposes of the trap loss to estimate the collision frequency. To do this we use the value of the most probable velocity given earlier in Section 1.2

$$f_c = \frac{\lambda_{mfp}}{v_{mp}} = 1.45 \text{ Hz} \tag{3.3}$$

One purpose of the MOT used in this research is to remove virtually all thermal energy from a portion of a room temperature gas, cooling those atoms to temperatures of less than a milliKelvin. In so doing, we are moving from a thermal regime to a cold regime. To avoid confusion, we will classify temperature ranges as cold or ultracold. There has been some debate over where these temperature ranges actually start and end, but the cooling and trapping community seems to be reaching a consensus, agreeing on the classification of Suominen [SUOMI 96] . Temperatures in the range of 1 μK $\rightarrow$ 0 will be referred to as ultracold, while temperatures in the range of 1 mK - 1 μK will be classified as cold. The boundary between cold and ultracold temperatures is commonly taken to be the limit of optical cooling processes.

To discuss these cold collisions, we have to move from the classical to the quantum regime. Classical theories are unable to fully describe the physics at these low temperatures. We cannot think of atoms as being point particles and we cannot think of atomic collisions as being elastic collisions between hard shell particles. At cold and ultracold temperatures, the interactions between atoms can cover extremely long ranges and inelastic processes have significant effects. At temperatures where Bose-Einstein condensation occurs, the deBroglie wavelength extends far beyond the range of a chemical bond to distances of the order of 10 micron [WEINE 99]. In addition to the long interactions dominating collision processes, the collision process itself extends over a much longer time scale.

To gain insight into the trap losses from a MOT, we need to gain some understanding of the atomic collision processes in a gas. Classical theories for room temperature gases are unable to fully describe collision processes in the cold and ultracold regimes. Consequently, we need to investigate the current theories for cold collisions.

3.2 Cold Atom Collisions

We will now briefly run through the theory of cold atom collisions, with the intention of pointing out processes that can give rise to trap losses. This discussion is not meant to be an in-depth review of cold and ultracold atom collisions. The reader is directed to the original sources of Weiner *et al.* [WEINE 99], Metcalf and van der Straten [METCA 99], [WEINE 95], Julienne *et al.* [JULIE 92] for more details on the present theory of these cold atom collisions. A very good topical review of present theory and experiment is given by Weiner *et al.* [WEINE 99].

A common approach to the scattering of atoms at low temperatures is to employ a partial wave analysis of a potential scattering problem [WEINE 99], [METCA 99]. A total cross section for these atomic collisions is expressed in terms of the partial waves by

$$\sigma = \frac{4\pi}{k^2}\sum_{\ell=0}^{\infty}(2\ell+1)\sin^2\delta_\ell \qquad 3.4$$

A central potential Schrödinger equation can be defined for the cold atom system, where an effective interaction potential is used and is given by

$$U(R) = -\frac{C_n}{R^n} + \frac{\hbar^2\ell(\ell+1)}{2\mu R} \qquad 3.5$$

where the centrifugal barrier term has been combined with the interaction potential to give the effective interaction potential. If we restrict ourselves to discussions of collisions of identical alkali atoms, we can classify collisions according to the electronic state of the incident particles. The first classification is for a collision between two particles, both in the ground, S-state, henceforth referred to as a ground state collision. For this type of collision, $n = 6$, and the interaction is a van der Waals interaction. If the colliding atoms are both in the excited P-state, which we will refer to as a doubly excited state collision, we have $n = 5$ and the interaction is a quadrupole-quadrupole interaction. If one of the colliding atoms is in the ground S-state, while the other is in the excited P-state, $n = 3$ and the collision is a dipole-

dipole interaction. We will refer to this type of collision as an excited state collision.

Ground state collisions can be either elastic or inelastic. The elastic collisions are responsible for the cooling process referred to as evaporative cooling used extensively in the formation of Bose Einstein condensates. Inelastic collisions of ground state atoms that result in trap losses are the result of spin dependent processes. During the inelastic collision there can be a spin exchange for the system, or we can have spin dipole-dipole interactions. This first mechanism is generally the stronger of the two inelastic processes. Both types of interactions are referred to as hyperfine-changing collisions, and both can lead to substantial trap losses. Note that these *hyperfine-changing collisions* are not attributed to optical processes but rather are a result of the close proximity, or overlap, of the charge clouds of the colliding species.

For the excited state collisions in a laser field tuned to the S - P transition, there are a variety of processes that can occur. The excited state collision is a very long range dipole-dipole interaction. Perhaps the best way to visualize the collision is to think of the colliding atoms as a quasi-molecule. This is a reasonable assumption given the long range of the interaction, and the long time scale of the collision. To help visualize the excited state collision, we will make use of the potential energy diagram given in Fig. 3.1.

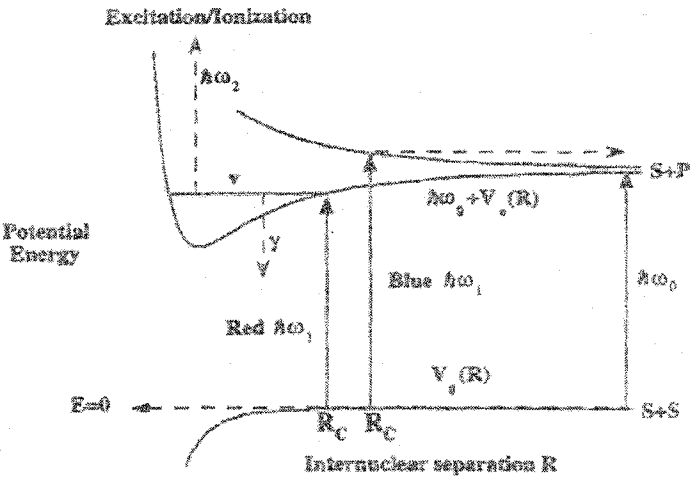

Figure 3.1: Potential energy diagram for an excited state collision between two cold (ultracold) atoms, taken from [WEINE 99].

One of the most interesting features of these excited state collisions is that the state of the quasi-molecule can be controlled through the laser. The S + P excited state is a dipole-dipole interaction covering a very long range, and consists of both a repulsive and attractive state. Promotion to the excited state by laser absorption puts the quasi-molecule

into the attractive or repulsive state depending on the laser detuning. This is attributed to the fact that the Condon region, R_C, can be moved over a considerable range of internuclear separation by varying the laser frequency to match the energy separation of the states. For red detunings, there is promotion to a vibrational level of the bound state, or for blue detunings there is a promotion to a purely repulsive state. From the vibrational level, the molecule can be promoted to a higher state or ionized, or can decay back to the ground state. This gives rise to photo-association spectroscopy of cold molecules.

During the excited state collision, there can be several inelastic processes. The first process is a *radiative escape*, in which the quasi-molecule is formed in the bound state for intermediate separation R and evolves to smaller internuclear separations before decaying to the ground state. When the complex decays, the emission frequency can be appreciably less than the absorption frequency, with the difference in energy going into kinetic energy of the atoms. The second inelastic process for excited state collisions is a *fine-structure changing collision*, in which the complex is formed as before, but evolves into a new state with the difference in potential between the two states going into kinetic energy of the atoms. The parent of the new state is the other fine-structure level, as shown in Fig. 3.2.

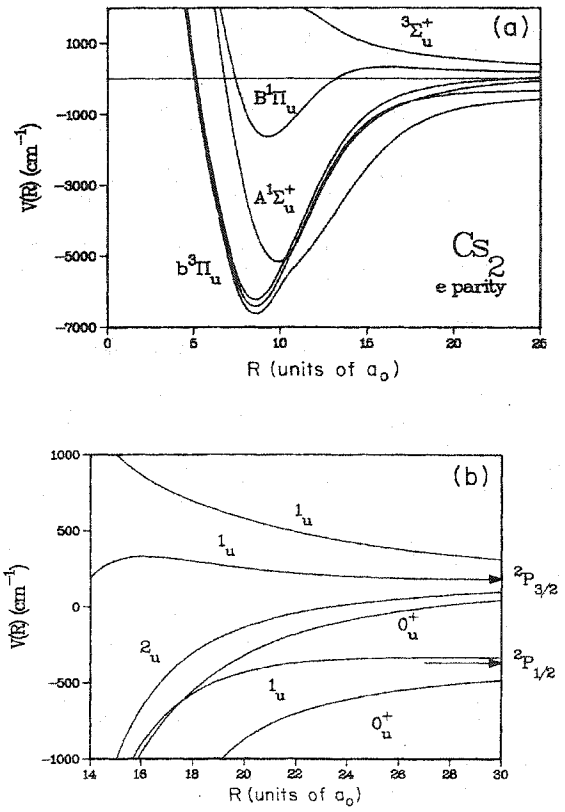

Figure 3.2: (a)Adiabatic potential energy curves for Cs_2 (b) long-range adiabatic potentials. Both taken from [JULIE 91].

Just as there is the possibility of fine-structure changing collisions, there is the possibility of hyperfine-changing collisions for the excited state. The hyperfine-changing collisions typically occur at lower laser intensities than for fine-structure changing collisions.

3.3 Trap Losses

The effects of these processes will now be considered, as they relate to the measurement of trap loss rates used in this research. Ground state elastic collisions in the trap serve to thermalize the sample of trapped atoms, similar to its role in evaporative cooling. This ensures that the spatial density of atoms in the trap is uniform. Thus, removing the trapping fields will result in a uniform thermal expansion of the cold atom cloud. However, due to the small momenta of the trapped atoms, gravitational effects on the atom cloud are discernible when the trapping fields are removed. Over the interaction times (milliseconds) of this research, we have a free-falling cloud of cold atoms that increases in size due to thermal expansion.

Trap losses, in the presence of the trapping fields, are attributed mainly to ground state inelastic collisions and excited state collisions. The hyperfine-changing collisions for the ground state gives rise to a substantial trap loss, particularly at low intensities. It has been found in cesium [SESKO 89] that a hyperfine-changing collision in the ground state transfers as much as 5 m s^{-1} to each of the colliding ground state atoms. This increase in atomic velocity is comparable with the capture velocity of the MOT, suggesting that atoms undergoing this type of collision will almost certainly be ejected from the trap.

Moving on to the excited state collisions, we find that according to the Julienne - Vigue theory as presented by Weiner *et al.* [WEINE 99], loss rates for radiative escape and fine-structure changing collisions are approximately equal. However, this theory does not consider the effects of hyperfine structure. We know that during a fine-structure changing collision, each of the recoiling atoms leaves with an additional kinetic energy corresponding to half of the energy separation of the fine-structure multiplet. Cesium has an extremely large fine-structure splitting, so we can be assured that this increase in kinetic energy is large enough to eject the colliding atoms from the MOT. If we assume that the Julienne-Vigue theory is valid, then the loss rate for radiative escape will be just as large as the fine-structure changing collisions. There are certainly going to be excited state hyperfine-changing collisions in the MOT. However, the kinetic energy changes resulting from these collisions

may not be sufficient to eject atoms from the trap, due to the relatively small energy separations of the excited state hyperfine levels in cesium, as compared with the ground state hyperfine separation and the fine structure splitting.

The trap losses associated with cold collisions are strongly dependent on the number density of the trapped atoms. Furthermore, the excited state collisions have an additional dependence on the laser parameters, such as laser intensity and frequency detuning. This makes it difficult to quantify the relative strengths of these competing processes. The situation becomes even more complex when radiation trapping is incorporated. Radiation trapping can help with thermalization of the ground state, and can drastically alter the competition between inelastic processes. The fact that the amount of radiation trapping is also dependent on the laser intensity and number density of atoms in the trap makes any attempt to analyse the relative contributions of the inelastic collisions to the trap loss more complex.

Fortunately, it is not necessary to know exactly how each inelastic process is contributing to the overall loss rate of atoms from the trap. For the purposes of the trap loss rate measurements in this research, all trap losses not resulting from the electron interaction, are collected together and treated as a single loss rate. Our only requirement is that the trap loss mechanisms not vary between two consecutive trap removals that occur within one second. This assumption is a reasonable one since the laser fields remain consistent during this time. The main source of fluctuations is the statistical variations of the trap population between consecutive trap reloadings. To compensate for these statistical variations, the trap losses are measured by averaging over hundreds or thousands of trap removals.

We can now discuss the trap loss processes that will occur for the MOT in the absence of any electron interactions. The first trap loss mechanism is obviously collisions between the trapped atoms and the background vapour. However, from the estimate of the collision frequency in Eq. 3.3, the background collisions will be infrequent and will not account for a significant trap loss. The MOT empties in times far less than background collisions alone can account for. If we assume a classical picture scattering within the trap, we still cannot account for the observed rate of trap loss. Combining these classical

collisions, with cold atom collisions gives a full description of the losses observed with a MOT.

For this research, the number of atoms in the trap is measured by the amount of resonance fluorescence emitted from the trap. Care must be taken when viewing the fluorescence decays from the trap, as drops in fluorescence can not always be interpreted as a drop in the trap population. A prime example of this is the drop in observed fluorescence when the repumping laser is momentarily switched off. The fluorescence quickly drops within several microseconds to the background fluorescence level. One could mistake this as an abrupt discharge of the trap. The correct interpretation is that the trap atoms are still cold and localized to the trapping region, but in a dark state. The reason for the abrupt decrease in fluorescence, is that atoms quickly decay to a dark hyperfine ground state through spontaneous Raman transitions [SCHAP 95]. The use of fluorescence detection is a suitable means of determining the trap population, or more specifically the changes in trap population, but caution must be exercised in directly relating the trap fluorescence with the trap population.

The evolution of the trap population can be expressed as

$$\frac{dN(t)}{dt} = \Lambda - \Gamma_b N(t) - \Gamma_{GSC} N(t) - \Gamma_{ESC} N(t) \qquad 3.6$$

where Λ is a constant loading rate into the trap from the background vapour, Γ_b is the loss rate of atoms from the trap incurred by collisions with the background vapour, Γ_{GSC} is the loss rate of atoms from the trap due to ground state cold collisions, and Γ_{ESC}, is the loss rate from excited state cold collisions. The loss rate for the excited state cold collisions can be decoupled into radiative escape, and fine-structure changing collisions, but it is not necessary for this treatment. Here we are assuming that the loss rates from cold collisions are constant and not functionally dependent on the number density or time, so that the loss rates can be combined into an effective loss rate.

$$\frac{dN(t)}{dt} = \Lambda - \left(\Gamma_b + \Gamma_{GSC} + \Gamma_{ESC}\right)N(t) = \Lambda - \left(\Gamma_0\right)N(t) \qquad 3.7$$

The interaction of the electron beam with the trapped atoms gives rise to an additional loss mechanism, denoted Γ_e that is expressed as [SCHAP 95]

$$\Gamma_e = \frac{\sigma_T J_e}{e} \tag{3.8}$$

where Γ_e is the loss rate due to electron interactions, σ_T is the total electron scattering cross section, J_e is the current density of electrons through the trap, and e is the charge of the electron. The trap evolution is then modified accordingly for times with the electron beam present

$$\frac{dN(t)}{dt} = \Lambda - \left(\Gamma_0 + \Gamma_e\right)N(t) \tag{3.9}$$

This primary focus of this research is to measure a variety of electron collisions cross sections using Eq's. 3.8 and 3.9 to relate the electron scattering cross section to the trap loss.

CHAPTER 4. ELECTRON COLLISIONS

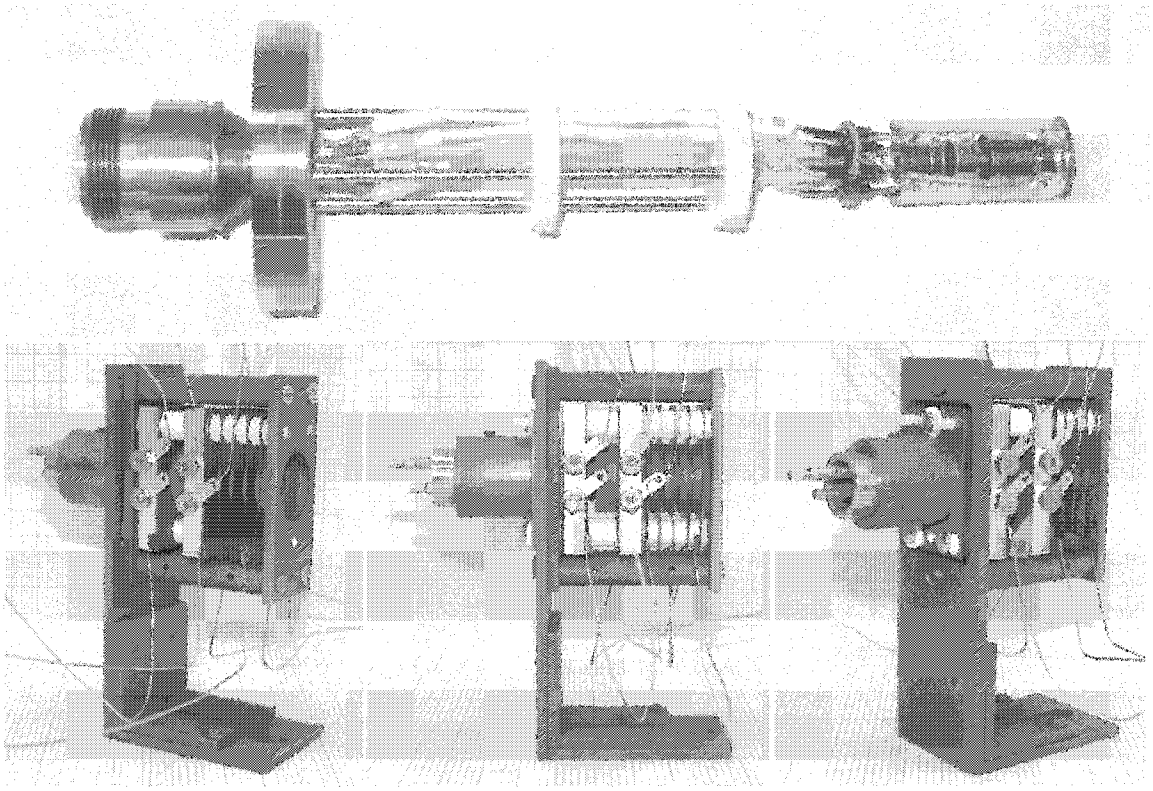

Photographs of the electron guns used in the first and second generation electron MOT systems

4.1 Electron Collisions

The fundamental quantities used in the discussion of the interactions of an electron with an atomic or molecular target are cross sections. There are a variety of interactions that can occur during the course of a scattering event between a projectile electron and a target atom or molecule. These interactions fall into one of three categories, elastic scattering, inelastic scattering, and superelastic scattering.

Elastic scattering events are those events where an incident electron suffers a net change in momentum, without losing energy. The target atom or molecule consequently suffers a net change in momentum due to the recoil absorbed from the incident electron.

$$e(E_i, \theta = 0^{\circ}) + \mathrm{A}(n,l) \rightarrow e(E_i, \theta) + \mathrm{A}(n,l) \qquad 4.1$$

These collisions involve changes only to the particle dynamics, without any effect to the internal state of the target.

Inelastic scattering events are those events in which the incident electron suffers not only a net change in momentum, but also a net loss in kinetic energy as a result of the collision. The kinetic energy lost as a result of the impact is transferred to the target to alter one (or more) of the internal degrees of freedom. In the case of atomic targets, the electron's kinetic energy may be transferred to the target resulting in excitation to a higher lying electronic state, or ionization. In the case of a molecular target, a scattering event can still result in ionization, or excitation (although there are varying molecular excitation mechanisms, electronic, vibrational, or rotational), but there is also the possibility of dissociative processes occurring.

$$\begin{aligned} e(E_i, \theta = 0^{\circ}) + \mathrm{A}(n,l) &\rightarrow e(E_i - \Delta E, \theta) + \mathrm{A}^{*}(n',l') \\ &\rightarrow e(E_i - \Delta E, \theta) + \mathrm{A}^{q+}(n',l') \end{aligned} \qquad 4.2$$

Superelastic scattering events are those events where the incident electron actually gains energy as a result of the collision process. The energy gain of the scattered electron is the result of preparation of the target, typically via laser excitation, to promote the target to

a higher lying state. The target can then undergo any one of the processes mentioned above for the inelastic collisions, but there is now an additional channel open to the target, decay to a lower lying state by transferring energy to the projectile. Superelastic scattering has several advantages, but we will not discuss them. Rather we will restrict ourselves to elastic and inelastic scattering.

Each of the processes mentioned thus far has a certain probability of occurring during the course of a collision event. This probability is measured in the form a cross section. And so, just as there are a multitude of processes that can occur as a result of an electron-target collision, there are a multitude of cross sections that are used to quantify these collision processes. These cross sections provide fundamental insight into the internal structure of atoms and molecules and the interactions that govern over these microscopic domains.

The definition of a cross section, σ, is given by Bederson and Kieffer [BEDER 71]

$$\sigma_{ij} = \int \sigma_{ij}(\theta,\phi)\mathrm{d}\Omega \qquad 4.3$$

where $\sigma_{ij}(\theta,\phi)\mathrm{d}\Omega$ is the flux of particles scattered into the solid angle $\mathrm{d}\Omega$, per unit flux, per unit target density, per unit scattering length. The subscripts i,j refer to the initial and final states of the target particle, respectively. The quantity σ_{ij} is usually referred to as the total cross section for the excitation $i \rightarrow j$. Alternatively, we may speak of the cross sections σ_{ii} and $\sigma_{ii}(\theta,\phi)$ which are the total and differential elastic cross sections, respectively, for the state i. Finally, we may also take into account all possible processes, elastic and inelastic, originating from the state i, in which case we speak of the total and differential cross sections, σ_i and $\sigma_i(\theta,\phi)$. In the case where no subscript appears, it is understood that the σ and $\sigma(\theta,\phi)$ actually refer to σ_i and $\sigma_i(\theta,\phi)$. In addition to these total and differential cross sections, we will make note of the momentum-transfer cross section, σ_{MT}, which is related to the elastic differential cross section, $\sigma_{ii}(\theta,\phi)$, by the relation

$$\sigma_{\mathrm{MT}} = \int \sigma_{ii}(\theta,\phi)(1-\cos\theta)\mathrm{d}\Omega \qquad 4.4$$

The electron collision cross sections that were measured in this research were all absolute cross sections. The measurement process gave a definitive value of the cross section

at each incident electron energy. There are experiments that can measure variations in cross sections but cannot give an absolute value of the cross section. These are termed relative cross sections. Typically, relative cross sections must be scaled to some intermediate cross sections that serves as a standard to make the relative cross section absolute. Most of the cross sections presented here are absolute, with a few exceptions. A note will be made of which cross sections are relative, and we will attempt to recount the scaling process used. One final general note on cross sections: cross sections are an area by definition, but there are no standardized units. Theoretical cross sections are usually given in atomic units as these units are most convenient for calculation. Measured cross sections typically are given as centimeters squared versus electron volts. Older cross sections are typically given as an electron absorption coefficient versus electron velocity. Some convenient conversion factors for converting units of cross sections are given in Appendix 2.

4.2 Cross Section Experiment and Theory

The discussion in Section 4.1 gives working definitions of scattering processes and the cross sections that are used to describe them. This section will attempt to provide a very general overview of the experiments that are available to measure electron collision cross sections. In addition, an overview will be presented of some common theoretical treatments used to calculate these cross sections.

4.2.1 Electron Collision Cross Section Experiments

There are a variety of techniques for measuring cross sections. The first techniques used were the so-called transmission and swarm experiments. These experiments were developed in the early twentieth century, circa 1921, and were used to measure total cross sections (transmission) and momentum-transfer cross sections (swarm). The technological achievements made following World War II allowed a second-generation of cross section experiment to be developed. Most notable of these experiments was the crossed beam experiment, developed circa 1970. These crossed beam experiments have been used extensively to measure total, differential, excitation and ionization cross sections. Following the crossed beam experiment, various sophisticated experiments have emerged over the past thirty years. These include merged ion electron beam, spin-polarized electron beam, coincidence experiments, and COLTRIMS [DORNE 00], just to name a few. This research is just one of the more recent variations of electron scattering experiments where the thermal gas target has been replaced with a MOT target.

A brief overview of the major experimental techniques used to measure electron collision cross sections will now be presented. The first of these experimental techniques to be discussed are the transmission and swarm experiments. For a more in-depth description of these experiments, the reader is directed to an excellent topical review of electron collision experiments given by Bederson *et al.* [BEDER 71].

Transmission experiments are the oldest type of electron collision experiment. The Ramsauer experiment and the Franck-Hertz experiment are perhaps the most notable types

of transmission experiments. This type of experiment works on the premise that a current of electrons travelling through a gas will be attenuated. The current attenuation depends on the path length, l, of the electron beam through the gas, the pressure of the gas (number of particles, n), and the collision cross section σ (absorption coefficient) of the gas target.

$$I = I_0 \exp[-nl\sigma] \qquad 4.5$$

The simplicity of the measurement process makes the transmission experiment a robust one. However, the analysis of the data is quite cumbersome, requiring the assignment of several form factors to get the correct cross section. Transmission experiments have been used extensively for the measurement of total and ionization cross sections.

Swarm experiments have been used to make measurements of the momentum-transfer cross section. The principle of a swarm experiment is to perform a time of flight measurement of electrons through a target gas to determine their drift velocity. The electrons travel under the influence of an applied potential to a drift tube. The drift currents along the axis of the drift tube, and perpendicular to it, are measured and their ratio is then used to give the momentum-transfer cross section. As with the transmission type of experiment, the swarm experiment is a robust experiment providing good signal levels with excellent statistics. However, the swarm experiment also has an intensive analysis of the data to determine the cross section.

Crossed beam experiments are conceptually simple experiments. They consist of two cross-fired beams, one beam of target particles, the other of projectile particles. A detector is then placed, either in the plane defined by the two beams, or perpendicular to it. In some cases such as in coincidence experiments, detectors are placed both in and out of the scattering plane. Usually the detector is an electron detector, but this can modified to ion detectors, optical detectors, or metastable detectors. The common element is that the detection is performed on the products of the electron-target collision. The cross section for this type of experiment is defined by

$$I'_{ij}(\theta,\phi)\mathrm{d}\Omega = \sigma_{ij}(\theta,\phi)\mathrm{d}\Omega \int \eta(\theta,\phi:x,y,z)n(x,y)J_e(y,z)\mathrm{d}\tau \qquad 4.6$$

where I'_{ij} is the scattered signal, η is the collection efficiency for electrons scattered from (x, y, z) into (θ, ϕ), n is the target density, and J_e is the current density of the electron beam

One major advantage of crossed beam experiments over the earlier transmission experiments, is its ability to measure a differential cross section by recording the scattered electrons as a function of angle within the scattering plane. The crossed beam experiment also offers a simpler analysis of the raw data to determine the collision cross section. This comes at the expense of much lower signal levels and decreased statistics than the earlier transmission and swarm experiments.

The next experimental technique to be discussed is the atomic beam recoil technique [BEDER 68]. This experiment is actually quite similar to the crossed beam experiments, in its utilization of a cross-fired beam arrangement. It can also measure total and differential cross sections. The recoil technique involves the detection of the atom beam directly. A target detector is placed in the beam line and the subsequent loss of atoms from the beam is recorded for the electron beam turning on. The scattering-out of the target beam is then related to the cross section. This method of detecting the loss of target particles during the electron interaction is the opposite approach to the methods used in crossed beam experiments.

The atomic beam recoil experiment typically uses rectangular electron and atomic beams. It also assumes that the target density is uniform along the beam, and varies only across it. The mean speed of the atom beam is also assumed to be constant across it, and the entire electron beam passes through the atom beam. The cross section for this type of experiment is given by

$$\sigma_i = \frac{I'h\langle \mathrm{V} \rangle}{I_a I_e \bar{\eta}} \qquad 4.8$$

where I' is the total scattered out beam current, h is the height of the target beam, I_a is the target atom current per unit length, I_e is the electron current per unit length, η is the detection efficiency and $\langle \mathrm{V} \rangle$ is the mean speed of the atom beam.

4.2.2 Electron Collision Cross Section Theory

Several theories have been developed to describe electron scattering processes from atoms and molecules. A good review of general theoretical methods with specific emphasis on the convergent close-coupling (*CCC*) model is given by Bray and Stelbovics [BRAY 95]. One of the oldest theories in use is the Born approximation.

The Born approximation involves evaluating elements of the so-called *T*-matrix, where T satisfies the equation

$$T = V + VG_0T \qquad 4.9$$

where V is the matrix of potentials for the processes accessible to the scattering problem being considered, and G_0 is a diagonalized matrix of Green's functions. The Born approximation is generally well-suited for calculating electron collision cross sections at high energies (> 1 keV), but can give adequate results down to energies of the order of 100 eV. The biggest inadequacy of the Born approximation is that it does not include any short range interactions. To accommodate, the Born approximation can be modified to include the effects of these short range interactions, but serious discrepancies suggest moving to a more elaborate model.

More sophisticated versions of the Born approximation have also been developed to improve the model's capabilities. One such model commonly found in the literature is the Distorted Wave Born Approximation (*DWBA*). This version of the Born approximation separates the scattering potential into two parts to give

$$V \rightarrow (V - U) + U \quad . \qquad 4.10$$

The portion of the potential described by U is the dominant portion, while the remaining portion is quite small and can be treated in a manner similar to a perturbation. This modification extends the capability of the Born approximation to include short range effects There is a second-order version of the DWBA that is referred to as the *DW2BA*. The effect of moving from the first-order to second-order Born approximation is that the agreement is significantly better for lower energy collisions. Satisfactory results can be obtained from the

DW2BA down to energies of the order of 10 eV. Furthermore, the second-order Born approximations are capable of producing results for differential cross sections, which the first-order Born approximation is poorly equipped to handle.

The next model used for calculating collision cross sections is the *R*-matrix method. The *R*-Matrix model consists of separating the region surrounding the target into two parts, by placing a spherical boundary centred at the nucleus. The sphere is increased in size so that all initial and final states of the target are included within the sphere. This simplifies the calculation process by eliminating the need to calculate exchange interactions outside the boundary. The *R*-Matrix method works quite well for low to intermediate impact energies where the coupling of states inside the boundary, to the continuum become appreciable and cannot be ignored. The Intermediate Energy *R*-Matrix (*IERM*) method has been developed to increase the working energy range of the *R*-Matrix model. To increase the energy range, the model takes into account continuum channels for the internal region of the R-Matrix model.

The R-Matrix method provides good results for various cross sections, including total, ionization, and differential, at low impact energies. The R-Matrix approach also uses an iterative algorithm for calculating the cross section which makes it well suited for handling resonance phenomena for an appropriate energy increment. Other models that don't use an iterative scheme must begin a new calculation for each energy and it is quite possible for cross section structures such as resonances to be missed entirely.

Another model commonly used for calculating cross sections is the Pseudostate-close -coupling method (*PSCC*). This model combines actual eigenstates of the target Hamiltonian with positive energy states that result from the diagonalization of the target Hamiltonian in a basis of Slater type orbitals. The PSCC method typically gives results that are in very good agreement with experimental data. However, one problem with PSCC model is the appearance of pseudoresonances on the cross sections arising from the use of the positive energy pseudostates. These pseudoresonances have no physical meaning and can be misleading.

The last theoretical model for calculating cross sections that we will consider is the

convergent close-coupling (*CCC*) model. This predictions of this particular model are quite accurate when compared with experimental data. As such, it is quickly becoming one of the most favoured methods among theoretical groups for calculating cross sections. The CCC method is quite similar to the PSCC method but includes many more states to reduce the probability of pseudoresonances. The basis set must also satisfy a convergence criteria, which is not applied within the framework of the PSCC. One other distinction between the two models is that the PSCC model works in position space, while the CCC is used in momentum space which provides for less intensive computations. Also, the CCC method must perform a new calculation for each impact energy , unlike the R-matrix method, which essentially provides a continuous cross section over an energy range through the use of an iterative calculation.

4.3 Electron - Cesium Collision Cross Sections

A review of the experimental and theoretical data for the electron-cesium collision cross sections relevant to this research will now be presented. The method of measurement or calculation will be discussed for each.

4.3.1 Total Cross Sections

Prior to this research, there was little information about the total cross section for cesium. The data of Robert Brode from 1929 [BRODE 29] was the only data available for the total cross section, until 1971 when the Visconti group [VISCO 71] performed a low-energy measurement. Jaduszliwer and Chan made another low-energy measurement of the total cross section in 1992 [JADUS 92]. There were several sets of theoretical calculations for the total cross sections, at low energies. We will consider only those performed by Klaus Bartschat [BARTS 93] in 1993, as they were the most recent. Bartschat provided a full description of the theoretical methods and results used for the previous calculations.

The Brode data was obtained using the transmission method with a modified Ramsauer-type experiment, shown in Fig. 4.1, for the energy range 0 - 400 eV. A tungsten filament, F, was placed in the centre of a cylinder C, with the beam emitted through a narrow slit, S_c. The beam was launched into a circular orbit, of radius 15 mm, by a large solenoid to pass through a series of 5 slits, before arriving at the box collector, B. Pressures of the order of 10^{-5} Torr were typical for the set of measurements he performed.

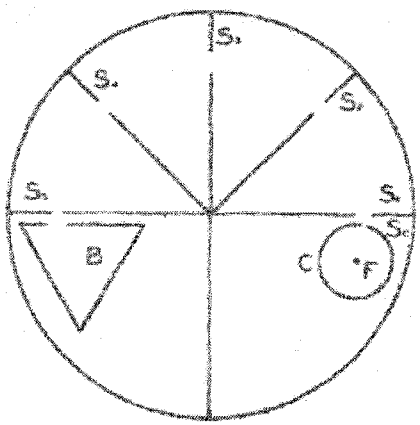

Figure 4.1: Schematic of the modified Ramsauer apparatus used by Brode to measure the cesium total cross section.

The total cross section for cesium that Brode measured was one of a series of absolute cross section measurements that he made for all of the alkali metals. The cross

section data he published was given originally as an absorption coefficient versus electron speed.

The Visconti group performed a measurement of the total cross section using the

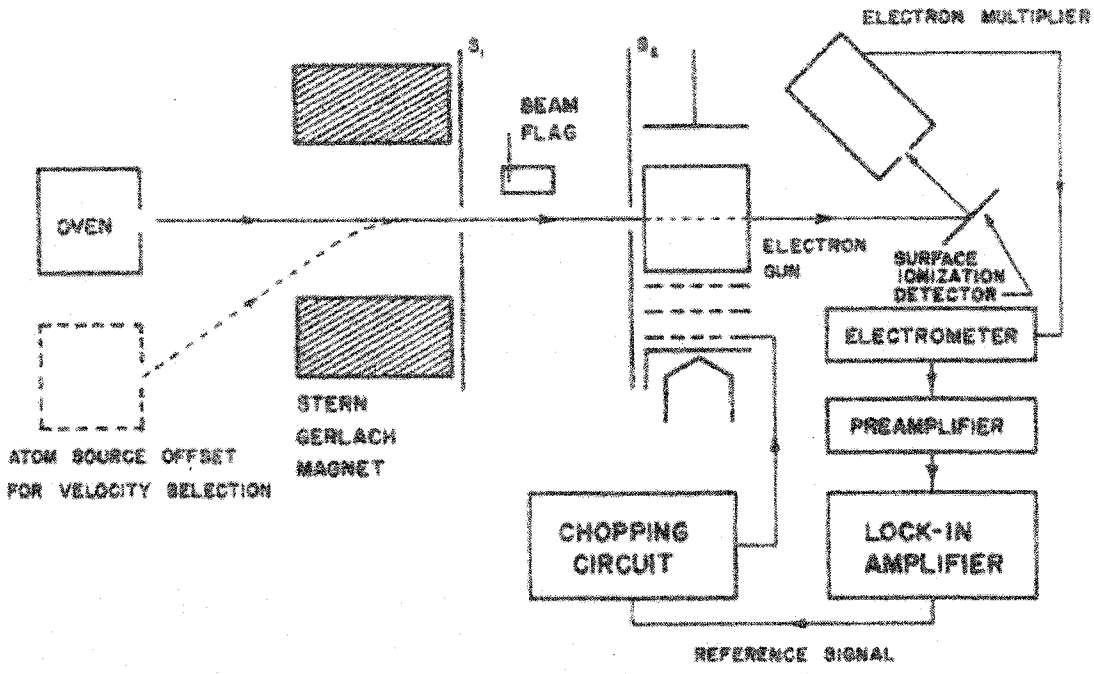

Figure 4.2: Schematic of the atomic beam recoil experiment used by the Visconti group to measure the total cross section of cesium.

atomic beam recoil technique. Their cross section measurements covered the energy range of 0.3 to 9 eV. Their experiment used a Stern-Gerlach magnet and movable atom beam source to perform velocity selection of the beam. The principle behind this arrangement was that the atomic beam could only pass through collimating slits, S_1 and S_2, for a certain velocity class of atoms following deflection by the magnet. After velocity selection, the atomic beam was cross-fired with the electron beam, and sent to the detector. Two measurements of the atomic beam current were made. The first was with the detector in-line with the atomic beam. In the presence of the electron beam, a small decrease in atomic beam current was detected. This decrease was recorded as the scattering out signal. The detector was then moved out of the atomic beam line, and parallel to the electron beam until the deflected beam from the electron interaction was found. This detected signal outside of the

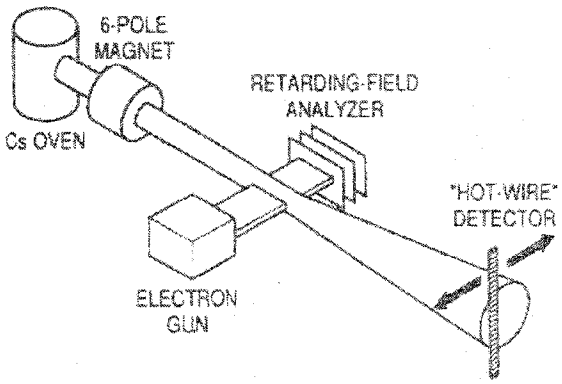

Figure 4.3: Schematic of the atomic beam recoil experiment of Jaduszliwer and Chan.

atomic beam line, was recorded as the scattering in signal. From these two signals, the total cross section was determined.

The total cross section measurements of Jaduszliwer and Chan were performed using an atomic beam recoil experiment, shown in Fig. 4.3. Their measurements were made over the energy range of 2 - 18 eV. The experimental arrangement was similar to the Visconti experiment. The atomic beam was velocity-selected and collimated with a hexapole magnet. The electron beam system of the Jaduszliwer experiment was quite similar to that in the Visconti experiment, but included a retarding field energy analyser. In place of the surface detector, a hot-wire beam probe was used for recording the atomic beam current.

The theoretical calculations of Bartschat for the cesium total cross section covered an energy range of 0 - 4 eV. The calculations were made using a sophisticated *R*-matrix model to clarify a discrepancy between a previous *R*-matrix calculation with a relativistic Dirac treatment. These earlier calculations will not be discussed here as the results of Bartschat's calculations were in excellent agreement with all but one set of recent calculations.

4.3.2 Ionization cross sections

There is a considerable amount of data available for the total ionization cross section of cesium. The oldest set of experimental data is the measurements of Tate and Smith [TATE 34] from 1934. Brink made measurements of the total ionization cross section in [BRINK 62], [BRINK 64] the alkali metals in the early 1960's but his data for cesium contains only a few points. Experimental investigations of the total ionization cross section were also carried out by McFarland and Kinney [MCFAR 65]in 1965, and Heil and Scott [HEIL 66] in 1966. Nygaard [NYGAA 68], [NYGAA 73] studied the total ionization cross section as

well as the metastable ion yield. Zapesochnyi and Aleksakhin [ZAPES 69], and Korchevoi and Przonski [KORCH 67] also carried out experimental measurements of the total ionization cross section. The only recent theoretical treatments for the total ionization cross section were carried out by Deutsch, Becker, and Mark [DEUTS 99].

Tate and Smith performed their measurements of the total ionization cross section, ionization cross sections for charge states up to Cs VIII, and provided energy thresholds for each charge state. The experiment was a transmission type. A schematic of their experimental system is shown in Fig. 4.4. The experiment consisted of a cylindrical interaction region, with a circular drift section attached that was used for collecting the ions

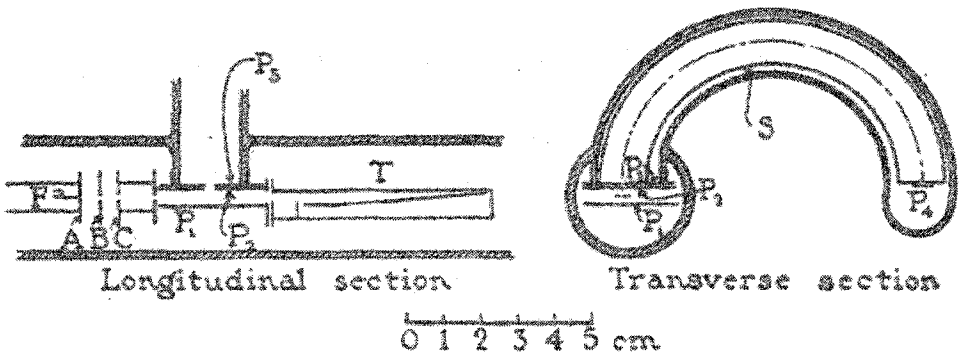

Figure 4.4: Schematic of the transmission experiment used by Tate and Smith for measurements of ionization cross sections in cesium.

and defining their energy. This arrangement is a popular design, that is reproduced almost identically in several other experiments. Tate and Smith measured their cross sections over the energy range 0 - 700 eV. However their results are given as relative cross sections.

The data set of Brink includes only two definite points for the ionization cross section and a third point that gives the peak cross section value, but not the corresponding energy. His cross section values were absolute and were measured with a crossed beam experiment, shown in Fig. 4.5. The cross section value reported by Brink for cesium were at the intermediate energies 300 and 500 eV.

McFarland and Kinney made measurements of the total ionization cross section and the ionization cross section for Cs II over the energy range of 50 - 500 eV. Their

measurements were absolute and used a crossed beam experiment virtually identical to that of Brink.

Heil and Scott measured the total ionization cross section with a transmission experiment similar to the Tate and Smith, but in place of a circular drift tube, the walls of the cylinder acted as the ion collector. Their cross section was made absolute and covered the energy range from threshold to 50 eV.

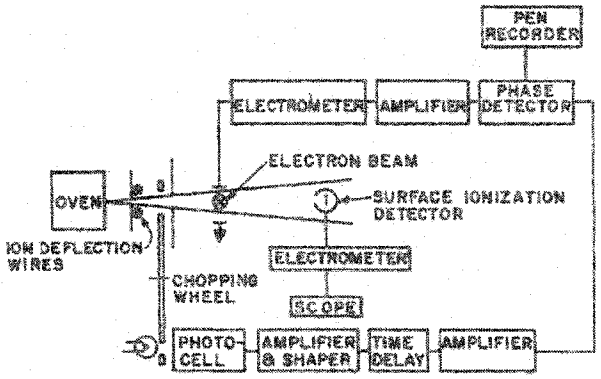

Figure 4.5: Schematic of the apparatus in the crossed beam experiment of Brink for measuring ionization cross sections.

Nygaard's experimental data for the total ionization cross section spanned the energy range of 0 - 100 eV and was also taken with a transmission experiment quite similar to the Tate and Smith apparatus. But with a surface ionization detector to record the ion yield.

The Zapesochnyi and Aleksakhin experiment involved a crossed beam experiment that also gave absolute results over the range of 0 - 300 eV.

The theoretical treatments of Deutch *et al.* used a DM formalism for calculating the the total ionization cross section. Their model was a semiclassical model that was based on the Borne-Bethe approximation. Their calculations were carried out for energies 0 - 30 eV.

4.3.3 Additional Cross Sections

Over the course of this research, there were several other cross sections found for momentum-transfer and excitation. These cross sections are not used in the results presented here, as there were no measurements made with the electron MOT system at the time of writing. For completeness, these cross sections will be briefly mentioned.

Momentum-transfer cross sections were measured by Saelee and Lucas [SAELE 79], and by Nighan and Postma. [NIGHA 72]. A set of perturbation calculations were used by Crown and Russek [CROWN 65] to model the momentum-transfer cross section. Stefanov [STEFA 80] performed some empirical fits to the existing data

Excitation cross sections for cesium were produced by Yong-Ki Kim [KIM 01], Chen and Gallagher [CHEN 78], and Zapesochnyi [ZAPES 76]. Calculations of excitation cross sections were performed by Zeman, *et al.* [ZEMAN 94], [ZEMAN 95] for the fine structure multiplet of cesium.

CHAPTER 5. EXPERIMENT I

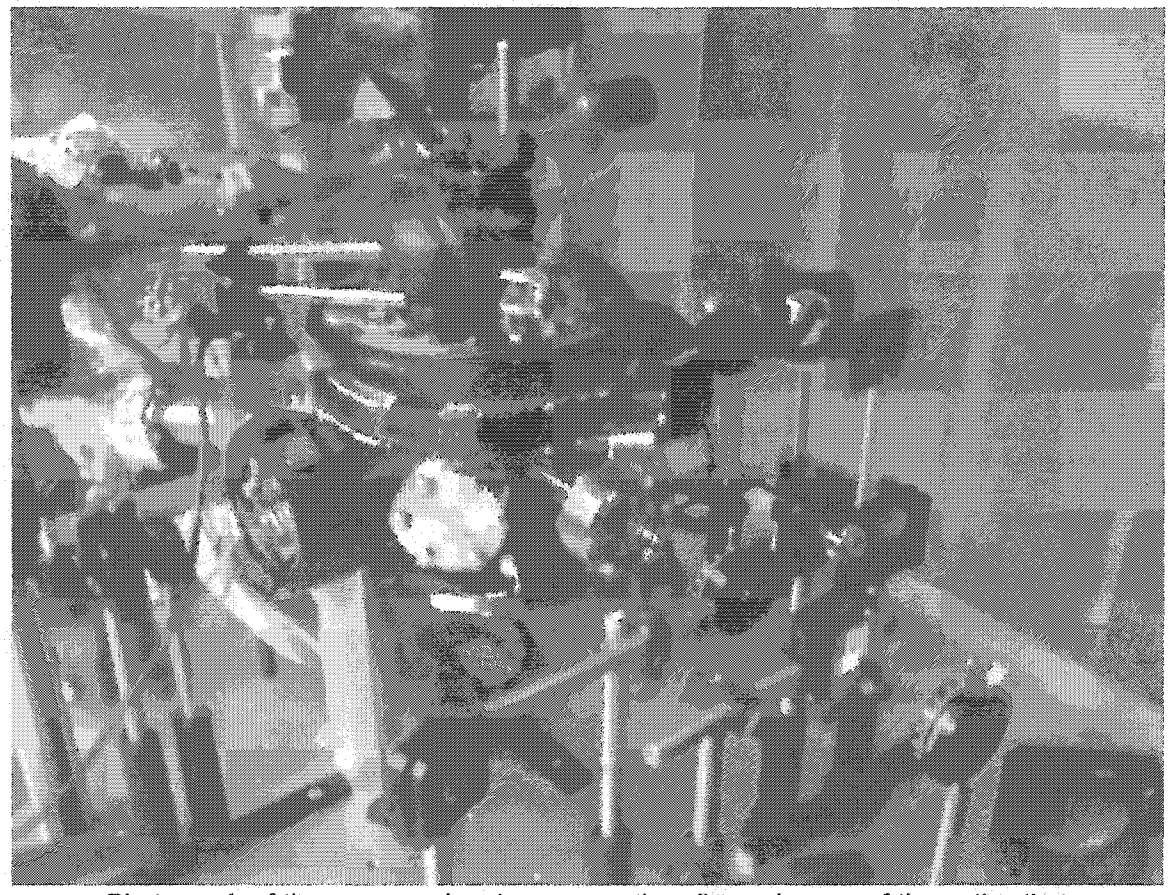

Photograph of the vacuum chamber, magnetic coils, and some of the optics that were used with the first generation electron MOT system.

This section discusses the experimental details of the first generation electron-MOT system used for measuring electron collision cross sections. This system used the first MOT developed in the Electronic and Photonic Collisions Laboratory, in conjunction with a commercial, unselected electron gun. Construction of the system began in September, 1999 and reached full operational status in August, 2001. This system was decommissioned in May 2002 in favour of a new system, described in Chapter 6, which uses a more elaborate electron gun and allows additional detectors to be installed in the vacuum chamber.

5.1 Vacuum System

The vacuum chamber for this first generation electron-MOT system was an ultrahigh vacuum (UHV) system built around a central 6.00" diameter spool piece where the MOT was ultimately contained. Besides housing the MOT, this central spool piece contained the electron beam components, specifically the electron gun, the Faraday cup current detectors, and the thin-wire electron beam probe. A general layout of the chamber is given in Fig 5.1.

An ultrahigh vacuum system was chosen for construction of our cesium MOT to minimize the number of background collisions. These collisions would deteriorate the operation and stability of the MOT. Stable trapping requires typical pressures well below 10^{-7} Torr, which is bordering on the transition from the high-vacuum to the ultrahigh-vacuum regime.

Our UHV system was built upon industry standard, ConFlat® flange technology. With a ConFlat system, the traditional O-ring gasket is replaced with a metal gasket, as shown in Fig. 5.2, that is compressed between mating flanges. This compression forces the softer metal gasket to fill any leak channels between mating flanges.

ConFlat flanges and vacuum components are typically produced from an austenitic (vs ferrite or cementite) grade of stainless steel (an 18-8 grade such as 304, 310, 316, etc) due to the fact that these stainless steels have a superior resistance to corrosion, high temperature tolerances of at least 450 °C, and very low magnetic permeability. Typically, these flanges and components are cut and machined from stock such that no inclusions in the metal can

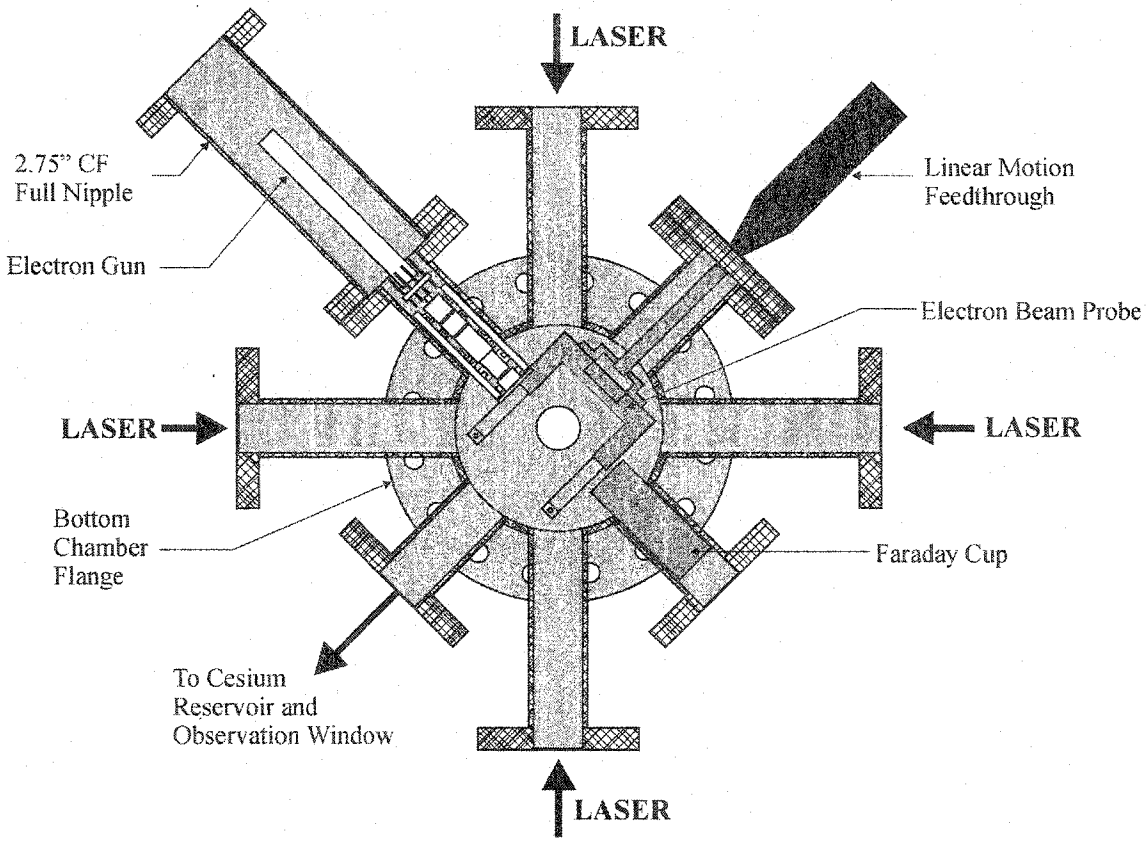

Figure 5.1: Internal view of the 6.00" CF spool piece forming the main chamber of the vacuum system. The orientation of the electron beam components are shown in relation to the laser beams. Not shown is the third pair of laser beams coming in and out of the page.

travel from the air side to the vacuum side, and in turn cause a virtual leak.

The flanges are tightened using fine-threaded, stainless steel bolts that are tightened using a "cross-corner", or star pattern to ensure the bolts are exerting a uniform pressure on the flange and gasket during the entire tightening process. A non-uniform pressure during tightening could result in a leak on the gasket and possibly even "roll-over" of the knife-edge itself. Strictly speaking, a torque wrench is should be used for tightening each ConFlat flange, but if such a wrench is not present, a standard ratchet may be used making sure that each bolt is tightened by no more than an eighth of a turn. To determine if a flange is tight enough, a good rule of thumb is that there should be no visible gaps between the flange's inner surfaces i.e. there should be no daylight showing. If the copper gasket is visible between the mating flanges, a flange leak is almost certainly present.

One additional note on ConFlat flanges is that during the tightening the bolts can generate a substantial amount of heat and in extreme cases, the nuts may become galled, or seized. To prevent this from happening, the bolt threads should be coated in a high temperature thread lubricant such as magnesium disulphide (e.g. "Never SEEZ") or silver suspension (e.g. "Silver Goop").

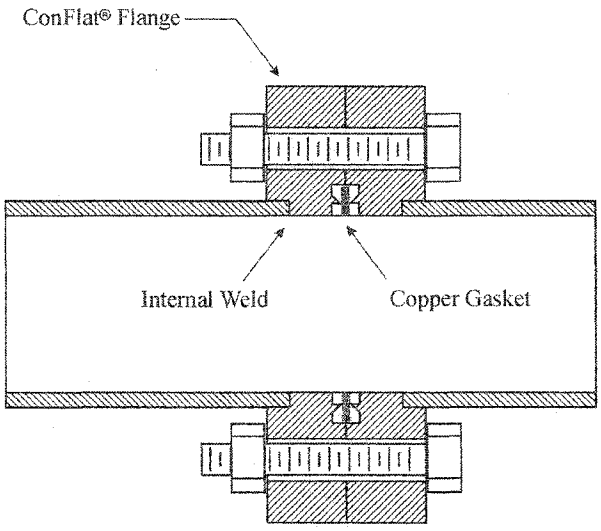

Figure 5.2: Cutaway diagram illustrating a typical Conflat®, all-metal UHV flange seal

In addition to using specialized, all-metal seals, a UHV system typically uses a more sophisticated pumping scheme than more traditional high-vacuum systems. A restriction commonly imposed on UHV systems, is the use of an oil free pumping scheme. Such a requirement prohibits the use of rotary-vane pumps for use as roughing pumps. It also prohibits the use of diffusion pumps or oil-based turbo-molecular pumps as the secondary, as such pumps inevitably contaminate the system with oil and water vapour.

The pumping scheme used in the first generation electron-MOT system was no exception. It used a three pump system containing a mechanical diaphragm roughing pump, turbo-molecular pump, and an ion pump, each with working ranges given in Fig 5.3. The primary, or roughing, pump was a four stage mechanical diaphragm pump that had a pumping speed of 12 l/min (approx 0.43 cfm) and had a quoted ultimate pressure of 10 mTorr. While this pump was implemented on the first generation electron-MOT system, a background pressure of no less than 40 mTorr could be obtained. Typical background pressures with this pump were in the 60-100 mTorr range. This diaphragm pump was used to back a Varian V70LP turbo-molecular pump.

The V70LP is an oil-free pump and can be mounted in any orientation due to its permanently lubricated ceramic bearings. This turbo pump has a compact, lightweight design that needs only an air cooling kit, in lieu of a water cooling kit that accompanies most larger

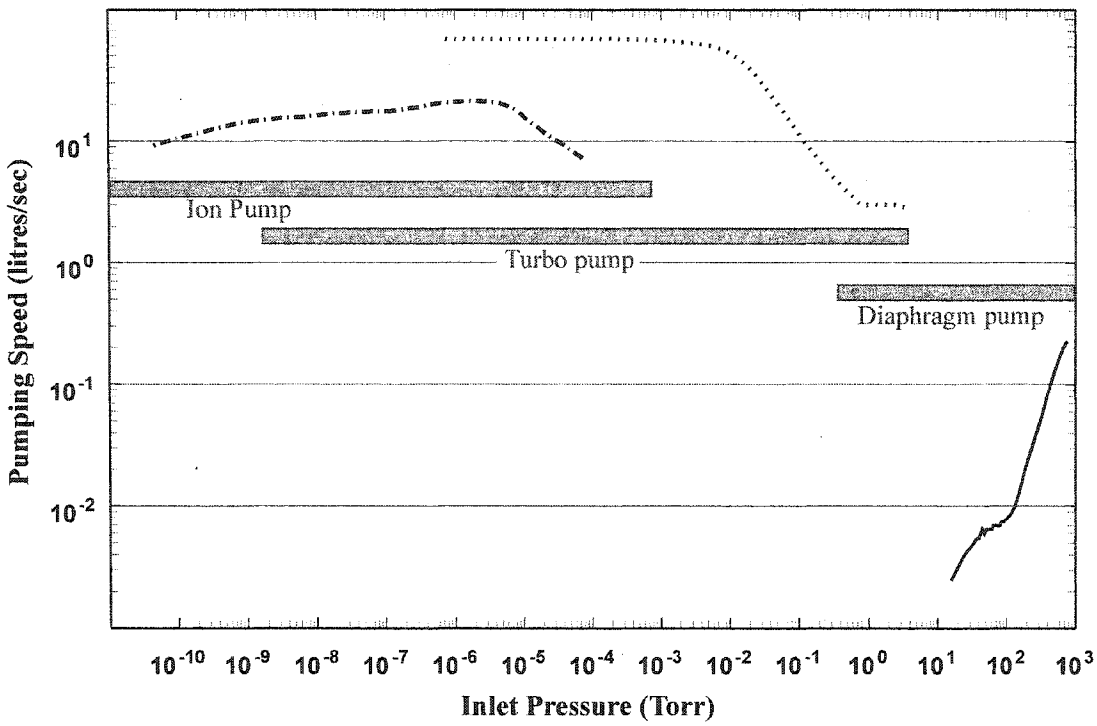

Figure 5.3: Pumping speeds for the various pumps used in the first generation electron-MOT system. Note that the threshold between the high vacuum and ultrahigh vacuum regime occurs at approximately 10^{-8} Torr.

turbo pump systems. With the turbo pump, an ultimate background pressure of 1.5×10^{-9} Torr is attainable according to the manufacturer's specifications. However, during typical operation with the first generation electron-MOT system, the pressure was usually in the low 10^{-7} range and seldom dropped below that without the aid of the ion pump.

The ion pump is a Varian StarCell 20 l/s ion pump with ferrite magnets. This model of ion pump is a variation of a triode type ion pump that offers superior performance over many other designs, as it has the highest total combined capacity for all gases including the getterable gases (O_2, CO_2, CO), the noble gases (He, Ar), methane and hydrogen. The ultimate pressure attainable with the ion pump is less than 10^{-11} Torr according to the manufacturer's specifications.

The process normally used for pumping the first generation electron-MOT system entailed an initial roughing phase, where the chamber was roughed with the diaphragm pump until the pressure reached approximately 10^{-2} Torr at which point the turbo-molecular pump

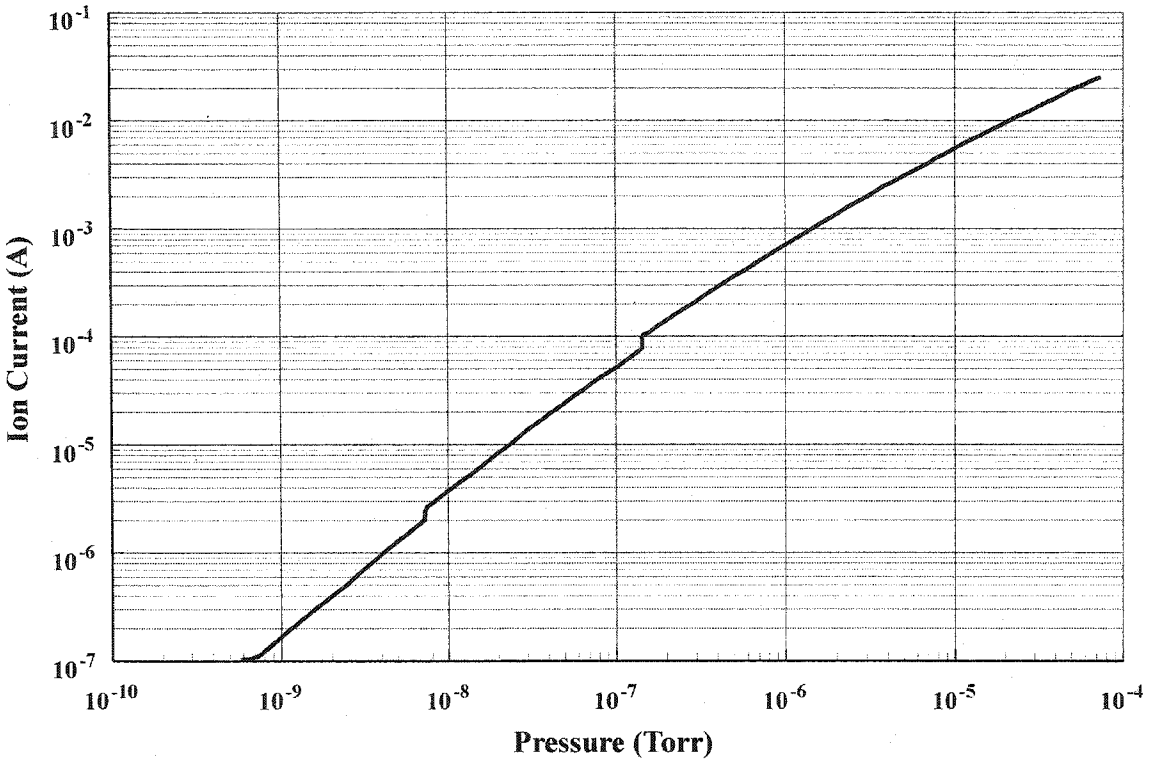

Figure 5.4: Calibration curve from Varian Inc. for the Starcell 20L/s ion pump to convert from ion current to pressure. The ion current is read from the front end of the pump controller as a voltage that is 1000 times the actual current.

was switched on to bring the system down further in pressure to the 10^{-6} Torr. At this point, the chamber was baked-out, using a process to be discussed later in this chapter, in order to reach the 10^{-7} to 10^{-8} Torr scale. Once this pressure range was reached, the ion pump was switched on and after it had completed outgassing and had reached its maximum pumping speed, the diaphragm pump and the turbo-molecular pump were valved off from the main chamber, and finally switched off. At this point, the chamber was in a sealed state being pumped only by the StarCell 20 ion pump. Pumping with only the ion pump has the noted advantages of being quiet and free of mechanical vibration due to the lack of moving parts in the pump.

Three pressure gauges were used with the first generation electron-MOT system. The first was a thermocouple gauge that was attached to the roughing line connecting the diaphragm and turbo-molecular pump. This gauge gave pressure readings in the range of 2.0 Torr to 1 mTorr. The second pressure gauge was a Bayard-Alpert ionization gauge with a

single, tungsten filament and capable of reading pressures in the range of 10^{-4} to 2 x 10^{-10} Torr although pressures below mid 10^{-9} Torr were somewhat questionable due to the sensitivity and non-linearity of the gauge and controller as well as the non-negligible background ion current resulting from the electron beam. The last pressure transducer was the ion pump itself. From the basic principle of operation of an ion pump, it is possible to read the ion current produced from the background gas directly from the pump. The readout of the ion pump is actually given as a voltage rather than current, but the ion current, and hence, pressure can be determined using the calibration curve supplied by the manufacturer, given in Fig. 5.4.

When running with only the ion pump, the chamber is isolated from atmosphere through a series of UHV compatible, pneumatic gate valves. These valves are capable of pressure gradients over the full range of pressures from atmosphere to 10^{-11} Torr. These valves are fully interlocked with the use of electrical solenoid gas valves that shut all gate valves automatically in the event of a power outage. In addition, the ionization gauge is interlocked as well so that in the event of a power failure the gauge controller must read a pressure below 10^{-3} Torr before the ion gauge can be turned on. Otherwise, in the event of an extremely large ion current from the collector, the ion gauge immediately shuts down before the built-in electrometer is damaged.

In typical UHV systems, it is necessary to bake-out the vacuum system to traverse the threshold between the high-vacuum and ultrahigh-vacuum regime. A bake-out refers to a procedure whereby the entire vacuum system is brought up to a high temperature (typically >100 °C) for extended periods of time. The reason for these high temperature bake-outs is to expedite the outgassing process and liberate as many of the vacuum residuals as possible so that they may be pumped out of the system. In any vacuum system, vacuum residuals such as atmospheric contaminants, solvents, pump oils, etc are adsorbed onto the inner surfaces of the vacuum system. The pumping speed or pump-out time for these residuals depends on a variety of factors such as partial pressure, molecular weight, and bonding of these residuals. Furthermore, these residuals may react chemically with internal vacuum components. As the pressure of the vacuum system is lowered, more and more of these residuals are liberated

affecting the ultimate pressure. However, the time scale of this liberation may be so long that an ultra-high vacuum is unattainable. Heating the inner surfaces of the vacuum system greatly increases the liberation of these residuals to the extent that they can be rapidly pumped out of the system, providing a cleaner vacuum at much lower pressure.

The bake-out procedure typically used with the first generation electron-MOT system involved wrapping the entire system with several Fibrox® insulated heating tapes from Barnstead-Thermolyne (B00101-040). Each of these tapes was then connected to a Variac® variable AC transformer to provide a variable control of the current in the heating tapes, and hence a control of the ultimate temperature. After this, the vacuum system, now wrapped in heating tapes, was wrapped again with aluminum foil to help retain heat. At this point, the Variac transformers were turned on and their voltage gradually increased until a temperature of between 100 °C and 250 °C was reached. The temperature necessary for the bake-out was determined by the length of prior exposure to atmosphere and the amount of solvent contamination. If the system was open for only a few hours, and with a minimal amount of solvent use, then a "gentle" bake-out was used. Essentially the system was heated to slightly over a 100 °C to degas the surfaces of water and atmospheric traces. However, with an extensive chamber servicing, a more rigorous bake-out was used, where the temperature was increased to over 200 °C.

These bake-outs ranged in duration from two days to two weeks, depending on the amount of vacuum residuals. The first bake-out of the system was the longest as all joints, gaskets, and internal components were heavily contaminated, primarily with water and solvent residue. The system bake-outs extended until the pressure reached a minimum, at which point the heat was removed from the system. During each bake-out, a temperature increase of no more than 2 °C/min was used on the system to prevent components from becoming thermally stressed, particularly at glass-metal interfaces.

To assist in keeping the system clean, dry nitrogen was used to bring the system up to atmosphere for servicing. While being serviced, latex gloves were used when any internal surface was touched. Vinyl gloves typically are not used as these gloves can leave deposits on the surface. Only solvents with light molecular masses were used for cleaning. Acetone

was the primary solvent used for cleaning surfaces. After cleaning a surface with acetone, the surface was washed again with methanol. In some cases, ethanol was used in place of methanol, since cesium oxides are more soluble in ethanol. Internal components were placed in an ultrasonic bath of an acetone or acetone/methanol mixture prior to insertion into the vacuum system. Finally, only lint-free tissues were used for wiping surfaces. A quadrupole mass spectrometer was used to to monitor residual gases in the system and to check for small leaks.

After the ultimate background pressure had been reached, cesium vapour was injected into the vacuum system. The cesium was loaded from a reservoir that consisted of a glass ampoule containing a 10 g charge of cesium metal, which had been broken under vacuum. The ampoule was housed inside of a set of 1.33" mini CF, edge-welded bellows (Kurt J. Lesker, part# MEW1030551C3) that were capped on one end with a 1.33" CF blank. The other end of the bellows was attached to an all-metal, bakeable, right-angle needle valve (Kurt J. Lesker, part# VZCRT97R). The valve was then attached to CF Tee piece, via a 2.75" CF to 1.33" CF reducing flange. This Tee piece was mounted on a side port of the main 6" diameter spool piece.

5.2 Electron Beam System

The electron beam system used in the first generation electron MOT system consisted of a standard design of gun, shown in Fig. 5.5, that was used in the manufacture of television tubes. It consisted of an oxide cathode for the emitter, with a two aperture lens system combined with a cylindrical lens stack that was configured for use in an Einzel mode. The first aperture was used as a Wehnelt cylinder [BRANS 83] to provide electron extraction from the oxide cathode. The second aperture acted as the anode and provided initial focussing into the Einzel lens. The Einzel lens was used to change the focus. At the location of the MOT, the Einzel lens could be used to create a tightly focussed beam, or a very broad,

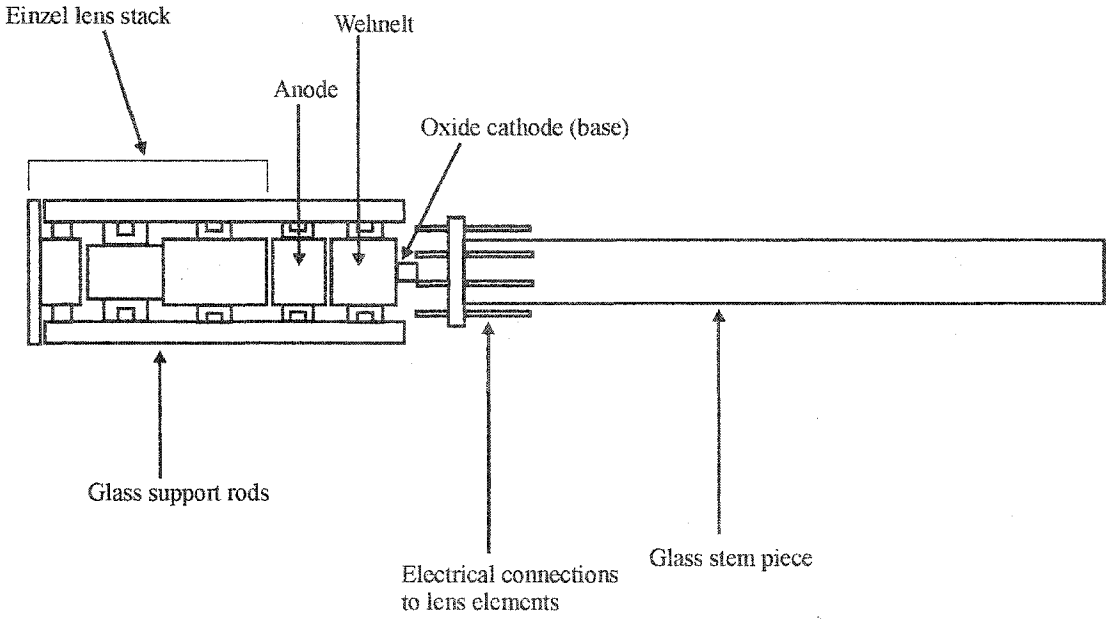

Figure 5.5: Schematic of the electron gun used in the first generation electron MOT system, showing the various lens elements, oxide cathode, and electrical connectors.

defocussed beam.

There are several key advantages to the use of an oxide cathode. The first is that the emitting surface of an oxide cathode provides a circular beam of uniform intensity, due to the geometry of the emitter. With a tungsten wire source, the emission forms an elliptical beam due to the emission anisotropy associated with a line source. The second advantage is

that the energy resolution is much better than in the case of a tungsten wire source. Electrons produced from an oxide cathode typically have an energy spread of 0.2 to 0.5 eV. In the case of a tungsten wire source, the energy spread is largely a function of the voltage across the

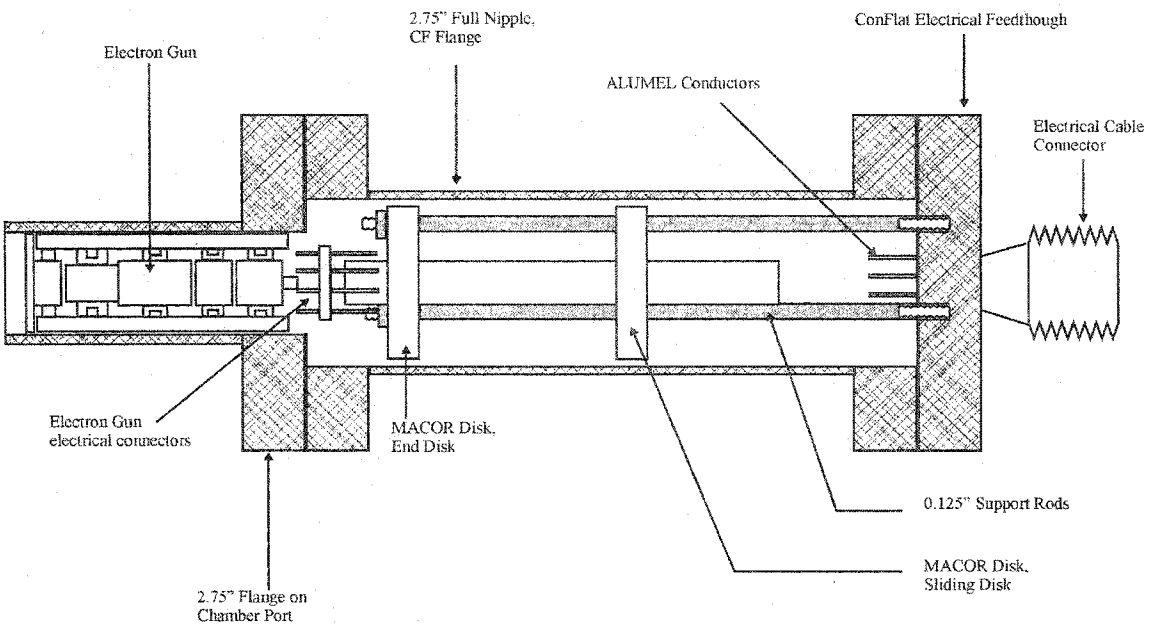

Figure 5.6: Mounting of the electron gun in the first generation electron MOT system.

wire, with typical energy spreads of 1 to 2 eV. Another distinct advantage to the oxide cathode is that it runs much cooler than a tungsten wire source. Normally, oxide cathodes reach optimum emission at approximately 1100 K. Tungsten filament sources normally reach optimum emission at approximately 2500 K. With the increased temperature of the emitter there is an increase in background light emission from the filament.

The electron gun was mounted on a 2.75" CF, 6 pin electrical feedthrough, as shown in Fig. 5.6, using a specially designed carriage system that was constructed in the University of Windsor Physics machine shop. The mounting carriage positioned the electron gun centrally, so that the orientation of the gun was fixed by the alignment of the flanged port on the chamber. The carriage was constructed so that the electron gun could be moved along the central axis. This allowed the gun to be moved as close as possible to the MOT without obstructing the laser beams.

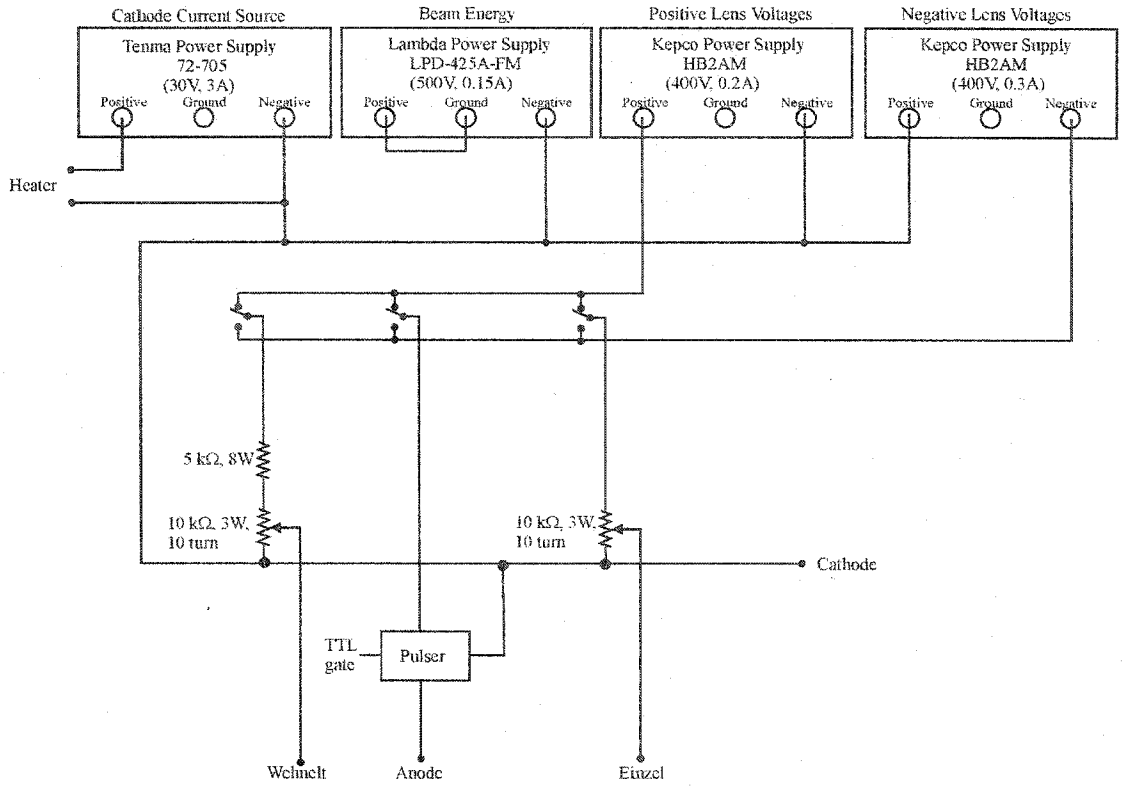

Figure 5.7: Wiring diagram for the electron gun showing the arrangement of power supplies and the insertion of the pulsing circuit.

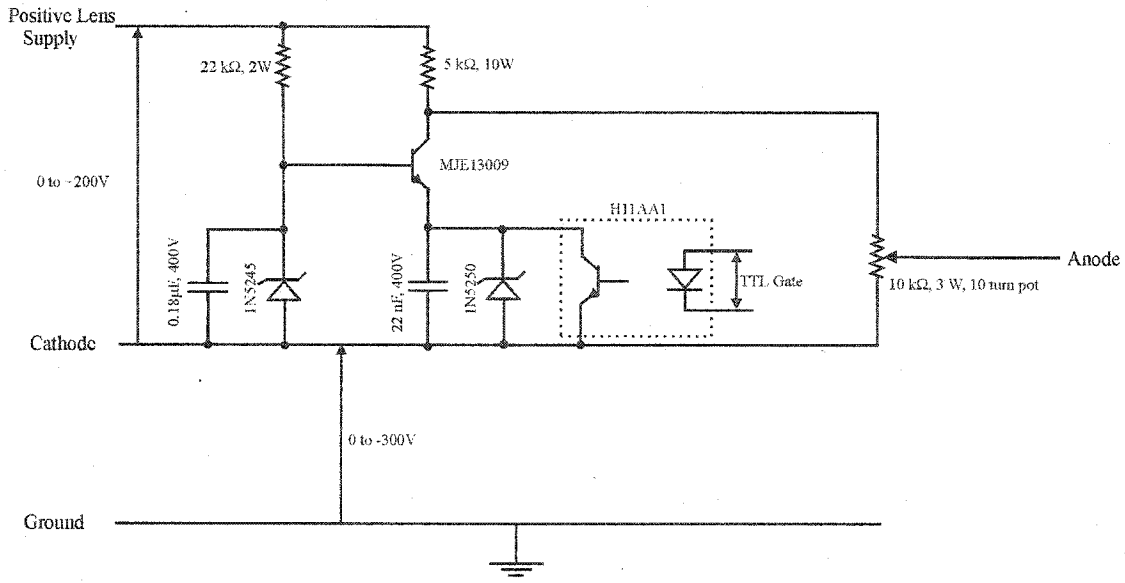

Figure 5.8: Circuit diagram for the electron gun pulsing circuit used in the first generation electron MOT system. The component labelled H11AA1is an opto-coupler.

The power supplies used for the electron gun were arranged as show in Fig. 5.7. The in-vacuum electrical connections to the gun were made using an 18-80 grade of stainless steel wire, of approximately 20AWG. The stainless steel wires were spot-welded to the feedthrough connections on the vacuum side. The wires were then covered with ceramic beads to provide electrical insulation. Once the wires were completely covered, the wires were then spot-welded to the connections on the electron gun.

The electron gun was converted from DC operation to pulsed operation with the use of a home-made pulsing circuit, shown in Fig. 5.8, that was constructed in the University of Windsor electronics workshop. The pulsing circuit accepted a TTL pulse and output an analog pulse ranging in amplitude from 0 V to +20 V, and followed the TTL pulse with typical risetimes of the order of tens of microseconds. The circuit was designed to operate on a floating potential so that 0 V could be referenced from the cathode potential. The analog output pulse was sent to the anode and provided an effective means of switching the beam off, by removing the extraction potential. This method of pulsing the electron gun is analogous to shuttering an optical beam.

The total electron beam current was measured with the use of a Faraday cup current detector, shown in Fig. 5.9. The outer Faraday cup was a stainless steel cylinder, approximately 15 mm in diameter, with a threaded connector spot-welded to the back of the cup to allow an electrical connection to be made to an electrical feedthrough. The inner Faraday cup was also constructed of stainless steel. Due to size restrictions with the vacuum chamber, however, the inner cup was conical in shape to help minimize the loss of current resulting from reflection or secondary emission, from the outer Faraday cup.

The Faraday cup was placed inside the tube opposite the electron gun, and situated with the aid of a corrugated, ceramic disc to isolate the cup electrically and to centre it within the port. Both Faraday cups were connected to separate pins of a 6-pin, electrical feedthrough. The current on each cup was monitored with separate digital, high precision, Hewlett-Packard multimeters. Separate external connections also enabled the cups to be biased independently.

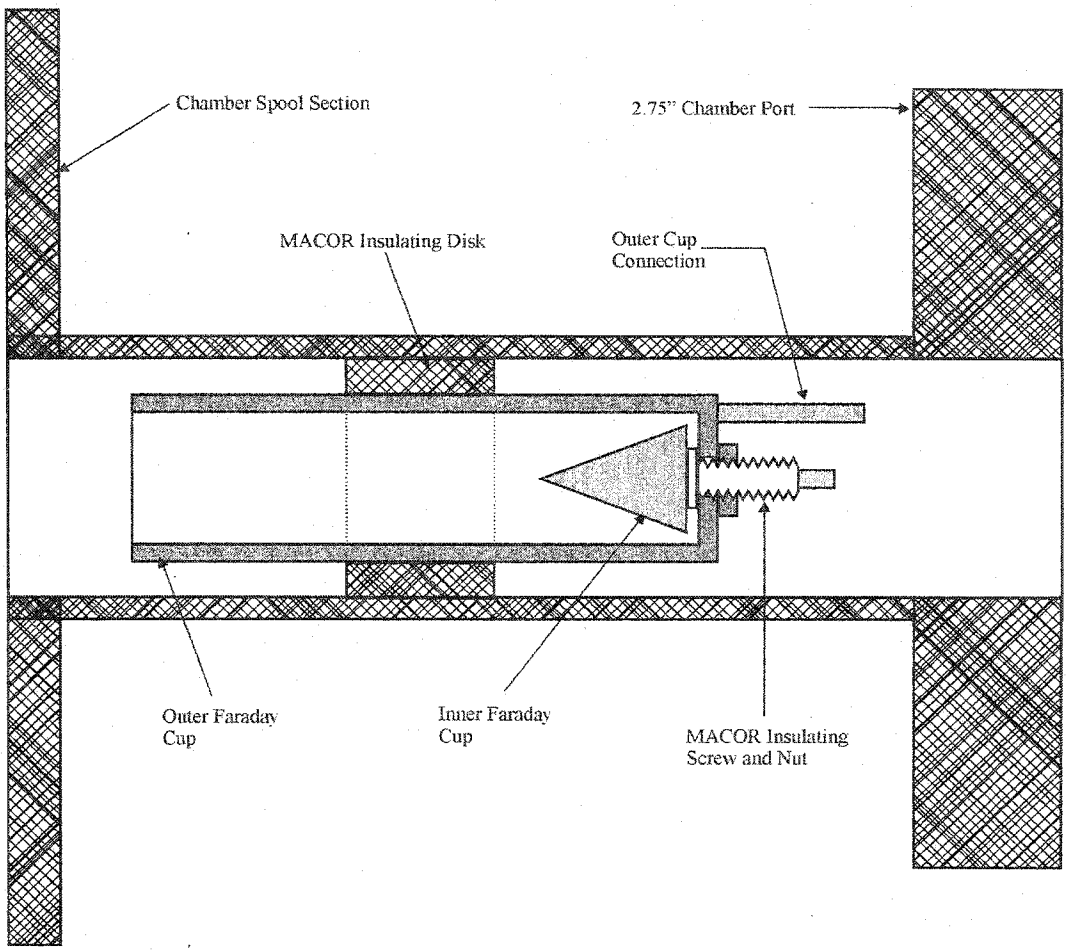

Figure 5.9: Faraday cup current detector used in the first generation electron MOT system. The outer diameter of the outer Faraday cup is 15 mm.

The current density in the electron beam was determined with the use of a scanning, thin-wire, electron beam probe, shown in Fig. 5.10. The beam probe was a piece of 0.010" diameter, stainless-steel wire mounted on a tracked bracket that was driven with a linear-motion, UHV feedthrough with a micrometer drive. The wire was mounted vertically on the bracket and the tracks were aligned perpendicular to the electron beam axis. The micrometer drive pushed the beam probe through the beam in precise increments and the current on the probe was recorded as a function of position.

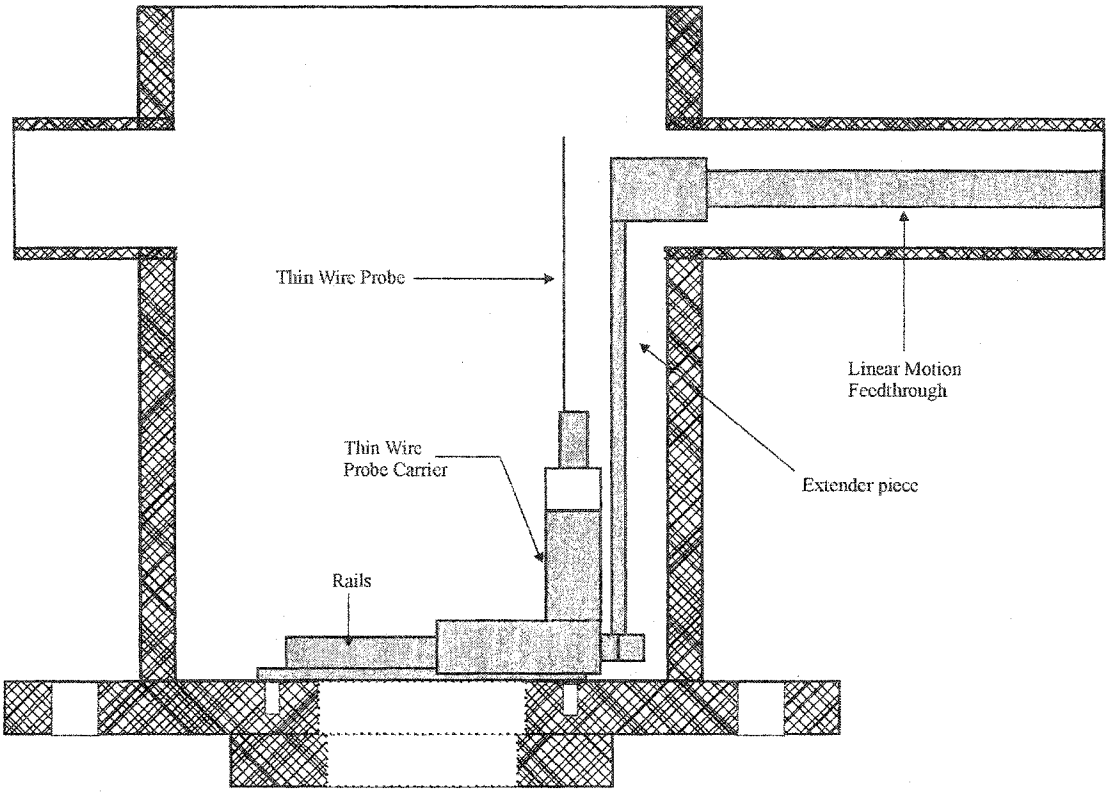

Figure 5.10: Side view of the layout of the electron beam probe and drive mechanism used in the first generation electron MOT system. The electron beam is directed out of the page.

5.3 Laser System and Optics

5.3.1 Laser cooling optical system

The lasers used in the first generation electron MOT system were distributed Bragg reflector (DBR), single mode, CW diode lasers that were originally manufactured by SDL (part# 5712-H1). Although this company, SDL no longer exists, these diode lasers are identical to the 5400 series of lasers from JDS Uniphase. Each laser was capable of producing up to 100 mW of output power at 852 nm, with 180 mA of injection current, as shown in Fig. 5.11. The output of the each laser was a polarized, diverging elliptical beam. Due to the DBR of the laser, the output was spectrally very narrow, with linewidths of the order of a few MHz. The frequency of the lasers was controlled by the drive current into the diode, and also by controlling the diode temperature, via a thermo-electric cooler mounted on the laser head. The frequency tuning could easily allow the laser frequency to be moved throughout the cesium D_2 resonance line.

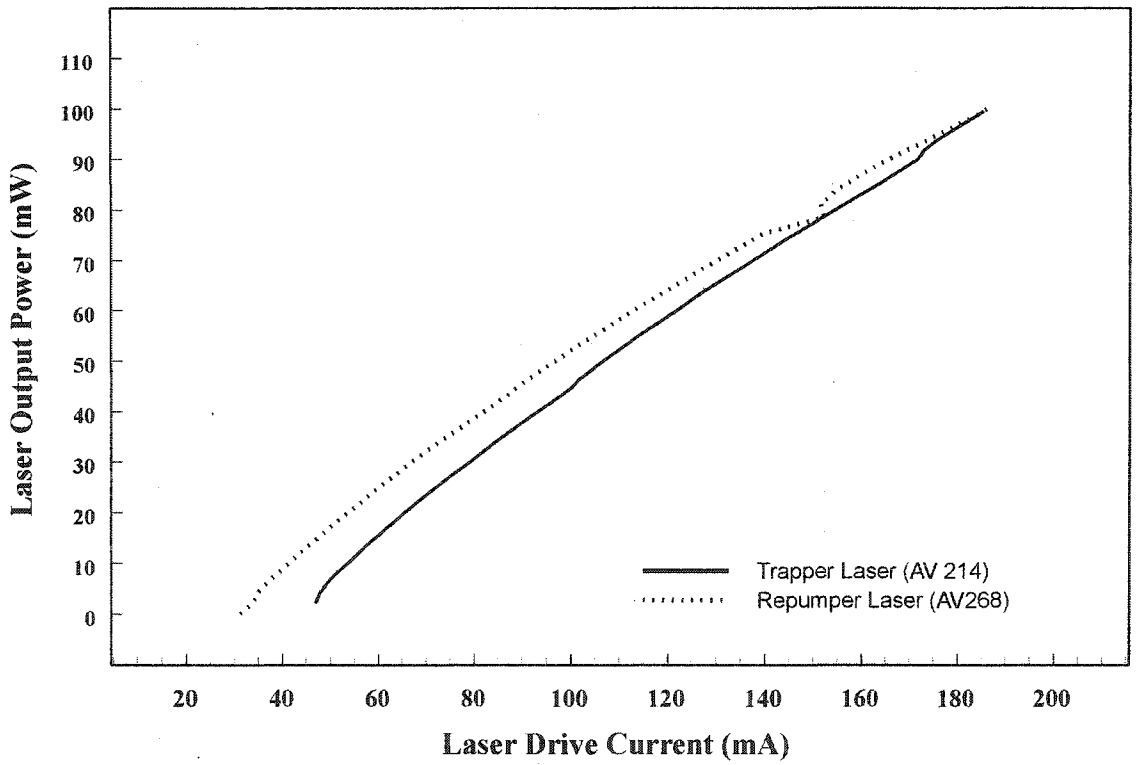

Figure 5.11: Output powers for the SDL model 5712, 852 nm diode lasers used in the first generation electron MOT system, as a function of drive current for the trapping and repumping lasers.

The laser frequency was monitored as a function of temperature and injection current with a wavemeter (Burleigh, part# WA-1500) to isolate the settings where mode-hopping occurred. Mode-hopping leads to instability within the laser cavity and caused a poor output. In addition, mode-hopping creates a hysteresis in the frequency tuning, illustrated in Fig. 5.12

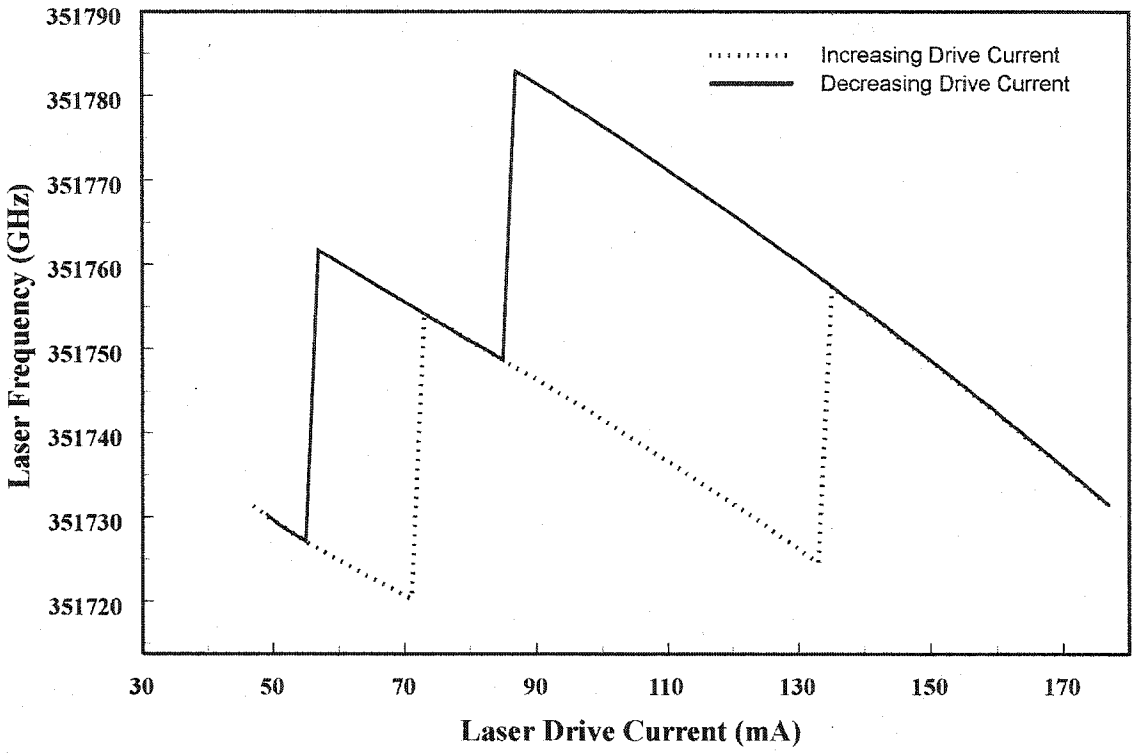

Figure 5.12: Plot of the hysteresis in the frequency tuning of the trapping laser for a fixed temperature of 19.01 ^{o}C. This hysteresis behaviour gives a clear indication of mode-hopping within the laser cavity.

that can make stabilization impossible.

The layout of the optical system is given in Fig. 5.14. The output from the trapping laser was collimated to form an elliptical beam approximately 1 mm x 3 mm in size. After collimation, the beam was passed through an anamorphic prism pair to convert the elliptical beam to a circular beam. The output was then passed through a Faraday rotator opto-isolator (Optics for Research, part# IO-10-852-HP) to prevent virtually all reflected light from returning to the laser cavity. Following this, the beam was passed through a polarizing cube beam splitter that was used to divert part of the beam to the saturation absorption spectroscopy arrangement, that would eventually be used for frequency stabilization. The

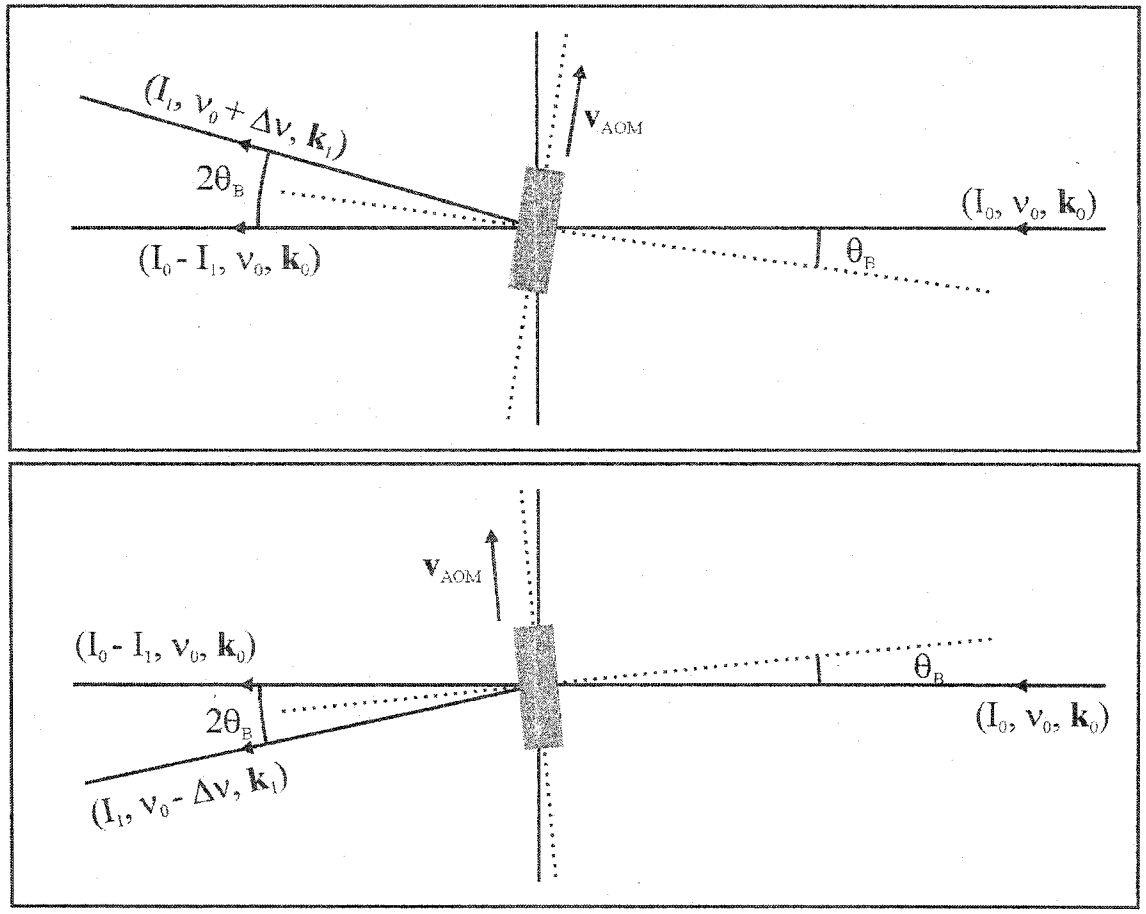

Figure 5.13: Alignment of AOM to produce positive (upper panel) and negative (lower panel) frequency shifts of the fundamental beam. θ_B is the Bragg angle, **k** denotes propagation vectors of the lasers, $\mathbf{v}_{AOM}$ the acoustical wave velocity, and I_0 and I_1 the intensities of the fundamental and side band respectively.

remainder of the beam was sent to an acousto-optic modulator (*AOM*) that was configured for use as a frequency shifter (Isomet, part# 's1206C andD323 driver). The intensity ratio of the two beams emerging from the polarizing cube beam splitter was controlled via the half wave plate mounted on the exit aperture of the opto-isolator.

The beam, upon entering the AOM, would be split into two beams within the plane, as shown in Fig. 5.13. The first beam is the fundamental beam that remains virtually undeflected and has a frequency equal the incident beam. The second beam, or *sideband*, is deflected by twice the Bragg angle and has a frequency shift proportional to the input voltage on the AOM driver. This frequency shift is in the range of 85 - 135 MHz. The sideband can also be gated with a TTL pulse input to the AOM driver. It is important to note that the

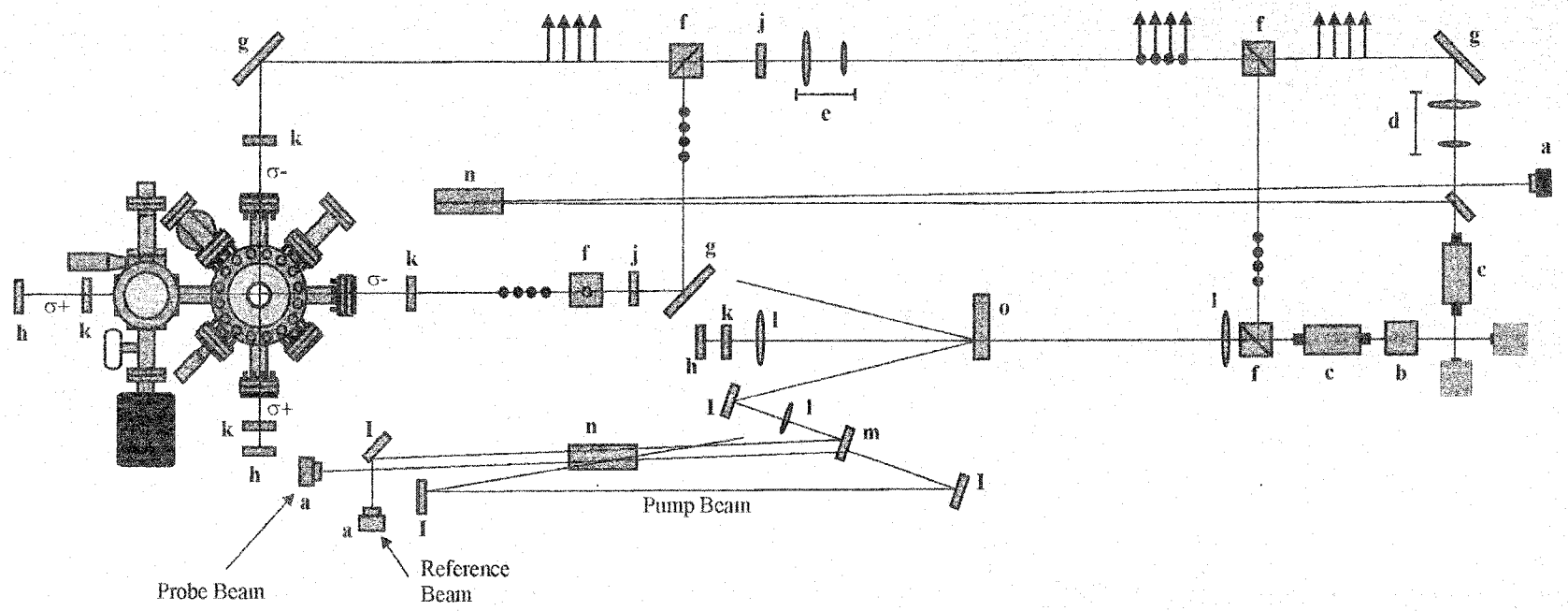

Figure 5.14: A typical optics layout used for the first generation electron MOT system. In this particular layout there is no AOM used on the repumping laser. Also, the saturated absorption spectroscopy for the trapping transition is configured for a differential absorption spectrum. Note that the trapping laser beam for the MOT is taken from the fundamental beam of the AOM.

frequency shift is either positive or negative depending on the alignment of the AOM with respect to the incident beam.

The sideband from the AOM would ultimately be used for trapping. This had a distinct advantage in allowing the trapping laser to be gated at extremely fast speeds, as opposed to using a much slower optical shutter. However, with this configuration the power of the beam sent to the chamber is greatly reduced by the power transfer efficiency of the AOM. Furthermore, since the sideband of the AOM is deflected by the Bragg angle, which is frequency dependent, any attempt to change the frequency of the sideband's output repositions the beam at the chamber. The sideband was then sent onwards to a polarizing cube beam splitter, that was configured for beam merging with the repumping laser's output.

The output of the repumping laser was also collimated to form a parallel, elliptical beam. This beam was then sent into another opto-isolator. Following that, the beam was clipped with a small 1" aluminum mirror to divert a portion of the beam towards the saturated absorption spectroscopy set-up. The remainder of the beam was passed through a Keplerian beam expander comprised of a cylindrical lens pair that had the effect of converting the elliptical beam to a circular beam. Then, the beam passed through another AOM (Isomet, part#'s 1250C with D325 driver) that was configured for frequency shifting. The repumping laser's AOM had the sole purpose of providing a means of gating the laser output. As with the trapping laser's AOM, the repumping laser's was used for gating by supplying a TTL pulse to the AOM driver.

In the beginning stages of operation, the repumping laser was stabilized using external circuitry. However, it was quickly determined that the stabilization was unnecessary due to the fact the repumping laser and its driver were sufficiently stable on their own. The repumping laser could be tuned to a resonance transition and remain there unaided for several hours. This kind of free-running operation is more than adequate for the repumping laser as there is no need for the repumping frequency to be fixed in one position relative to a transition, as is the case with the trapping laser. So long as the repumping laser frequency overlaps with some portion of the repumping transition, the trap will continue to operate at optimum efficiency.

The repumping laser, after passing through the cylindrical lens pair, travelled to the merging cube to combine with the trapping laser. The emerging beam had two polarization components. One component, from the trapping laser, was linear and in the horizontal plane. The second component, from the repumping laser, was linear but in the vertical plane. The combined beam, after leaving the merging cube, was sent through a Gaussian beam expander to magnify the beam to approximately 19 mm in diameter. Following this, the beam was sent through a series of half-wave retarders, and polarizing cube beam splitters to form three mutually orthogonal beams, such that each beam contains an equal intensity of trapping laser radiation. These three beams are oriented to travel through the optical viewports of the vacuum chamber centrally so that they intersect in the geometric centre of the chamber. Prior to entering the chamber, each of the three beams was converted from linear polarization to circular polarization with the use of quarter-wave retardation plates.

The circularly polarized beams then travelled through the chamber and after emerging from the chamber, were incident on another quarter-wave retarder and mirror. The quarter wave plate served to convert the beam from circularly polarized back to linear. The beam then strikes the mirror and retroflects back along its incident path. The beam must pass back through the quarter-wave retardation plate, which converts the beam back to a circular polarization, but with opposite handedness from the incident beam.

In order to form the MOT, one must spend an extensive period of time aligning mirrors, adjusting wave plates, varying magnetic fields, and adjusting the laser parameters. The first crucial step in obtaining the MOT is the optical alignment of the incident optics trying to ensure that the beams are positioned centrally with respect to the chamber viewports (as these ports are mutually orthogonal) and that there is optimum overlap of the beams in the centre of the chamber with a minimum amount of clipping and scattering inside the system. Before one can begin aligning the lasers, it must be possible to see the lasers.

As the laser system is comprised entirely of 852 nm light, an alternative means of viewing the laser output is necessary. There were two viewing methods used with these lasers. The first was to place the output of the laser on a IR sensitive viewing card from Melles-Griot (part# 06 DLA 001). With this card, the laser output appeared as an orange spot

from the phosphorescence of the chemical coating on the laminated card. This card worked quite well in most applications, although in a dark environment the card would eventually cease to emit any phosphorescence and require exposure to a visible source to rejuvenate. The second method was to use a camera that was sensitive in the near infrared. The first camera used with the MOT was a CCD based, black and white, security camera. The second camera was a PC-based web camera with a CMOS detector. These cameras are naturally sensitive in the near infrared, but manufacturers insert filters or use coated optics to block out anything in the infrared. In our case, the web camera had to be disassembled and the filtering optic replaced. All camera outputs are sent to the computer through either a USB connection in the case of the web camera, or a TV capture card (ATI TV Wonder VE) for the security camera.

Once the incident beams are aligned, it was necessary to align the retroflected beams. This alignment was achieved by using a series of iris diaphragms and viewport covers with central pinholes to send a narrow pencil of light through the chamber onto the retroflecting mirror and back to the first iris. The retroflecting mirror was adjusted until the spot formed by the returning beam was coincident on the iris. A good indication of the alignment of the retroflector was the level of noise on the saturated absorption spectroscopy. If the beam was perfectly retroflecting, the absorption spectrum viewed on the oscilloscope was completely destroyed due to the extremely small percentage of reflected light transmitted through the opto-isolator and entering into the laser cavity. In most cases, it was necessary to purposely introduce a slight misalignment in each of the retroflecting mirrors (and sometimes waveplates) to prevent the laser light from returning to the laser cavities.

Once the laser beams were aligned, the next step in getting the MOT functioning was to ensure the proper polarizations of each beam. The polarization scheme was setup to form a right-handed (positive) coordinate system from the right-handed circularly polarized (σ^+) beams. This involved rotating the quarter wave retarders on the incident laser beams ±45° with respect to the incident laser polarization. To create a σ^+ beam, the quarter-wave plate's crystal axis should be rotated +45° from the incident laser polarization vector, as viewed along the laser propagation direction. Similarly, to create a σ^- beam, the crystal axis of the

plate should be rotated -45°. The alignment of the quarter-wave plates on the retroflectors is immaterial and does not affect the performance of the MOT.

After the polarizations of the beams have been properly setup, it was necessary to ensure that each beam had the proper ratio of trapping laser intensity. To do this, a power meter was placed in the path of each of the three beams, with the repumping laser has been blocked off. The half-wave plate before the first polarizing beam splitter cube, following the merging cube, was rotated so that the trapping laser intensities in the beams leaving the splitter were 2:1, with the more intense beam being the one sent to the second polarizing cube beam splitter and the less intense being sent directly to the chamber. At the second polarizing cube beam splitter, the half-wave plate was adjusted to give an intensity ratio of 1:1 on the emerging beams.

At this point, the optics were sufficiently well aligned for creating the MOT, barring some minor alignment on the retroflecting mirrors. Getting the MOT to function was now an issue of selecting the proper laser frequency and stabilization settings, and also the proper magnetic field gradient and orientation.

5.3.2 Saturated absorption spectroscopy system

The key to getting the MOT functioning and keeping it running was stabilization of the trapping laser frequency. Diode lasers are quite susceptible to thermal drift. To successfully trap atoms, the trapping laser frequency must be stabilized against this drift and also must be fixed relative to the cesium resonance transition. The first step was obtaining a hyperfine spectrum for the transition used for stabilizing the laser. One of the most popular and successful methods for obtaining a hyperfine absorption spectrum is the use of saturated absorption spectroscopy.

The first case we will discuss is the saturated absorption spectroscopy used for the trapping laser. A cesium vapour cell was mounted on the optics table and a portion of the laser beam diverted from the fundamental beam emerging from the AOM, and oriented to pass through the cell. This diverted beam typically contained <1 mW of power. A thick-plate glass beamsplitter was used to form three new beams from this diverted beam. The stronger,

transmitted beam was used for the pump beam. Because the beam splitter was a thick glass plate, there were two reflections coming off of it, with roughly equal intensities that were 4% of the pump beam's intensity. The first reflected beam was used for the probe beam, while the second reflected beam was used for a reference beam when a differential spectrum was required.

In most cases it was only the probe beam that was used for the laser stabilization. The trapping laser's stabilization involved sending the photodiode signal into a 200MHz,

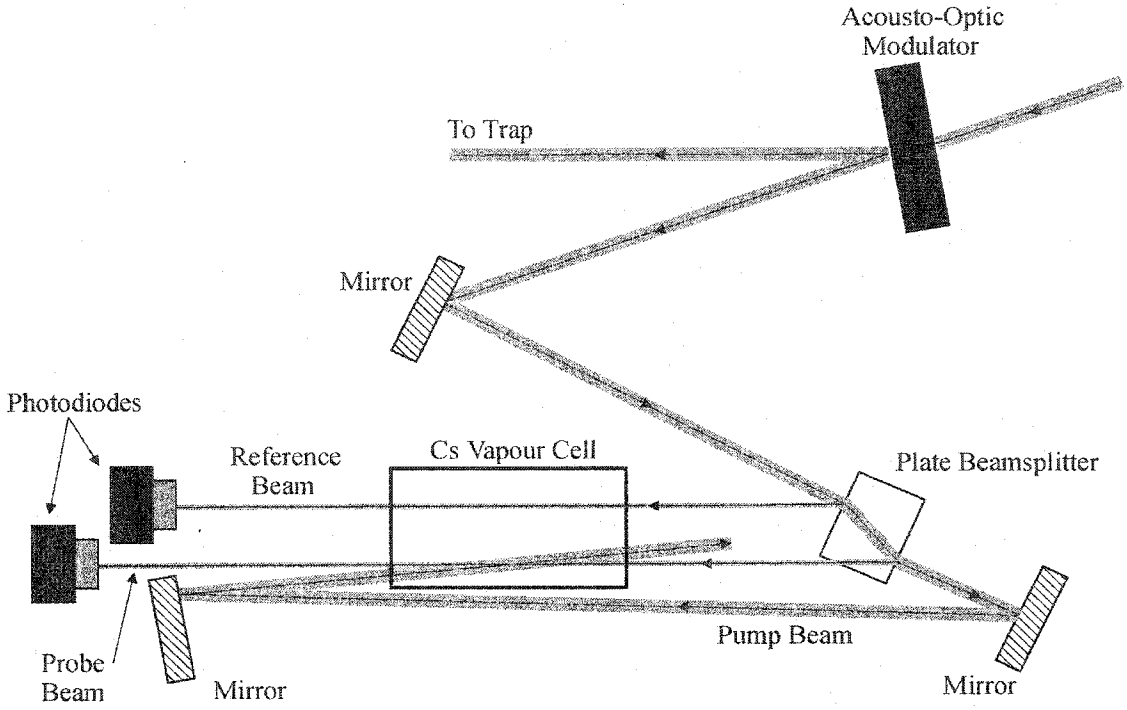

Figure 5.15: Typical layout for performing saturated absorption spectroscopy for the trapping laser. In this particular arrangement, the laser is stabilized using the fundamental beam from the AOM, while the trapping beam is taken off the sideband to allow for the beam to be gated by the AOM.

digital signal processing (*DSP*), lock-in amplifier(*LIA*) (Stanford Research System's model SR844). Along with the photodiode signal, there was a high frequency, small amplitude reference sine wave sent in to the LIA for frequency scanning, as well as a manual DC voltage offset and phase adjust from a home-made signal mixer. The signal layout is shown in Figure 5.16.

The purpose of the LIA was to scan the photodiode signal at a rate specified by the

frequency of the reference sine wave. The magnitude of the scan is determined by the amplitude of the reference sine wave. The LIA then amplifies the portion of the photodiode signal that is in phase with the reference, and feeds back to the modulation input of the laser driver. Selecting the appropriate phase and filtering settings can put the LIA into a minimum- or maximum-seeking mode. For stabilization, we desired a maximum-seeking mode on the LIA. In this way, the LIA forces the laser driver to move to a location that gives a maximum photosignal, within the scanning range specified by the amplitude of the reference sine wave. The manual DC offset could move the scanning frequency range of the LIA throughout the entire hyperfine spectrum until a local maximum, corresponding to a transition (or a crossover), was reached. At this point the LIA automatically takes over and forces the laser frequency to the peak of this transition (or crossover).

Once the trapping laser is stabilized to a transition (crossover), the laser frequency is ready to be detuned from the resonance transition. It may appear that the easiest way of

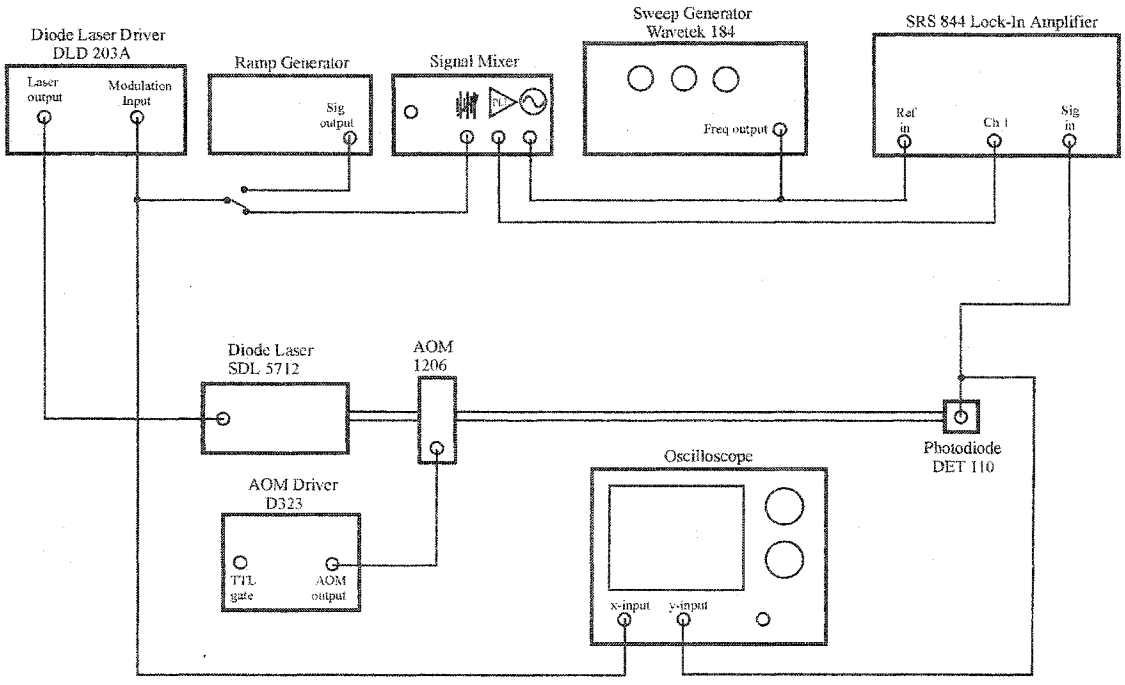

Figure 5.16: Block diagram of the circuitry used to provide frequency stabilization of the trapping laser.

detuning would be to stabilize to the trapping transition and use an AOM to provide a red shift of roughly half the natural linewidth of the trapping transition. It was actually easier to

stabilize to the crossover adjacent the trapping transition, and to blue shift towards the trapping transition. The primary reason for this is apparent from Fig 5.17. The signal on the crossover adjacent the trapping was much larger than that of the trapping transition itself. The crossover was easily distinguished even on the saturated absorption signal of Fig. 5.17(b), while the trapping transition was barely visible.

To achieve the proper detuning for trapping, the laser was stabilized against the crossover midway between the $F' = 4$ and $F' = 5$ transitions, denoted $CO_{4,5}$. From here the

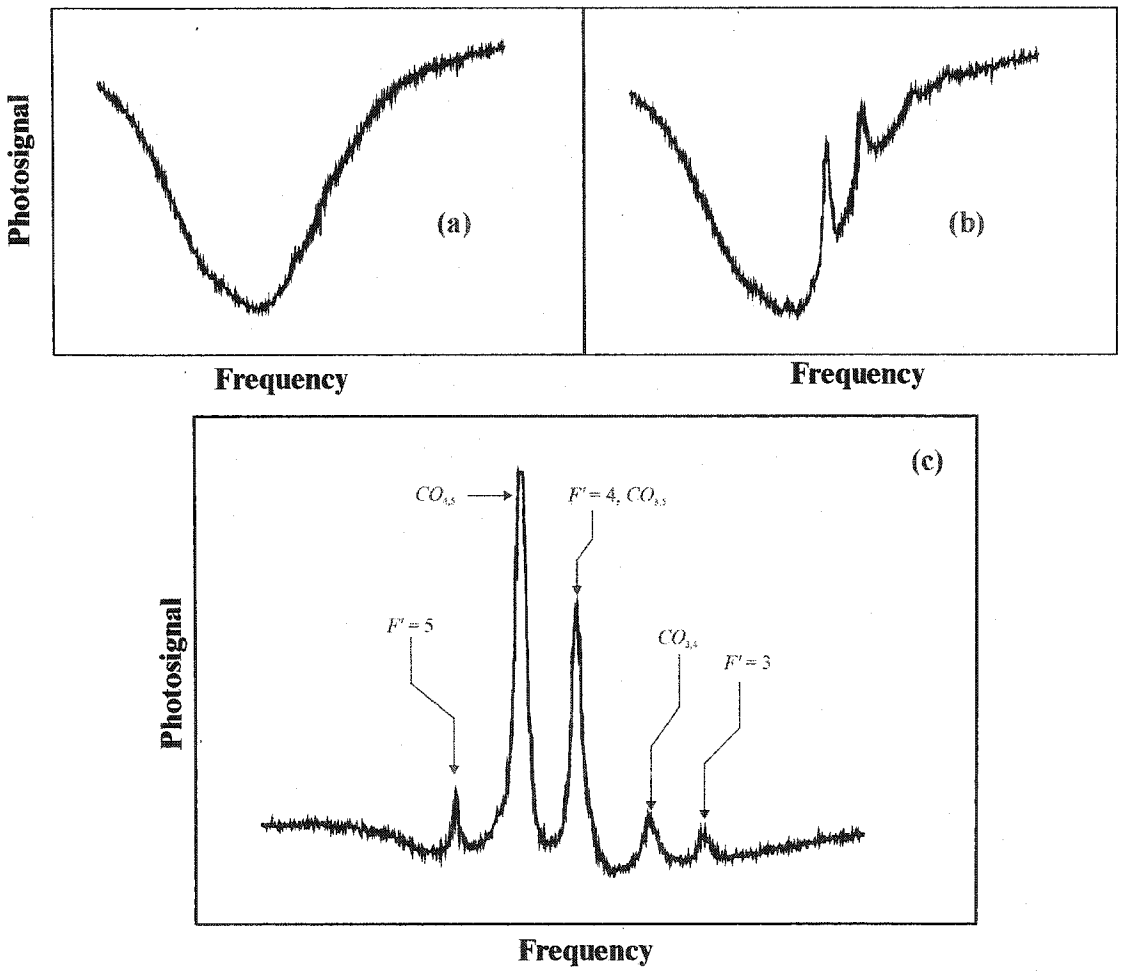

Figure 5.17: Absorption spectra for the trapping laser, showing all optical transitions from the $6^2S_{1/2}$ ($F = 4$) ground state. (a) doppler-broadened transition recorded from reference beam (b) saturated absorption spectrum recorded from probe beam, showing the doppler-broadened spectrum with hyperfine components superimposed. (c) differential absorption spectrum showing doppler-free hyperfine spectrum, given by the difference of *a* and *b*.

laser frequency was shifted approximately +110.0 MHz with the AOM, by varying the tuning voltage on the AOM driver. As the crossover occurs exactly half way between two transitions, which in this case corresponds to 251.00 MHz from Fig 1.5, the separation between the trapping transition and the crossover was 125.50 MHz. Shifting the laser frequency by 110 MHz then gave a total frequency detuning of 125.50 - 110.0 = 15.5 MHz, approximately half of the natural linewidth of the trapping transition.

The repumping laser used a similar process for stabilization. A vapour cell, separate from the one used with the trapping laser, was positioned on the table, and a portion of the repumping laser diverted to travel through the vapour cell. Before entering the cell, the beam went through another AOM with the fundamental beam going to the vapour cell and the sideband going to the chamber. The vapour cell was then aligned such that the reflection from the back face of the cell could be placed on a photodiode. This setup gave a saturated absorption spectrum similar to that in Fig. 5.17(b), with the main advantage of allowing the repumping laser to be gated with a TTL pulse to the AOM driver.

As mentioned earlier, external frequency stabilization was not always used with the repumping laser. The primary reason being that the laser and driver combination was extremely stable on its own. Secondly, the LIA (Thor Labs, LIA100) used with the repumping laser was quite slow, typically 1 - 10 kHz as opposed to the 200 MHz capability of the LIA used with the trapping laser. Since there was no noticeable change in the laser

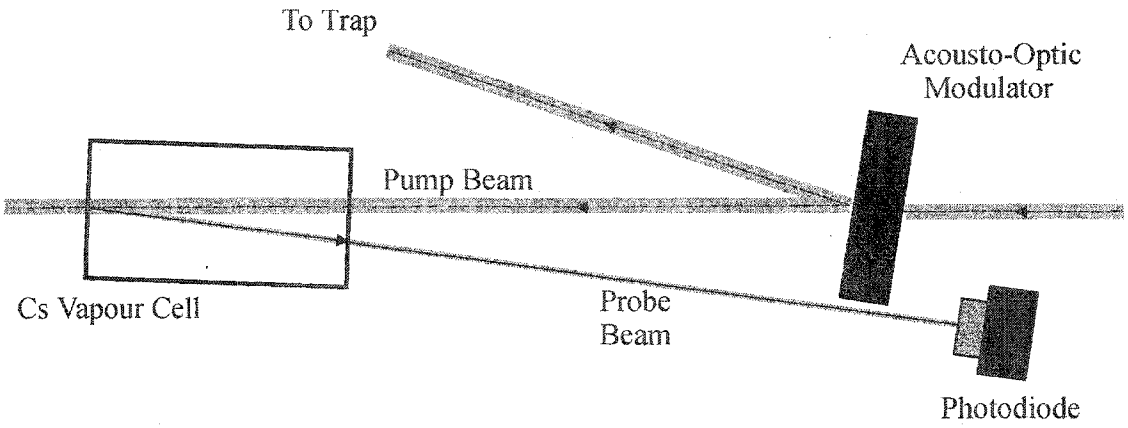

Figure 5.18: Optical layout used for performing saturated absorption spectroscopy with the repumping laser.

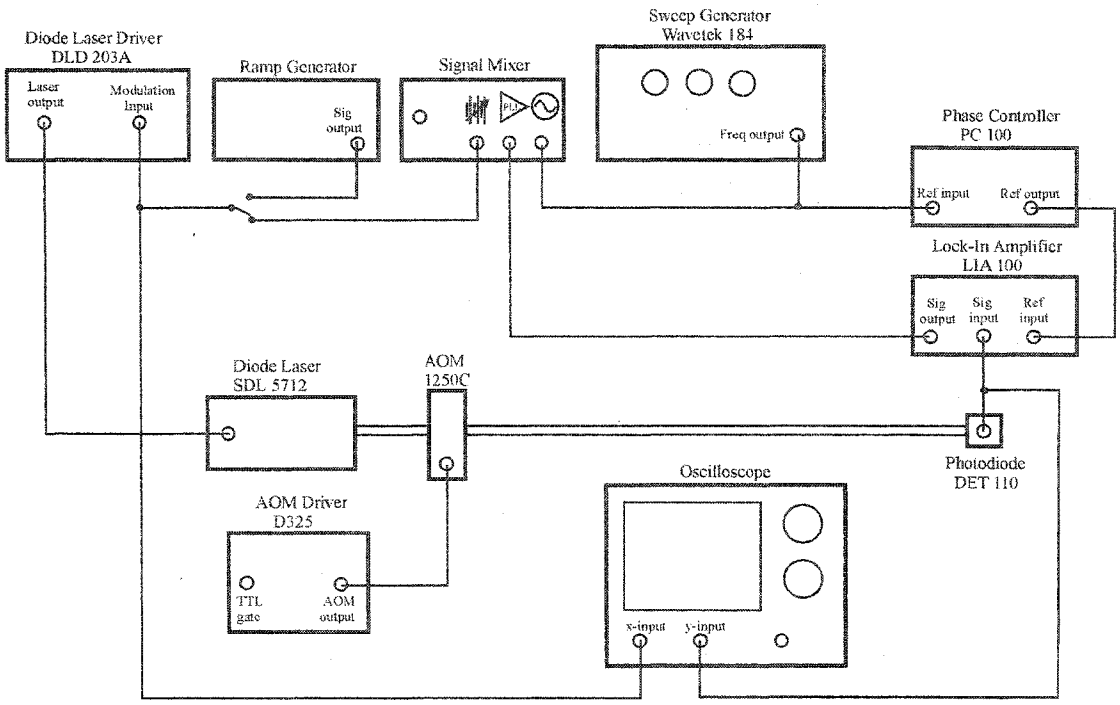

Figure 5.19: Circuitry used for stabilizing the repumping laser to a hyperfine transition (crossover) of the saturated absorption spectrum.

frequency stability with the stabilization circuit on and off, the stabilization was eventually removed to prevent extra noise from entering the laser driver.

With the AOM used on the repumping laser, the laser was tuned to the $F' = 3$ transition. The AOM was then used to shift the laser frequency from the $F' = 3$ to the $F' = 4$ transition. From Fig. 1.8, the frequency shift required for this was +201.24 MHz. The frequency range of the D325 and 1250C driver/AOM combination was 150 MHz - 250 MHz, thus it was well equipped for providing the $F' = 3$ to $F' = 4$ frequency shift. To better illustrate, the results of a differential absorption spectrum for the repumping laser is shown in Fig 5.20.

Now that we have the saturation absorption spectra for both lasers, they could be adjusted to their proper stabilizing points, and their lock-ins were used if necessary. Both lasers could also be gated, through their respective AOM's in the configurations given in Fig 5.15 and 5.18, with a TTL pulse to allow the MOT's properties to be modified during the electron interaction time. With the MOT's optics aligned, and the laser frequencies stabilized

to atomic transitions, the remaining task to get the MOT operational is installing a magnetic

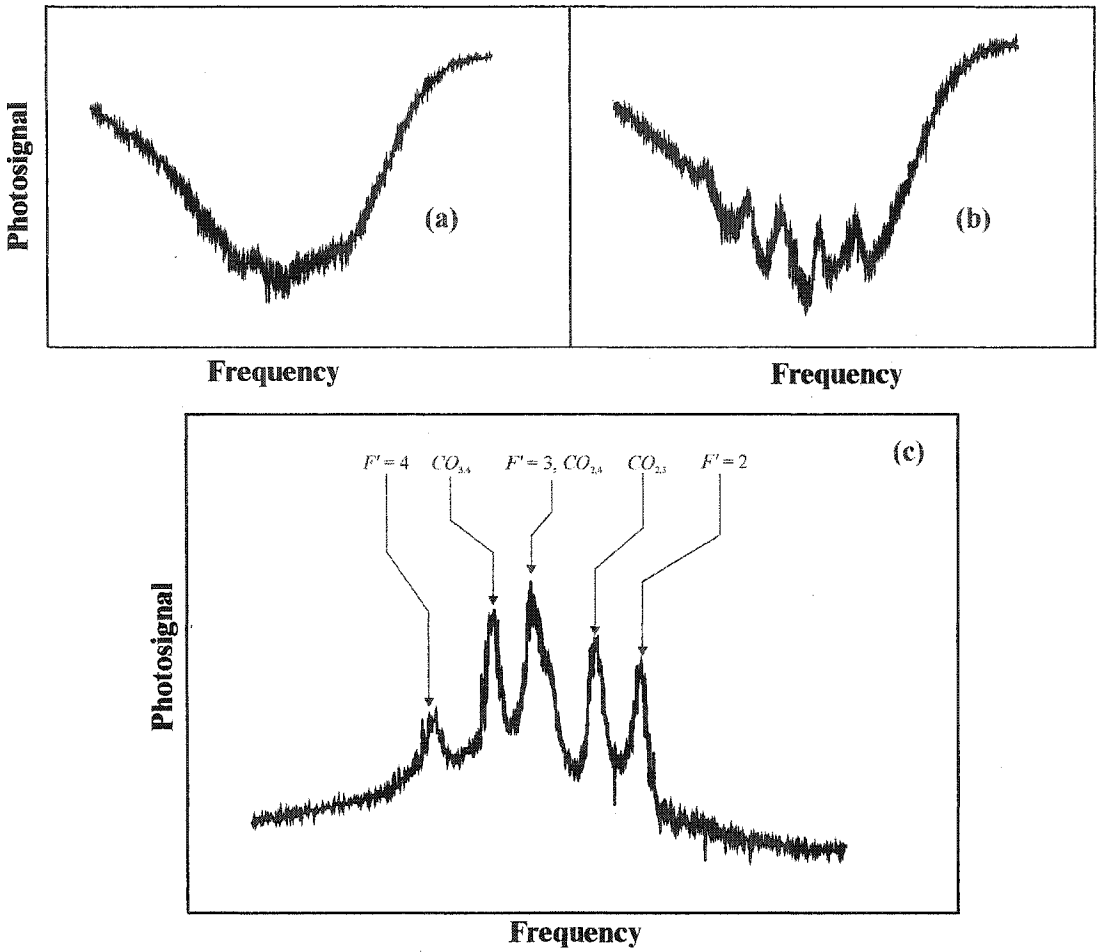

Figure 5.20: Absorption spectra for the repumping laser, showing all optical transitions from the $6^2S_{1/2}$ (F = 3) ground state. (a) The doppler-broadened transition recorded by the reference beam, (b) Saturated absorption spectrum recorded by the probe beam, showing the doppler-broadened transition with the hyperfine components superimposed. (c) Differential absorption spectrum showing the doppler-free hyperfine spectrum.

field with the proper field gradients and orientation with respect to the incident laser polarizations.

5.3.3 Photomultiplier optical system.

Before getting to the magnetic field used with the first generation electron MOT system, there is one remaining optical system to be considered and that is the photomultiplier

and its associated optics. We were ultimately interested in determining the loss rates of atoms from the MOT. The most direct way of determining these loss rates was to record the time evolution of the resonance fluorescence. Initial tests showed that the fluorescence decays of the trap could be monitored with a fast photodiode (ThorLabs, DET110), but the signal to noise, and acquisition speed was greatly increased with the use of a photomultiplier tube (*PMT*).

The first step in installing the PMT on the MOT system was to mount an 852 nm, interference filter on the entrance of the PMT. This removed virtually all photon signal from background sources that were not produced from the MOT, such as room lighting, ionization gauges, electron gun cathodes, etc. The main source of background was then the scattered laser light inside the vacuum chamber, and the resonance fluorescence from the background cesium vapour. Fortunately, the radiation from the MOT was much more intense than the background fluorescence so that neutral density (*ND*) filters can be used to suppress the background signal.

The PMT has its own viewport, in the horizontal plane, directly across from the electron beam probe, and 45° from the two pairs of horizontal trapping laser beams. The viewport has a tee-piece attached, to mount the cesium reservoir on the underside. Due to

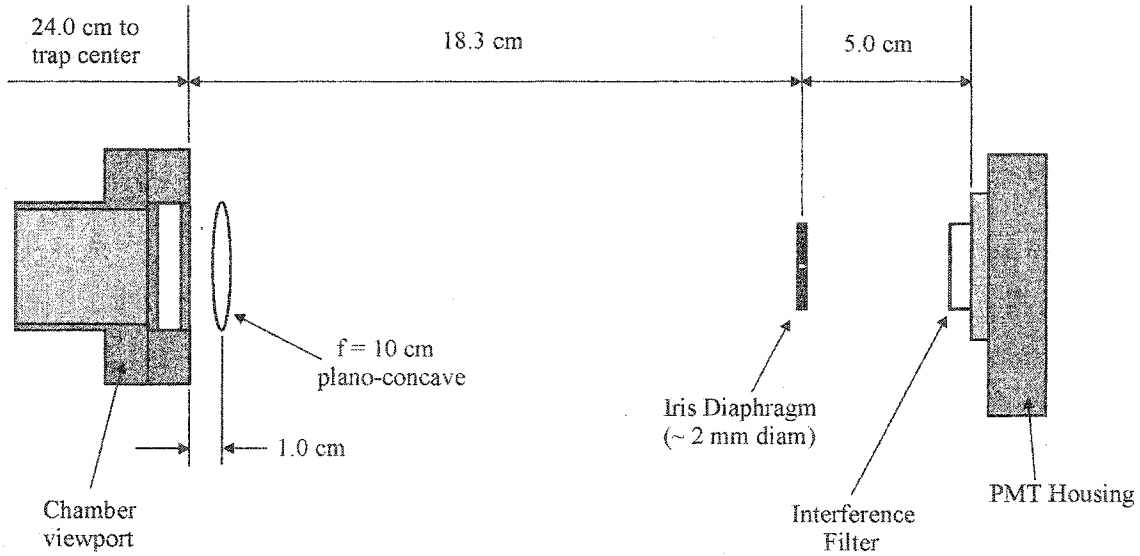

Figure 5.21: Optics layout used for imaging the MOT with the PMT used in the first generation electron MOT system. Not shown is the ND filter which would normally be inserted just prior to the iris diaphragm on the trap side.

the distance between the viewport and the chamber centre, and the small dimension of the trapped atom cloud, it was necessary to use a telescope arrangement to project an image of the MOT onto the photocathode to increase the signal level. A diagram of a simple telescoping arrangement typically used in the first generation electron MOT system is given in Fig 5.21.

An iris diaphragm was placed inline with the PMT to act as an optical stop of variable aperture size. This also helped to minimize the amount of background signal recorded by the PMT. However, the diameter of iris could not be decreased too far as the MOT underwent a gravitational free fall and thermal expansion when the magnetic field was removed prior to recording the fluorescence decay. It was crucial for the PMT to be able to view the trapped atoms during the entire time for which the magnetic field was off.

5.4 Magnetic Fields

In the first generation MOT, anti-Helmholtz coils were used to generate a spherical quadrupole magnetic field like that discussed earlier in Section 2.5. The coils were designed to be mounted externally on the chamber, with a vertical coil axis. The coils were constructed with 14 AWG (1.6 mm diam.) copper wire with varnish insulation. Each coil was wrapped around a brass form with approximately 185 turns of wire. Each form also had a piece of copper tubing soldered to the outer surface of the form to help dissipate heat generated from the coils with the aid of water cooling.

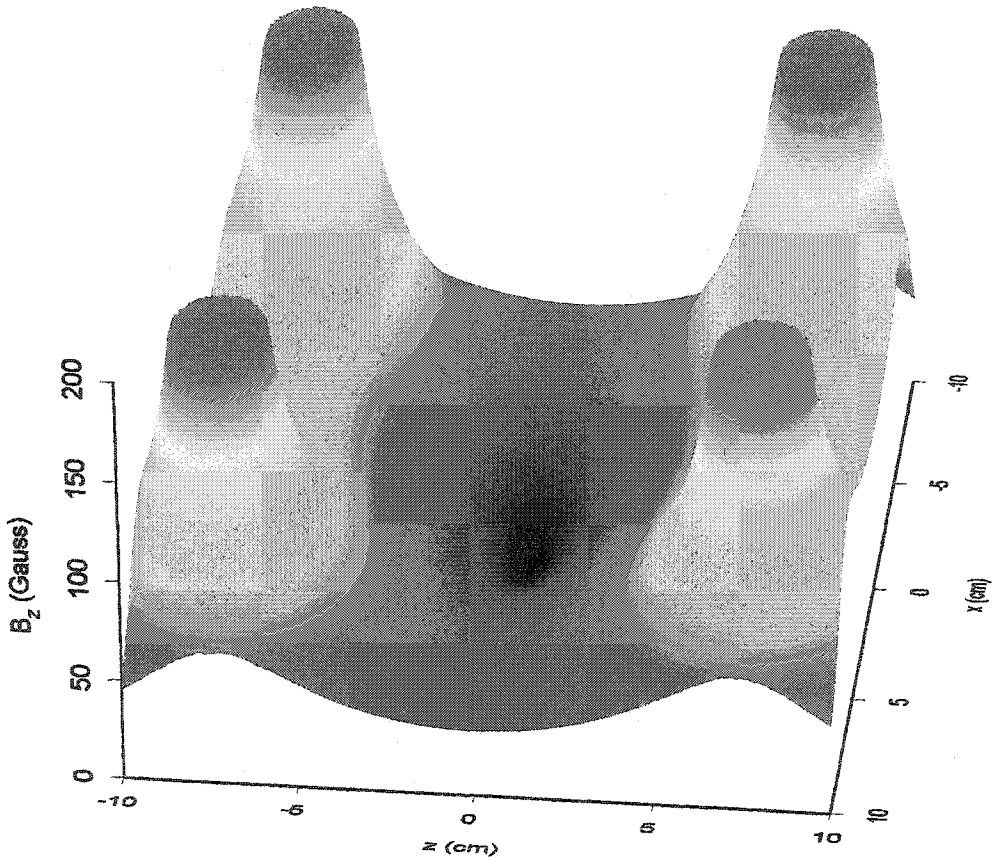

Figure 5.22: Spherical quadrupole magnetic field generated by the Anti-Helmholtz coils used on the first generation electron MOT system. The coil axis is along z with a coil separation of 7.6 cm and a coil radius of 7.6 cm.

The coils were designed to generate a magnetic field such that the field gradient at the centre of the trap was approximately 15 G/cm. A gaussmeter (Bell, part# 640) was used to verify the calculated field gradients inside the chamber and excellent agreement was found. The coils each had an inner diameter of 6.00" (15.2 cm), while the coil spacing was also 6.00". This coil geometry lent itself quite well for use with the first generation electron MOT system, as the coils could be mounted concentrically around the top and bottom flanges. The coils were driven from a high current power supply to deliver approximately 8 A of current to establish the proper field gradients. As it was necessary to be able to pulse the magnetic field off during the electron interaction time, a high current pulser [DEDMA 01] was used on the coil power supply. This home-made pulser, shown in Fig. 5.24, allowed

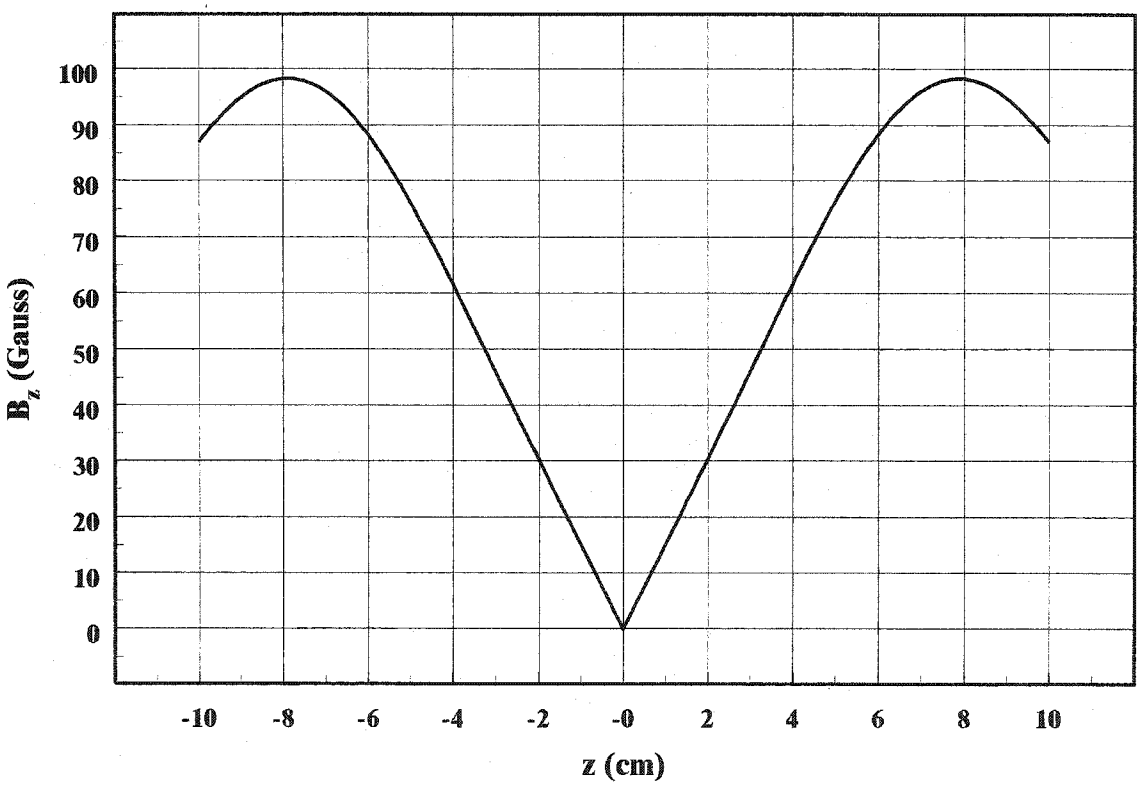

Figure 5.23: Magnetic field strength versus position along the coil axis, for the coils used in the first generation electron MOT system. The calculated field was for 185 turns of 14 AWG copper wire carrying 8 A of current. From this graph it is apparent, the axial field gradient for such a configuration is 15 G/cm.

the coil current to be gated with a TTL pulse. It turned out that the magnetic coils had the slowest response of all the pulsed components used on the first generation electron MOT

system. This was primarily due to the current in the coils generating eddy currents in the walls of the chamber. The pulser was designed to minimize the decay time of the magnetic coils, by preventing any back EMF travelling through the coils after pulsing. This was achieved by providing a very fast transfer of energy from the coils to a high voltage capacitor, where the energy was temporarily stored until the coils are pulsed back on.

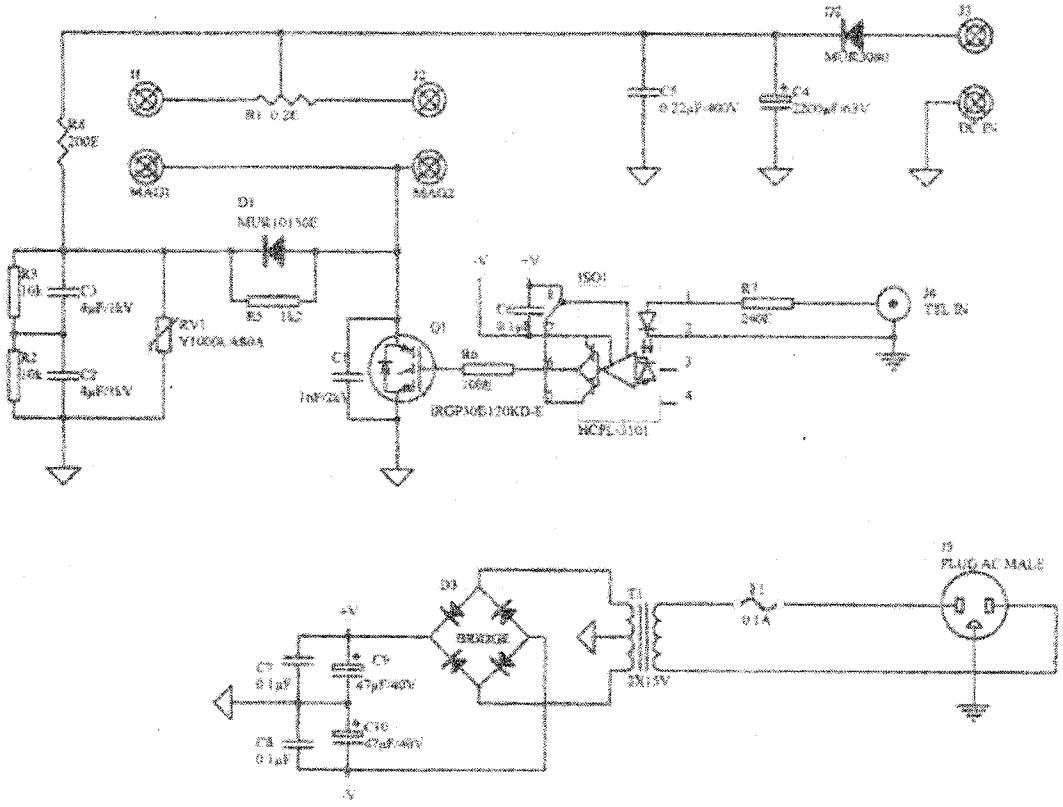

Figure 5.24: Circuit diagram for the high-current pulser unit used for pulsing the anti-Helmholtz coils.

In addition, to the trapping anti-Helmholtz coils, three pairs of Helmholtz shim coils were constructed for use with the first generation electron MOT system. The reason such shim coils were necessary was due to the lack of a beam steering capability with the electron gun. Thus, if it was ever deemed necessary, the trapped atoms could be moved into the beam by using one or more pairs of shim coils to reposition the field zero of the trapping field. However, it was quickly determined that the use of shim coils, even with minimal drive

current, had profound effects on both the electron beam and the trapped atoms. Thus, it was not a trivial matter to establish overlap by applying a DC magnetic field, and so this technique was rarely used.

So far we have covered the optical alignment of the trapping and repumping lasers for forming the MOT, including the setup necessary to establish the proper polarization scheme. We have detailed the processes used to stabilize and tune the frequencies of both lasers. Once the coils were situated and powered on, the MOT was ready for operation. The vacuum chamber was loaded with enough cesium such that the laser beams were visible with the infrared cameras. When the coils were switched on, there was a noticeable change in the fluorescence emission, and the retroflectors were adjusted to try to form the MOT. It was usually easier to perform the adjustment with two cameras focussed on the trap centre, and with the magnetic coils pulsing at ~1 Hz, to better distinguish between the optical molasses

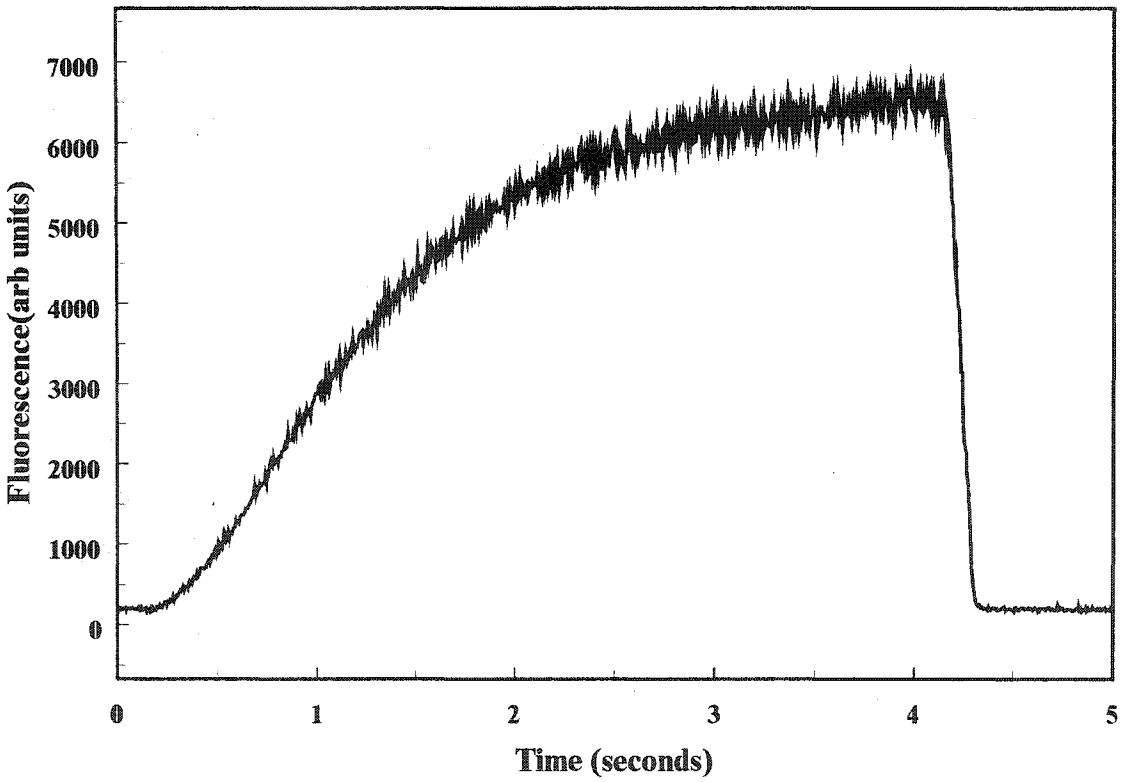

Figure 5.25: Typical loading curve for the cesium MOT starting from a zero population. The curve was measured with a PMT and a multichannel scaler. The curve ends at ~ 4.2 sec, but this was actually the end of the data acquisition, and not the MOT switching off. We note that the MOT has essentially filled after 2 seconds of loading.

in the background and the initial formation of the MOT.

The basic procedure used in forming the MOT for the first time was to get all three returning beams as close to retroflecting as possible, then make small adjustments on each mirror one at a time, for both current polarities on the magnetic coils. It was necessary to adjust the quarter-wave plates if all combinations of retroflector alignments had been exhausted. In such an event, the retroflectors were returned to a near perfect alignment. Each wave plate was then rotated ±45° in turn, about their respective crystal axes. If in doubt where the crystal axis was, the quarter-wave plate was dismounted from the rotation stage to find the cleave mark on the circumference of the plate that indicates the crystal axis. A simpler method was to reposition the wave plate in front of a polarizing cube beam splitter and use a power meter to identify the crystal axis. The latter was the preferable method as

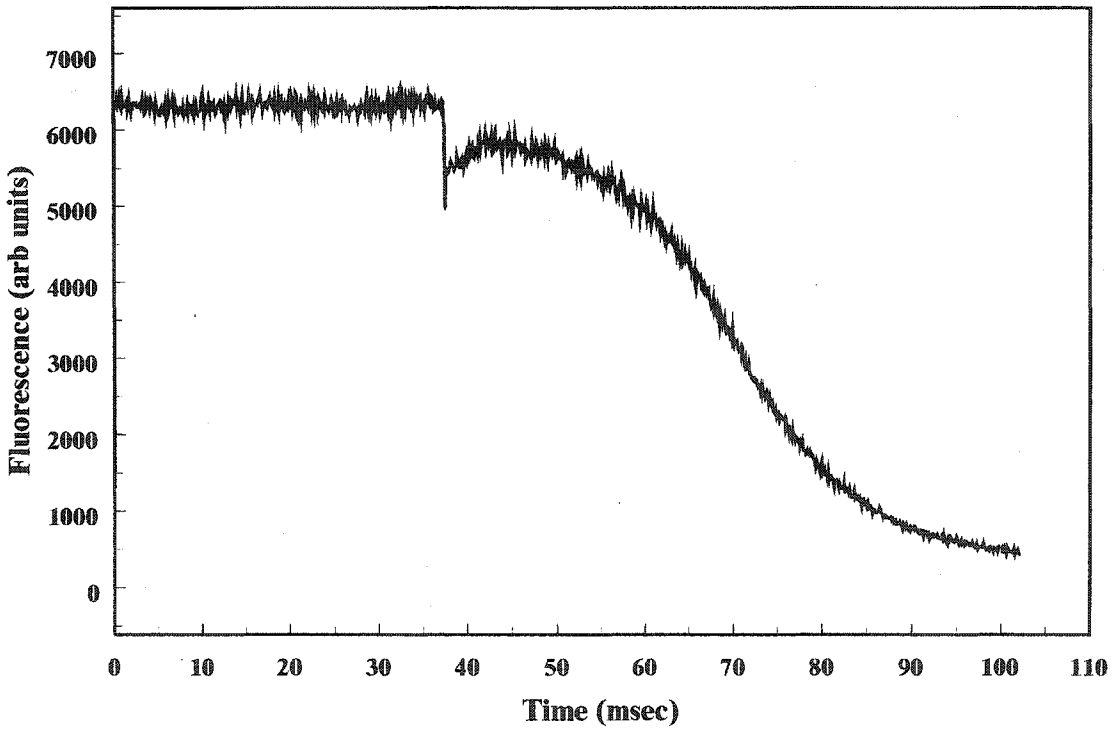

Figure 5.26: A typical loss curve for the MOT showing the time necessary for the trap to completely empty. The magnetic field was removed at approximately 37 msec, as indicated by the glitch in the fluorescence. The trap emptied after roughly 50 msec.

there was always some error introduced into the alignment of the wave plate in inserting it

back into the rotation stage.

Once the MOT was operational, it was then necessary to make a few key tests of its performance. The first test is to ascertain the loading time of the MOT starting from a zero population. A typical loading curve is given in Fig 5.25. If we had a good alignment on the system the MOT filled in approximately two seconds. The next test, which gave a much better indication of the optical alignment, was the trap loss. Essentially, the better the alignment of the system, the longer it took for the MOT to completely empty. A typical loss curve is given in Fig. 5.26. For purposes of obtaining data for electron-induced trap loss rates, the minimum acceptable emptying time was 40 msec.

5.5 Experiment Control and Data Acquisition

With the MOT functioning and electron beam working properly, the experiment was almost ready to commence. The only remaining issue was the installation of the pulse control to be used for pulsing the individual MOT components, and connecting the circuitry for digitizing and recording the fluorescence decays of the MOT. Each of the necessary components was installed with the intention of running in a pulsed mode. This included the electron gun, the magnetic coils, the PMT, and the trapping and repumping lasers.

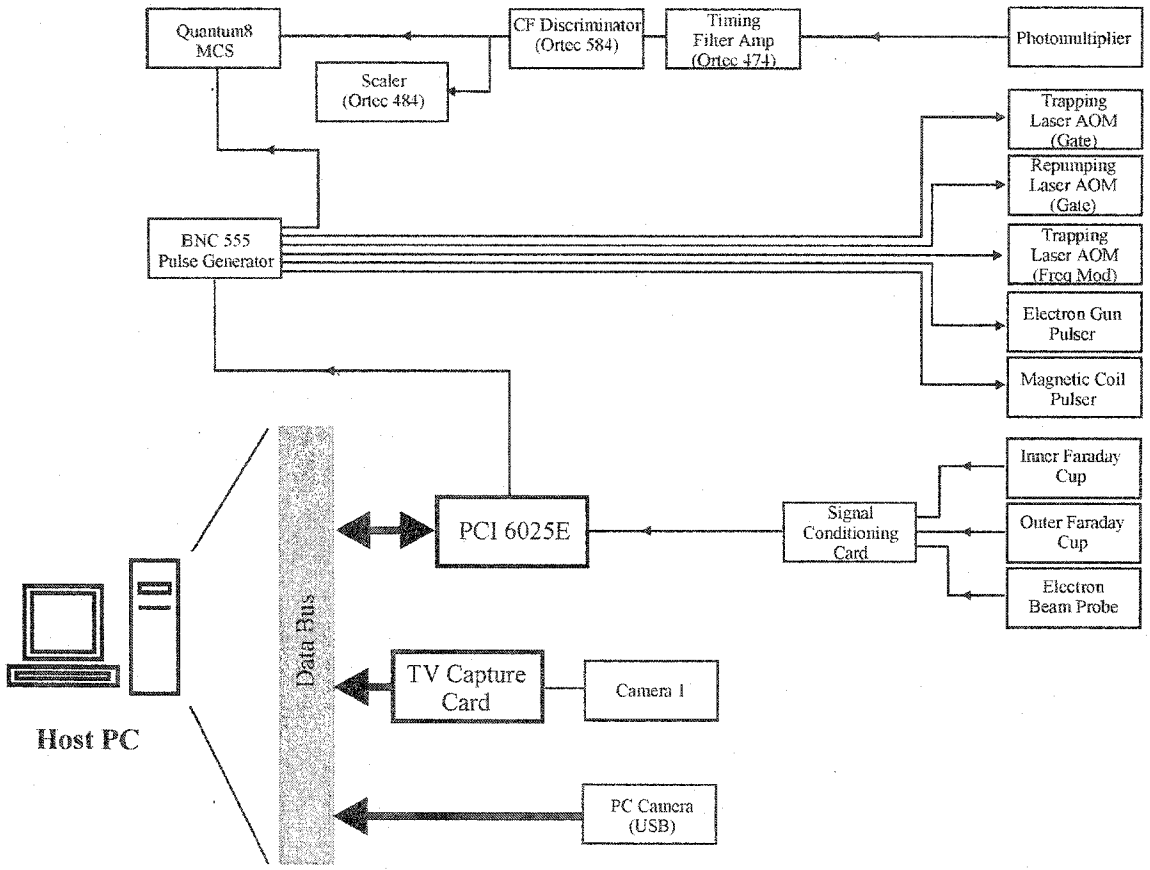

Figure 5.27: Schematic of the experimental control and data acquisition system implemented with the generation electron MOT system.

In the early stages of operation, the experiment was controlled with a Berkley Nucleonics Corp, 4 channel, digital delay generator (BNC, part# 555-4). Unfortunately, this could only provide pulsing for the electron gun, the coils, and the Quantum8 (Nucleus Inc.)

multichannel scaler (*MCS*) used on the PMT. This also required that the host PC be used as the master oscillator, through a National Instruments multifunction, data acquisition card (PCI 6025E). This setup was later modified, to the set-up depicted in Fig. 5.27, to include an 8 channel version of the same digital delay generator (BNC 555-8). With this unit, the host PC was not needed for continuous rearming and firing of the digital delay generator, and allowed the capability of pulsing up to 6 instruments besides the MCS.

The pulser for the coils accepted an active low TTL input to gate the field off. The pulser for the electron gun also required an active low TTL pulse to gate the electron beam on. Both the AOM's required active low TTL pulses to gate their respective beams off. The MCS required two TTL inputs, one to trigger and one to gate. The first triggering pulse was to prepare the MCS for an acquisition and start the internal analog to digital converter (*ADC*), the second pulse was to gate the signal input to the MCS that was to be scaled.

The photomultiplier was setup in a digital, or photon counting mode. The photosignal from the PMT was sent to a series of NIM units to provide a digitized, TTL pulse train corresponding to photon events on the photocathode. The signal from the PMT was a small current derived from the electron multiplier at the end of the PMT. This was fed into a timing filter amplifier (Ortec, part# 474), that was sent to a constant fraction discriminator (Ortec, part# 584). The output from the discriminator was sent in parallel to an analog scaler(Ortec, part #484) and to the MCS.

Each of the pulsed units, barring the electron gun, were pulsed twice per acquisition cycle. The electron gun was only pulsed once. This gave fluorescence decays in the presence and absence of the electron pulse, so that trap loss rates due to electron collisions could be determined. This entire acquisition was recorded as one sweep with the MCS and the process repeated for several thousand sweeps to build good statistics on the fluorescence curves.

The electron beam profile was originally recorded manually. The currents from the electron beam probe, inner Faraday cup, and outer Faraday cup were recorded by hand for each beam probe position. This was a tedious procedure and a possible source of error. The PCI 6025E was later given the task of recording these currents as the beam probe was manually moved through the electron beam. To accomplish this, a custom designed printed

circuit board was ordered from Express PCB. This circuit board was then fitted with a variety of components including voltage dividers, 1 MHz, 8-bit, successive approximation ADC's (National Semiconductor, part# ADC0820), and several quad op-amp's (National Semiconductor, part# LM2902) configured for use as inverting and non-inverting amplifiers. This card was designed as a general purpose signal conditioning card. All three electron beam current detectors were wired to send their signal to external meters or to the signal conditioning card where the currents were converted to voltages and amplified before they were sent to the PCI-6025E. A Labview® routine was then written to sample each of the cups and the beam probe up to 1000 times, average the results and record them along with the probe position each time the probe was moved, by simply clicking a button with the mouse. This greatly increased the recording speed and reliability of the electron beam profile.

CHAPTER 6. EXPERIMENT II

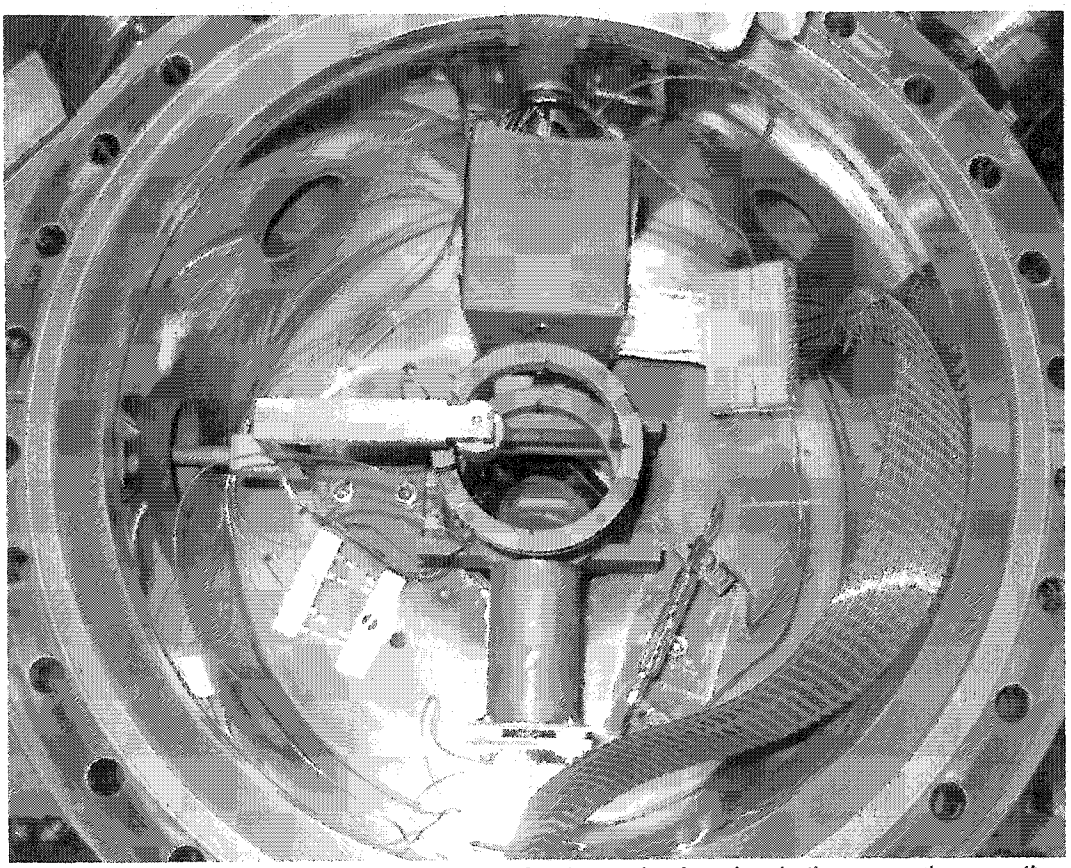

Internal view of the 13.25" spool piece used for the main chamber in the second generation electron MOT system.

6.1 Vacuum System

The vacuum system from the first generation electron MOT system was eventually decommissioned in favour of a new vacuum system with a variety of improvements over the old system. The primary reason for moving to the second generation system was the failure of the electron gun. There were no replacement guns available at the time that could easily be integrated into the existing vacuum system. Since the electron gun was to be replaced, and a new chamber section installed, it was decided that the entire system should be overhauled, from the vacuum system to the experimental control. As we progress through the experimental details of this second generation electron MOT system, the advantages over the older first generation system will be highlighted.

The replacement electron gun that was to be used in the second generation system was a home-made gun, that was designed by Peter Hammond in 1986 and built in the University of Windsor machine shop. This gun had the advantages of using replaceable, standardized filaments and also had two beam steering stages built in. While this gun offered more far more flexibility than the TV gun used in the previous system, it was considerably larger. In order to accommodate this larger, improved gun a new chamber spool piece had to be designed and constructed. Of course increasing the volume of the main chamber spool piece by roughly a factor of 5, would require several design changes to the original vacuum system to accommodate it.

The spool piece that was to replace the older 6.00" CF spool, was a 13.25" CF spool piece of the same height as the older 6.00" spool. A layout of the 13.25" system is given in Fig. 6.1. This new spool section had a 10.0" inner diameter, and offered enough room to mount the replacement electron gun, without clipping laser beams. The spool piece had eight side-mounted tubes, just as the older system had. However, the tubes each had a 1.5" outer diameter, versus the 1.0" tubes used on the first generation system. Both spools were manufactured from 304 stainless steel and had an electropolished inner surface.

The new system was considerably larger, and heavier, and required a much more rugged system for mounting the chamber to the optics bench. Four 1" diameter stainless steel

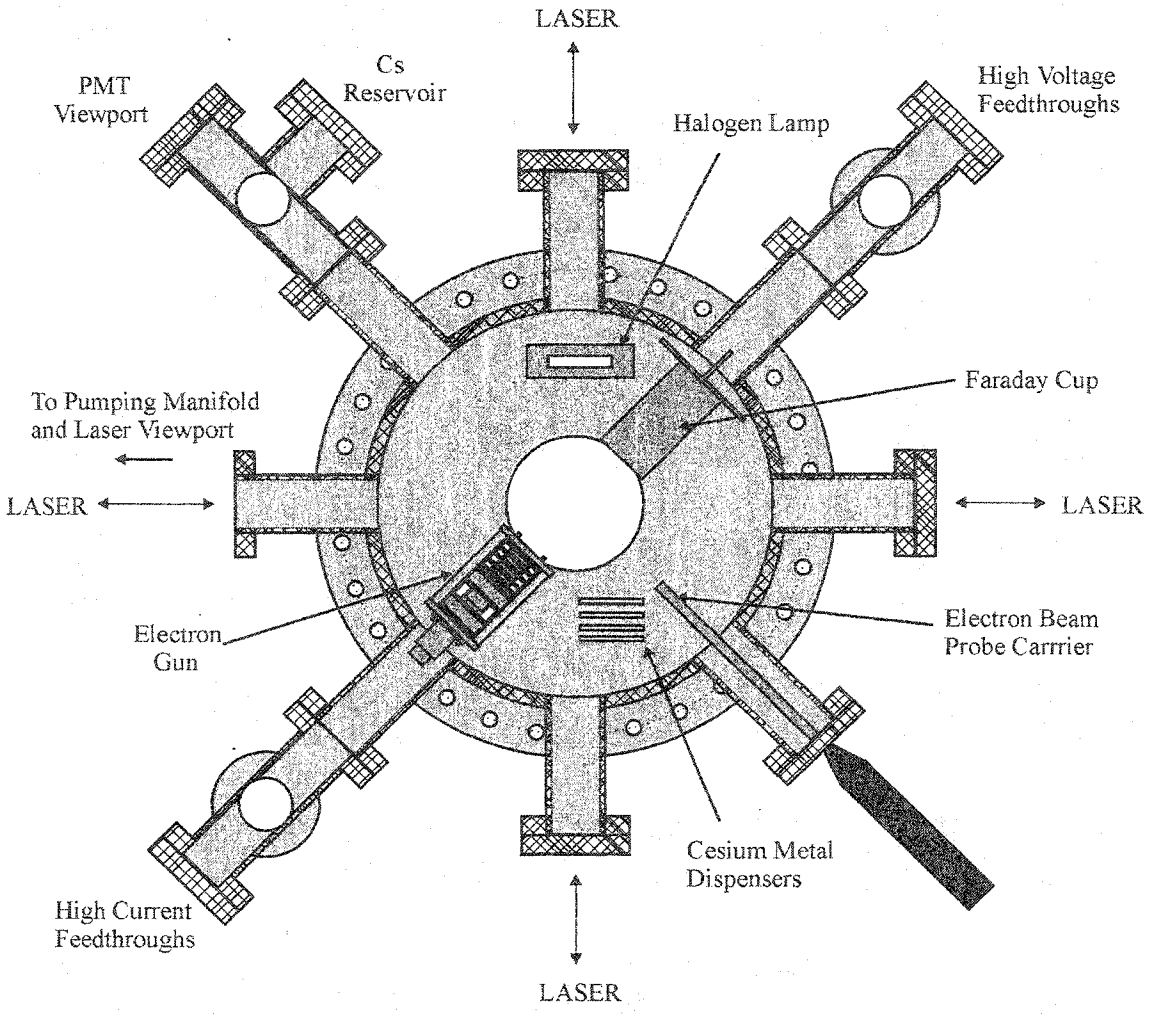

Figure 6.1: Internal layout of the 13.25" CF spool piece forming the main vacuum chamber of the second generation electron MOT system. Not shown is the third pair of laser beams, coming in and out of the page, and the internal magnetic coils.

optics pillars were ordered from ThorLabs and modified in the University of Windsor machine shop to allow the pillars to be plate mounted and to screw into the bottom flange of the 13.25" spool. The pillars were machined to accommodate the 6.00" anti-Helmholtz coils from the first generation electron MOT system that were mounted on the new system.

To help alleviate the amount of scattered light inside the vacuum system, optical viewports were sent to Applied Physics Specialties in Toronto to get broadband anti-reflection coatings centred at 852 nm. This reduced the amount of light trapped inside the system from reflections from the inner glass surfaces. To further reduce scattering inside the system, the inner surfaces were coated with colloidal graphite to try absorb the light and

minimize reflection.

An additional consequence of moving to the more sophisticated gun was that many more electrical connections were necessary. This required more electrical instrumentation feedthroughs to be mounted on the system. All internal connections were first made with ~20 AWG stainless steel wire covered with fibreglass cladding. These connections were eventually discarded in favour of a UHV ribbon cable from Accu-Glass. This ribbon cable featured 25 conductors of 30 AWG, stranded, silver-coated copper wire with a Kapton® film wrap to provide electrical insulation. The ribbon cable terminated at the feedthrough end with AMP crimped push-on connectors with Be-Au coatings to fit on the Alumel pins of the vacuum feedthrough. On the gun end of the ribbon cable, connections were made through a PEEK (poly-ether-ether-ketone) connector with gold-coated pin contacts.

The use of the ribbon cable assembly for the electrical connections inside the second generation electron MOT system provided a rugged, yet convenient means of connecting and disconnecting the gun during servicing periods. The ribbon cable and connector had a 260°C maximum temperature tolerance making it ideal for use in UHV systems. The plastic material had an extremely high temperature tolerance, and maintained a low vapour pressure of less than 10^{-10} Torr, with CO and H_2 being the primary outgassing products.

The pumping scheme was also changed in the second generation electron MOT system, to better handle the increased volume of the new chamber. A diagram of the pumping speeds for the pumps used with this system is given in Fig. 6.2. First, the diaphragm roughing pump was replaced with a 100 L/sec dry-scroll pump. This greatly reduced the time required to rough the system after exposure to atmosphere. In addition, the Starcell 20 L/sec ion pump was supplemented with a 100 L/sec Varian triode ion pump to assist with any increased outgassing of the system following isolation from the roughing and turbo pumps.

The pumping manifold was also changed in the second generation electron MOT system. The first modification involved the installation of a manual UHV gate valve to separate the main chamber and the pumping manifold. This allowed the pumping manifold or main chamber to be serviced separately while the other section remained sealed off from atmospheric contamination. All CF reducing flanges were removed and replaced with conical

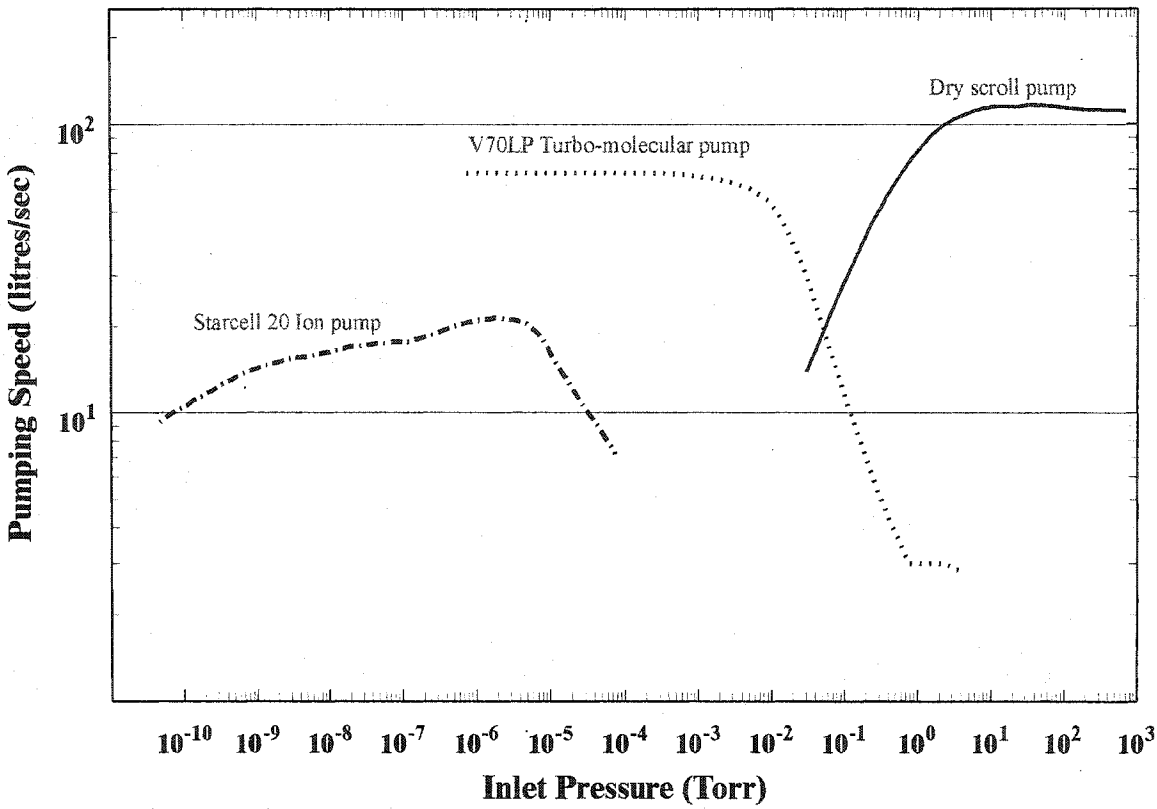

Figure 6.2: Pumping speeds for the three of the four pumps used on the second generation electron MOT system. Not shown is the pumping speed for the 100 L/sec Varian ion pump as the technical specifications for this inherited pump could not be found.

reducers to help increase conductance. Finally, one of the arms of the manifold from the first generation system was eliminated by replacing a 4-way cross with a 6-way cross. This had the effect of decreasing the total volume of the manifold and placing the pumps and gauges closer to the main chamber.

To assist with the chamber bake-outs, a 250 W halogen bulb was mounted inside the spool piece. The use of heat tapes proved to be quite inefficient in achieving high chamber temperatures with the first generation electron MOT system. The chamber was in thermal contact with the optics bench which acted as a very large heat sink. This meant that there was rapid heat dissipation due to both convection and conduction. The halogen lamp proved to be quite effective at baking out the main chamber while heating tapes were used to heat localized areas such as feedthroughs and the chamber sidearms.

One last major modification to the vacuum system was the cesium injection. The

cesium reservoir from the first generation electron MOT system was moved over to the second generation system. Shortly after the transplant, the needle valve on the bellows section failed and contaminated the main chamber with cesium metal, to the extent that large metal deposits were visible on the windows and inner surfaces of the spool piece. The entire reservoir section was replaced with a new system that incorporated dual, UHV gate valves for vacuum isolation and a 2.75" CF nipple to replace the 1.33" bellows. Since the nipple could not be bent to break the ampoule, as was done with the bellows, the entire arm was dismounted after baking, while keeping both valves closed, and the entire assembly shaken until the ampoule broke. To augment the cesium loading process, several cesium metal dispensers from SAS Getters were inserted into the chamber. The dispensers worked very well, but contained relatively small charges of cesium that were quickly spent. More importantly, the dispensers began to glow red hot when they were activated. As this radiation would be detrimental for fluorescence measurements at 852 nm, the dispensers were never used during data runs, but rather only for initial chamber loadings.

6.2 Electron Beam System

The electron beam system was completely overhauled, with the incorporation of a new electron gun, a new Faraday cup and a new electron beam probe into the second generation electron MOT system. As mentioned in the previous section, the electron gun was a home-made gun that included two deflection stages and a housing to accommodate a filament with a standard AEI base. A schematic of the gun is given in Fig. 6.3.

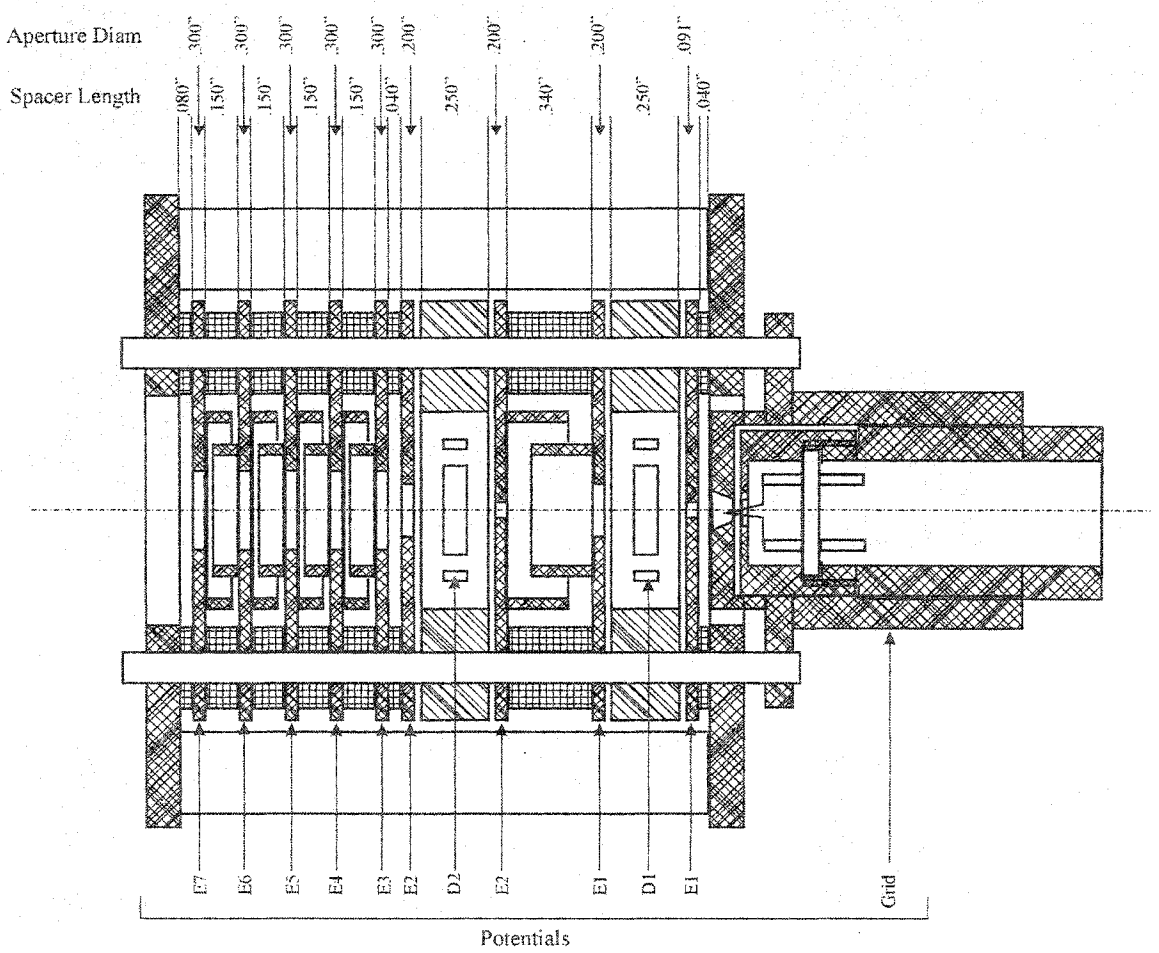

Figure 6.3: Schematic of the electron gun used in the second generation electron MOT system, The gun was designed by Dr. P. Hammond in 1986, and constructed in the University of Windsor machine shop. The deflector stages are labelled D1 and D2.The lens elements are labelled E1 through E7 beginning at the filament that is housed in the Wehnelt cylinder labelled Grid.

The gun was designed with a filament contained within a detachable Wehnelt cylinder, followed by a deflection stage, and then a diode for acceleration and primary

focussing. After the diode is another deflection stage for aligning the beam into a pentode for additional focussing, if necessary. The last element of the pentode is held at ground, to ensure that the energy of the electron beam is defined by the beam energy power supply (PS 2 in Fig. 6.4).

The electron gun was originally used with a tungsten wire filament. As mentioned earlier, the connections to the electron gun lens elements were made with stainless steel wire covered with fibreglass cladding, but later replaced with a UHV ribbon cable assembly. The lens elements were coated with aerosol graphite to prevent burn marks and charging. The new gun required a lot more control circuitry than the older TV gun from the first generation electron MOT system, due to the increased number of lenses and the two deflection stages.

The power supplies used on the electron gun in the second generation system were connected in a floating arrangement. This allowed all lens voltages to be referenced with respect to the beam energy, and allowed each of the 4-component deflector stages to be referenced from their respective lens potentials. The arrangement of these power supplies is shown in Fig. 6.4. To make the alignment process easier, a polarity reversing switch was added to each of the lens elements to quickly switch between source supplies. In addition, grounding switches were added to each of the lenses in the pentode stack.

The control circuitry for the gun was combined with all of the various signal conditioning and interfacing circuitry, and assembled into one master control unit for the experiment. All power supplies for the electron gun, Faraday cup biassing, and the magnetic coils were connected to this unit. This allowed all connections to the vacuum system to be made from one point with minimal cabling. Furthermore, all signals from the experiment were connected to this unit for conditioning and inputting to the host PC for analysis. The front panel of this unit contained all of the adjustments necessary for tuning the electron beam. This control unit provided a very compact arrangement that was rack-mountable. In addition, this unit had the advantage of being extremely flexible and providing a safer means of cabling the high voltages and currents associated with operation of the experiment.

An extensive period of time was spent performing studies of the electron beam produced with the tungsten filament. The beam quality was assessed for a variety of

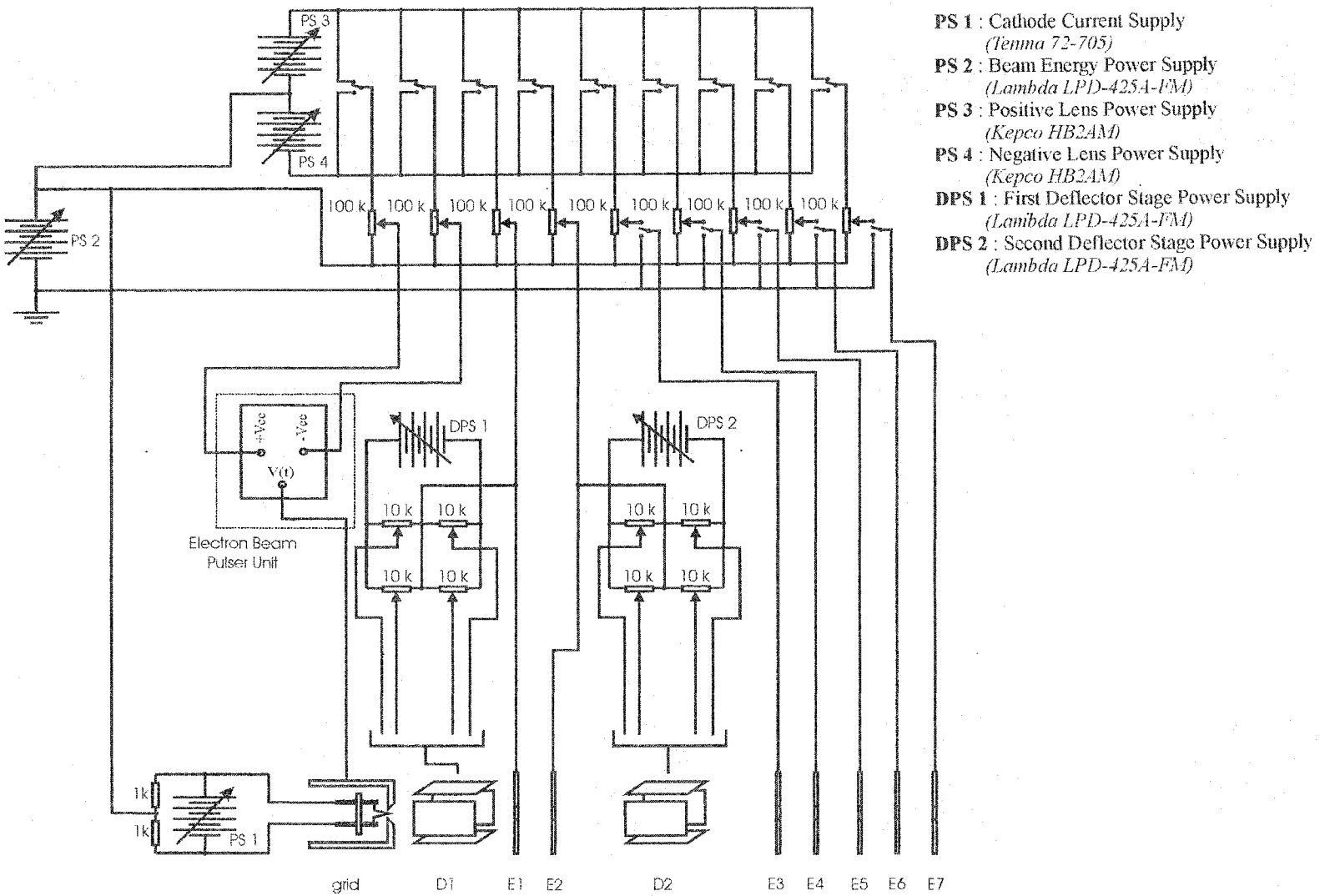

Figure 6.4: Control circuitry used on the second generation electron MOT system, showing the arrangement of power supplies. Also shown is the arrangement of the new pulsing unit.

operating conditions on the electron gun. The beam profile in Fig. 6.5a is for a focussed beam, and shows a sharply peaked beam of narrow diameter. In this particular profile, the beam appears superimposed on a relatively broad, asymmetric background, which could actually be removed from the beam by driving the Wehnelt negative with respect to cathode to suppress the stray portions of beam that gave rise to this background. The result from this

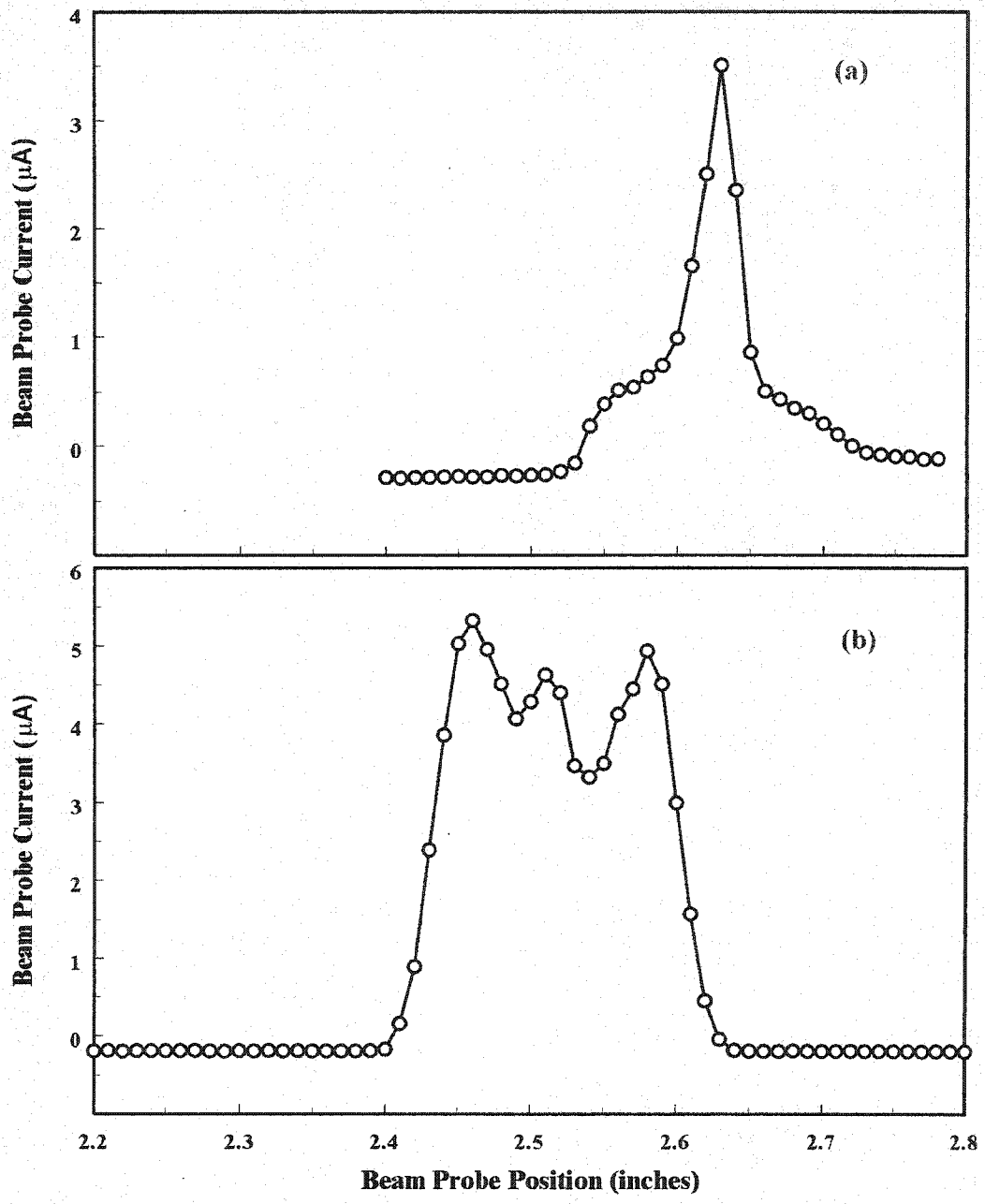

Figure 6.5: Electron beam profiles with the second generation electron MOT system using a Tungsten wire filament, for (a) a focussed beam, and (b) a defocussed beam.

suppression was a very narrow beam, with a Lorentzian profile. It must be mentioned that using the Wehnelt in this fashion greatly reduced the emission current of the gun. While this background could be removed, with relative ease, from the focussed beams, it was virtually impossible to remove when it came to defocussing the beam.

When defocussed, as depicted in Fig. 6.5b, the background gave rise to large asymmetries in the profile that made the electron beam completely unusable for scattering experiments with the MOT. This background appeared in virtually all profiles for the de-focussed beams, to varying degrees, regardless of the tuning of the gun, and the mode in which it was run. This led to the conclusion that the filament, as a line source, was emitting an elliptical, diverging beam. While this does not pose a problem for focussing, it makes de-focussing the beam impossible due to the cylindrical symmetry of the electron gun lens elements.

For this reason, the tungsten filament was replaced with a barium oxide (BaO) emitter from Kimball Physics. This cathode had a maximum emission of 3 mA and current densities up to 0.25 A/cm^2, versus a maximum emission of 50 μA and current densities of 0.05 mA/cm^2 for the older tungsten filament (these are the values quoted by Kimball Physics). Furthermore, the BaO cathode runs at a temperature of approximately 1000 K, versus 2200 K for the tungsten filament, thus the light emission from the cathode is greatly reduced. The BaO cathode was a disc emitter, giving a planar, circular geometry that gave beams of uniform current density that could easily be focussed or de-focussed. In fact, the beam from the oxide cathode could be de-focussed without the use of either deflection stage, or the pentode. A typical beam profile for the de-focussed beams from the oxide cathode is given in Fig. 6.6. The beams from the second generation system using the oxide cathode, had profiles that were virtually identical to those of the TV gun from the first generation system.

The gun was converted from DC to pulsed operation with the use of a new pulser, designed and constructed in the University of Windsor electronics workshop. This new pulser was similar in design to that in Fig 5.8, but offered a maximum pulsing amplitude of 50 V, better heat dissipation and fusing to provide more reliable operation. For use with the new gun in the second generation system, the pulser unit was used in conjunction with the

Wehnelt cylinder. To shut the beam off, the Wehnelt was pulsed ~20 - 30 V negative with respect to cathode potential. Since the pulser unit was designed for only uni-polar operation, it could not be directly referenced with respect to cathode potential. Rather, the positive and

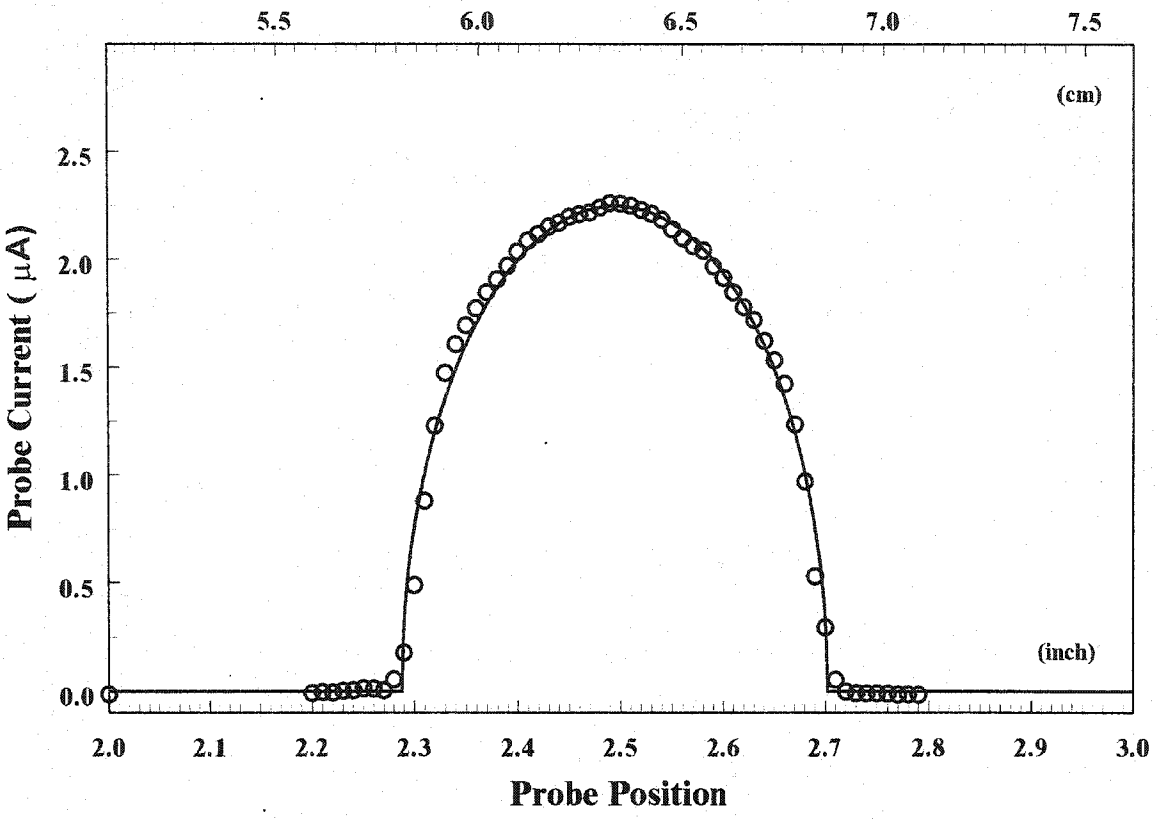

Figure 6.6: Typical electron beam profile made with the electron gun from the second generation system using the BaO cathode. The line represents the results of a calculation for the beam profile of modelled beam with constant current density. This modelling will be discussed later in Chapter 7.

negative inputs were each connected to separate pots that were wired into the positive and negative lens power supplies (PS 3 and PS 4 in Fig. 6.4), just as the electron gun lens elements were. Using this configuration, the negative input of the pulser was driven down to cathode potential minus 30 V, and the positive input of the pulser set to the desired Wehnelt voltage for DC operation. The TTL pulse to the electron gun pulser was then inverted from active high to active low.

The second generation electron MOT system also used Faraday cup current detectors, but of a different design from those of the first generation system. The Faraday cups of the

second generation system were substantially larger, as there was much more room available. The larger cups meant that a greater electron beam divergence could be accommodated. The geometry of the inner Faraday cup was also changed from a cone design to a cup design, with a depth to diameter ratio of 5:1 to minimize the loss of electrons from the inner Faraday cup due to reflection or secondary emission.

The acquisition software was overhauled to provide better statistics in the sampling of the inner and outer Faraday cups, as well as the electron beam probe. It was also modified to store the voltages settings of the electron gun for each beam profile. In addition a new software program was developed to perform the analysis of the beam profiles to determine the current density of the beam. The analysis software will be discussed in detail in Chapter 7.

6.3 Laser System and Optics

The optical systems remained largely intact during the switch from the first generation to the second generation system. The optics associated with the preparation of the laser, including the collimating lenses, opto-isolators, anamorphic prism pair (trapping laser), and cylindrical lens pair (repumping laser) were left unchanged.

The biggest change to the laser system was the incorporation of optical shutters on the lasers. These shutters were installed so that the AOM's were not necessary for gating the lasers. The shutters provided a slower means of switching the lasers off, than with the AOM's, however up to twice the laser power could be transferred to the MOT without the use of the AOM's. The AOM was completely removed from the repumping laser system as there was no need for any frequency shifting or stabilization. The repumping laser remained stable against long-term thermal drift, and the repumping laser was tuned manually to resonance with the $6^2S_{1/2}$ ($F = 3$) to $6^2P_{3/2}$ ($F' = 4$). The repumping laser would stay on-resonance with the repumping transition for several hours, after a sufficient warm-up period, without requiring any adjustment.

The saturated absorption spectroscopy for the trapping laser was also overhauled in the second generation system. The AOM for the trapping laser was moved from the MOT beam to the saturated absorption spectroscopy system. The layout of the absorption spectroscopy system was rearranged to look like that of the repumping laser as depicted in Fig. 5.18. In addition, the vapour cell and photodiode were separated by a much larger distance to give a better overlap between the pump and probe beams within the vapour cell. Finally, the power was minimized on the portion of the beam being split from the primary trapping beam to be diverted to the saturated absorption spectroscopy.

The trapping laser's hyperfine spectrum from the first generation system, shown in Fig 5.17, had one major deficiency. The frequency resolution was not sufficient to resolve the difference in frequency between the ($F \leftarrow 4$) transition and the ($F \leftarrow 3, 5$) cross-over. The frequency resolution necessary to resolve these hyperfine structures is of the order of half the natural linewidth of the trapping transition. There were two problems with the original set-up

for the trapping laser's saturated absorption spectroscopy from the first generation system. The first problem was the geometry of the pump and probe beams. There was insufficient overlap between the two beams to remove the Doppler broadening completely. Essentially, the probe beam travelled a substantial distance through the vapour cell without the presence of the pump beam, thereby allowing the probe beam to become slightly doppler-broadened. The second problem with the saturated absorption spectroscopy was the input power was too high with the incident beam used to form the pump and probe beams. This allowed for a substantial amount of power broadening [METCA 99]of the hyperfine transitions.

After these problems were addressed with the second generation system, the hyperfine spectrum of the trapping laser was sufficiently well resolved in frequency to allow the ($F \leftarrow 4$) transition and the ($F \leftarrow 3, 5$) cross-over to be clearly distinguished, as shown in

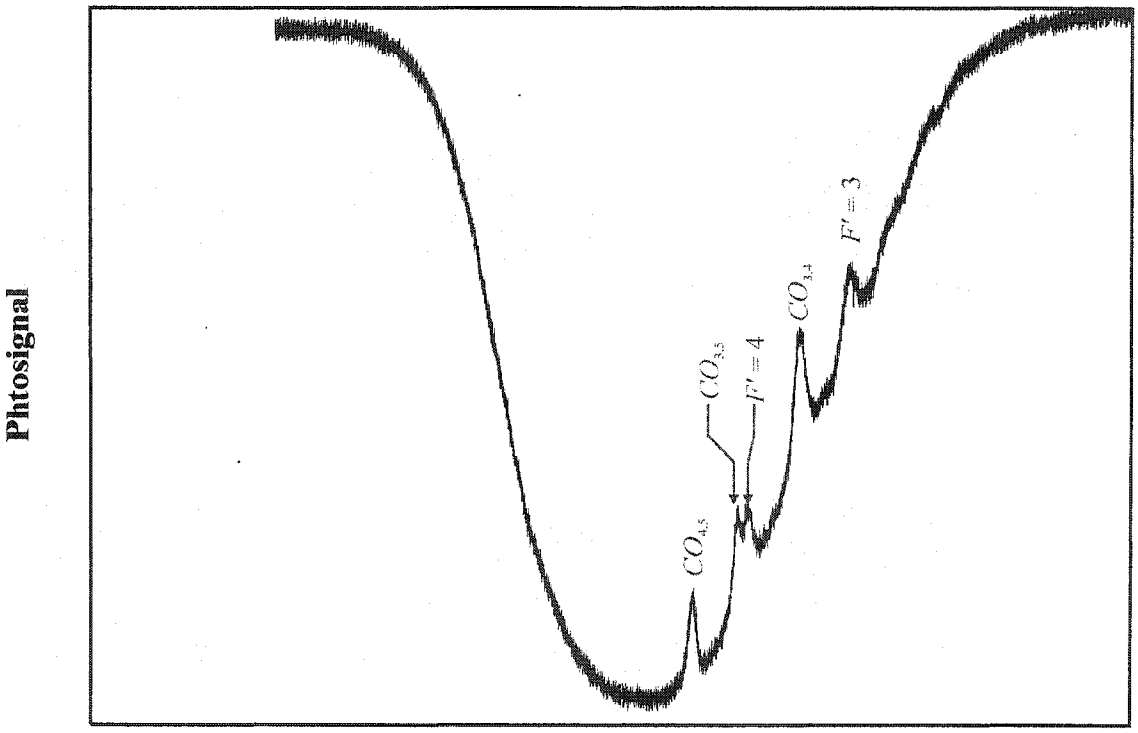

Figure 6.7: Hyperfine spectrum for the $6^2S_{1/2}$ ($F = 4$) ground state using saturated absorption spectroscopy. The spectrum was made with a low incident power on pump and probe beams from the trapping laser. The $F' = 5$ transition is barely visible due to the low power, but the frequency resolution is high enough to fully resolve the central cross over and $F' = 4$ transition.

Fig. 6.7.

There was a slight change made to the optical arrangement of the PMT system. The increase in chamber diameter meant the PMT optics had to be moved farther away from the trap. This was rectified by increasing the focal length of the lens, and moving the PMT back slightly to accommodate the increased image distance. The optical layout on the PMT for the second generation had a magnification that was slightly less than unity, typically 0.70 to 0.75. In order to move the PMT back farther, an extension had to be mounted on the optics bench. A 0.75" thick aluminum plate was bolted to the optics bench and the PMT secured to it using 1" optics pillars from Thor Labs. An enclosure was built on this aluminum plate, that was then wrapped with black laser cloth to provide a black box for the PMT. The components for the enclosure were also supplied by Thor Labs.

6.4 Magnetic Fields

The 6" anti-Helmholtz magnetic coils from the first generation system were used with the second generation system initially. The MOT was successfully operated with these coils but it was found that the decay time for the magnetic field was considerably longer with the second generation system. The decay time was determined by the response of the MOT following the magnetic coils switching off. In addition, the response of the electron beam could also be used to ascertain the decay time of the trapping coils. In most cases, the electron beam suffered a 6 - 8 msec delay in reaching the Faraday cups while the magnetic coils were pulsing. This delay time disappeared when the magnetic field was completely removed.

The high-power pulser unit for the coils was capable of sub-millisecond decay times, which were dramatically less than those observed with the coils running on the second generation system. This was attributed to the generation of eddy currents within the chamber walls. There was a considerable increase in the amount of stainless steel between the trapping coils, in transferring from the first generation to second generation systems. The extra material producing larger currents that need longer times to subside. There were very few options available to remove the eddy currents. One option, presented in [DEDMA 01], was to implement a current feedback amplifier. This amplifier would have the effect of reversing current flow in the coils to attempt to damp out the eddy currents. The second option available was to use smaller coils.

The current feedback option required more circuitry to be implemented and left room for more problems to arise with the experimental arrangement. It may also have generated extra noise in the experimental arrangement due to the rapid switching of large currents. Weighing this with the possibility that the current feedback may not be completely successful in removing the eddy currents, led to the decision to install smaller coils on the system. However to reduce the size of the coils at all, would require the coils to go inside the vacuum chamber.

There were issues that had to be addressed during the design stages. First of all the

coils would have to UHV compatible, and due to the proximity of the coils with the halogen lamp, capable of temperatures of greater than 200 °C. Secondly, the power consumption of the coils would have to be minimized to try avoid heating the background Cs vapour. The geometry of the coils and coil mounting would have to be addressed as well. There were 3 mutually orthogonal, laser beam pairs each ~19 mm in diameter, 1 electron beam measuring up to 25 mm, at 45° to the two horizontal laser beam pairs, and one electron beam probe that all needed access to the trapping region without obstruction.

The design plans for the inner coils are shown in Fig. 6.8. The coils were 6 cm in diameter and were constructed with 44 turns each of 24 AWG Kapton-wrapped wire. The original designs were for 18 - 20 AWG wire, but the only available sizes for Kapton-wrapped wire, in stock without custom ordering, was 24 AWG or 30 AWG wire in 10 m lengths. Using the smaller wire increased the power consumption slightly by requiring a higher voltage to get the same current flow in the coils. The field gradients in the trapping region were virtually identical to those of the 6" external coils. However, the field strength of the internal coils could not be increased to get the higher gradients produced by the external coils, as the heat generated by the coils would cause substantial pressure increases due to the increased coil temperature. There was also the risk of burning out the coils at these higher fields since the coil resistance begins to increase with temperature, more heat is generated which in turn raises the temperature of the coils and raising the resistance in the process. The optimum coil current versus heat dissipation can be assessed from the chamber pressure. The coil current can be increased so long as the pressure remains fixed.

There was one additional problem that was found with the external coils in use on the second generation electron MOT system. The position of the trapped atoms was approximately 4 - 6 mm out of the horizontal plane. This made overlap with the electron beam almost impossible and indicated that there was a severe problem with the existing experimental arrangement. It was found that the bottom 13.25" flange was magnetized. A small magnet would stick to the flange surface in a few locations. The flange was made from grade 304 stainless steel, which is supposed to be non-magnetic. However there may have been a problem with the machining process used to produce the flange, such as not ensuring

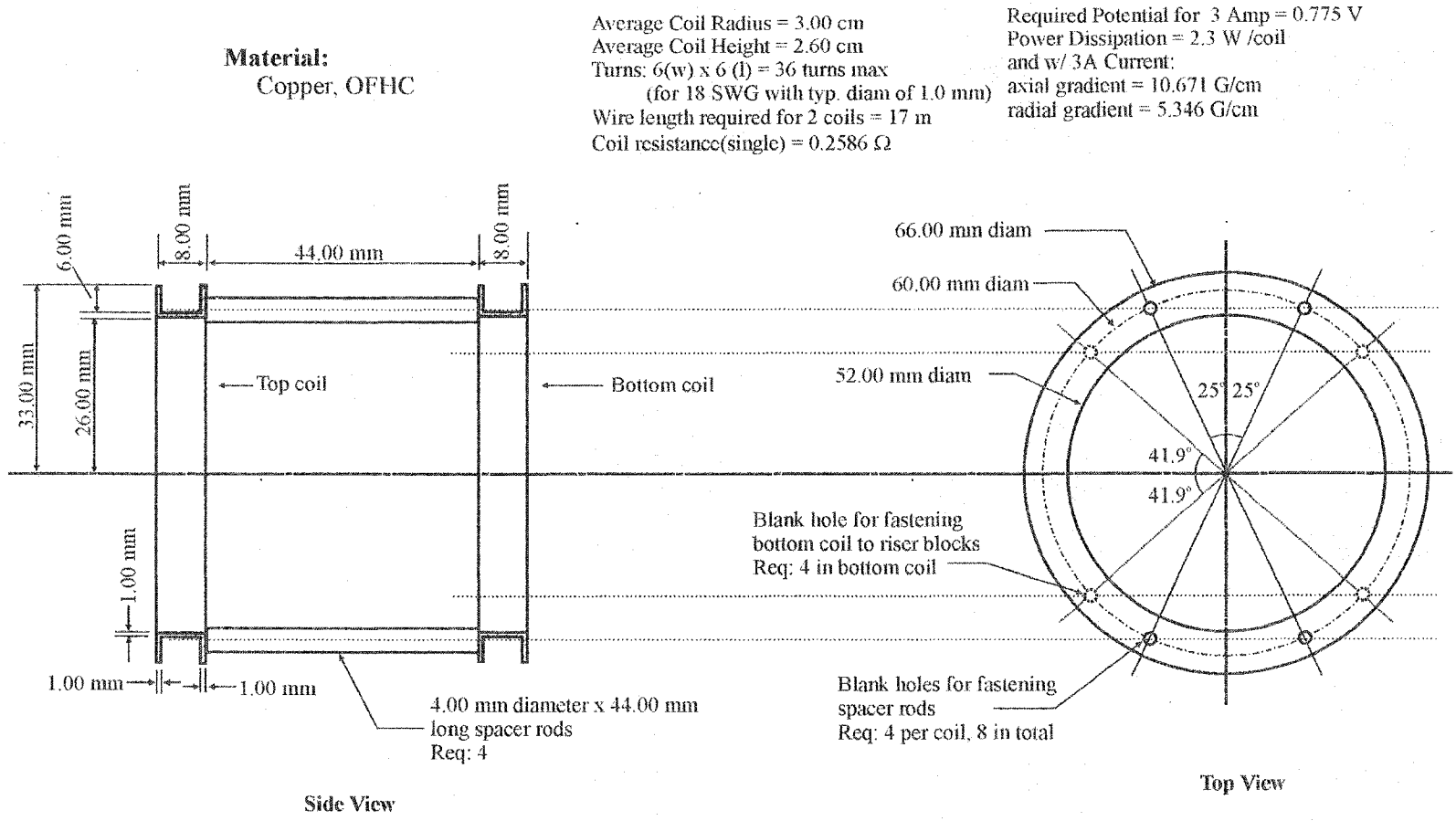

Figure 6.8: Design plans for the internal anti-Helmholtz coils that were used in the second generation system. The coils were mounted centrally within the 13.25" spool piece, with the coil axis vertical.

a cold-working process to prevent the formation of magnetic domains.

To remedy this, a custom order for a new 13.25" CF flange was sent to Torrovap. The new flange was to be cold worked, 316 LN to reduce any possibility of magnetization from occurring. This replacement flange also had to be machined to provide the necessary screw

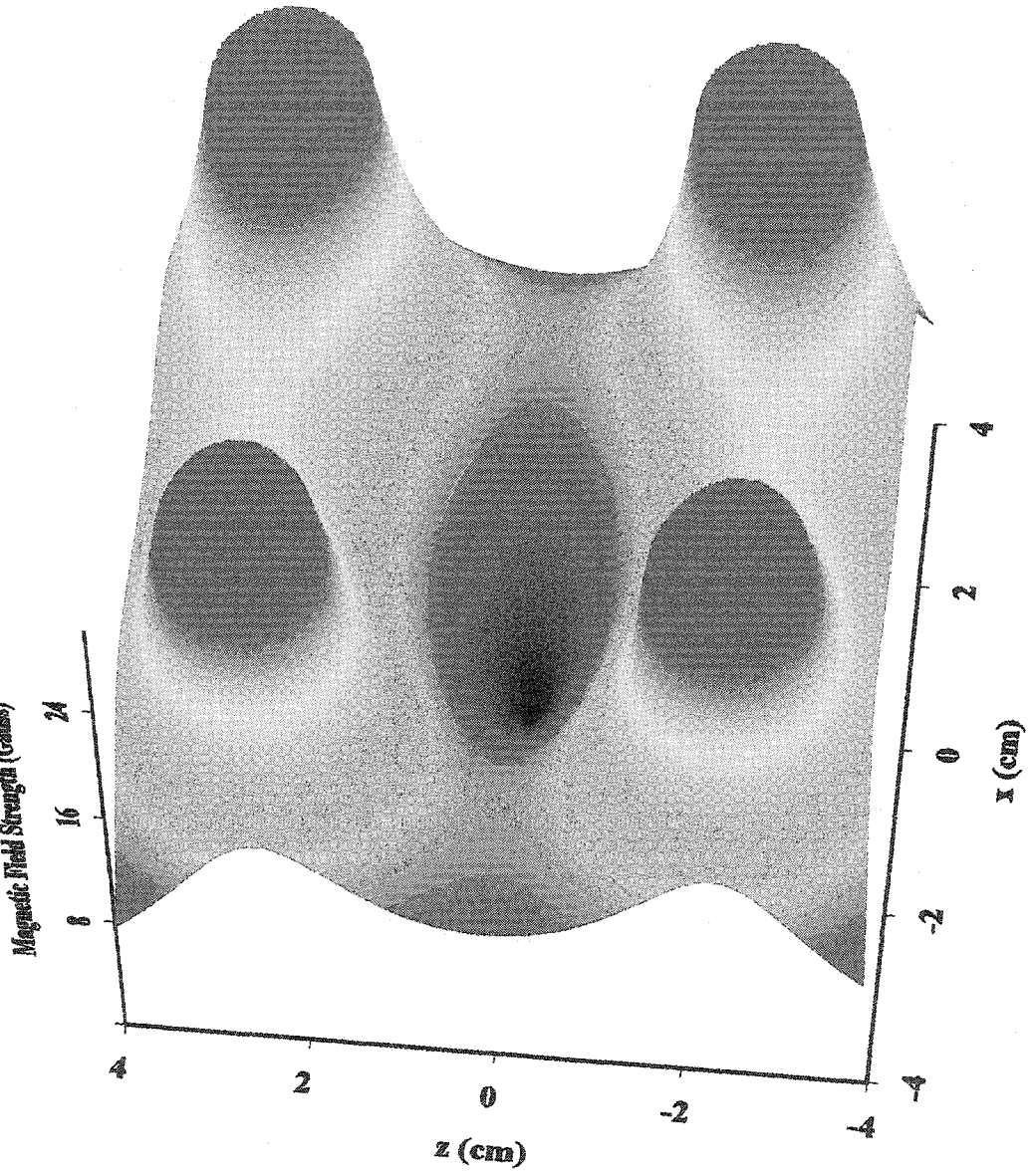

Figure 6.9: Contours of the spherical quadrupole magnetic field generated by the anti-Helmholtz coils used in the second generation electron MOT system. The coil axis is along z. The coil radius is 3.0 cm and the coil separation is 4.4 cm.

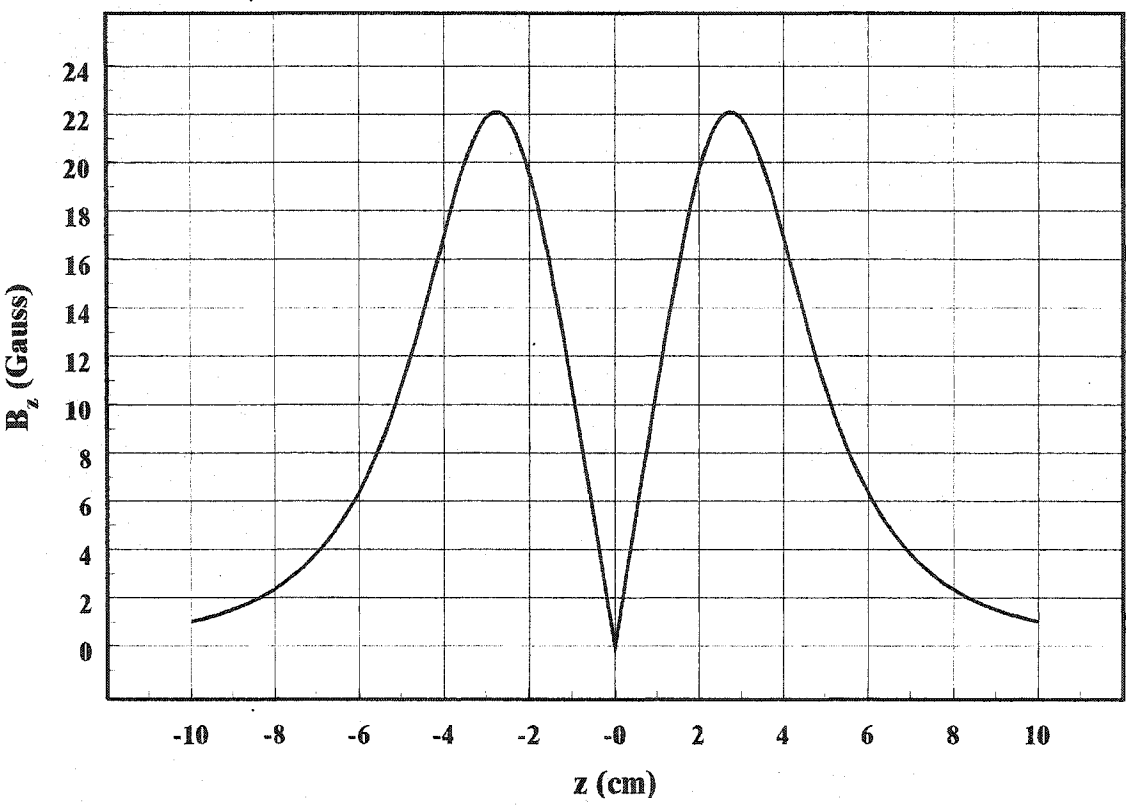

Figure 6.10: Axial field for the anti-Helmholtz coils used in the second generation electron MOT system. From the graph it is clear that the field gradient is constant at 10 G/cm over the trapping region.

holes for mounting the chamber onto the pillar supports, and also to mount the internal components for the electron beam, the magnetic coils, halogen lamp, etc. Although the replacement flange was less magnetic than the original, localized magnetic regions within the flange could be identified with the use of a very strong magnet, but the strength was comparable to other components in use with the system. After the replacement flange was installed, and the MOT was functioning, the MOT appeared on the correct location for establishing overlap with the electron beam.

6.5 Experiment Control and Data Acquisition

The photomultiplier system was modified during the change from the first generation to second generation systems. The PMT operation was converted from photon counting to analog. The signal output of the PMT was taken across a 1 MΩ resistor and sent directly into a differential analog input of the PCI 6025E National Instruments data acquisition card. The analog operation of the PMT allowed for better statistics to be obtained from the fluorescence decays, as electronics for the photon-counting operation were limited by precision, acquisition speed, and saturation of the photosignal.

The use of the PCI-6025E acquisition card to replace the NIM-based ADC and the Quantum8 MCS turned out to be a significant improvement over the previous acquisition setup of the first generation system. The fluorescence scans could be made with up to twenty times the sampling rate of the previous arrangement, to give much more information for the fluorescence decay. Due to the analog operation, the statistics after a few hundred sweeps with the second generation system were comparable to that of the first generation system after several thousand sweeps. Due to the increased sampling times of the second generation system, there was also a greater reliability of the results. Since the collection times were significantly shorter, there were less fluctuations, such as drifts in electron beam current, laser stabilization, laser frequency, etc., that could affect the results.

The second generation system also had the mass spectrometer interfaced to the PCI 6025E acquisition card. This allowed mass spectra, such as that shown in Fig. 6.11 of the system to be quickly recorded and proved to be quite useful during leak testing. With the first generation system, mass spectra were recorded manually with partial pressures recorded at 0.5 u increments in the range of 0.0 - 60.0 u. This was a time consuming process that didn't provide a continuous spectra. With the mass spectrometer interfaced to the computer, a continuous spectrum covering the entire operable mass range of 0.0 - 100.0 u could be recorded in 10 seconds.

The mass spectrometer was easily interfaced to the PCI 6025E acquisition card. The mass spectrometer was designed for use with an external XY plotter, with a voltage ramp

from 0 to 8 V corresponding to the mass scale 0.0 to 100.0 u., and a 0 to 10 V signal for the partial pressure. These two voltages were sent directly to two separate referenced, single-ended analog inputs of the PCI 6025E acquisition card. A LabView software was written to provide an on-screen display of the mass spectrum, and to dump it to an ASCII file. A mass spectrum that was made during a bake-out following a servicing is shown in Fig. 6.12.

In addition to interfacing the mass spectrometer, the ion pump and ion gauge were interfaced to the computer, to provide an additional means of monitoring the pressure. The ion gauge pressure was read from the back of the KJL 4400 gauge controller as a voltage in the range 0 to 10 V, that was fed directly to the PCI 6025E card. The voltage was outputted directly from the electrometer, and converted to a pressure, with a logarithmic conversion factor of 1 V/decade. The pressure read by the computer was also calibrated to correspond to the pressure indicated on the gauge controller. The ion pump pressure was read from the

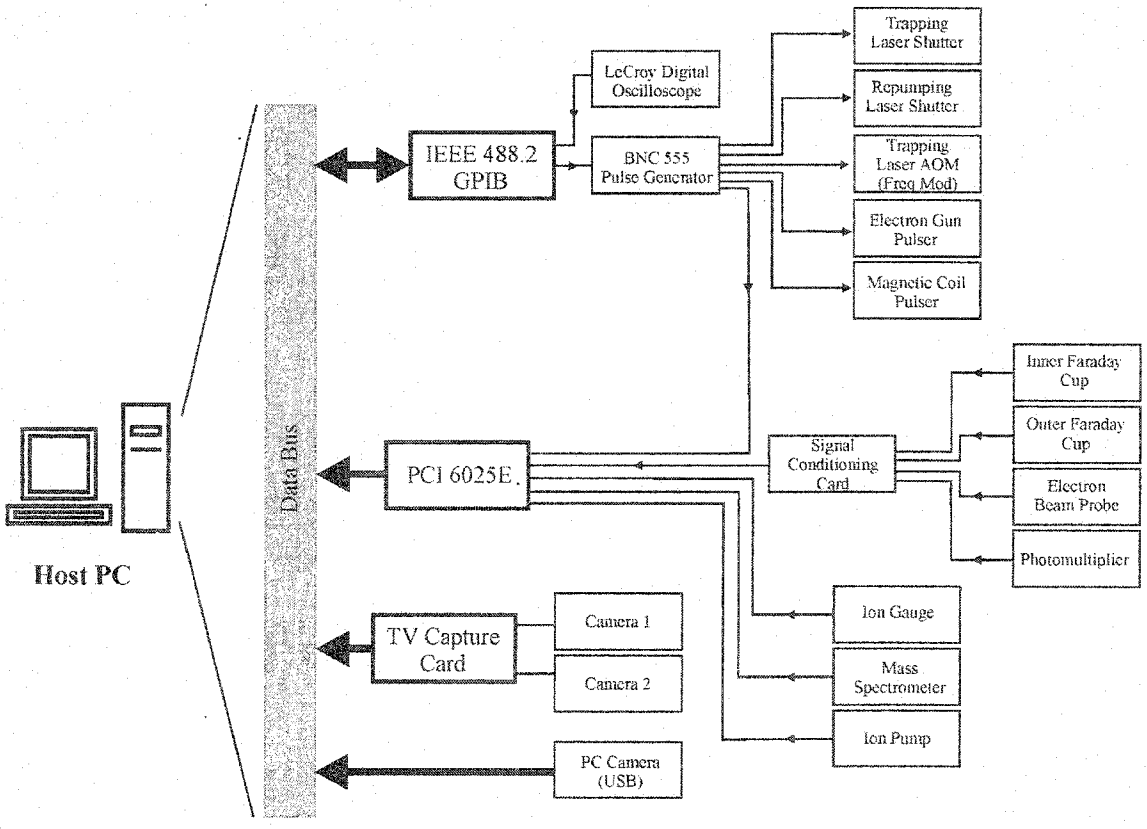

Figure 6.11: Block diagram of the experimental control and data acquisition system used with the second generation electron MOT system. All signals were directly recorded by the host PC.

front end of the ion pump controller as a voltage. The voltage was the fed directly to the PCI 6025E, then converted to a current using the fact that the voltage output of the controller is 1000 times the ion current. This ion current is then converted to a pressure using the calibration curve given earlier in Fig. 5.3.

The BNC 555 digital delay generator was interfaced to the host PC with an IEEE interface. The interface allowed for all parameters of the internal timebase and the individual channel settings to be programmed remotely by the host PC. The internal timebase was configured for continuous pulsing as opposed to the burst operation with the first generation system. This meant the BNC 555 could operate in a stand-alone mode without the need for external arming or triggering pulses. In fact, the BNC 555 was used to trigger the PCI 6025E to begin sweep acquisitions.

A single LabView software was developed to control the experiment and perform the data acquisition. This software was responsible for changing all of the timing for the

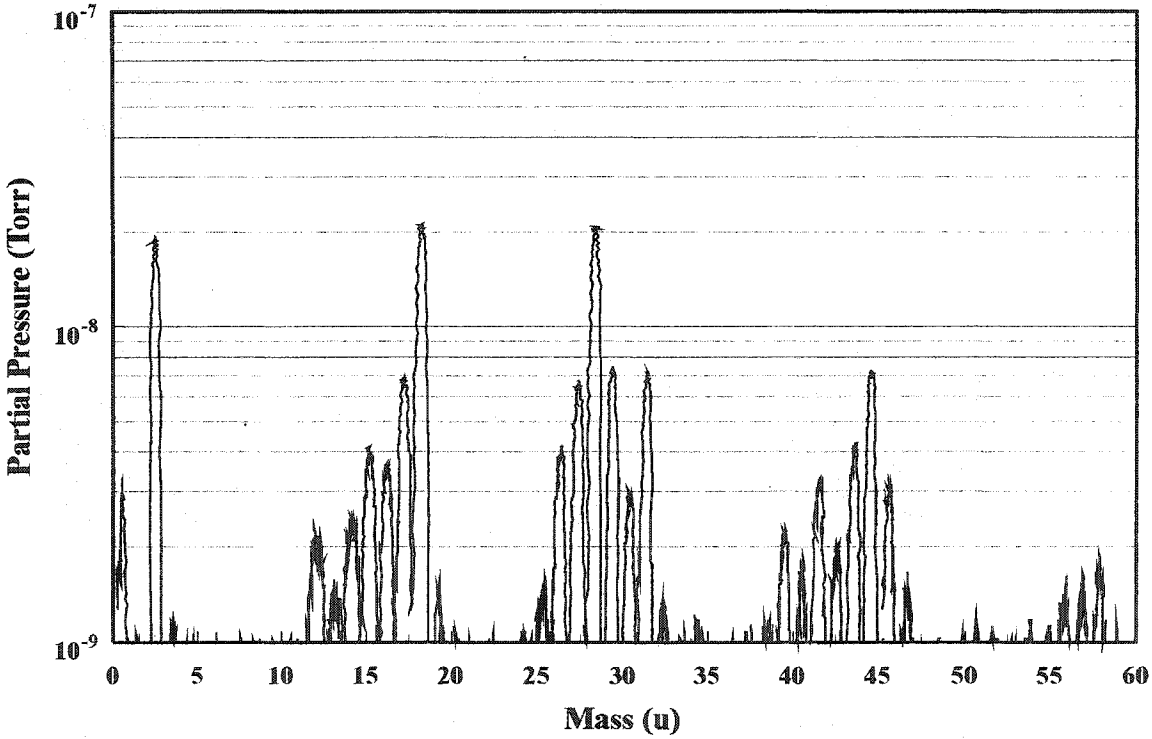

Figure 6.12: A mass spectrum for the vacuum system of the second generation electron MOT system made with the use of the PCI 6025E acquisition card. The mass spectrum was taken while the system was undergoing a bake-out.

experiment. It also performed the multichannel scaling of the trap fluorescence, the inner and outer Faraday cups, and up to two other devices if necessary. As the multichannel scaling was entirely software based, the sampling rate, signal level, and number of channels were controlled by the computer. This software also performed the electron beam profiling. For each beam profile, all of the gun voltages, floating and with respect to ground, were stored to file with all of the beam profile data, including currents from the beam probe, inner, and outer Faraday cups. For each fluorescence run, two separate data files were stored to disk. The first file contained all of the timing information for each channel of the BNC 555, as well as all of the settings for the multichannel scaling. The second file contained all of the data from the multichannel scaling. This included the digitized fluorescence, and the Faraday cup currents. Each of these signals were measured and stored for trap-off periods with the electron beam present and absent.

CHAPTER 7. RESULTS

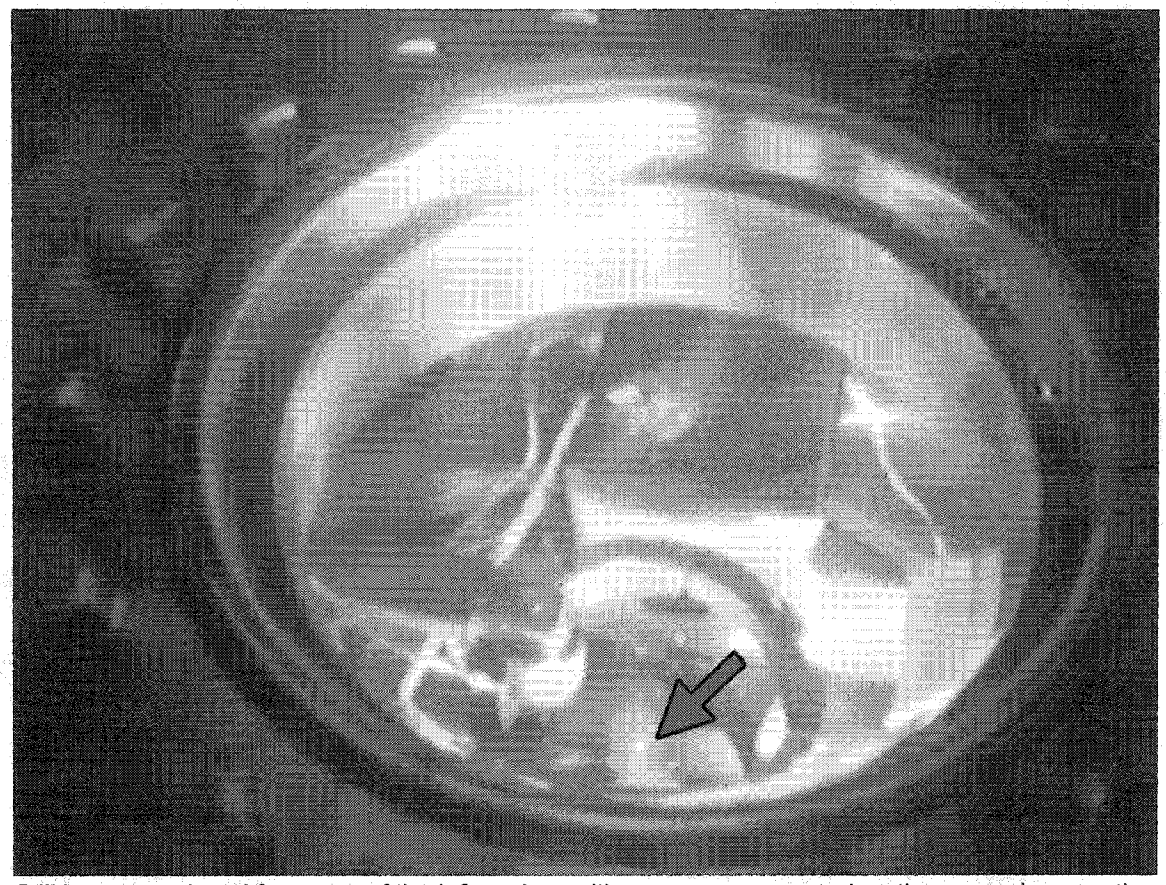

Still image produced from one of the infrared sensitive cameras mounted on the second generation electron MOT system, during operation. The bright spot, indicated by the arrow, is the cloud of trapped atoms.

7.1 Current Density

The first quantity that must be determined for the measurement of a cross section is the current density of the electron beam. During data collection, the beam energy is adjusted to the desired value, and the lenses of the gun adjusted to give a broad, symmetric beam profile. Once adjusted to give the desired profile, the electron gun remains in that state for the duration of the data collection at that energy, with periodic checks to ensure the beam has remained intact.

We will consider the simple experimental setup illustrated in Fig. 7.1. The three current detectors, the outer Faraday cup, inner Faraday cup, and thin wire beam probe record all the information necessary for ascertaining the current density of the electron beam. We make the following definitions for the individual current measurements

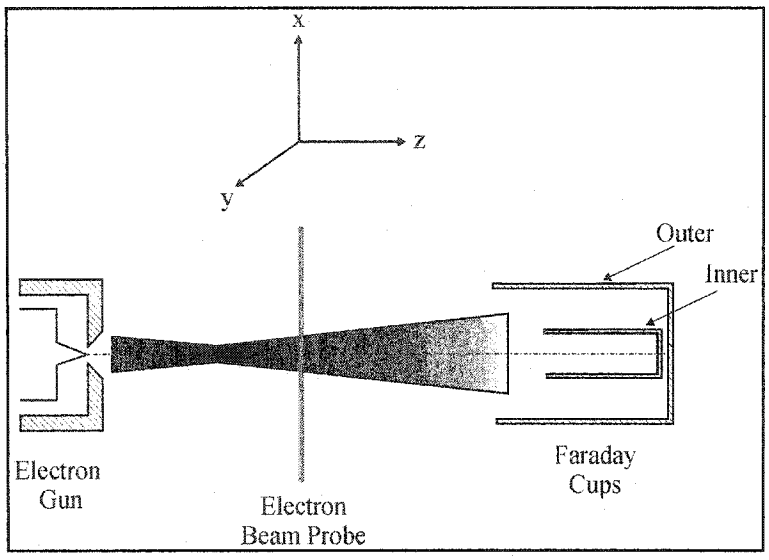

Figure 7.1: Simplified electron beam arrangement

I_O = Outer Faraday cup current

I_I = Inner Faraday cup current

$i_n = n^{th}$ probe wire current reading at probe position y_n, as measured on translational stage

An electron beam carrying a current, I, with a cross sectional current distribution described by a two-dimensional current density function, $J(x,y)$, has the following property

$$\int_A J(x,y)\mathrm{d}A = I \tag{7.1}$$

For a parallel, collimated beam, the current density function is independent of position along the propagation axis. However, if the beam possesses some divergence or convergence, then the current density function varies along the propagation axis. Despite the changing current density along the beam axis, the total beam current remains constant.

If we assume that the entire beam is incident on the Faraday cups, and there is no net secondary emission out of the cups, then the total beam current is simply the sum of the individual Faraday cup currents

$$I = I_O + I_I \tag{7.2}$$

We now consider the current density of the beam at the probe, that is the current density in the plane perpendicular the propagation axis, and positioned at the probe. We relate the two-dimensional current density to the Faraday cup currents, and extend the region of integration to include all space.

$$\int_{-\infty}^{\infty}\int_{-\infty}^{\infty} J(x,y)\mathrm{d}y\mathrm{d}x = I_O + I_I \tag{7.3}$$

Moving the wire probe through the beam with small position increments gives a one-dimensional beam profile, or current distribution, as illustrated in Fig. 6.6. An alternative method to finding the total beam current is to make the probe position increment equal to the probe wire diameter. In doing so, the sum of the beam probe currents will give an estimation of the total beam current

$$\sum_n i_n \propto I = I_O + I_I \tag{7.4}$$

In the ideal case, where there is no secondary emission from the probe wire, while immersed in the electron beam, the proportionality constant in the above relation is unity. However, in most cases there are significant amounts of secondary emission from the probe, which is dependent on the probe material and the beam energy [BAGLI 00], as depicted in Fig. 7.2.

Consequently it is necessary to rescale the profile so that the summed probe currents, (for probe steps equal to the probe diameter) equal the total beam current as measured by the Faraday cups. This profile rescaling is achieved by applying the transformation

$$i_n \rightarrow i'_n = i_n \left(\frac{I}{\sum_n i_n} \right) \quad . \tag{7.5}$$

The basis for this transformation lies in the fact that the beam profile is easily converted into a probability distribution that can be normalized to the total beam current. The departure of the scaling parameter from unity can be used to give a measure of the secondary emission current from the probe wire. (i.e., the net loss of electrons from the probe wire, per impacting electron).

Prior to rescaling the profile, it is necessary to remove the background current, if any is present, from the profile. For this reason all of the beam profile contain several points

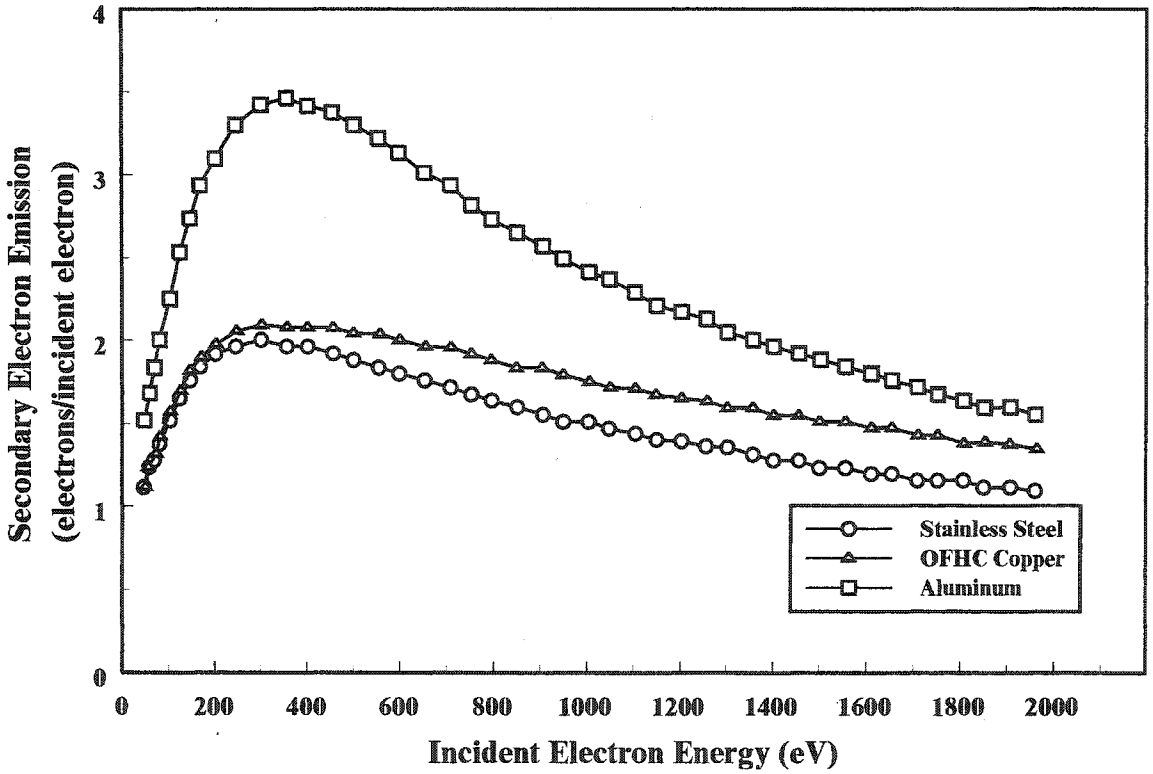

Figure 7.2: Secondary electron yields for 304 stainless steel, OFHC copper, and aluminum for the energy range 0 to 2keV.

outside of the main beam. This is to determine the amount of background current present, as well as its spatial dependence. There are several mechanisms that can give rise to this background current, including ion production, ion bombardment, secondary electron emission, and space charge effects. So long as the background current is small in comparison with the beam current, we can be certain that removing it from the profile will have a negligible effect on the calculated current density.

So far we have dealt with the preparation of the one-dimensional beam profile for purposes of determining a beam's current density. Now we will proceed with the calculation of the current density. By placing a thin wire probe in the beam, and measuring the current from the wire, we have effectively performed a line integration of the two-dimensional surface representing the current distributed within the beam. We will assume the beam's cross section is circular and that the thin wire probe is infinitesimally small with respect to the beam dimension. An individual probe current reading is related to the current density function by

$$\frac{i_n'}{\mathrm{d}y_n} = \int_{-\alpha}^{+\alpha} J(x, y_n)\mathrm{d}x; \quad \alpha = \sqrt{r^2 - y_n^2} \quad . \tag{7.6}$$

This is an ideal assumption in that it fails to take into account the physical size of the wire. To treat the case of a finite thickness wire with diameter d, we must assume that the current density in the beam is not changing dramatically over the wire thickness, in which case we may state

$$i_n' = \left[\int_{-\alpha}^{+\alpha} J(x, y_n)\mathrm{d}x\right] d \quad . \tag{7.7}$$

So that dividing the probe currents of the beam profile by the probe thickness gives the line integrated current density.

The studies performed with both the first and second generation electron MOT systems, suggest that there are two special cases of current density that are well suited for

describing the electron beams that were used. The first case is for a tightly focussed beam, where the current density is gaussian. The second case is for a broad, symmetric beam, where the current density is best described by a constant.

For the focussed beams, we assign a two-dimensional Gaussian function for the current density

$$J(x,y_n) = J_0 \exp\left[-a\left(x^2 + (y_n - c)^2\right)\right] \tag{7.8}$$

where a is a scale factor for the gaussian, J_0 is the amplitude, and we have introduced the quantity c to denote the centre position as measured on the scale of the micrometer drive of the linear motion feedthrough. Inserting this equation into Eq. 7.7, we find that the line integral of Eq. 7.8 is

$$\int_{-\alpha}^{+\alpha} J_0 \exp\left[-\left(x^2 + (y_n - c)^2\right)\right]dx = J_0\sqrt{\frac{\pi}{a}}\,\mathrm{erf}\left[\sqrt{a}\sqrt{r^2 - (y_n - c)^2}\right]\exp\left[-a(y_n - c)^2\right] \tag{7.9}$$

where we have introduced the quantity r to represent the radius of the electron beam, and erf is the error function. We have also made the following transformation of the integration limits

$$\alpha = \sqrt{r^2 - (y_n - c)^2} \tag{7.10}$$

to take into account the translational shift introduced by the quantity c, of Eq. 7.8. The relation in Eq. 7.9 can now be inserted into the right hand side of Eq 7.7 to provide a relation between the probe current and the current density

$$\frac{i_n'}{d} = J_0\sqrt{\frac{\pi}{a}}\,\mathrm{erf}\left[\sqrt{a}\sqrt{r^2 - (y_n - c)^2}\right]\exp\left[-a(y_n - c)^2\right] \tag{7.11}$$

We now have a means of relating the transformed probe currents of the beam profile with the current density using the four quantities, J_0, a, r, and c. There is one difficulty associated with the relationship in Eq. 7.11. We are ultimately interested in fitting some model function

such as that in Eq. 7.11 to the beam profile to provide a best estimate for the current density. The relation in Eq. 7.11 cannot be fitted using any linear least-squares method. A Marquardt-Levenberg nonlinear least-squares fitting algorithm [MARQU 63] was explored to help perform the fitting of Eq. 7.11. In order for the Marquardt-Levenberg algorithm to give a successful, best estimate of the current density parameters an iterative process must be employed to perform the optimization. However, the iteration will usually increase the parameter values, r and c, to the point where they extend beyond the boundaries for the physical beam. In this case, the result of the algorithm quickly diverges and the algorithm fails completely, or returns values that are clearly erroneous.

This left only one option, to fit the model of Eq. 7.11 manually to the beam profile. This was a time consuming process that required trying to manually optimize four parameters to provide the best fit. As it was a manual fit, there was an increased chance of error in the calculated current density. For this reason, the systematic error associated with the current density was maximized to take into account the inconsistencies of manual fitting. This provided an additional motivation to work with broadened, de-focussed electron beams.

The current density of a focussed beam is much more difficult to calculate, has a very strong spatial dependence, and limits the interaction time with the MOT during its thermal expansion and gravitational free-fall. Furthermore, the use of a focussed beam required the assignment of an arbitrary overlap factor in the collision cross section calculation to describe the overlap of the electron beam with the MOT at different times. This makes the calculation of the collision cross section much more intensive, assuming it is even possible.

During the work with the modelling of the focussed beams, it was found that as the electron beam was increased in size, the beam was modelled best by a constant current density. The broadened electron beams could be fit with the gaussian model by setting the scale factor a, close to zero. The broader the beam became, the closer a had to be set to zero, and the gaussian more closely resembles a constant function. This led to the use of a constant to describe the current density, which proved to be quite successful.

For the broad, defocussed beams, we make the following assignment for the current density

$$J(x, y_n) = J_0 \tag{7.12}$$

Performing the line integration to relate to the probe current yields

$$\int_{-\alpha}^{+\alpha} J(x, y_n)\mathrm{d}x = \int_{-\alpha}^{+\alpha} J_0 \mathrm{d}x = 2J_0\sqrt{r^2 - (y_n - c)^2} \tag{7.13}$$

where we have used the same definition for α as before in Eq. 7.10. This gives the following relation between the probe currents and the current density

$$\frac{i_n'}{d} = 2J_0\sqrt{r^2 - (y_n - c)^2} \tag{7.14}$$

which at first glance, has a more compact and simpler form than that of the gaussian fit in Eq. 7.11. As a check, we should be able to integrate Eq. 7.14 over the y-dimension of the electron beam and get the total beam current. To perform the integration we replace the probe thickness, d, by the differential $\mathrm{d}y_n$. For the right-hand side of Eq. 7.14, we find

$$\int_{c-r}^{c+r} 2J_0\sqrt{r^2 - (y_n - c)^2}\,\mathrm{d}y_n = J_0(\pi r^2) \tag{7.15}$$

The left-hand side of Eq. 7.14 is obviously the total beam current divided by the probe diameter, so that

$$I = (J_0)(\pi r^2) \tag{7.16}$$

Which we would expect for a constant current density. The current density should be the total beam current divided by the beam's cross sectional area.

The constant current density modelling of the electron beam provided a much simpler analysis of the beam profile than the gaussian current density modelling. However, the function in Eq. 7.14 that is used to relate the probe currents with the current density still cannot be treated with a linear least-squares analysis, evident from the fact that there are three parameters that need to be optimized. An attempt to perform a linear least-squares fit

yields a redundant set of differential equations. The iterative approach of the Marquardt-Levenberg nonlinear least-squares method for the constant current density model would run into the same problem as with the gaussian model. Namely, if the algorithm approaches the beam boundary, the algorithm fails.

All of the results obtained with the first generation electron MOT system employed a manual fit that was performed for all of the electron beam profiles. There was a significant amount of human error introduced in determining the best estimates of the current density using this method. Refitting a beam profile several times would not always give exactly the same value for the current density, due to the difficulty of the manual fitting process. For this reason, the systematic error was overestimated.

However, during the implementation of the second generation system, a LabView software was developed to address this problem of manual fitting to the electron beam profiles. This software would read in the beam profile data from file and perform a transformation to the model function, then do a linear regression to the transformed function to give a least-squares best fit for the current density. In addition, it would also provide a statistical error for the current density.

The process used with this software was relatively straightforward. The starting point is Eq. 7.14. In the form given, it cannot be used with a least-squares fit. To get to a state where we can apply a least-squares fit, we must first square both sides of Eq. 7.14.

$$\left(\frac{i_n'}{d}\right)^2 = \left(2J_0 r\right)^2 - \left(2J_0\right)^2\left(y_n - c\right)^2 \qquad 7.17$$

and make the following transformations

$$\begin{aligned} \left(\frac{i_n'}{d}\right)^2 &\rightarrow \mathrm{u} \\ \left(y_n - c\right)^2 &\rightarrow \mathrm{v} \end{aligned} \qquad 7.18$$

to give a linear equation to which we can apply a least-squares fit. One obvious flaw is that there has to be some prior knowledge of the value for the centre of the beam, c, before

making the transformations of Eq. 7.18. The software is configured to split the profile into two halves and perform the operations in Eq's. 7.17 and 7.18 to each. This gives two slopes of the linearized beam profile, that are combined to give a single value of the current density. This process requires that the user enter only the boundary points of the beam on the profile and the centre point, c. The value of c, is then altered to minimize the deviation between the two slopes used to calculate the current density. This also has the effect of minimizing the statistical error in the current density.

The major requirement for this technique to be successful in estimating the current density is that the beam profile be as symmetric as possible. When the profile becomes asymmetric, the linearized function from Eq's 7.17 and 7.18 becomes skewed to the point where, with extremely asymmetric profiles, the two halves of the linearized profile are no longer linear and it becomes impossible to match their slopes.

One final note that should be made in the discussion of the analysis of the electron beam is the simulation that was performed with the second generation electron MOT system. The geometries of the electron gun's lens elements were programmed into Simion. Then the BaO disc emitter was incorporated into the model, with a two-dimensional plate held at cathode potential with electrons launched normal to the disc. The results of one such simulation are shown in Fig. 7.3.

For this particular configuration, the cathode potential was set to 200 eV (-200 V with respect to ground). The electron gun was running with the entire pentode stack at ground potential. In addition, the Wehnelt cylinder was operated at cathode potential. The deflection stages were not used, but left equipotential with their respective lenses. This left only the diode, which was configured with the first lens, E1, set to +250 V with respect to cathode, and the second lens, E2, set to +95 V with respect to cathode.

The disc emitter was defined to be 0.040" in diameter, corresponding to the actual size of the BaO cathode from Kimball Physics. The electrons were launched normally from the disc emitter with initial launch sites chosen to be equally spaced along the diameter. There were 16 launch sites in total extending from -0.015" to +0.015" for each diameter. In total there were 8 diameters used for the simulation and were arranged at 22.5° intervals.

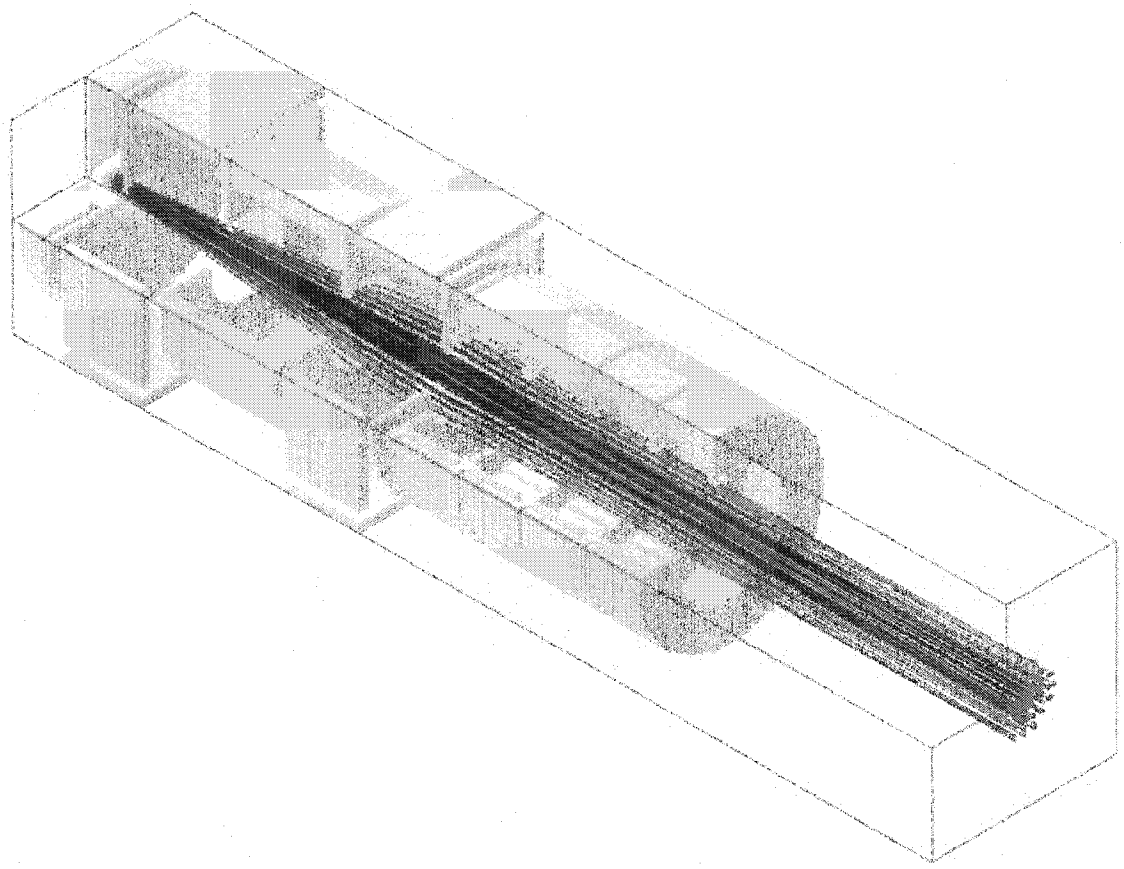

Figure 7.3: Diagram of the output from a simulation of the electron gun with Simion. Each of the lines represents a separate electron trajectory originating from a different location on the disc emitter used to represent the BaO cathode.

This simulation yielded a very interesting result. The simulation was run with exactly the same settings as was used in the experiment. The beam profile for the gun with these settings indicated that the real beam diameter was virtually identical to that of the simulated electron beam. This gave greater confidence in our assessments of the beam quality. It also provided a means of determining the level of divergence in the beam, and whether or not the entire beam was incident on the Faraday cups. From Fig. 7.3, it may appear as though the beam's current density is not constant, but this is slightly misleading and is a result of the choice of initial launch sites from the emitter. Recalling the geometry of the emitter, we see that there is a tighter clustering of initial trajectories at the centre of the emitter, which leads to the clustering of trajectories within the beam, as depicted above.

7.2 Fluorescence Decays

The next piece of information necessary for calculating collision cross sections using a MOT is the trap loss rate. The trap loss rate is determined by performing time resolved measurements of the fluorescence decay of the trapped atoms following removal of the magnetic trapping field. The process for extracting trap loss rates from the fluorescence decays curves is the same, regardless of the type of cross section we are measuring. However, the fluorescence decays can have very different shapes, depending on the collision cross section being studied. We will now discuss the process for measuring trap loss rates from the fluorescence curves.

The experimental control and data acquisition in both the first and second generation electron MOT systems were configured for generating two consecutive trap-off periods by quickly removing the magnetic field. These trap-off periods ranged from 20 to 40 msec in duration, and were separated by roughly 500 msec. The time in between trap-off periods was necessary to replenish the trap and bring it back to a steady-state population, before the next

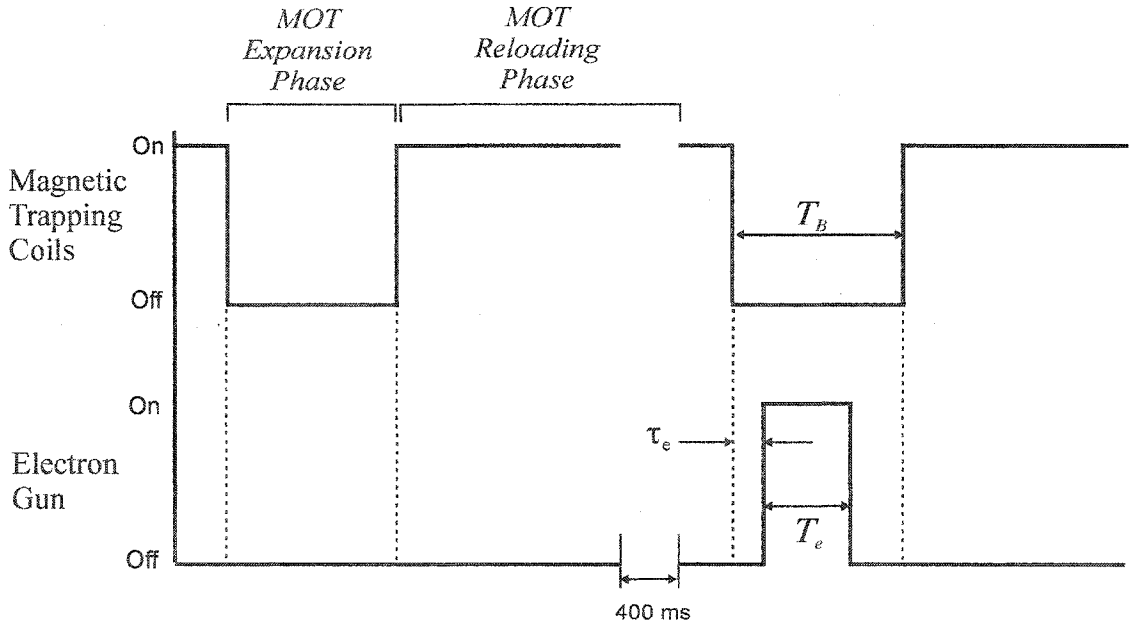

Figure 7.4: Timing diagram common to all of the trap loss measurements for a single acquisition cycle, showing the trap-off periods, duration T_B, with the electron gun pulse with duration T_e and with a relative delay of τ_e.

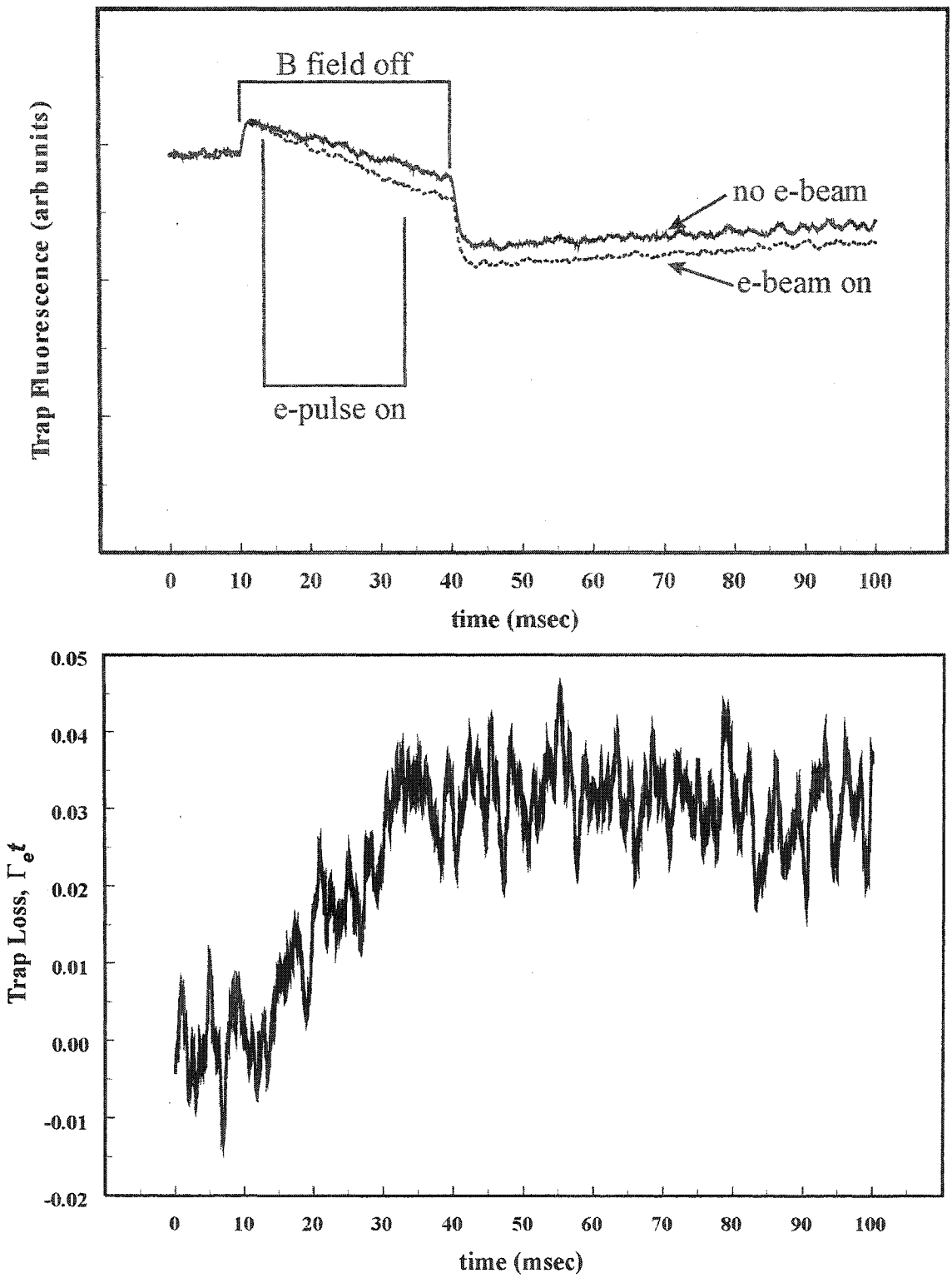

Figure 7.5: Typical fluorescence decay curves (upper) with the corresponding trap loss (lower), showing the linear increase in trap loss corresponding to the electron pulse, and how this trap loss levels off immediately after the end of the electron pulse.

trap-off period. This gave a single acquisition cycle that was slightly greater than one second in duration and was the maximum rate at which the trap could be operated. With the first generation system, there were up to 10 000 successive acquisition cycles, or sweeps, made for each run, with the electron pulse occurring on alternating trap-off periods. This process of alternating electron beam pulses measurements ensured that any systematic errors would be consistent between fluorescence decay measurements with and without the electron beam. An example of a typical set of fluorescence decays is shown in Fig. 7.5. The same process was used with the second generation electron MOT system, although the number of sweeps was typically only several hundred per data run.

After each data run was completed, the two fluorescence decays were dumped to file and analysed. The fluorescence analysis has evolved significantly from the first sets of measurements. Initially, the analysis was performed manually for each file using Corel Quattro®. In later stages with the first generation MOT, the analysis was streamlined with the development of a LabView software. Several improvements were made to this software with the implementation of the second generation electron MOT system, including real-time displays of the trap fluorescence and the trap loss, multichannel scaling of the Faraday cup currents, and an automated storage and recall of experimental parameters.

The analysis procedure for the trap loss began with overlapping the fluorescence decays with and without the electron beam present. With the first generation electron MOT system, this was done by aligning the glitches from the magnetic coils switching off that appeared on both decay curves. This was necessary because the Quantum8 MCS had to store both decay curves within the same memory bank. With the second generation system, there was no need for aligning the decays curves to glitches as the measurement of the decay curves started at precisely the same time. Also, each decay curve was given its own memory bank with the computer-based MCS setup.

The analysis procedure continued with a rescaling of the second decay curve that contained the electron-induced trap loss, so that both curves had the same averaged, initial value for the steady-state fluorescence. The next step was to remove the background component from the decay curves. The background was determined by performing another

run, immediately afterwards, and with exactly the same settings but with the magnetic field removed. These background runs were typically much shorter than the data runs. The background level was normalized to the same number of sweeps as the data run, and then subtracted. At this point, the calculation of the trap-loss rate could be performed. The calculation was quite simple, and involved taking the natural logarithm of the ratio of the two fluorescence curves. The resulting curve was then plotted with respect to time, to give a trap loss curve. At this point there are two options for determining the trap loss rate.

The first option is to perform a linear regression of the trap loss curve over the time range corresponding to the electron beam pulse, as shown in Fig. 7.5. The second option is to obtain an average value of the trap loss during the reloading phase of the MOT, which appears as the raised, flat portion of the trap loss curve in Fig. 7.5. Then obtaining a value of the trap loss during steady state operation prior to removal of the magnetic field, which should be zero due to the rescaling of the original fluorescence curves mentioned earlier. Subtracting these two average values, and dividing by the width of the electron beam pulse gives another value of the trap loss rate, we will refer to this method as simply the difference method.

There are advantages and disadvantages with both methods. Using the linear regression method typically provides a higher statistical error due to the short pulse widths of the electron beam. Also, some of the cross section measurements, to be discussed later in this chapter, are made with the MOT in a dark state during the electron interaction time. There is no fluorescence from the MOT due to the fact that the optical pumping has been removed, so the PMT records only a constant background. However, when possible, the linear regression method gives a direct measurement of the trap loss rate, and the evolution of the MOT can be observed over the whole interaction time with the electron beam.

Using the difference method typically gives a much better statistical error, as the reloading time is much longer than the electron beam pulse. However, this method provides an indirect measurement of the trap loss rate. In most cases, the evolution of the MOT during the interaction time is not observable. This can cause some uncertainty with the overlap of the electron beam with the trapped atoms during the trap-off period. Several periodic tests

must be performed to ensure that there is overlap for the duration of the electron beam pulse.

We will now run through the mathematical details of the trap loss rate calculations. The differential equation describing the trap population, N, was given earlier in Eq. 3.7

$$\frac{dN}{dt} = \Lambda - \Gamma N \tag{7.19}$$

for a constant loading rate Λ, from the background vapour, and a loss rate Γ. The measurements for the cross section are made with the magnetic field off so that $L = 0$, giving

$$\frac{dN}{dt} = -\Gamma N \tag{7.20}$$

which has the general solution

$$N(t) = N_0 \exp[-\Gamma t] \tag{7.21}$$

where N_0 represents the initial, steady-state value of the trap population when the loading rate is switched to zero, and is given by the initial condition.

$$N_0 = N(t = 0) \tag{7.22}$$

with $t = 0$ corresponding to the moment the magnetic field is removed (or slightly before).

We first consider the case without the electron beam present during the trap-off period. The trap loss rate describing the evolution of the population is a background loss rate due to inelastic collisions within the trap, collisions with background residuals, hyperfine-changing collisions, etc. It is not necessary to precisely know what gives rise to the trap loss, but rather, that it is well described by a linear loss rate. Denoting the background loss rate by Γ_0

$$N(t) = N_0 \exp[-\Gamma_0 t] \tag{7.23}$$

Proceeding to the trap loss with the electron beam present during the trap-off period, we will denote the trap population by $\widetilde{N}$. The same approach is taken, starting with the differential equation in Eq. 7.20 we can write

$$\frac{d\widetilde{N}}{dt} = -\Gamma \widetilde{N} \tag{7.24}$$

which has the general solution

$$\widetilde{N}(t) = \widetilde{N}_0 \exp[-\Gamma t] \tag{7.25}$$

that is analogous to the solution given in Eq. 7.21. We can apply the same initial conditions

$$\widetilde{N}_0 = \widetilde{N}(t = 0) \quad . \tag{7.26}$$

The difference between Eq. 7.25 and 7.21 is in the trap loss rate, Γ. For Eq. 7.25, we have a loss rate that is a combination of the background loss rate, Γ_0, and an electron-induced trap loss rate Γ_e. We assume that these two loss rates are independent of each other, so that their effects are additive, and Eq. 7.25 becomes

$$\widetilde{N}(t) = \widetilde{N}_0 \exp\left[-\left(\Gamma_0 + \Gamma_e\right)t\right] \quad . \tag{7.27}$$

We now have a mathematical expression for both decay curves. To isolate the electron-induced trap loss rate, for calculating the electron collision cross section, we can divide Eq. 7.21 by 7.27 to get

$$\frac{N(t)}{\widetilde{N}(t)} = \frac{N_0}{\widetilde{N}_0} \exp\left[\Gamma_e t\right] \quad . \tag{7.28}$$

If the steady state populations with and without the electron beam are the same the expression reduces to

$$\frac{N(t)}{\widetilde{N}(t)} = \exp\left[\Gamma_e t\right] \quad . \tag{7.29}$$

Finally, we take the natural logarithm of Eq. 7.29 to get

$$\ln\left(\frac{N(t)}{\widetilde{N}(t)}\right) = \Gamma_e t \quad . \tag{7.30}$$

which is then plotted with respect to time. The trap loss rate is then isolated using either the linear regression or the difference method as discussed earlier in this section.

7.3 State Selection of Scattering Target

As mentioned earlier, the use of a MOT as a scattering target for performing electron collision studies has the advantage of allowing properties of the target to be modified, by adjusting the laser parameters. This provides a relatively simple, yet effective method of controlling the state of the scattering target.

We first consider the features of the trap during normal operation. The presence of both the trapping and repumping lasers maintains a fraction of the total trap population in the $6^2P_{3/2}$ excited state. Depending on the trapping laser's intensity and frequency, the excited state fraction can be saturated, or nearly saturated, at 50%. Provided the frequency detuning of the trapping laser remains intact, the excited state fraction is given by

$$\rho_{ee} = f_e = \frac{1}{2}\frac{s_0}{1 + s_0 + 4\left(\frac{\delta}{\gamma}\right)^2} = \frac{1}{2}\frac{\frac{I}{I_s}}{1 + \frac{I}{I_s} + 4\left(\frac{\delta}{\gamma}\right)^2} \qquad 7.31$$

where δ is the trap laser frequency detuning, γ is the natural linewidth of the trapping transition, and s_0 is the on-resonance saturation parameter, which is just the laser intensity, I, divided by the saturation intensity, I_s of the trapping transition. Also, while the frequency of the trapping laser remains detuned from the trapping transition, the cooling force remains at a maximum and the atoms can be thought of as moving within a very viscous medium.

In terms of a scattering target, what we have is a dense ($> 10^{11}$ cm^{-3}) cloud of atoms that cycle between ground and excited states due to the presence of the trapping and repumping lasers. The atoms within the cloud, whether in the ground or excited state, are stationary, also due to the presence of the trapping field. Furthermore, our scattering target is not comprised of free particles. An additional consequence of having the trapping laser present is that the atoms within the MOT will be insensitive to any momentum transfer from the electron beam. This is particularly true with a cesium MOT target since cesium is such a massive target. This is another advantage of using the MOT for target preparation.

The trapping and repumping lasers are tuned to frequencies corresponding to specific

transitions within the hyperfine manifolds of the $6^2S_{1/2}$ ground and $6^2P_{3/2}$ excited states. This does not, however, imply that the measured cross sections are for specific hyperfine levels. The cross section measurements are made with the cesium target atoms in specific hyperfine levels, with very large populations due to the presence of the lasers. The increased hyperfine level populations brought on by the lasers causes a larger statistical weighting for the hyperfine levels associated with the lasers. Furthermore, since the hyperfine levels share the same features of their parent fine-structure levels, such as lifetime, we argue that the oscillator strength, or branching ratios are also equal. If we consider the situation where both lasers are operating, the $6^2P_{3/2}$ excited state will consist of roughly equal populations for the F = 4 and F = 5 levels, and near-zero populations for the F = 2 and F = 3 levels. With equal branching ratios for the hyperfine levels within a manifold, the situation mentioned above is equivalent to the situation with equal populations of all the levels in a hyperfine manifold, which is a $6^2P_{3/2}$ target

The fact that the MOT, in its normal configuration, is insensitive to any momentum-transfer from an electron beam makes it difficult to perform a measurement of a total cross section. The momentum-transfer cross section, which is the elastic contribution to the total cross section, is effectively removed by the trapping field. Any momentum transferred to an atom is quickly dissipated by the trapping laser before it can travel an appreciable distance. This can be quite useful for measuring inelastic cross sections, but the MOT's operation must be modified in order to get a total cross section. Also, the MOT in its normal configuration has an admixture of ground and excited state atoms. A cross section measurement is then a combination of two cross sections. If we are interested in a ground state cross section than we must modify the MOT to temporarily alter the optical pumping scheme.

The first modification to the MOT's operation is to the trap laser detuning. The detuning in most cases is reduced almost to zero. A very small, red-shifted detuning is kept to prevent any direct heating of the MOT, and to minimize the cooling effect of the laser. This has the effect of maintaining the optical pumping so that there is a sustained, non-zero excited state fraction, but the atoms in the MOT can now be scattered as free particles, and

there is virtually no dissipation of the momentum-transfer to an atom from the electron beam.

We are interested in how the excited state fraction is modified by eliminating the trap laser detuning. Going back to Eq. 7.31 and substituting $\delta = 0$, we find

$$f_e = \frac{1}{2}\frac{\frac{I}{I_s}}{1+\frac{I}{I_s}} \qquad 7.32$$

As mentioned earlier, a small, red-shifted detuning is kept to prevent any heating of the atoms in the MOT. This detuning was typically 1 to 4 MHz. As the natural linewidth of the trapping transition is approximately 32 MHz, the detuning terms that appears in Eq. 7.31 will now be much smaller than the value of the on-resonance saturation parameter, and can be ignored. To show this we look at the graph of Eq. 7.31 for various trap laser detunings, shown in Fig. 7.6. From this plot we clearly see that there is only a 1 to 2 % maximum deviation in the excited state fraction as one changes the detuning value from 0 to 5 MHz. Provided we stay slightly to the red-shifted side of the transition, we can be assured that there

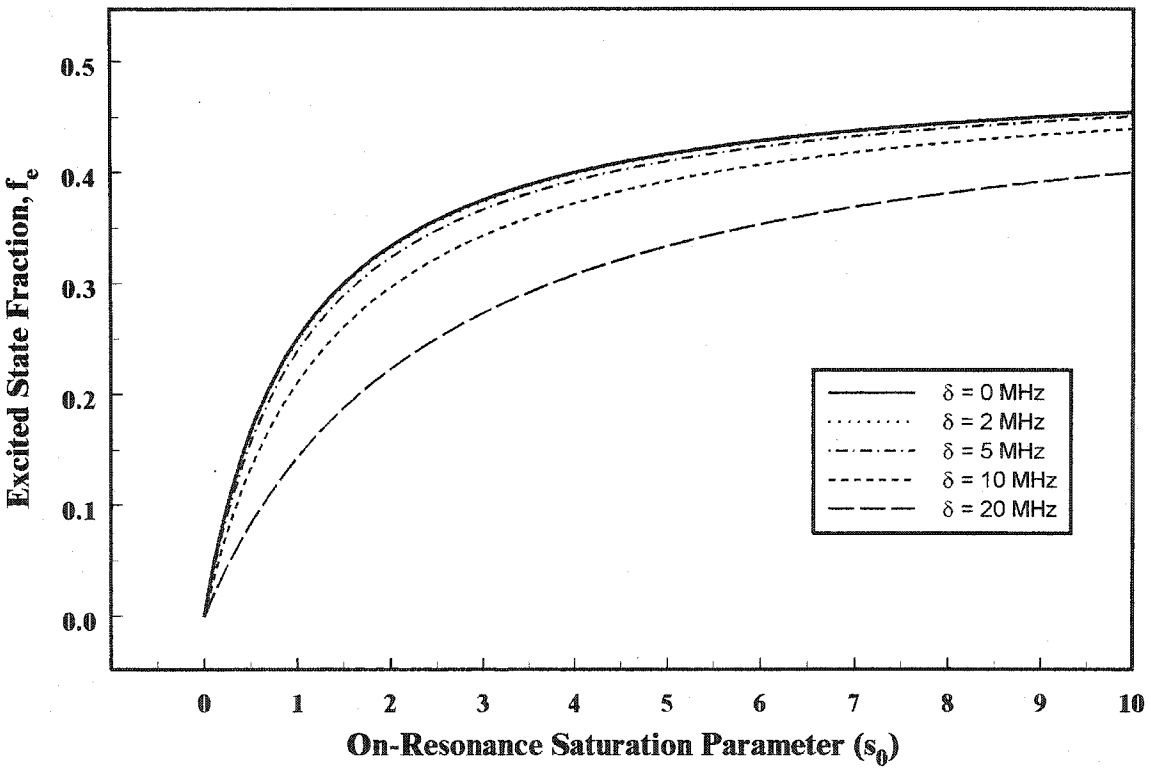

Figure 7.6: A plot of the excited state fraction versus s_0 using Eq. 7.31 for various values of the trap laser detuning. Note that the δ = 2 MHz curve is virtually indistinguishable from the δ = 0 MHz curve.

is no heating of the MOT, the radiation force (cooling effect) will be minimal, and the excited state fraction will behave as the expression given in Eq. 7.32.

Another modification that must be made to the operation of the MOT is the removal of the repumping laser. This means that the entire trap population invariably ends up in the $6^2S_{1/2}(F=3)$ ground state, and cuts off virtually all excitation to the excited state. This gives a convenient means of selecting a target of either pure ground state, or an admixture of ground and excited state, by simply shuttering the repumping laser.

There will be very little collisional excitation from the $6^2S_{1/2}(F=3)$ to the $6^2S_{1/2}(F=4)$. The energy separation of these two ground state hyperfine levels is well within the range of thermally accessible energies at room temperatures. However such collisions would have to be with vacuum residuals since the thermal energies of the atoms within the MOT are far below the energy required to promote an atom to the higher hyperfine ground state. But due to the background pressure, the collision frequency is quite low, of the order of 1 Hz. So virtually all of the atoms remain in the $6^2S_{1/2}(F=3)$ ground state. This means that the presence of the trapping laser becomes irrelevant once everything has been pumped into the dark ground state.

If the entire population of the MOT is within the $6^2S_{1/2}(F=3)$ ground state, we may think that the cross section obtained from the MOT in this state will be a hyperfine cross section, and require a branching ratio to get the $6^2S_{1/2}$ cross section. The $6^2S_{1/2}$ cross section is a combination of hyperfine cross sections that are given statistical weighting according to the hyperfine population distribution. As the entire population has been forced into the $F=3$ ground state, the statistical weighting is unity, and our cross section made with the pure $F=3$ ground state, is the same as the $6^2S_{1/2}$ cross section with equal populations distributed among both hyperfine levels.

7.4 Total Cross Section ($6^2S_{1/2}$)

The total cross section measurements for the $6^2S_{1/2}$ ground state were made with the laser parameters adjusted, as mentioned in the previous section, to drive the atoms in the MOT into the ground state by removing the repumping laser. The trapping laser was usually left in its normal operating condition, as it was found that its presence did not affect the numerical results of the measurements. The repumping laser was usually switched off for the entire trap-off period, so that the timing diagram, shown in Fig. 7.7, would appear similar to that of Fig. 7.4. In addition to removing the repumping laser, the electron gun pulse was positioned so that the pulse began as soon as possible following the removal of the magnetic field. The delay was decreased until the rising edge of the electron beam pulse just cleared the transient from the coil switching, and the dissipation of the eddy currents in the chamber walls. The duration of the electron beam pulse was increased so that the end of the electron

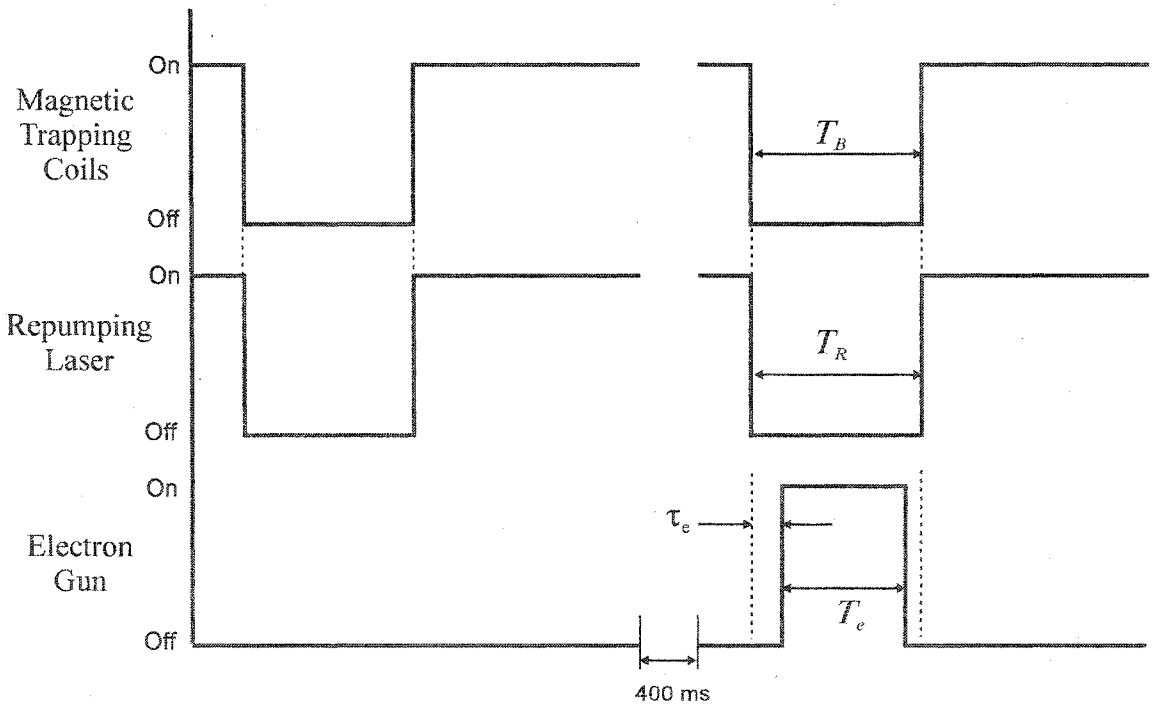

Figure 7.7: Typical timing diagram for the trap loss measurements of the total cross section for the $6^2S_{1/2}$ ground state. The timing is identical to that in Fig. 7.4, but with the coil pulse duplicated on a separate channel and used to gate the repumping laser. T_B, T_R, and T_e are the pulse widths of the magnetic coils, repumping laser, and electron gun respectively. τ_e is the realtive delay of the electron pulse relative to the magnetic coil pulse.

pulse occurred at least 4 to 5 msec before the magnetic coils were switched on. The delay between the end of the electron beam pulse and the coil pulse was to allow a sufficient transit time for any elastically scattered atoms to leave the line of sight of the PMT and the trapping region, so that a trap loss was recorded for those atoms. These changes to the laser field and to the experimental timing prepared a scattering target of atoms that were all in the ground state. In addition, these atoms could be scattered as free particles, and if so were given sufficient time to exit the observation region. In other words, we have prepared a target of pure $6^2S_{1/2}$ ground state atoms for a total cross section measurement.

The fluorescence decay for this measurement is obviously dark during the interaction with the electron beam, as we have removed the repumping laser. The results of a typical run are shown in Fig. 7.8. The appreciable rise and fall times of the trap fluorescence are due to the slow response (> 1 msec) of the optical shutter used to gate the repumping laser. We see from Fig. 7.8 that the steady state population for both decay curves is virtually identical,

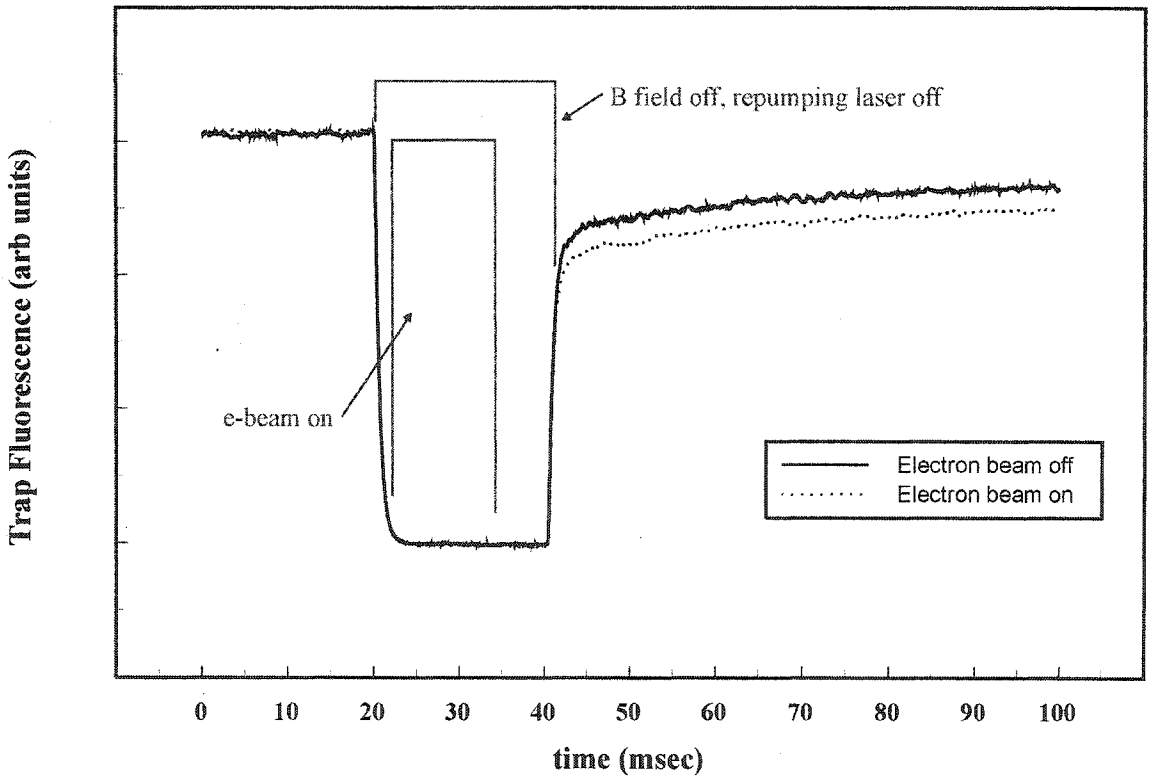

Figure 7.8: Digitized fluorescence decays for the electron beam off and the electron beam on for an electron impact energy of 200 eV. This particular set of fluorescence curves were produced with the second generation system.

despite the fact that there has been no rescaling performed. The trap then goes into a dark state, indicated by the lack of fluorescence between 20 and 40 msec. Thus, it is impossible to discern any (optical) information about the trap evolution during this time. Following the restoration of the magnetic trapping field and repumping laser, the trap becomes visible again and there is a clear difference in the two decays. The difference between the two decay curves, which is due solely to the interaction of the electron beam, is constant over the entire reloading phase observed by the PMT. This constant separation of the curves during reloading is what allows us to use the difference method, mentioned earlier in Sect. 7.2, for obtaining the trap loss rate. To better illustrate this argument, the trap loss for the decays in Fig. 7.8 is shown in Fig. 7.9.

As mentioned in the caption of Fig. 7.8, the fluorescence decays shown were part of a test for determining beam overlap. Once the tests were complete, the data runs were started

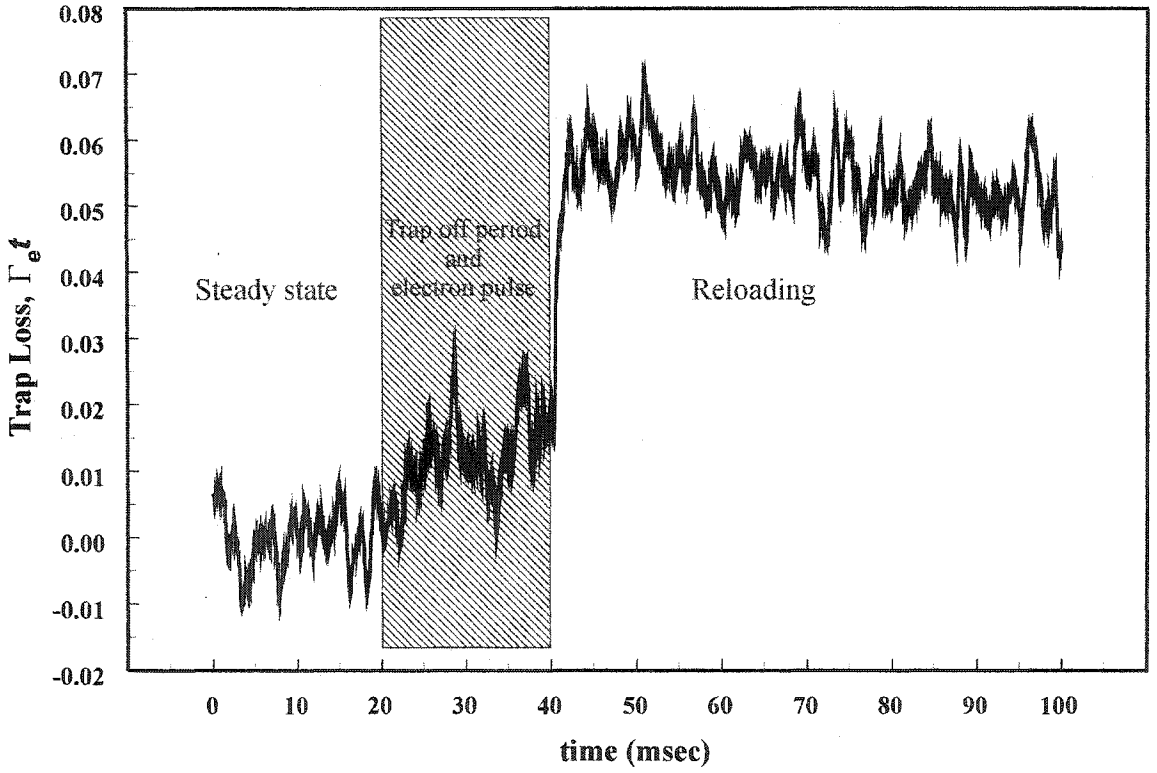

Figure 7.9: A plot of the trap loss resulting from an analysis of the fluorescence decay curves given in Fig. 7.8. The time window corresponding to the coils off, repumping laser off, and electron pulse on has been blacked out. The trap loss from the steady state is clearly zero, while the trap loss from the reloading portion is approximately 5.5 %.

and the trap loss rates determined using the difference method. The data collection is repeated until several points with satisfactory noise levels are obtained. These runs are then averaged to give a cross section value for one energy. The beam energy is then changed and the entire process starts from scratch again.

The results obtained from the trap loss method for the total cross section (TCS) for the $6^2S_{1/2}$ ground state are shown in Fig. 7.10. The data has been sorted into groups from the

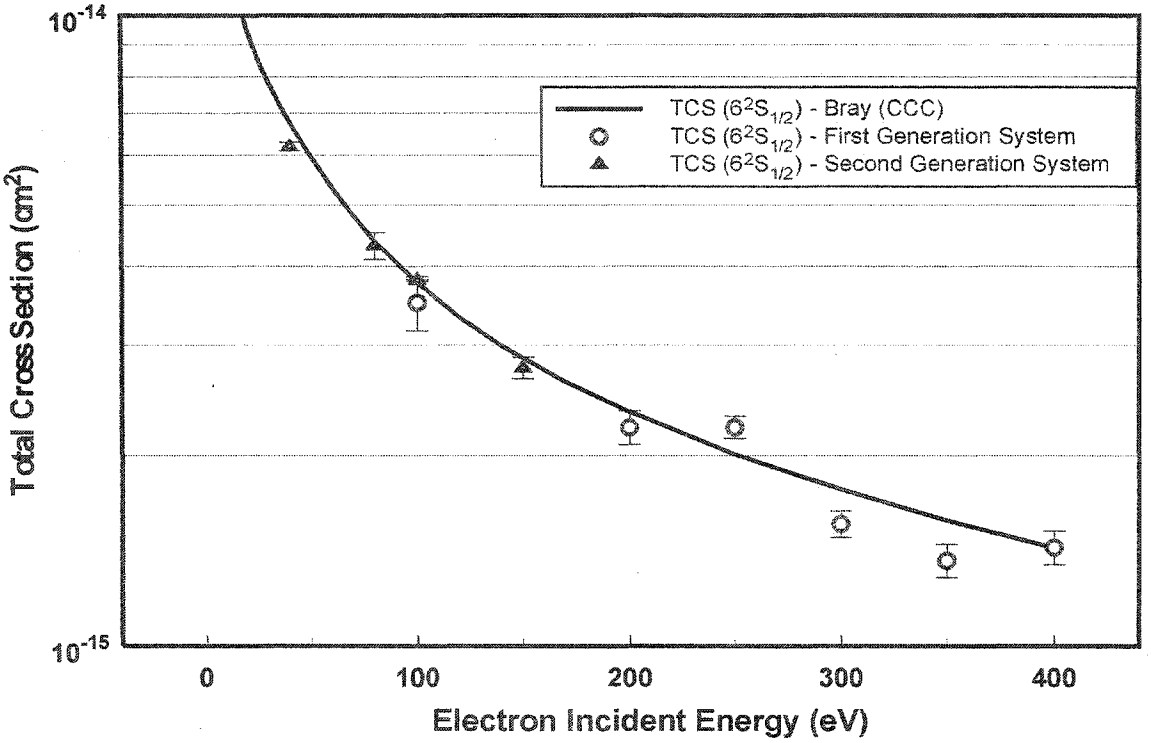

Figure 7.10: Data measured for the total cross section of the $6^2S_{1/2}$ ground state of cesium using the trap loss technique. The solid line represents the CCC calculations of Brode.

first and second generation electron MOT systems for comparison purposes. Also shown with the data are the results of a CCC calculation to provide an overall comparison with theory. Fig. 7.11 shows these data combined with all presently known data for the total cross section of the ground state.

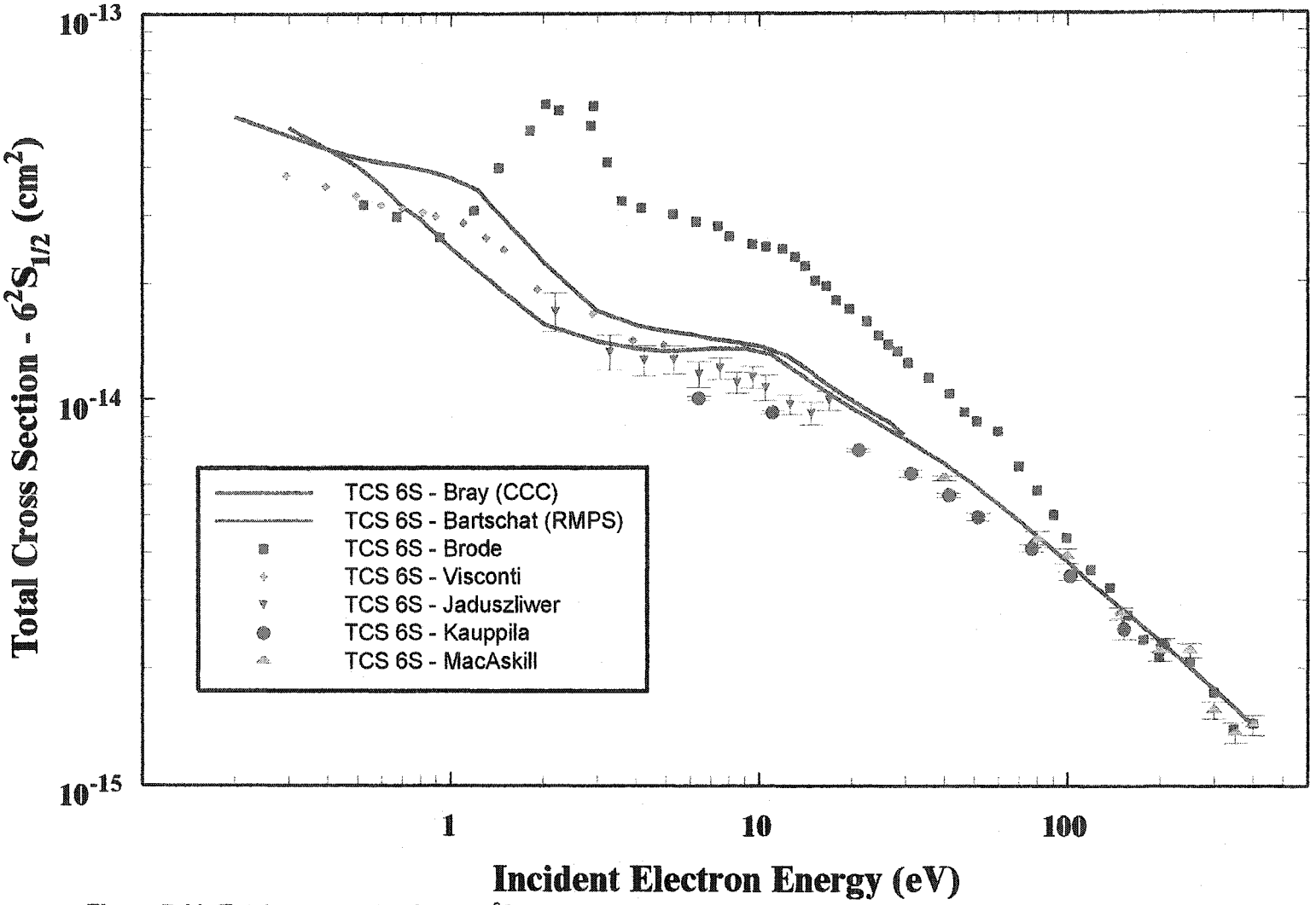

Figure 7.11: Total cross section for the $6^2S_{1/2}$ ground state of cesium including the original Brode data and the most recent theoretical results including the CCC treatment of Bray, and the RMPS treatment of Bartschat.

7.5 Total Cross Section ($6^2P_{3/2}$)

The total cross section measurements for the $6^2P_{3/2}$ excited state were made with no changes to the repumping laser, as was done with the total cross section measurements for the ground state. However, the trapping laser had its frequency detuning modified during the interaction time between the electron beam and the MOT. The trapping laser's frequency detuning was reduced from the 10 to 15 MHz used during normal operation, to a few MHz. To provide the necessary modulation of the trapping laser frequency, the trap laser's acousto-optic modulator was used.

The driver for the acousto-optic modulator uses a stabilized voltage to frequency converter to adjust the frequency shift of the sideband. We can then change the frequency of the sideband by changing the DC voltage supplied to the tuning input. A simple, dual-stage op-amp circuit was configured as a non-inverting adder. to combine a DC voltage, with an analog pulse from the BNC 555. The DC voltage gave the 10 to 15 MHz detuning used for optimal trapping during normal operation of the MOT. The analog pulse from the BNC was added to this to supply the voltage necessary to reduce the detuning to near zero.

The timing configuration for the total cross section measurements of the excited state was identical to that of the total cross section measurements of the ground state, as discussed in the previous section, with one exception. The trap population decreased so quickly following the removal of the trap laser detuning that the pulse width of the trap laser AOM was usually reduced to coincide with the electron beam pulse. A timing diagram is shown in Fig. 7.12. Recall that the pulse for the repumping laser, in the total cross section measurement of the ground state, coincided with the pulse for the magnetic coils.

A typical set of decay curves for a total cross section measurement of the excited state is shown in Fig. 7.13. The effect of removing the trapping laser's detuning is evident from the very sharp drop in fluorescence. The increased trap loss resulting is the motivation for using shortened electron pulses, because if the pulse were too long, the trap will be empty at the end of the pulse and require significantly longer reloading times to build up to the steady state population.

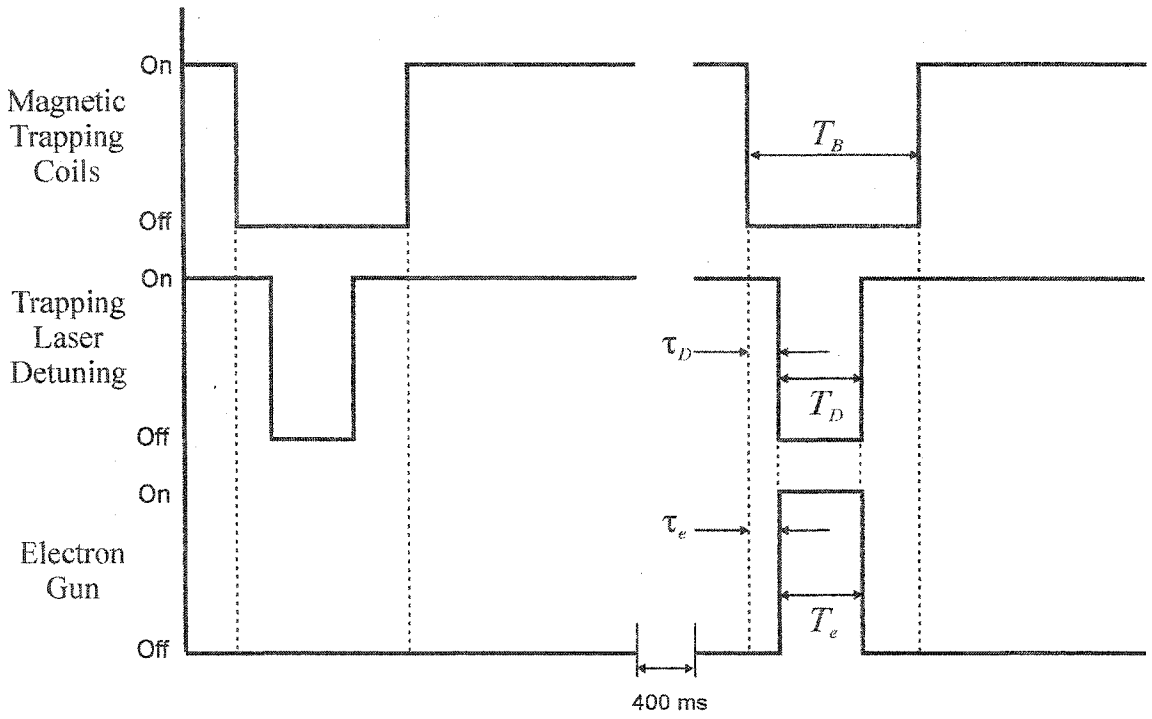

Figure 7.12: Typical timing diagram used for the trap fluorescence measurements of the total cross section for the $6^2P_{3/2}$ excited state.

From the trap loss curve and the fluorescence curves shown in Fig. 7.13, we see that the trap fluorescence is not suitable for use with the linear regression method to provide a value of the trap loss rate. However, the reloading portion of the curve is quite flat and can be used with the difference method to give a value for the trap loss rate. Another striking feature of the trap loss curve in Fig. 7.13 is the trap loss increases very slightly for some time following the end of the electron pulse and prior to restoration of the magnetic field. This suggests that there is some additional trap loss, incurred by the electron impact, that persists after the end of the electron pulse. This additional loss is attributed to the escape of elastically scattered atoms form the trapping region. This is the reason that a suitable delay must be used following the end of the electron pulse and the start of the next magnetic field pulse.

It is worth noting that most fluorescence runs used for the measurement of the $6^2P_{3/2}$ total cross section did not display the same sort of abrupt behaviour during the electron pulse that is shown in Fig 7.13. This particular fluorescence run was used because it showed a clear

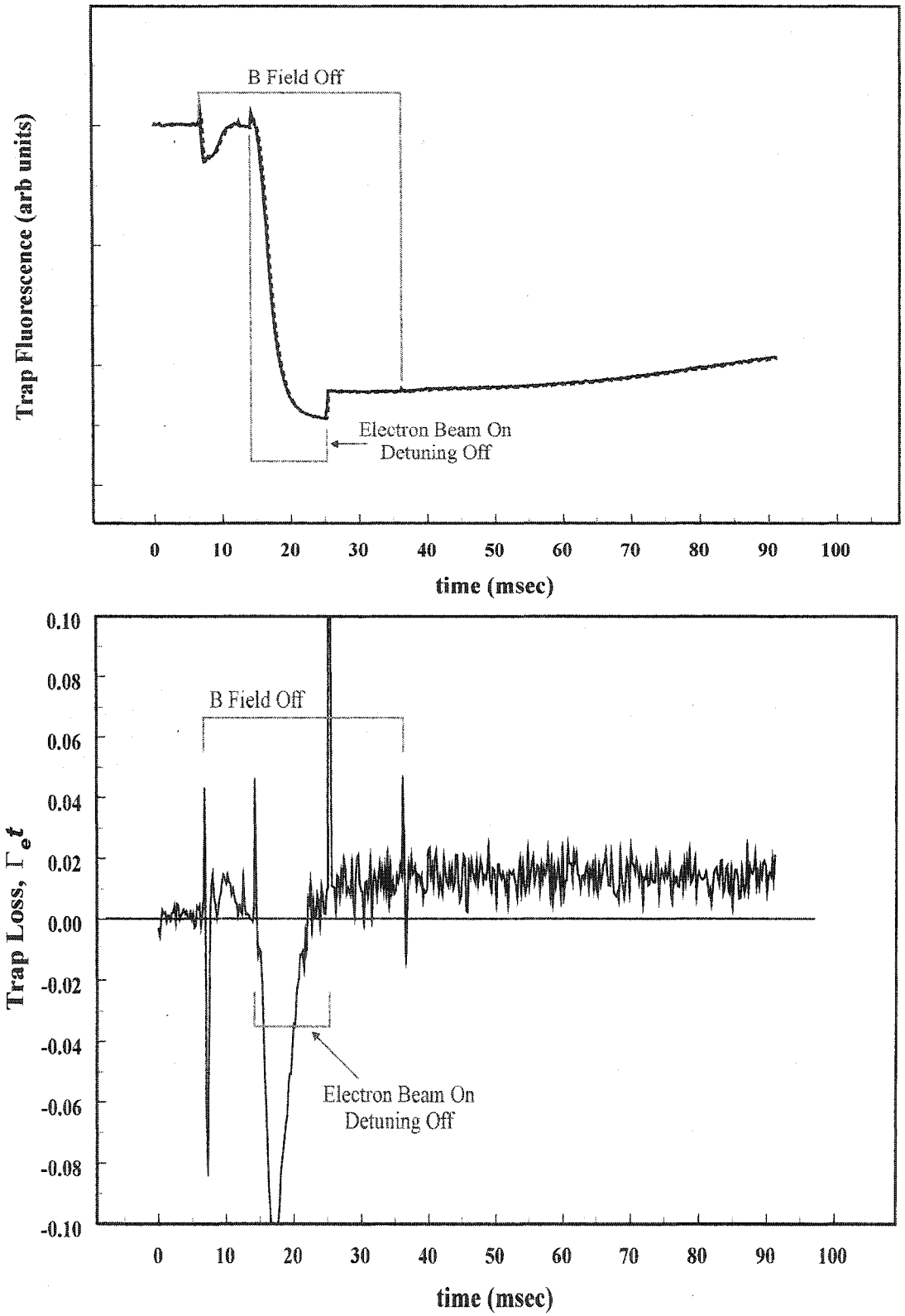

Figure 7.13: Fluorescence decay (upper) and trap loss curve (lower) for measurements of the total cross section for the $6^2P_{3/2}$ excited state.

increase in the trap loss following the end of the electron pulse. As such, it can be used to support our claims that the elastically scattered atoms are leaving the trapping region and the PMT's field of view.

The cross section values calculated from the trap loss rates were actually for an admixture of ground and excited state atoms, not for the excited state directly. To isolate the portion of the cross section belonging strictly to the excited state, we express the measured

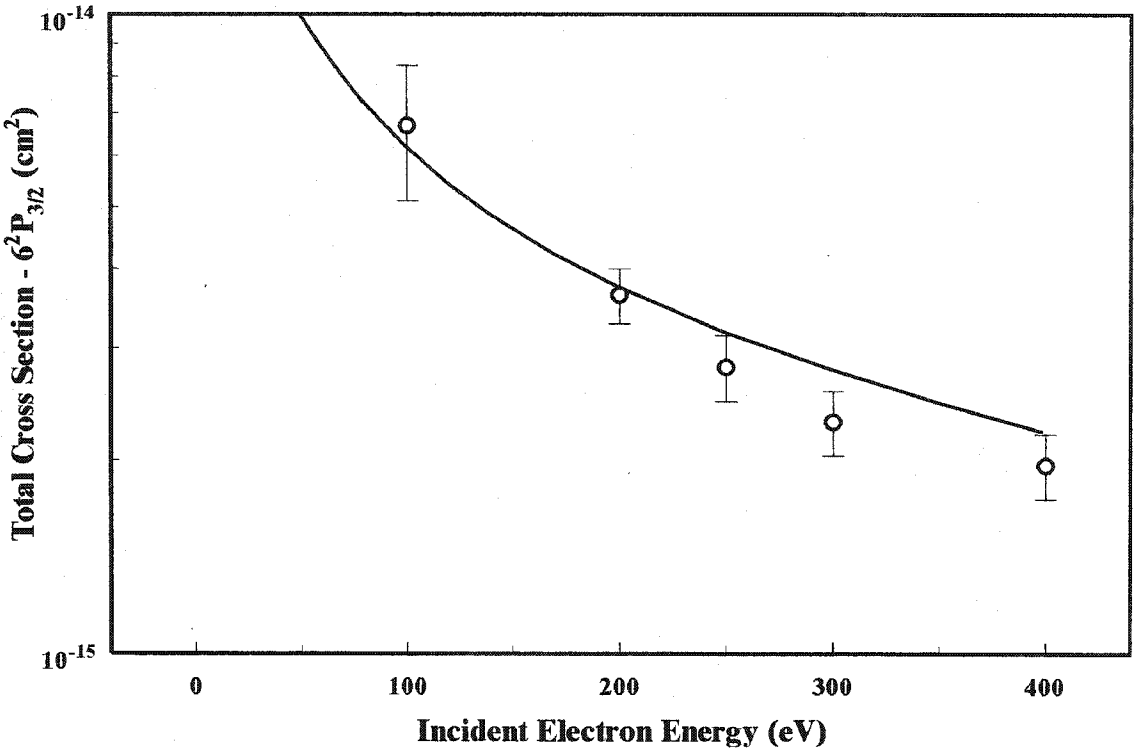

Figure 7.14: Results for the total cross section of the $6^2P_{3/2}$ excited state. The experimental data are compared with a recent calculation of I. Bray [MACAS 02].

cross section, σ_M, as the sum of the ground and excited state cross sections with coefficients corresponding to the ground and excited state population fractions, f_g and f_e respectively.

$$\sigma_M = f_g\sigma\left[6^2S_{1/2}\right] + f_e\sigma\left[6^2P_{3/2}\right] \qquad 7.33$$

which we can express solely in terms of the excited state fraction

$$\sigma_M = \left(1 - f_e\right)\sigma\left[6^2\mathrm{S}_{1/2}\right] + f_e\sigma\left[6^2\mathrm{P}_{3/2}\right] \qquad 7.34$$

The results shown in Fig. 7.14 were obtained by measuring the cross section with the timing and laser settings discussed so far in this chapter. Then the excited state fraction was determined by making some precise measurements of the trap laser intensity going to the MOT, taking into account transmission and reflection losses. This allows the excited state fraction from Eq. 7.31 to be calculated. Using the excited state fraction, in conjunction with the total cross section for the ground state, allows one to isolate the total cross section for the excited state using Eq. 7.34.

Despite the extra measurements involved with the total cross section calculation that were introduced by the excited state fraction, the dominant source of error was the trap loss rate from the fluorescence decays. The faster decay of the excited state measurements required very precise optical alignments, and pulse timings, to ensure that an electron-induced trap loss signal was even visible. Also, due to the statistical nature of the MOT's operation combined with the long run times (~2 - 3 hours) associated with the first generation system meant that any incurred alignment deterioration, loss of lock-in, power glitches, external noise, etc. had detrimental effects on the collected trap loss curves. This was also a motivation for the move to a second generation system, with increased stability and data acquisition.

The data presented in Fig. 7.14 is the only data presently in existence for the $6^2\mathrm{P}_{3/2}$ excited state of cesium. As such, there is no other data for comparison purposes. In fact, it was our ability to make such a measurement in combination with the ground state total cross section (i.e., using the same experimental system and same technique for both sets of measurements), that prompted the theoretical groups to "return" to cesium for a renewed investigation.

7.6 Total Ionization Cross Section ($6^2S_{1/2}$)

While performing the first total cross sections measurements, it was found that the cross sections were up to an order of magnitude lower than any other existing data. This was soon determined to be the consequence of trying to scatter the cesium atoms out of an optical molasses. Any time that both lasers were on, the trap loss rate was noticeably lower than expected. While this problem was circumvented by ensuring that either the repumping is removed (for a ground state measurement), or the trapping laser's detuning is removed (for an excited state measurement).

After some consideration, the decrease in trap loss was attributed to the Doppler cooling effect of the laser, damping out the momentum transfer contribution of the total cross section. Obviously, laser cooling cannot act on ionized cesium, or cesium in a higher lying electronic state. As the thermal average speed of the trapped atoms is of the order of 1 m/s, and the recoil transferred from an electron to a massive cesium atom is so small, the laser field can quickly dissipate any electron-induced velocity before the atom gets a chance to leave the trapping region.

This allowed for the possibility of measuring another total cross section, but with the momentum-transfer component damped out, so that the total cross section was asymptotic to the inelastic cross section. This inelastic contribution turns out to be the total ionization cross section as the PMT can view only 852 nm light, so that it views only the results of ionization processes, and excitation at the 852 nm resonance. But since the electron beams are competing with the lasers in the resonance excitation, the lasers are saturating the transition, and the optical oscillator strength is so large for the resonance line, we can attribute the trap loss entirely to ionization processes.

To get an ionization cross section measurement for the ground state, we proceed as before for the total cross section of the ground state, but alter the timing setup of the experiment, as shown in Fig. 7.15, to move the electron pulse so that it ends at the same time the magnetic trapping field is restored. This greatly reduces the chance of elastically scattered atoms to vacate the trapping region and the PMT's field of view where a trap loss would be

recorded. Furthermore, the width of the electron pulse is minimized to further reduce the possibility of the elastically scattered atoms to leave the trapping region. Typically the electron beam pulse widths were of the order of 4 msec, or less. Of course, the major problem with reducing the width of the electron beam pulse is that the trap loss signal is proportional to the duration of the electron interaction.

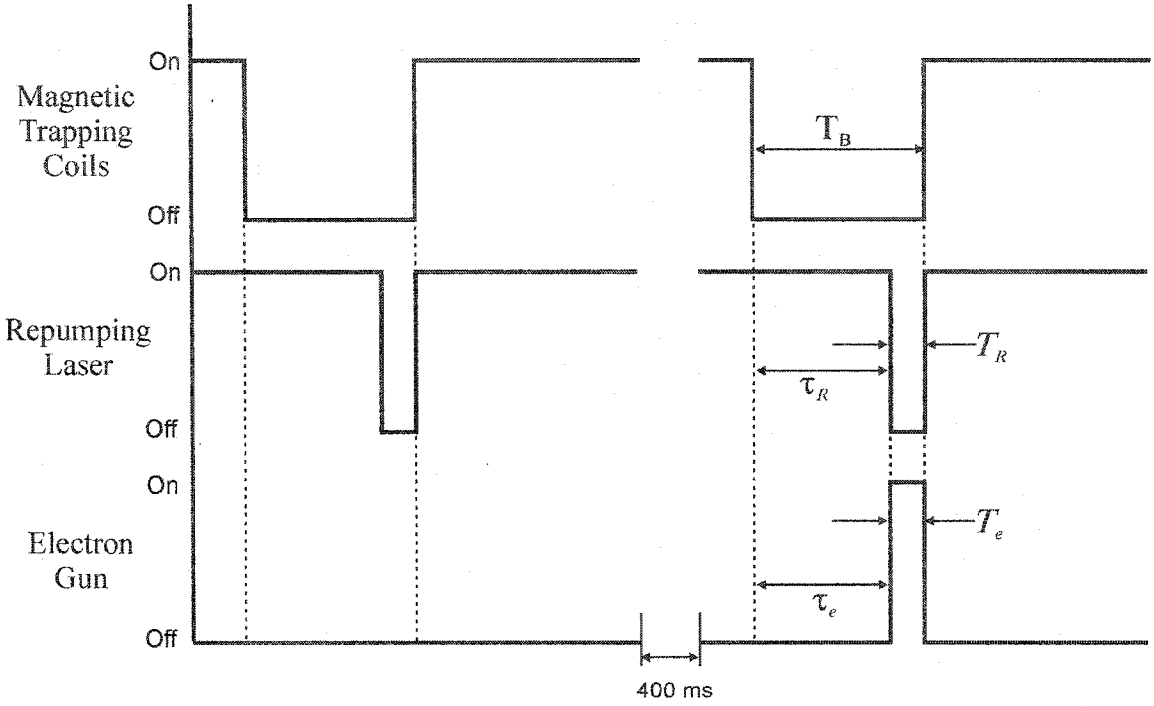

Figure 7.15: A typical timing diagram used for the measurement of the total ionization cross section for the $6^2S_{1/2}$ ground state. The timing is virtually the same as that in Fig. 7.7 for the total cross section measurement of the ground state, with the exception of the shortened electron beam pulse and the increase in the relative delay between it and the coil off pulse.

The measurements for the ground state ionization cross section proceed exactly the same as those of the total cross section measurements of the ground state. There is again, no possibility of using the linear regression method, so all calculations rely on the use of the difference method. A set of fluorescence curves from the measurement of the total ionization cross section for the ground state is given in Fig. 7.16.

The data from these measurements is combined with all of the existing data for the

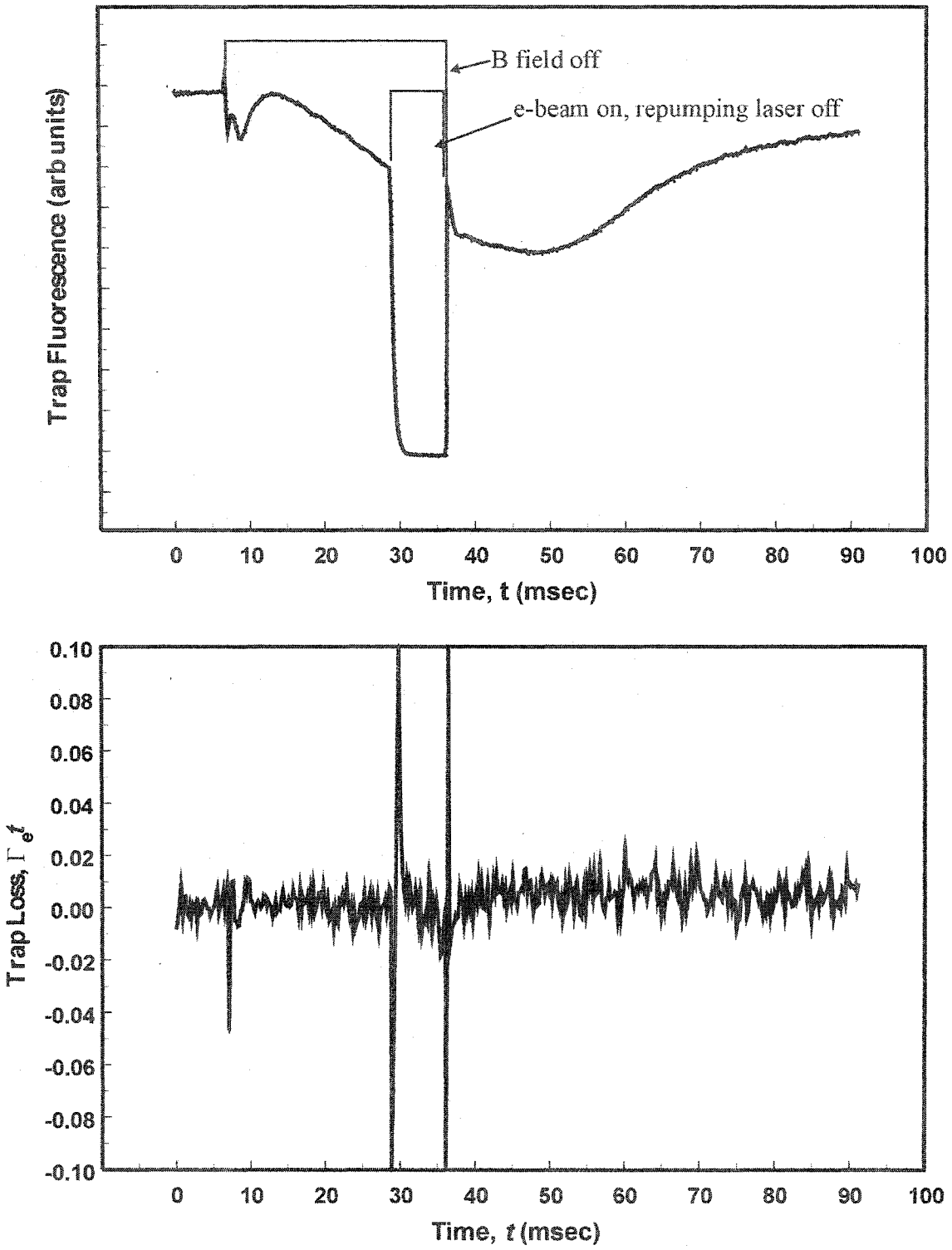

Figure 7.16: Fluorescence decays curves (upper) and trap loss curves (lower) for a cross section measurement of the total ionization cross section of the $6^2S_{1/2}$ ground state.

total ionization cross section of the cesium ground state in Fig. 7.17. Perhaps the most striking feature of the data from this experiment is the relatively large scatter of the points about the previously measured and calculated data sets. This is mostly due to the poor statistics in the trap loss curves that result from having a low signal to noise ratio, and very long run times that have a higher probability of systematic errors occurring. The bulk of the data for this cross section was measured with the first generation system. Although, there is a fairly wide spread in our data, there is enough of an agreement to suggest that the technique works and the principle is valid. However, more time is necessary to better the statistics and reduce the error. It's hoped that the second generation system will improve the data and provide a much better evaluation of the cross section.

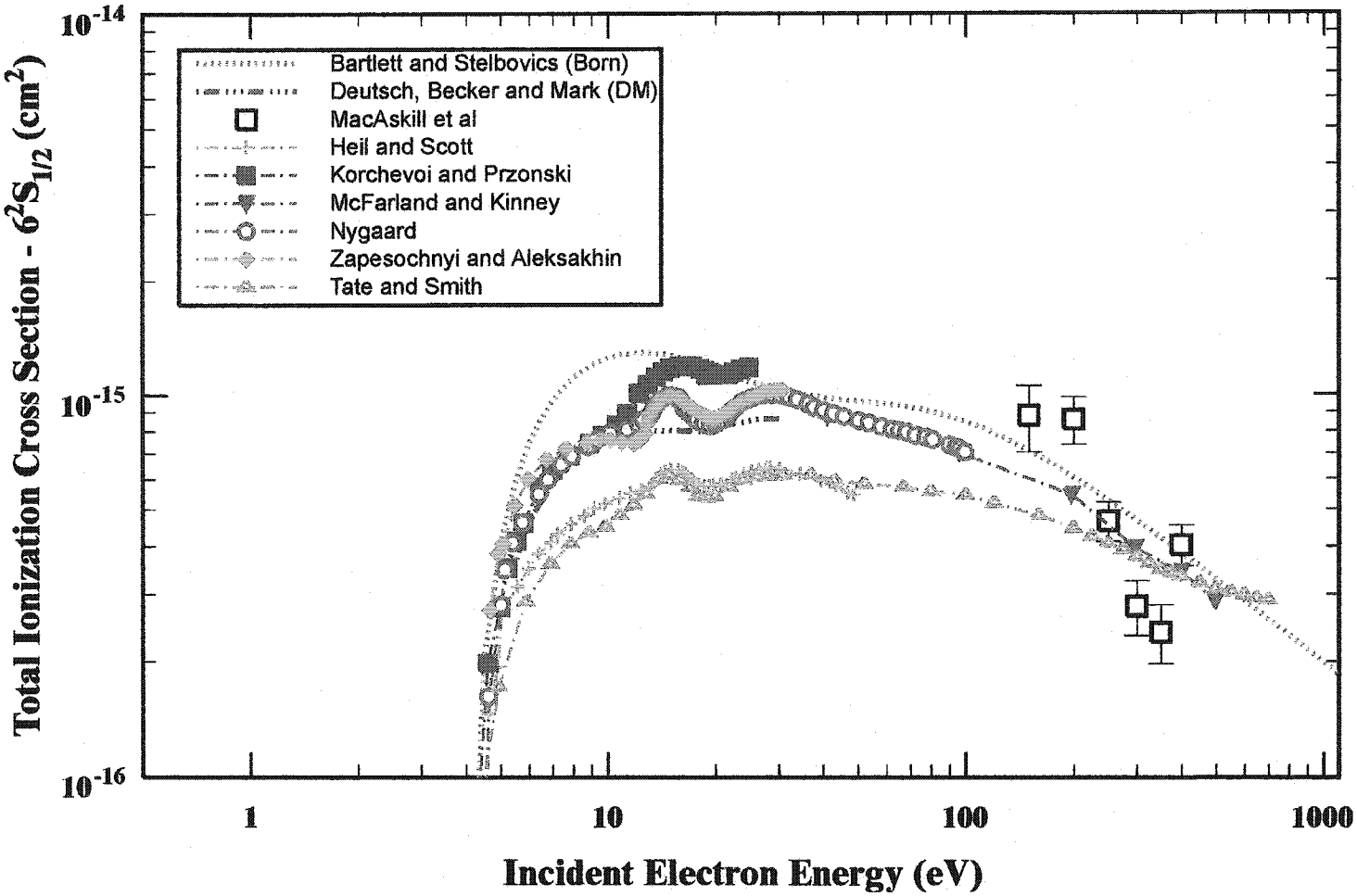

Figure 7.17: Total ionization cross sections for the $6^2S_{1/2}$ ground state of cesium. The data sets seems to be converging at higher energies (> 100 eV), but a large discrepancy exists at lower energies. The Tate and Smith cross section is a relative cross section and was scaled to fit the McFarland and Kinney cross section at high energy.

7.7 Total Ionization Cross Section ($6^2P_{3/2}$)

The measurements for the total ionization cross section of the $6^2P_{3/2}$ excited state were made in a similar fashion to those for the total ionization cross section of the ground state, but there were no changes to the laser system. The repumping laser was left in DC mode, and the trapping laser was left fully detuned from the trapping transition. The electron pulse had the same timing as for the ground state ionization. A timing diagram for the total ionization cross section fluorescence measurements is shown in Fig. 7.18.

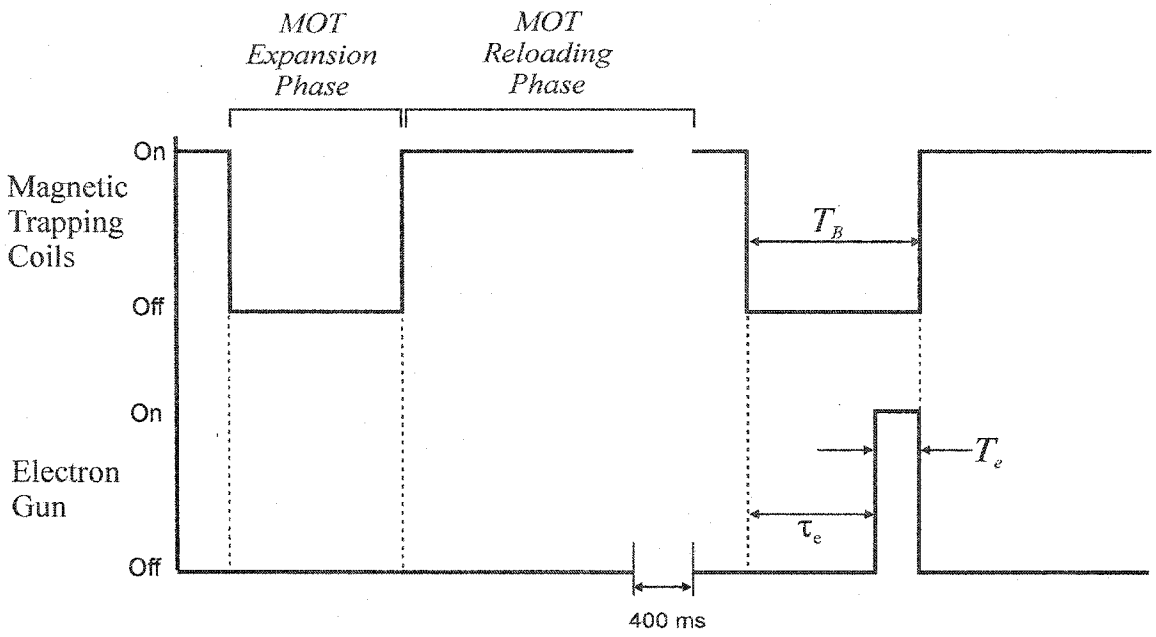

Figure 7.18: Timing diagram for the measurement of the total ionization cross section of the $6^2P_{3/2}$ excited state of cesium. Note that there are no modifications to either the trapping or repumping lasers.

The set of fluorescence decay curves from the total ionization cross section measurements are shown in Fig. 7.19. These curves do allow the use of both the linear regression method and the difference method to calculate the trap loss rates. The calculated values for the trap loss have a larger error associated with them, just as the values from the total ionization cross section, due to the shorter interaction time with the electron beam.

The values obtained for the total ionization cross section of the excited state are shown in Fig. 7.20. The data points have the same spread as those for the ground state

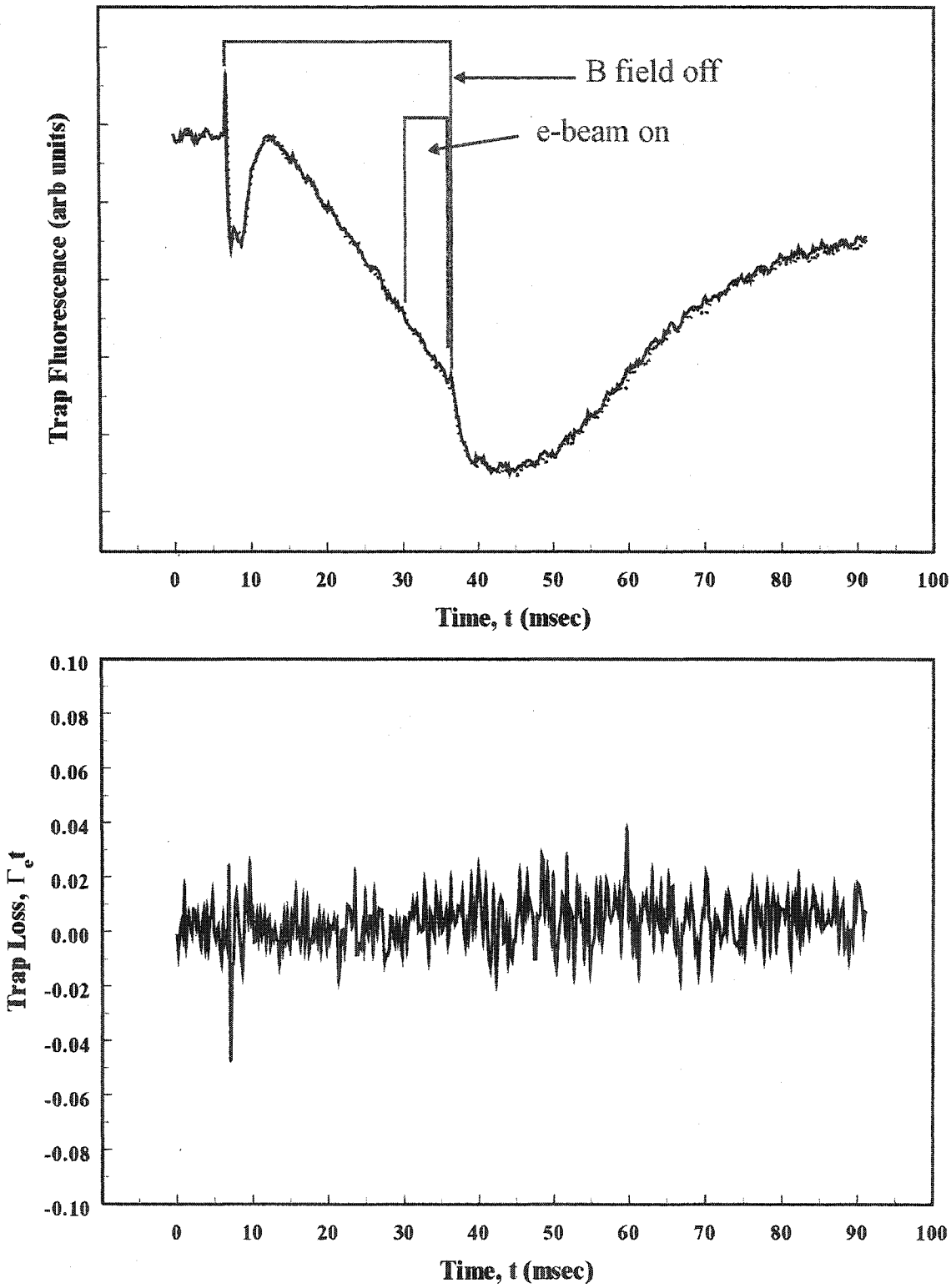

Figure 7.19: Fluorescence decay curves (upper) and trap loss curve (lower) for the measurement of the total ionization cross section of the $6^2P_{3/2}$ excited state.

ionization cross section shown in Fig. 7.17. The values for the excited state ionization cross section are at roughly the same value as those for the ground state. Any difference between the actual cross sections is not discernable, with the uncertainty associated with both data sets, and suggests that continued efforts are needed with the second generation system to provide more accurate data for both of the ionization cross sections. At present, there are no other data for the excited state ionization cross section.

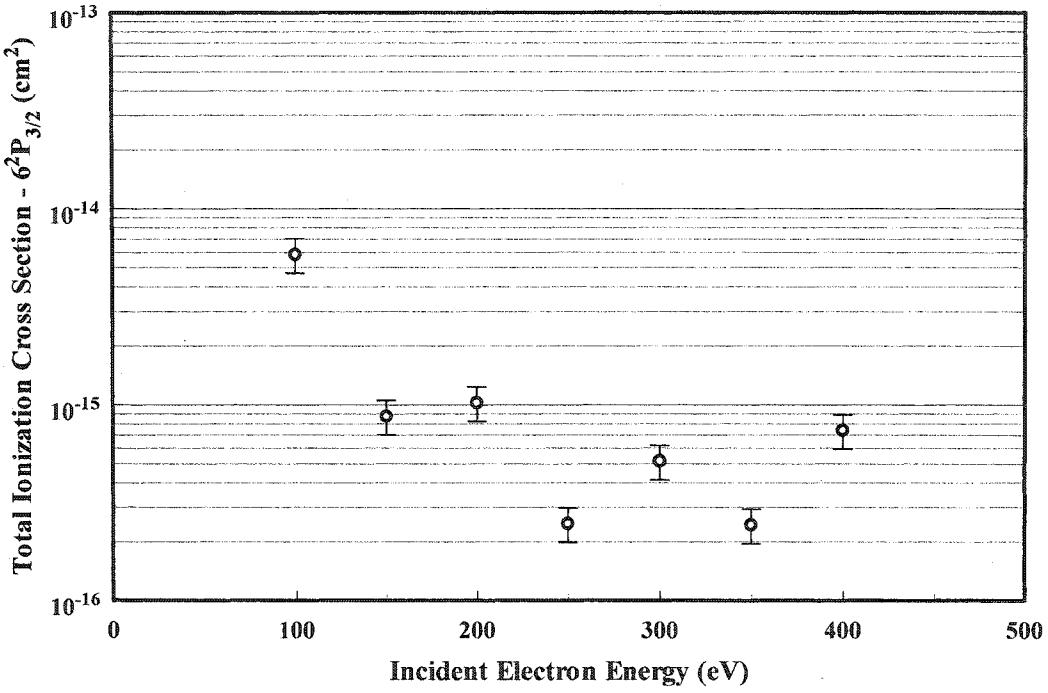

Figure 7.20: Measured data for the total ionization cross section of the $6^2P_{3/2}$ excited state of cesium. The data shown here were measured entirely with the first generation electron MOT system.

CHAPTER 8. CONCLUSION

The ground state total cross section data gathered from this experiment provided a very good agreement with the existing cross section data from Brode, despite the claims of other groups that his data was consistently off over the entire energy range. The addition of these results with the results of the Kauppila and Stein group give a range of data covering high energies down to the low energy data sets of Visconti and of Jaduszliwer. The combined data sets from the four groups provides an entirely experimental determination of the total ground state of cesium from 0 to 400 eV, which converges with the Brode data at high energy. The overlap of the results from the four experimental groups is remarkable, showing excellent agreement over the entire energy range.

The modifications made by Brode were rebuked by his contemporaries [BRODE 29]. They argued that his apparatus would only yield qualitative results due to deficiencies arising from his simplifications to the Ramsauer apparatus. Despite these arguments, Brode persisted with his claims that his apparatus could also give quantitative results. With the experimental measurements reported from this work, combined with the Kauppila and Stein data, show that the Brode data does in fact have the wrong energy dependence and is not off by a scale factor as suggested from earlier work. The cross sections has very good agreement at higher energies, but the increased Brode values at lower energies suggest that there was excessive scattering-out of his electron beam at these energies. Even with the excessive scattering-out, it is difficult to explain the appearance of the sharp maxima in his data near the first ionization potential.

The quality of the results is further reinforced by the excellent agreement with the convergent close-coupling calculations of Bray and the R-matrix pseudostate calculations of Bartschat. The remaining discrepancy in the total cross section lies with the theoretical calculations in the low energy. There are several differences in the types of calculations used, primarily in their assumptions of the target structure. With a target as complex as cesium, these structure effects become increasingly important. It is left to the theoretical groups to handle this discrepancy, and in the process make some advances with the theoretical models.

The data for the total cross section of the excited state shows a very good agreement with the calculations of Bray. The same kind of agreement for the excited state as is clear

with the results for the ground state, lends confidence to the results of the excited state. The experimental data for the excited state cross section was measured with the same apparatus and technique as was used for the ground state. Furthermore, the CCC data for the excited state came from the same set of calculations as for the ground state.

As these results are the first of their kind, there is no data for comparison. These results will prove useful for people in plasma physics, helping to improve the understanding of atomic collision processes as the atom moves from the ground state. Previous works on electron collisions with excited state targets consist primarily of collisions with metastable states, with some work on relative measurements of short-lived excited state beam targets. Although these previous works could not obtain the large excited state fractions possible with a MOT. This work involves absolute cross sections for electron collisions with short-lived excited states, that are not isolated from optical decay to the ground state.

The results for the total ionization cross section of the ground state show some agreement with the existing data. However, if we can consider the total cross section of the ground state as, essentially, complete over the energy range of 0 to 400 eV, the ground state ionization cross section is the opposite. The discrepancy between measurements is surprising considering the volume of data collected over the past 70 years. There is some general agreement at higher energies. However, there is no definitive set of results at the lower energies, with the agreement becoming worse as the ionization threshold is approached.

This may be the result of high signals from metastable ion yield in the previous experiments, the use of some questionable methods for making cross sections absolute, or for excessive scattering-in or scattering-out of the electron beams. However, it is impossible to determine exactly the cause of the discrepancies with the presented data from this research, as the disagreements between experimental measurements is pronounced at energies less than 100 eV.

The theoretical data from Bartlett and Stelbovics provides the latest, and most sophisticated calculations available for cesium. The absence of data from the CCC theory is a result of problems the theory has with ionization of a complex target such as cesium. Bray had initiated some CCC calculations for the ionization cross sections but met with limited

success during his investigation. This has prompted an investigation of the workings of the close coupling theoretical models to determine the reasons for the lack of success. To date, the best theoretical description for the total ionization cross section is the modified Born approximation calculations

The data from this research for the total ionization cross section of the excited state is the only data presently available. This work is significant to all aspects of plasma physics. There has been no theoretical data provided for this cross section, at the time of writing. The bulk of the existing theory closest to this would be for a simultaneous, or two stage process where the target is first excited followed by ionization. The experimental method used for this research has posed an entirely new problem for the theoretical groups.

There are a wide variety of future experiments that can be investigated with the electron MOT apparatus. In terms of electron scattering experiments, obviously, more work can be carried out on the cross sections presented here for lower impact energies. In addition, the measurements for the ionization cross sections can be performed again with ion detectors *in situ*. There is also the capability with the electron MOT system to perform absolute measurements of excitation cross sections from both the $6^2S_{1/2}$ ground and the $6^2P_{3/2}$ excited states.

There is also the ability to perform probe laser studies of the MOT, with and without the impacting electrons. For instance, absorption and saturated absorption spectroscopy can be performed on the trapped atoms, with and without the electron beam present. There is also the possibility of probing the trapped atoms with a far-off resonance laser, with the electron beam present to observe any effects.

There are also experiments that can be carried out on the trap itself, where the properties of the MOT are explored. Experiments such as studying the classic mechanical properties of a MOT performed by Xu *et al.* [XU 02] and using a probe laser to measure trap populations performed by Chen *et al.* [CHEN 01] can easily be carried out with the existing system. They would also be suitable for high school or undergraduate research projects. These experiments would provide a relatively easy experimental method and analysis, while conveying the techniques of laser cooling and trapping.

APPENDIX 1 - Physical Constants

Taken from CODATA values from NIST (http://physics.nist.gov/constants)

Original Sources:

Peter J. Mohr and Barry N. Taylor, CODATA Recommended Values of the Fundamental Physical Constants, (1998)
Journal of Physical and Chemical Reference Data, Vol. 28, No. 6, (1999)
Review of Modern Physics, Vol. 72, No. 2, (2000)

Universal Constants

Speed of light in vacuum	c	299 792 458 (exact)	m s^{-1}
Magnetic constant	μ_0	$4\pi \times 10^{-7}$ (exact)	N A^{-2}
Electric constant			
$\varepsilon_0 = 1/\mu_0 c^2$	ε_0	8.854 187 817... $\times 10^{-12}$ (exact)	F m^{-1}
Planck constant	h	6.626 068 76(52) $\times 10^{-34}$	J s
$\hbar = h/2\pi$	$\hbar$	1.054 571 596(82) $\times 10^{-34}$	J s

Electromagnetic Constants

Elementary charge	e	1.602 176 462(63) $\times 10^{-19}$	C
Bohr magneton			
$\mu_B = e\hbar/2m_e$	μ_B	927.400 899(37) $\times 10^{-26}$	J T^{-1}
Nuclear magneton			
$\mu_N = e\hbar/2m_p$	μ_N	5.050 783 17(20) $\times 10^{-27}$	J T^{-1}

Atomic and Molecular Constants

Fine structure constant			
$\alpha = e^2/4\pi\varepsilon_0\hbar c$	α	7.297 352 533(27) $\times 10^{-3}$	
Rydberg constant			
$R_\infty = \alpha 2m_e c/2h$	R_∞	10 973 731.568 549(83)	m^{-1}
Bohr radius			
$a_0 = \alpha/4\pi R_\infty$	a_0	0.529 177 2083(19) $\times 10^{-10}$	m
Electron mass	m_e	9.109 381 88(72) $\times 10^{-31}$	kg
Electron charge to mass ratio	$-e/m_e$	-1.758 820 174(71) $\times 10^{11}$	C kg^{-1}
Electron magnetic moment	μ_e	-928.476 362(37) $\times 10^{-26}$	J T^{-1}
Electron magnetic moment anomaly			
$a_e = \lvert\mu_e\rvert/\mu_B - 1$	a_e	1.159 652 1869(41) $\times 10^{-3}$	
Electron g-factor			
$g_e = -2(1+a_e)$	g_e	-2.002 319 304 3737(82)	
Electron gyromagnetic ratio			
$\gamma_e = 2\lvert\mu_e\rvert/\hbar$	γ_e	1.760 859 794(71) $\times 10^{11}$	s^{-1} T^{-1}
Neutron mass	m_n	1.674 927 16(13) $\times 10^{-27}$	kg
Neutron magnetic moment	μ_n	-0.966 236 40(23) $\times 10^{-26}$	J T^{-1}
Neutron g-factor			
$g_n = 2\mu_n/\mu_N$	g_n	-3.826 085 45(90)	
Neutron gyromagnetic ratio			
$\gamma_n = 2\lvert\mu_n\rvert/\hbar$	γ_n	1.832 471 88(44) $\times 10^{8}$	s^{-1} T^{-1}
Proton mass	m_p	1.672 621 58(13) $\times 10^{-27}$	kg
Proton magnetic moment	μ_p	1.410 606 633(58) $\times 10^{-26}$	J T^{-1}
Proton g-factor			
$g_p = 2\mu_p/\mu_N$	g_p	5.585 694 675(57)	

Proton gyromagnetic ratio $\gamma_p = 2\mu_p/\hbar$	γ_p	2.675 222 12(11) x 10^{8}	$s^{-1}\,T^{-1}$

Physico-Chemical

Avogadro constant	N_A	6.022 141 99(47) x 10^{23}	mol^{-1}
Atomic mass constant	m_u	1.660 538 73(13) x 10^{-27}	kg
Molar gas constant	R	8.314 472(15)	$J\,mol^{-1}\,K^{-1}$
Boltzmann Constant	k	1.380 6503(24) x 10^{-23}	$J\,K^{-1}$

APPENDIX 2 - Conversion Factors

1 m = 10^9 nm = 10^{10} Å = 1.889726 x 10^{10} a_0
1 J = 6.2415097 x 10^{18} eV = 10^7 erg
1 eV = 1.6021765 x 10^{-19} J = 1.6021765 x 10^{-12} erg
1 Torr = 133.322 Pa = 1.33322 x 10^{-3} bar = 1.31579 x 10^{-3} atm = 1 mm Hg
1 bar = 10^5 Pa
1 atm = 1.01325 x 10^5 Pa
1 Tesla = 10^4 Gauss

kT = 8.617 x 10^{-5} eV at 1K
= 0.0086173 eV at 100 K
= 0.025852 eV at 300K

hc = 1.986445 x 10-25 J m
= 1.239842 x 10-6 eV m
= 1239.842 eV nm

1 eV is equivalent to
11604.50595 K (from E = kT)
241798.95 GHz (from E = $h\nu$)
1239.842 nm (from E = hc/λ)
8065.545 cm^{-1} (from E = $hc\,\overline{\nu}$)

Cross Section Abscissa
electron velocity (cm/s) = [voltage (volt)]$^{1/2}$ x 5.93097 x 10^7

Cross Section Ordinate
σ (cm^2) = 2.80029 x 10^{-17} x σ (a_0^2) = 8.79736 x 10^{-17} x σ (πa_0^2) = x 10^{-24} σ (barn)
σ (cm^2) = (absorption coefficient) x 2.83 x 10^{-17}

APPENDIX 3 - Cesium Physical Data

Atomic Mass	m	132.905 451 931(27)	u	[RAINV 01]
		2.206 94650(17)	kg	
Density	ρ_m	1879	kg m^{-1}	
Melting Point	T_m	301.55	K	
Boiling Point	T_b	942.5	K	
Vapour Pressure	P_v	1.26 x 10^{-6}	Torr (@298K)	
Specific Heat	c_p	0.242	J g^{-1} K^{-1}	
Heat of Vapourization	H_m	67.7	kJ mol^{-1}	
Heat of Fusion	H_f	2.09	kJ mol^{-1}	
Thermal Conductivity	j_u	35.9	W m^{-1} K^{-1}	
Electrical Conductivity	j_e	4.891 x 10^6	Ω^{-1} m^{-1}	
Electronegativity				
Pauling		0.79	Pauling units	
Allred-Rochow		0.86	Pauling units	
Crystal Structure		BCC		
Effective Nuclear Charge				
Slater		2.20		
Clementi		6.36		
Froese-Fischer		8.56		
Nuclear Spin	I	7/2		
Ionization Potential	I_p	31 406.467 66(15)	cm^{-1}	[WEBER 87]
		3.893 905 (15)	eV	
Electron spin *g*-factor	g_s	2.002 319 304 373 7(80)		
Electron orbital g-factor	g_l	0.999 995 87		
Fine structure Landé g-factor				
$6^2S_{1/2}$	g	2.002 540 32(20)		[ARIMO 77]
$6^2P_{3/2}$	g	1.3340(3)		[ARIMO 77]
Nuclear g-factor	g_I	-0.000 398 853 95(52)		[ARIMO 77]

APPENDIX 4 - Dipole Matrix Elements

$6^2S_{1/2}(F=4, m_F) \longrightarrow 6^2P_{3/2}(F', m'_F = m_F + 1)$

F' \ m'_F	-4	-3	-2	-1	0	1	2	3	4
5	$\sqrt{\frac{1}{90}}$	$\sqrt{\frac{1}{30}}$	$\sqrt{\frac{1}{15}}$	$\sqrt{\frac{1}{9}}$	$\sqrt{\frac{1}{6}}$	$\sqrt{\frac{7}{30}}$	$\sqrt{\frac{14}{45}}$	$\sqrt{\frac{2}{5}}$	$\sqrt{\frac{1}{2}}$
4	$\sqrt{\frac{7}{120}}$	$\sqrt{\frac{49}{480}}$	$\sqrt{\frac{21}{160}}$	$\sqrt{\frac{7}{48}}$	$\sqrt{\frac{7}{48}}$	$\sqrt{\frac{21}{160}}$	$\sqrt{\frac{49}{480}}$	$\sqrt{\frac{7}{120}}$	
3	$\sqrt{\frac{7}{72}}$	$\sqrt{\frac{7}{96}}$	$\sqrt{\frac{5}{96}}$	$\sqrt{\frac{5}{144}}$	$\sqrt{\frac{1}{48}}$	$\sqrt{\frac{1}{96}}$	$\sqrt{\frac{1}{288}}$		

σ^+ - polarization

$6^2S_{1/2}(F=4, m_F) \longrightarrow 6^2P_{3/2}(F', m'_F = m_F)$

F' \ m'_F	-4	-3	-2	-1	0	1	2	3	4
5	$-\sqrt{\frac{1}{10}}$	$-\sqrt{\frac{8}{45}}$	$-\sqrt{\frac{7}{30}}$	$-\sqrt{\frac{4}{15}}$	$-\sqrt{\frac{5}{18}}$	$-\sqrt{\frac{4}{15}}$	$-\sqrt{\frac{7}{30}}$	$-\sqrt{\frac{8}{45}}$	$-\sqrt{\frac{1}{10}}$
4	$-\sqrt{\frac{7}{30}}$	$-\sqrt{\frac{21}{160}}$	$-\sqrt{\frac{7}{120}}$	$-\sqrt{\frac{7}{480}}$	0	$\sqrt{\frac{7}{480}}$	$\sqrt{\frac{7}{120}}$	$\sqrt{\frac{21}{160}}$	$\sqrt{\frac{7}{30}}$
3		$\sqrt{\frac{7}{288}}$	$\sqrt{\frac{1}{24}}$	$\sqrt{\frac{5}{96}}$	$\sqrt{\frac{1}{18}}$	$\sqrt{\frac{5}{96}}$	$\sqrt{\frac{1}{24}}$	$\sqrt{\frac{7}{288}}$	

π - polarization

$6^2S_{1/2}(F=4, m_F) \longrightarrow 6^2P_{3/2}(F', m'_F = m_F - 1)$

F' \ m'_F	-4	-3	-2	-1	0	1	2	3	4
5	$\sqrt{\frac{1}{2}}$	$\sqrt{\frac{2}{5}}$	$\sqrt{\frac{14}{45}}$	$\sqrt{\frac{7}{30}}$	$\sqrt{\frac{1}{6}}$	$\sqrt{\frac{1}{9}}$	$\sqrt{\frac{1}{15}}$	$\sqrt{\frac{1}{30}}$	$\sqrt{\frac{1}{90}}$
4		$-\sqrt{\frac{7}{120}}$	$-\sqrt{\frac{49}{480}}$	$-\sqrt{\frac{21}{160}}$	$-\sqrt{\frac{7}{48}}$	$-\sqrt{\frac{7}{48}}$	$-\sqrt{\frac{21}{160}}$	$-\sqrt{\frac{49}{480}}$	$-\sqrt{\frac{7}{120}}$
3			$\sqrt{\frac{1}{288}}$	$\sqrt{\frac{1}{96}}$	$\sqrt{\frac{1}{48}}$	$\sqrt{\frac{5}{144}}$	$\sqrt{\frac{5}{96}}$	$\sqrt{\frac{7}{96}}$	$\sqrt{\frac{7}{72}}$

σ^- - polarization

Dipole matrix elements for transitions from the $F = 4$ hyperfine ground state cesium. There are three tables for each of the three possible incident polarization. The values in the tables are relative to the transition matrix element.

$$\langle J=1/2 \| er \| J'=3/2 \rangle$$

$6^2S_{1/2}(F=3, m_F) \longrightarrow 6^2P_{3/2}(F', m'_F = m_F + 1)$

F' \ m'_F	-3	-2	-1	0	1	2	3
4	$\sqrt{\frac{5}{672}}$	$\sqrt{\frac{5}{224}}$	$\sqrt{\frac{5}{112}}$	$\sqrt{\frac{25}{336}}$	$\sqrt{\frac{25}{224}}$	$\sqrt{\frac{5}{32}}$	$\sqrt{\frac{5}{24}}$
3	$\sqrt{\frac{3}{32}}$	$\sqrt{\frac{5}{32}}$	$\sqrt{\frac{3}{16}}$	$\sqrt{\frac{3}{36}}$	$\sqrt{\frac{5}{32}}$	$\sqrt{\frac{3}{32}}$	
2	$\sqrt{\frac{5}{14}}$	$\sqrt{\frac{5}{21}}$	$\sqrt{\frac{1}{7}}$	$\sqrt{\frac{1}{14}}$	$\sqrt{\frac{1}{42}}$		

σ^+ - polarization

$6^2S_{1/2}(F=3, m_F) \longrightarrow 6^2P_{3/2}(F', m'_F = m_F)$

F' \ m'_F	-3	-2	-1	0	1	2	3
4	$-\sqrt{\frac{5}{96}}$	$-\sqrt{\frac{5}{56}}$	$-\sqrt{\frac{25}{224}}$	$-\sqrt{\frac{5}{42}}$	$\sqrt{\frac{25}{224}}$	$\sqrt{\frac{5}{56}}$	$\sqrt{\frac{5}{24}}$
3	$-\sqrt{\frac{9}{32}}$	$-\sqrt{\frac{1}{8}}$	$-\sqrt{\frac{1}{32}}$	0	$\sqrt{\frac{1}{32}}$	$\sqrt{\frac{1}{8}}$	$\sqrt{\frac{9}{32}}$
2		$\sqrt{\frac{5}{42}}$	$\sqrt{\frac{4}{21}}$	$\sqrt{\frac{3}{14}}$	$\sqrt{\frac{4}{21}}$	$\sqrt{\frac{5}{42}}$	

π - polarization

$6^2S_{1/2}(F=3, m_F) \longrightarrow 6^2P_{3/2}(F', m'_F = m_F - 1)$

F' \ m'_F	-3	-2	-1	0	1	2	3
4	$\sqrt{\frac{5}{24}}$	$\sqrt{\frac{5}{32}}$	$\sqrt{\frac{25}{224}}$	$\sqrt{\frac{25}{336}}$	$\sqrt{\frac{5}{112}}$	$\sqrt{\frac{5}{224}}$	$\sqrt{\frac{5}{672}}$
3		$-\sqrt{\frac{3}{32}}$	$-\sqrt{\frac{5}{32}}$	$-\sqrt{\frac{3}{16}}$	$-\sqrt{\frac{3}{16}}$	$-\sqrt{\frac{5}{32}}$	$-\sqrt{\frac{3}{32}}$
2			$\sqrt{\frac{1}{42}}$	$\sqrt{\frac{1}{14}}$	$\sqrt{\frac{1}{7}}$	$\sqrt{\frac{5}{21}}$	$\sqrt{\frac{5}{14}}$

σ^- - polarization

Dipole matrix elements for transitions from the $F = 3$ hyperfine ground state cesium. There are three tables for each of the three possible incident polarization. The values in the tables are relative to the transition matrix element.

$$\langle J=1/2 \| er \| J'=3/2 \rangle$$

APPENDIX 5 - Error Analysis

Propagation of Error

i) Sum Rule:
For a function of the form

$$y = a_1x_1 + a_2x_2 + \ldots + a_Nx_N \tag{A5.1}$$

the standard error, δy, in the function y is given by

$$\delta y = \sqrt{\left(a_1\delta x_1\right)^2 + \left(a_2\delta x_2\right)^2 + \ldots + \left(a_N\delta x_N\right)^2} \tag{A5.2}$$

ii) Product Rule:
For a function of the form

$$y = \left(a_1x_1\right)\cdot\left(a_2x_2\right)\cdot\ldots\cdot\left(a_Nx_N\right) \tag{A5.3}$$

the relative error, $\delta y/y$, in the function y is given by

$$\frac{\delta y}{y} = \sqrt{\left(\frac{\delta x_1}{x_1}\right)^2 + \left(\frac{\delta x_2}{x_2}\right)^2 + \ldots + \left(\frac{\delta x_N}{x_N}\right)^2} \tag{A5.4}$$

iii) Power Rule:
For a function of the form

$$y = x^m \tag{A5.5}$$

the relative error, $\delta y/y$, in the function y is given by

$$\frac{\delta y}{y} = \left|m\frac{\delta x}{x}\right| \tag{A5.6}$$

iv) Exponential Rule:
For an exponential function of the form

$$y = Ae^{bx} \tag{A5.7}$$

the relative error, $\delta y/y$, in the function y is given by

$$\frac{\delta y}{y} = |b|\delta x \tag{A5.8}$$

Linear Regression

For a linear function with slope m, and intercept b,

$$y = mx + b \tag{A5.9}$$

we wish to define a quantity d_i, such that

$$d_i = y_i - \left(mx_i + b\right) \tag{A5.10}$$

that is used to define a new function, u

$$u = \sum_{i=1}^{N} d_i^2 \tag{A5.11}$$

Perform an optimization of the function u to yield a minimum deviation

$$\frac{\partial}{\partial m}\left(\sum_{i=1}^{N} d_i^2\right) = m\sum_i x_i^2 + \sum_i x_i - \sum_i x_i y_i \qquad \text{A5.12}$$

$$\frac{\partial}{\partial b}\left(\sum_{i=1}^{N} d_i^2\right) = m\sum_i x_i + bN - \sum_i y_i \qquad \text{A5.13}$$

Setting expressions for partials equal to zero and solving the resulting set of equations for m and b gives

$$m = \frac{N\sum x_i y_i - \sum x_i \sum y_i}{N\sum x_i^2 - \sum x_i \sum x_i} \qquad \text{A5.14}$$

$$b = \frac{\sum y_i \sum x_i^2 - \sum x_i \sum x_i y_i}{N\sum x_i^2 - \sum x_i \sum x_i} \qquad \text{A5.15}$$

which are the "best-fit" values for the slope and intercept

Applications

i) Current Density(Constant Current Model)

The current density is given by

$$J_e = \frac{I_T}{\pi r^2} \qquad \text{A5.16}$$

Combining Eq's. A5.6 and A5.4 gives the relative error

$$\frac{\delta J_e}{J_e} = \sqrt{\left(\frac{\delta I_T}{I_T}\right)^2 + 4\left(\frac{\delta r}{r}\right)^2} \qquad \text{A5.17}$$

that gives the systematic error in J_e.

For an individual beam probe current reading, with

$$J_e = \frac{1}{2}\frac{i_n}{\sqrt{r^2 - (x_n - c)^2}} \qquad \text{A5.18}$$

the error is given by the following procedure. Let

$$u_n = r^2 - (x_n - c)^2 \qquad \text{A5.19}$$

and then find the relative error

$$\frac{\delta J_e}{J_e} = \sqrt{\left(\frac{\delta i_n}{i_n}\right)^2 + \left(\frac{1}{2}\frac{\delta u_n}{u_n}\right)^2} \qquad \text{A5.20}$$

by first determining the standard error in u_n

$$\delta u_n = \sqrt{\left(\delta r^2\right)^2 + \left(\delta\left[x_n - c\right]^2\right)^2} \qquad \text{A5.21}$$

to give the relative error in a probe reading

$$\frac{\delta J_e}{J_e} = \sqrt{\left(\frac{\delta i_n}{i_n}\right)^2 + \frac{r^2\delta r^2 + \left(x_n - c\right)^2\left(\delta x_n^2 + \delta c^2\right)}{r^2 - \left(x_n - c\right)^2}} \qquad \text{A5.22}$$

Alternatively, using the quasi-linear regression discussed in the Chapter 6, the profile is transformed to allow c, the beam centre, to be dropped from the error calculations, by reducing the difference in slopes between the separated halves of the profile. Then the two halves are recombined and a linear regression performed, where the slope of the transformed line is the current density. In this case, the error in the slope gives a statistical error for the current density. (we use statistical here since the standard deviation of the probe readings is used to give the error in the slope)

ii) Trap Loss

The error in the trap loss is determined in one of two ways, depending on the method used. If a linear regression method is used, the error in the trap-loss rate is given in the usual way. If a difference method is used, then the error in the trap loss is given by the standard deviation of the trap loss over the reloading section, so that

$$\delta\Gamma_e = \frac{s_{\Gamma_e}}{\sqrt{n}} \qquad \text{A5.23}$$

iii) Cross Section

Each cross section value is found by combining the errors in the current density and the loss rate using the product rule to give a standard error in each cross section value. When each cross section value is combined, there are two errors that are calculated. The first is the systematic error in the cross section and is given by

$$\delta\bar{\sigma} = \frac{1}{N}\sqrt{\left(\delta\sigma_1\right)^2 + \left(\delta\sigma_2\right)^2 + \ldots + \left(\delta\sigma_N\right)^2} \qquad \text{A5.24}$$

which arises from the sum rule, since we are averaging the cross section values. We can also determine the statistical error in the cross section. This is taken from the standard deviation of the cross section values

$$\delta\bar{\sigma} = \frac{s_\sigma}{\sqrt{N}} \qquad \text{A5.25}$$

where s_σ is the standard deviation of the cross section values, N is the number of cross section values being combined.

REFERENCES

[ALLEY 95] Alley, R., Aoyagi, H., Clendenin, J., Frisch, J., Garden, C., Hoyt, E., Kirby, R., Klaisner, L., Kulikov, A., Miller, R., Mulhollan, G., Prescott, C., Saez, P., Schultz, D., Tang, H., Turner, J., Witte, K., Woods, M., Yeremian, A.D., Zoltorev, M., "*The Stanford Linear Accelerator Polarized Electron Source*", Nucl. Instr. and Meth. A, 365, 1, (1995).

[ARIMO 77] Arimondo, E., Inguscio, M., Violino, P., "*Experimental Determinations of the Hyperfine Structure in the Alkali Atoms*", Rev. Mod. Phys., **49**, 31, (1977).

[ASPEC 86] Aspect, A., Dalibard, J., Heidmann, A., Salomon, C., Cohen-Tannoudji, C., "*Cooling Atoms with Stimulated Emission*", Phys. Rev. Lett., **57**, 1688, (1986).

[BAGLI 00] Baglin, V., Bojko, J., Grobner, O., Henrist, B., Hilleret, N., Scheuerlein, C., Taborelli, M., "*The Secondary Electron Yield of Technical Materials and its Variation with Surface Treatments*", Proceedings of EPAC 2000, Vienna, Austria.

[BAGNA 87] Bagnato, V. S., Lafyatis, G. P., Martin, A. G., Raab, E. L., Ahmad-Bitar, R. N., Pritchard, D. E., "*Continuous Stopping and Trapping of Neutral Atoms*",Phys. Rev. Lett., **58**, 2194, (1987).

[BARTL 02] Bartlett, P. L., Stelbovics, A. T., "*Calculation of Electron-Impact Total Ionization Cross-Sections*", Phys. Rev. A, **66**, 012707, (2002).

[BARTL 02a] Bartlett, P. L., Stelbovics, A. T., private communication, (2002).

[BARTS 93] Bartschat, K., "*Low-Energy Electron Scattering from Caesium Atoms - Comparison of a Semirelativistic Breit-Pauli and a Full Relativistic Dirac Treatment*", J. Phys. B, **26**, 3595, (1993).

[BECKE 00] Workshop on "*Electron-Driven Processes: Scientific Challenges and Technological Opportunities*" Stevens Institute of Technology, (2000). Available online at http://attila.stevens-tech.edu/physics/People/Faculty/Becker/EDP

[BEDER 68] Bederson, B., Methods Exptl. Phys., **7A**, 67, (1968).

[BEDER 71] Bederson, B., Kieffer, L. J., "*Total Electron-Atom Collision Cross Sections at Low Energies — A Critical Review*", Rev. Mod. Phys., **43**, 601, (1971).

[BERGE 87] Bergeman, T., Erez, G., Metcalf, H. J., "*Magnetostatic Trapping Fields for Neutral Atoms*", Phys. Rev. A, **35**, 1535, (1987).

[BRANS 83] Bransden, B. H., Joachain, C. J., *"Physics of Atoms and Molecules"*, Addison Wesley Longman Limited, Essex, England, (1983).

[BRAY 95] Bray, I., Stelbovics, A. T. , "*Calculation of Electron Scattering in Hydrogenic Targets.*" Adv. At. Mol. Opt. Phys. **35**, 209 (1995).

[BRINK 62] Brink, G. O., "*Ionization of Alkali Atoms by Electron Bombardment*", Phys. Rev., **127**, 1204, (1962).

[BRINK 64] Brink, G. O., "*Absolute Ionization Cross Sections of the Alkali Metals*", Phys. Rev., **134**, A345, (1964).

[BRODE 29] Brode, R. B., "*The Absorption Coefficient for Slow Electrons in Alkali Metal Vapors*", Phys. Rev., **34**, 673, (1929).

[BROWN 96] Brown, J. W., Churchill, R. V., "*Complex Variables and Applications*", McGraw-Hill, New York, (1996).

[CAITL 00] Caitlin, G. A., Roger, Y. V., "*Equilibrium Chemistry in a Brown Dwarf's Atmosphere: Cesium in GLIESE 229B*", Astrophys. J., **532**, L59, (2000).

[CHEN 78] Chen, S. T., Gallagher, A. C., "*Electron Excitation of the Resonance Lines of the Alkali-Metal Atoms*", Phys. Rev. A, **17**, 551, (1978).

[CHEN 01] Chen, Y.-C., Liao, Y.-A., Hsu, L., Yu, I. A., "*Simple Technique for Directly and Accurately Measuring the Number of Atoms in a Magneto-Optical Trap*", Phys. Rev. A, **64**, 031401(R), (2001).

[CHU 86] Chu, S., Bjorkholm, J. E., Ashkin, A., Cable, A., "*Experimental Observation of Optically Trapped Atoms*", Phys. Rev. Lett., **57**, 314, (1986).

[COHEN 98] Coehn-Tannoudji, C., Dupont-Roc, J., Grynberg, G., "*Atom-Photon Interactions*", Wiley

[CROWN 65] Crown, J. C., Russek, A., "*Electron-Alkali-Atom Interaction Potential and Elastic-Scattering Cross Section*", Phys. Rev., **138**, A669, (1965).

[DALIB 89] Dalibard, J., "*New Schemes in Laser Cooling*", Atomic Physics XI, World Scientific, Singapore, (1989).

[DALIB 89a] Dalibard, J., Cohen-Tannoudji, C., "*Laser Cooling Below the Doppler Limit by Polarization Gradients - Simple Theoretical Models*", J. Opt. Soc. Am. B, **6**, 2058, (1989).

[DEDMA 01] Dedman, C. J., Baldwin, K. G. H., Colla, M., "*Fast Switching of Magnetic Fields in a Magneto-Optic Trap*", Rev. Sci. Instr., **72**, 4055 (2001).

[DEUTS 99] Deutsch, H., Becker, K., Mark, T. D., "*Application of the DM Formalism to the Calculation of Electron-Impact Ionization Cross Sections of Alkali Atoms*", Int. J. Mass. Spec., **185/186/187**, 319, (1999).

[DORNE 00] Dorner, R., Mergel, V., Jagutzki, O., Speilberger, L., Ullrich, J., Moshammer, R., Schmidt-Bocking, H., "*Cold Target Recoil Ion Momentum Spectroscopy: a 'Momentum Microscope' to View Atomic Collision Dynamics*", Phys. Rep., **330**, 95, (2000).

[ESTER 47] Estermann, I., Foner, S. N., Stern, O., "*The Mean Free Paths of Cesium Atoms in Helium, Nitrogen, and Cesium Vapour*", Phys. Rev., **71**, 250, (1947).

[GEHEN 77] Gehenn, W., Reichert, E., "*Scattering of Electrons by Cs Atoms at Low Energies*", J. Phys. B, **10**, 3105, (1977).

[HANSC 71] Hansch, T. W., Shahin, I. S., Schawlow, A. L., "*High-Resolution Saturation Spectroscopy of the Sodium D Lines with a Pulsed Tunable Dye Laser*", Phys. Rev. Lett., **27**, 707, (1971).

[HANSC 75] Hansch, T. W., Schawlow, A. L., "*Cooling of Gases by Laser Radiation*",Opt. Commu., **13**, 68 (1975).

[HEIL 66] Heil, H., Scott, B., "*Cesium Ionization Cross Section from Threshold to 50 eV*", Phys. Rev., **145**, 279, (1966).

[JADUS 92] Jaduszliwer, B., Chan, Y. C., "*Absolute Total Cross Sections for the Scattering of 2-18 eV Electrons by Cesium Atoms*", Phys. Rev. A, **45**, 197, (1992).

[JULIE 92] Julienne, P. S., Smith, A. M., Burnett, K., "*Theory of Collisions Between Laser Cooled Atoms*", Adv. At. Mol. Opt. Phys. **30**, 141 (1992).

[KEELE 00] Keeler, M. L., Anderson, L. W., and Lin, C. C., "*Electron-Impact Ionization Cross Section Measurements Out of the 5^2P Excited State of Rubidium*", Phys. Rev. Lett., **85**, 3353, (2000).

[KIM 01] Kim, Y.-K., "*Scaling of Plane-Wave Born Cross Sections for Electron-Impact Excitation of Neutral Atoms*", Phys. Rev. A, **64**, 032713, (2001).

[KORCH 67] Korchevoi, Y. P., Przonski, A. M., Sov. Phys. *JETP*, **24**, 1089, (1967).

[MACAS 02] MacAskill, J. A., Kedzierski, W., McConkey, J. W., Domyslawska, J., Bray, I., "*Measuring Cesium Electron Impact Cross-Sections Using a Magneto-Optical Trap*", J. Elect. Spect. Rel. Phen., **123**, 173, (2002).

[MARQU 63] Marquardt, D. W., "*An Algorithm for Least-Squares Estimation of Nonlinear Parameters*", J. Soc. Indust. Appl. Math., **11**, 431, (1963).

[MCFAR 65] McFarland, R. H., Kinney, J. D., "*Absolute Cross Sections of Lithium and Other Alkali Metal Atoms for Ionization by Electrons*", Phys. Rev., **137**, A1058, (1965).

[METCA 99] Metcalf, H. J., van der Straten, P., "*Laser Cooling and Trapping*", Springer-Verlag, New-York, (1999).

[MEYST 01] Meystre, P., "*Atom Optics*", Springer-Verlag, New York, (2001).

[MIGDA 85] Migdall, A. L., Prodan, J. V., Phillips, W. D., Bergeman, T. H., Metcalf, H. J., "*First Observation of Magnetically Trapped Neutral Atoms*", Phys. Rev. Lett., **54**, 2596, (1985).

[MOORE 58] Moore, C. E., "*Atomic Energy Levels as Derived from the Analysis of Optical Spectra*", National Bureau of Standards, US Dept. of Commerce, Vol III, (1958).

[NESME 63] Nesmeyanov, A. N., "*Vapor Pressure of the Chemical Elements*", Elsevier, Amsterdam, (1963). English edition edited by Robert Gary.

[NIGHA 72] Nighan, W. L., Postma, A. J., "*Electron Momentum-Transfer Cross Section in Cesium*", Phys. Rev. A, **6**, 2109, (1972).

[NYGAA 68] Nygaard, K. J., "*Electron-Impact Ionization Cross Section in Cesium*", J. Chem. Phys., **49**, 1995, (1968).

[NYGAA 73] Nygaard, K. J., Hahn, Y. B., *"Production of Metastable Ions in Cesium-Atom-Electron Collisions*", Phys. Rev. A, **8**, 151, (1973).

[OMORI 91] Omori, T., Kurihara, Y., Nakanishi, T., Aoyagi, H., Baba, T., Furuya, T., Itoga, K., Mizuta, M., Nakamura S., Takeuchi, Y., Tsubata, M., Yoshioka, M., "*Large Enhancement of Polarization Observed by Extracted Electrons from the AlGaAs-GaAs Superlattice*", Phys. Rev. Lett., **67**, 3294 (1991).

[PRITC 86] Pritchard, D. E., Raab, E. L., Bagnato, V., Wieman, C. E., Watts, R. N., "*Light Traps Using Spontaneous Forces*", Phys. Rev. Lett., **57**, 310, (1986).

[RAAB 87] Raab, E. L., Prentiss, M., Cable, A., Chu, S., and Pritchard, D. E., "*Trapping of Neutral Sodium Atoms with Radiation Pressure*", Phys. Rev. Lett., **59**, 2631, (1987).

[RAINV 01] Rainville, S., Bradley, M. P., Porto, J. V., Thompson, J. K., Pritchard, D. E., *"Precise Measurements of the Masses of Cs, Rb and Na - A New Route to the Fine Structure Constant"*, Hyperfine Interactions **132**, 177-187, (2001)

[SAELE 79] Saelee, H., Lucas, J., "*Electron Drift Velocity and Momentum Transfer Cross-Section in Caesium Vapour*", J. Phys. D: Appl. Phys., **12**, 1275, (1979).

[SAKUR 94] Sakurai, J. J., "*Modern Quantum Mechanics*", Addison-Wesley, Reading, Massachusetts, (1994).

[SCHAP 95] Schappe, R. S., Feng, P., Anderson, L. W., Lin, C. C., and Walker, T., "*Electron Collision Cross-Sections Measured with the Use of a Magneto-Optical Trap*", Europhys. Lett., **29**, 439, (1995).

[SCHAP 96] Schappe, R. S., Walker, T., Anderson, L. W. and Lin, C. C., "*Absolute Electron-Impact Ionization Cross Section Measurements Using a Magneto-Optical Trap*", Phys. Rev. Lett., **76**, 4328, (1996).

[SESKO 89] Sesko, D. W., Walker, T., Monroe, C., Gallagher, A., Wieman, C., "*Collisional Losses from a Light-Force Trap*", Phys. rev. Lett., **63**, 961, (1989).

[SOVEY 99] Sovey, J.S., Rawlin, V.K., Patterson, M.J., "*A Synopsis of Ion Propulsion Development Projects in the United States: SERT I to Deep Space I*", NASA TM-209439, (1999).

[STECK 01] Steck, D.A., Ph. D. Thesis, University Texas of Austin, Austin, Texas, (2001).

[SUOMI 96] Suominen, K.-A., "*Theories for Cold Atomic Collisions in Light Fields*", J. Phys. B, **29**, 5981, (1996).

[STEFA 80] Stefanov, B., *"Electron Momentum-Transfer Cross Section in Cesium: Fit to Experimental Data*", Phys. Rev. A, **22**, 427, (1980).

[TANNE 88] Tanner, C. E., Wieman, C., "*Precision Measurement of the Hyperfine Structure of the ^{133}Cs 6 $P_{3/2}$ state*", Phys. Rev. A, **38**, 1616 (1988).

[TATE 34] Tate, J. T., Smith, P. T., "*Ionization Potentials and Probabilities for the Formation of Multiply Charged Ions in the Alkali Vapors and in Krypton and Xenon*", Phys. Rev., **46**, 773, (1934).

[VISCO 71] Visconti, P. J., Slevin, J. A., Rubin, K., "*Absolute Total Cross Sections for the Scattering of Low-Energy Electrons by Rubidium, Cesium, and Potassium*", Phys. Rev. A, **3**, 1310, (1971).

[WEBER 87] Weber, K.-H., Sansonetti, C. J., "*Accurate Energies of nS, nP, nD, nF, and nG Levels of Neutral Cesium*", Phys. Rev A, **35**, 4650, (1987).

[WEINE 95] Weiner, J., "*Advances in Ultracold Collsions: Experimentation and Theory*", Adv. At. Mol. Opt. Phys. **35**, 45, (1995).

[WEINE 99] Weiner, J., Bagnato, V. S., Zilio, S., Julienne, P. S., "*Experiments and Theory in Cold and Ultracold Collisions*", Rev. Mod. Phys. **71**, 1, (1999).

[WINEL 75] Wineland, D., Dehmelt, H., "*Proposed 10^14 Delta f < f Laser Fluorescence Spectroscopy on Tl+ Mono-Ion Oscillator III (side band cooling)*", Bull. Am. Phys. Soc.

20, 637 (1975).

[XU 02] Xu, X., Loftus, T.H., Smith, M.J., Hall, J.L., Gallagher, A., Ye, J., "*Dynamics in a Two-Level Atom Magneto-Optical Trap*", Phys. Rev. A, **66**, 011401(R), (2002).

[ZEMAN 94] Zeman, V., McEachran, R. P., Stauffer, A. D., "*Relativistic Distorted-Wave Calculation of Electron Impact Excitation of Caesium*", J. Phys. B, **27**, 3175, (1994).

[ZEMAN 95] Zeman, V., McEachran, R. P., Stauffer, A. D., "*A Test of the LS Approximation for Electron-Impact Excitation of Caesium*", J. Phys. B, **28**, 3063, (1995).

[ZAPES 69] Zapesochnyi, I. P., Aleksakhin, I. S., Sov. Phys. *JETP*, **28**, 41, (1969).

[ZAPES 76] Zapesochnyi, I. P., Postoi, E. N., Aleksakhin, I. S., "*Excitation of Resonance Levels of Alkali Metal Atoms by Electron Impact*", Sov. Phys. *JETP*, **41**, 865, (1976).

VITA AUCTORIS

John A. MacAskill was born in St. Catharines, Ontario and raised in Englishtown, Nova Scotia. He graduated from Baddeck Rural High School in 1992. In 1996, he started his undergraduate degree at St. Francis Xavier University, and graduated in 1999, with a Bachelor of Science, First Class Honours in Physics. He is currently a candidate for a Doctorate degree in Physics at the University of Windsor and hopes to graduate in the fall of 2003.